INVESTIGATION OF LOCAL GEOLOGY EFFECTS ON STRONG EARTHQUAKE GROUND MOTIONS

Thesis by

Moh-jiann Huang

In Partial Fulfillment of the Requirements
for the Degree of
Doctor of Philosophy

California Institute of Technology
Pasadena, California
1984
(Submitted July 18, 1983)

ACKNOWLEDGMENTS

The author wishes to express his sincere gratitude to his advisor, Professor G. W. Housner, for his guidance throughout this investigation. The counsel of Professor P. C. Jennings is greatly appreciated. The interesting discussions given by Professor R. F. Scott and by many members of the Earthquake Engineering Research Laboratory and the Seismological Laboratory are also acknowledged.

The financial support provided by the California Institute of Technology in the form of teaching and research assistantships is appreciated. The support of this investigation by a grant from the National Science Foundation is also acknowledged.

Finally, the author extends his heartfelt appreciation to his wife, Yueh-shya, for her patience and understanding throughout his years of graduate study.

ABSTRACT

Accelerograms recorded at four stations in the Pasadena area during the 1971 San Fernando, the 1970 Lytle Creek, the 1968 Borrego Mountain and the 1952 Kern County earthquakes are analyzed to investigate local geology effects on strong earthquake ground motions. Spatial variations of the ground motions at two nearby stations are also investigated. It is found that the ground motions in this area caused by the local geology effects depend on the 3-dimensional configuration of the local geology and the direction of arriving seismic waves. Local geology effects are less evident on the leading portions of the accelerograms than the trailing portions, indicating the effects of local geology on surface wave propagations. Comparison of the Fourier amplitudes of the motions recorded at the same station during different earthquakes shows that there are no significant spectral peaks can be identified as site periods. Hence, it is not appropriate to characterize such local sites by a site period.

A two-dimensional model considering inclined propagating P and S waves in a horizontal-layered structure, which is more realistic and closer to the actual seismic environment within a local geology than the one-dimensional model of vertically propagating waves, is studied. The transfer functions between the free surface and the half-space outcrop for a single incident P, SV or SH wave from the half-space at an incident angle are defined and derived by a matrix method. Two numerical examples are given to demonstrate the effects of incident angle and material damping on the transfer function. It is found that the transfer function between the free surface motions and the bedrock outcrop motions to multiple incident waves having different amplitudes, angles and arrival times is quite different from that for a single incident wave. Completely satisfactory results can not be expected when using the analytical model for evaluating the local geology effects on the motions during a nearby shallow-focus earthquake for which seismic waves emitted from different parts of the fault will approach the bedrock from different directions and at different angles.

The analytical model for assessing local geology effects is evaluated in the light of the data recorded at stations in the Pasadena area during the 1971 San Fernando earthquake. The observed site transfer functions between the alluvial and the rock sites are obtained and compared with the computed results from a two-dimensional model with 7-layers overlying a half-space. Values of model parameters are optimally adjusted to give a best least-squares fit between computed and observed amplitude ratios. It is concluded that the analytical model oversimplifies the local geological structure in the Pasadena area and the actual seismic environment in the area during the 1971 San Fernando earthquake.

It is concluded from these studies that the effects of the source mechanism and the seismic wave travel paths upon the site ground motion can be comparable to the effect of the local geology. The characteristics of the source mechanism, such as type of faulting, direction of fault-slip propagation, nature of stress drop across the fault surface, orientation of fault, depth beneath ground surface, etc., can appreciably influence the ground motion at the site. Also, the travel path can have a significant effect through influencing the types of waves that reach the site, and the directions of approach of the waves. The results of this study indicate that a better understanding of the spatial variation of ground motions, of the role played by different types of waves and their contributions to an accelerogram, and of the propagation directions of the waves is needed for assessing local geology effects on earthquake ground motions. A local array is desirable to provide data for giving a reasonably complete picture of the nature of ground motions in a local area.

TABLE OF CONTENTS

TABLE OF CONTENTS (Continued)

TABLE OF CONTENTS (Continued)

CHAPTER 1

INTRODUCTION

1.1 Introduction

It is well known that the nature of the ground shaking at a point depends on the source mechanism, the wave travel path and the local site geology. During the past decade several analytical methods have been proposed to model the local geology effects and to compute ground motion for design purposes. Most methods are usually based on the assumption of vertically propagating shear waves in a horizontal layered structure. However, these methods seem to oversimplify the actual seismic environment during a strong earthquake and the three-dimensional nature of the local geology configuration. Because of the lack of noticeable local geology effects in the earthquake records obtained at firm soil sites and the lack of measured bedrock motions, the ability of a simple model to evaluate local geology effects and calculate surface motions remains controversial.

The main objective of this thesis is to evaluate the analytical models in the light of recorded strong motions at stations in the Pasadena area, California. To this end, the records obtained at four stations in the Pasadena area during four past earthquakes are analyzed and the nature of strong ground motions are investigated. The two-dimensional model considering inclined propagating P and S waves, which is more realistic and closer to the actual seismic environment than the one-dimensional model, is studied. The limitations to the applicability of two-dimensional models to evaluate the local geology effects on earthquake ground motions are discussed.

1.1 General Features of Earthquake Ground Motion

Earthquake damage to engineering structures at a given location is known to depend on the nature of the arriving seismic waves as well as on the properties of the structures. For the purpose of engineering design, the significant characteristics of ground motions are the intensity of shaking, the duration of strong phase shaking and the frequency content of ground shaking. Broadly speaking, these characteristics are dependent on three factors: the earthquake source mechanism, the material properties of the earth media along which the seismic waves propagate from the source to the site, and the local site geology. It should be emphasized that the first two factors cover a scale of the order of tens of kilometers, while the third factor refers to a local region having a depth of approximately 300 meters and a horizontal dimension of less than several kilometers. A simple schematic representation of earthquake source region, transmission path, and the local site geology is shown in Fig. 1.1.

The complex nature of the earthquake source mechanism, the highly irregular structure of the earth's upper mantle and crust, and the need for special instrumental measurements make it difficult to clarify our understanding of the actual influences on ground motion. For example, the focus of a potentially destructive earthquake is not a point source but is a fault plane with dimensions ranging from several kilometers to several hundred kilometers. The fault slip does not necessarily take place along a plane, but may take place along an irregular surface. Generally speaking, there are four types of faulting, namely, strike-slip, thrust, normal and subduction faultings. Because of geometrical differences the characteristics of strong ground shaking in the vicinity of the causative fault may be significantly different for the different types of faulting. For example, theoretical studies, and some data, indicate that thrust-type

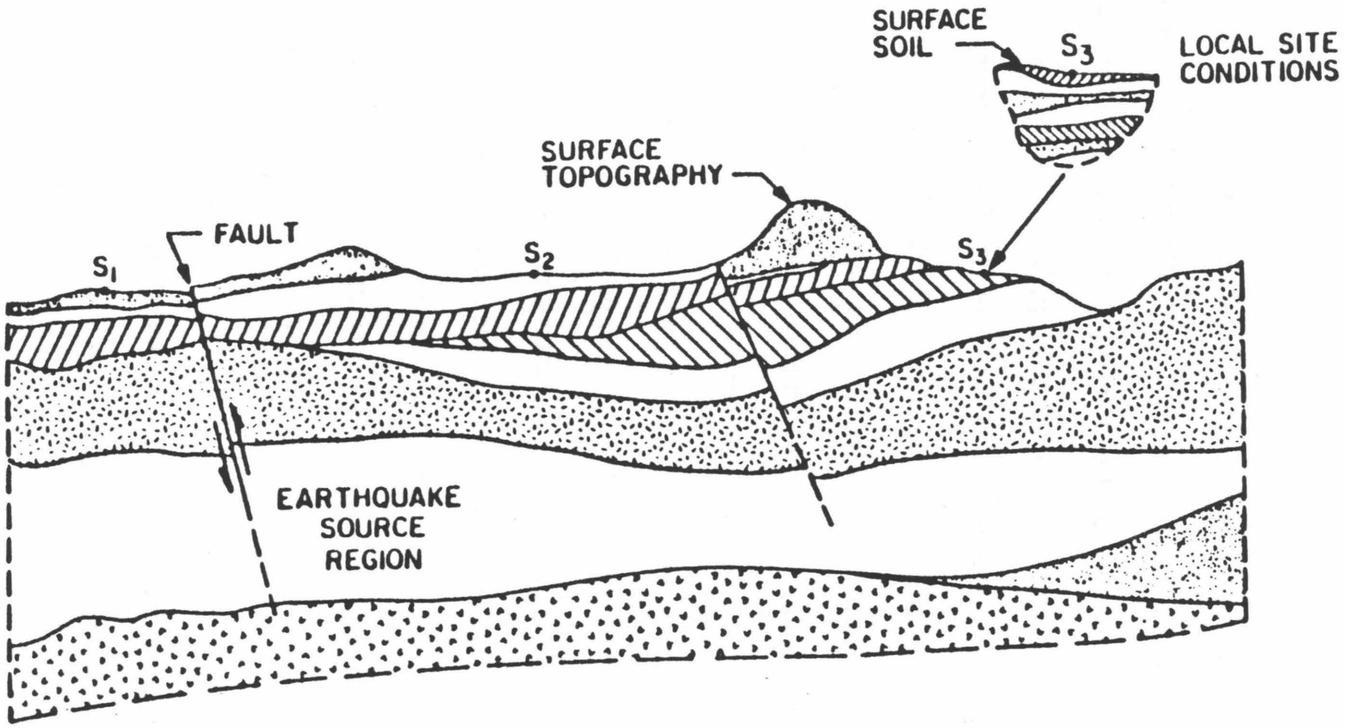

SCHEMATIC DIAGRAM SHOWING EARTHQUAKE SOURCE REGION, TRANSMISSION PATH, AND LOCAL SITE CONDITIONS

Fig. 1.1 A two-dimensional illustration of the problem of determining the effects of source mechanism, travel path and local geology on earthquake ground motions. (from Udwadia, 1972) earthquakes may produce significantly stronger near field shaking than strike-slip events.

Theoretical modeling of earthquakes and strong motion data have also indicated that the nature of the seismic waves generated by the fault slipping will depend on various source parameters such as the drop in stress across the fault during the faulting process, the speed at which the rupture travels over the fault surface, the relative direction of rupture propagation, the total fault dislocation, the frictional strength of the fault, the dimensions of the slipped area, the roughness of the slipping process, *etc.* These source parameters influence the frequency content, amplitude and duration of ground shaking. Furthermore, large magnitude earthquakes can be expected to be generated on fault areas that are elongated, that is, the length of faulting is much greater than the depth. More recently, strong-motion data has been used in seismology to deduce properties of the source mechanism (Jennings & Helmberger, 1978). This helps us understand the general features of the faulting mechanism. However, motions in the frequency ranges (1 Hz and higher) that dominate the ground velocity and acceleration are not as yet predicted successfully by deterministic models. To replicate motions at these frequencies would require more detailed models of the source mechanism and more detailed knowledge of the intervening geological structure. Earthquake engineers, on the other hand, have made considerable progress in empirical and statistical modeling of strong ground motion.

The seismic waves generated at the source are composed of both dilatational (P-wave) and shear (SH and SV waves) body waves. As the seismic waves radiate from the earthquake source, they undergo certain changes. The amplitudes of seismic waves will decrease with distance resulting from geometrical spreading as well as from media damping. High frequency waves attenuate more rapidly than low frequency waves. When a body wave encounters an interface or boundary that separates media of different properties, it will undergo reflection and transmission. Mode conversion between P and SV waves usually occurs, and the wave whose energy is trapped along the interface may exist. In addition to body waves there are also surface waves (Rayleigh and Love waves), whose energy is concentrated near the ground surface. The relative contributions of these waves to the total ground motion at a point and the corresponding arrival times for each type of wave depend on the focal depth of the earthquake source, the epicentral distance of the station and the configuration of the surface layers. At considerable distances from the earthquake source, P, S and surface waves separate from one another reasonably clearly, but near the source they are mixed in complicated ways. From past experience, the reader of the seismogram or accelerogram may roughly identify the arrivals of P and S waves. However, the exact partition of these waves is not known since the exact source mechanism is usually unknown and earth media are neither isotropic, homogeneous nor linear.

1.2 Influence of Local Geology on Earthquake Ground Motion

It has been reported that structures on loose soil are relatively more damaged during earthquakes than those on solid rock. This damage has long been ascribed to the influence of local site geology. The measured records of past earthquakes also illustrated the effects of local geology on the recorded motion. Gutenberg (1956, 1957) investigated small, distant earthquakes with sensitive seismometers located at several nearby sites in Pasadena, California. He observed relatively stronger shaking and longer duration at sites on alluvium than at those on crystalline rock, and large variations in ground shaking even at sites only a thousand feet apart. He also found that, for earthquake waves having periods of 1.0 to 1.5 seconds, the amplitude of the motion at sites on fairly dry alluvium more than 500 feet deep was about five times that recorded at the Seismological Laboratory of the California Institute of Technology, which is on an outcrop of crystalline rock. However, he considered that theoretical treatment of problems related to the effects of local site geology on ground shaking during strong earthquakes is difficult, since the surface layers are neither linear homogeneous nor bounded by horizontal planes.

Zeevaert (1964) has observed a dominant period of 2.5 seconds in the ground accelerations recorded at Mexico City in May, 1962 during two distant earthquakes (e.g., Fig. 1.2). Both earthquakes were located at approximately 260 kilometers from Mexico City and had focal depth of about 20 kilometers. The center of the city is on an old lake bed that has several hundred feet of very soft soil overlying firm material. The surface of the deep deposit oscillated essentially at the fundamental period of vibration of the soft soil. Herrera, *et al.* (1965) demonstrated the ability to calculate this fundamental period by a simple one-dimensional model with vertically propagating shear waves.

Hudson and Housner (1958) have presented and analyzed ground acceleration records obtained at five stations within 20 miles of the epicenter during the 1957 San Francisco earthquake (Fig. 1.3). The accelerograms in Fig. 1.3 clearly indicate the difference of the frequency content between the motions at the Golden Gate Park (rock site) and those at other four alluvial sites, having the depth of alluvium less than 300 feet.

The use of one-dimensional analyses has been encouraged by the quantitative comparisons of the predictions and observations at a number of sites where the local subsoils are soft, such as at Mexico City, San Francisco, Caracas and some locations in Japan. But records obtained during the 1971 San Fernando earthquake at stations on rock and firm alluvium indicate that such marked local

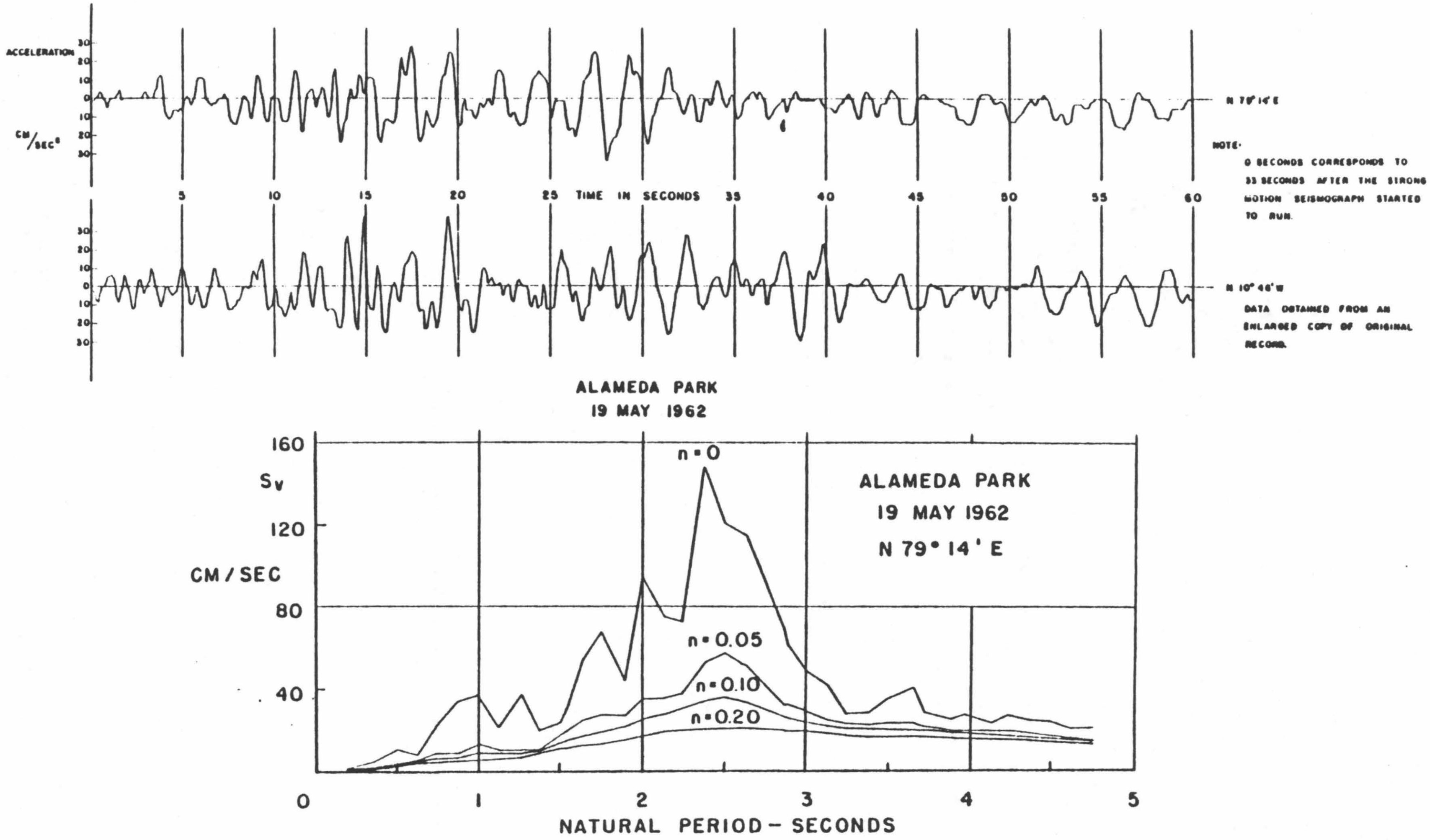

NOTE:
0 SECONDS CORRESPONDS TO 33 SECONDS AFTER THE STRONG MOTION SEISMOGRAPH STARTED TO RUN.

DATA OBTAINED FROM AN ENLARGED COPY OF ORIGINAL RECORD.

Fig. 1.2 Accelerations recorded at Alameda Park, Mexico City, during the earthquake of May 19, 1962 and the velocity response spectrum for the N79°14′E component. (from Jennings, 1962)

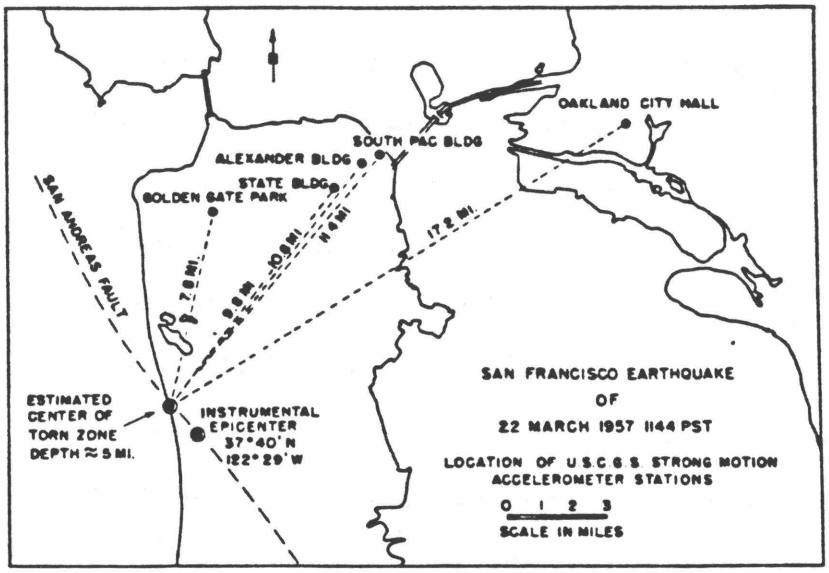

Locations of epicenter and strong-motion accelerometers.

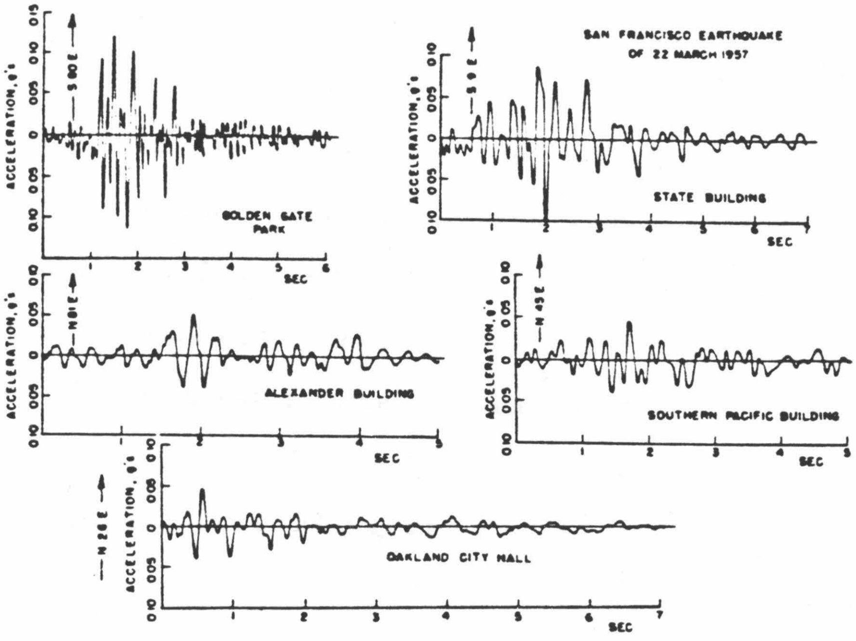

Typical accelerograms at the five recording stations. Note that acceleration scales are the same, but that the time scales vary.

Fig. 1.3 Strong-motion data from the San Francisco earthquake of March 22, 1957. (from Hudson and Housner, 1958) geology effects may not occur at these sites during strong earthquakes.

Based on a study of 15 accelerogams recorded at El Centro in southern California, Udwadia (1972) and Udwadia & Trifunac (1973) concluded that the characteristics of the source mechanism and travel path play dominant roles in determining the details of strong ground shaking at a site, and that no local site periodicities could be clearly identified in the spectra, which suggests that source and travel path effects overshadow the influence of local site geology. Hudson (1972) showed the local distributions of the maximum response of nineteen seismoscopes recorded in the Pasadena area during the 1971 San Fernando earthquake, and concluded that no single feature of local geology plays a dominant role in the resulting patterns. Crouse (1973) investigated and compared the accelerograms, Fourier amplitude spectra, and response spectra obtained in the 1971 San Fernando earthquake from a group of six tall buildings close together in Los Angeles and from seven surrounding buildings, two to three miles away. He found that local site conditions and soil-structure interaction were not major contributors to the observed difference in the response at these sites. A general discussion on the effect of local geology on recorded strong motions in southern California was presented by Jennings (1973). He recommended that concepts such as " the fundamental period of the soil " should be applied with caution unless recorded accelerograms have confirmed the existence of such site periods. Berrill (1975) examined the Fourier amplitude spectra of 71 strong-motion accelerograms obtained from the 1971 San Fernando earthquake in the 0.4 to 16 Hz frequency band and found no significant difference between accelerations recorded on sediments and basement rock.

At present, nobody doubts that local geology can influence the characteristics of earthquake ground motion. However, the question is: Under which circumstances will significant local geology effects occur in a predictable manner, and how adequate will simple models be for evaluating the effects? To answer this question on a theoretical basis is not a simple matter since there are many complexities in the propagation of seismic waves as well as irregularities and inhomogeneities in the geometric configurations and in the material properties of the local subsoil media. Hence, it is necessary to assess how well any local geology effect can be predicted by the available analytical methods using the soil profiles determined by geophysical and geotechnical methods, when compared with existing ground motion records.

Kanai (1952) and Takahasi (1955) were the first to propose a simple analysis. The most commonly used methods employ one-dimensional models for horizontally layered systems with vertically propagating shear waves. The analyses of two-dimensional models involving inclined propagating body waves or horizontally propagating surface waves, either considering horizontal layered structures or irregular structures, have been mainly of academic interest and have not been applied to earthquake engineering. The current analytical procedures in modeling the local geology effects are described in the state-of-the-art report by Lysmer (1978). A review of analytical models on this topic is given by Faccioli and Resendiz (1976). We shall not review the literature on the analytical methods that have been developed to study local geology effects. Detailed information can be found in the *Bulletin of the Seismological Society of America*. In the next section, we shall review some observations and applications of analytical models.

1.3 Observations and Applications

Earthquake engineers are most interested in the relative velocity response spectra of the ground motion, hence, tests of the validity of the one-dimensional model are in most cases done by comparisons of the observed with the predicted response spectra. The ground motion data available for testing analyses at specific sites have been limited. However, some case studies have been done and are reviewed here.

A classical example of the application of the one-dimensional model is given by the studies of the motions recorded at Mexico City by Herrera, *et al.* (1965). The soft ground, which was like jelly in a bowl, oscillated essentially at a relatively long period of 2.5 seconds which coincides with the fundamental period predicted by the one-dimensional model. However, Tsai and Housner (1970) point out that the epicenter of the earthquake was relatively distant so that the bowl of jelly was responding primarily to the passage of horizontally travelling waves of long wavelength rather than vertically incident waves. A period of 2.5 seconds corresponds to a half wavelength of about 4 kilometers which is sufficiently long for in-phase excitation of most of the bowl of jelly. The data recorded at four soil sites and one rock site during the 1957 San Francisco earthquake have been studied by Idriss & Seed (1968) using a lumped-mass model and equivalent linearization methods, and by Schnabel, Seed & Lysmer (1972b) by the one-dimensional continum methods. Schnabel *et al.* (1972a and b) suggested a procedure to predict the motions on soil deposits from the rock motions in an adjacent rock outcrop.

Ground motion data from downhole seismometer arrays have been studied by a number of researchers. Data from an array at the Tokyo Station were analyzed by Shima (1962) and Dobry, Whitman & Roesset (1971); data from a 31-m array in Union Bay, Seattle by Seed & Idriss (1970), Tsai & Housner (1970), and Dobry, Whitman & Roesset (1971); data from a 186-m array on the southwest shore of San Francisco Bay by Joyner, Warrick and Oliver (1976), and data from a 40-m array at the Richmond Field Station on the margin of San Francisco Bay by Johnson and Silva (1981). In all cases general agreement was claimed between observations and the predictions of simple one-dimensional analyses, but the amplitude of the motion was small and there are still appreciable errors in the details of the motion. It should be pointed out that the one-dimensional analysis has two parameters that can be adjusted for each layer: stiffness and damping, so that some degree of agreement can always be obtained, if the recorded motions are known.

Joyner, Warrick and Fumal (1981) studied the data obtained from the 1979 Coyote Lake, California, Earthquake, with local magnitude 5.9, and found no significant nonlinear soil behavior to occur during the earthquake. In an attempt to estimate quantitatively the effect of local geology on ground motion near San Francisco Bay, Borcherdt (1970) applied a spectral ratio method based on the theory of linear systems to the data obtained from nuclear explosions. This spectral ratio is the ratio of the absolute value of the Fourier transform obtained for a recording to that obtained from a simultaneous recording on a nearby bedrock location. Rogers & Hays (1978) and Hays, Rogers & King (1979) employed this method and used the data from nuclear explosions to study the consistency of site transfer functions between rock and soil sites for different events recorded at the same site.

The effect of local geology has been included in statistical studies of ground motion indices (e.g., Seed, Ugas & Lysmer, 1974; Trifunac & Brady, 1975; Trifunac, 1976; and Seed, Murarka, Lysmer & Idriss, 1976). To take into account the presumed effects of local geology on the ground motion, a site-structure resonance coefficient (S coefficient) was first added to the base shear equation in the 1976 Uniform Building Code, i.e.,

$$V = Z\,I\,K\,C\,S\,W\,.$$

The S coefficient depends on the degree of similarity between the fundamental period of vibration of the structure (T) and the fundamental period of the soil deposits (T_s) on which the structure is founded. Based on the current code, S can vary from 1.0 to a maximum of 1.5, depending on the ratio of T/T_s. However, the code does not define the meaning of fundamental period of the soil.

A simplified procedure for estimating the fundamental period of a soil profile based on the one-dimensional analysis is suggested by Dobry, Oweis and Urzua (1976). However, the spectra of California earthquakes usually do not show a dominant ground period. A site-matching process based on selecting individual strong motion records whose contributing factors approximately match those of the given site is suggested by Jennings and Guzman (1974). In considering local geology effects, the current earthquake resistant design process for major projects usually includes site response analyses and/or a site-matching procedure. For the site response analyses, the determination of the fundamental period of a given site is not an easy problem not only because of the simplifications employed in the models but also because of doubts about the degree to which laboratory or geotechnical measurements of soil properties are representative of the behavior of the soil during strong earthquakes.

Since 1975, the subsoil profiles at some accelerograph stations located in the United States have been investigated by Shannon & Wilson, Inc. and Agbabian Associates (SW-AA) under a contract with U.S. Nuclear Regulatory Commission and are published in several reports. A report by SW-AA (1980) summarizes the geotechnical data that were obtained from 83 accelerograph stations investigated during the period 1975-1979. It may be possible to test the reliability of the analytical approaches by means of these geotechnical data by comparing the calculated results with recorded ground motions.

1.4 Outline of This Thesis

This thesis is divided into five chapters. Chapter 1 is the Introduction.

Chapter 2 provides a basic review of the theory used to calculate the response of a multilayered structure to inclined incident body waves from the underlying half-space. The matrix method is reformulated to be suitable for using complex wave velocities, complex moduli and complex wavenumbers to analyze the wave attenuation effects in the soil. The transfer function between the free surface and the half-space outcrop for a single incident wave from the half-space at a specified incident angle is defined to represent the effect of the layered structure on the response to the incident wave. The effects of layer damping and incident angle on the transfer function are illustrated by two numerical examples: a single layered system and a multilayered system. The transfer functions for different incident angles and for different incident waves are also compared. The limitations of applying two-dimensional model to evaluate the local geology effects on earthquake motions are discussed.

In Chapter 3, all the data recorded at four stations in the Pasadena area during four past earthquakes, i.e., the 1971 San Fernando, the 1970 Lytle Creek, the 1968 Borrego Mountain and the 1952 Kern County earthquakes, are analyzed to investigate the nature of strong ground motions and examine local geology effects. The first shear wave and surface wave arrivals are approximately identified by using three components of recorded motions. The variation of the frequency content of recorded motions on the horizontal plane with the orientation of the accelerograph is shown by the maximum and the minimum Fourier amplitude spectra. The Fourier amplitude spectra of the accelerations recorded at each station during different earthquakes are compared to investigate possible site periods. The accelerograms recorded at two nearby stations are investigated in detail to study the spatial variations of ground motions.

In Chapter 4, the 1971 San Fernando earthquake records are used to evaluate the analytical model for a local site in the Pasadena area. The observed site transfer function is obtained by dividing the Fourier amplitude of the motions at an alluvial site by that at a rock site. The features of the observed site transfer functions are discussed. Due to the significant difference of the trailing motions between the rock site and alluvial sites, we also discuss the effects of local geology on the surface wave propagations. Observed amplitude ratios are compared with the computed amplitude ratios from the analytical model given in Chapter 2, having part of the soil properties available from geotechnical investigations. A systematic frequency domain identification technique is then employed to find the optimal model parameters which produce a least-squares match between the observed and the computed amplitude ratios. The quality of the analytical model is discussed and demonstrated by a comparison of computed and recorded motions.

The summary and conclusions are given in Chapter 5. Some suggestions for future research are also presented. The symbols used in Chapter 2 are listed in Appendix A. A brief description of the numerical minimization of a function of several variables by the method of steepest descent, which is adopted for the identification technique in Chapter 4, is given in Appendix B.

1.6 References

[1] Berrill, J. B. (1975), "A Study of High-frequency Strong Ground Motion from the San Fernando Earthquake," Soil Mechanics Laboratory, California Institute of Technology, Pasadena, 1975.

[2] Borcherdt, R. D. (1970), "Effects of Local Geology on Ground Motion near San Francisco Bay," *Bulletin of the Seismological Society of America*, Vol. **60**, No.1, February 1970, pp. 29-61.

[3] Crouse, C. B. (1973), "Engineering Studies of the San Fernando Earthquake," Report No. *EERL 73-04*, Earthquake Engineering Research Laboratory, California Institute of Technology, Pasadena, March 1973.

[4] Dobry, R., Whitman, R. V. and Roesset, J. M. (1971), "Soil Properties and the One-Dimensional Theory of Earthquake Amplification," Research Report No. *R71-18*, Department of Civil Engineering, Massachusetts Institute of Technology, Cambridge, May 1971.

[5] Dobry, R., Oweis, I and Urzua, A. (1976), "Simplified Procedures for Estimating the Fundamental Period of a Soil Profile," *Bulletin of the Seismological Society of America*, Vol. **66**, No.4, August 1976, pp. 1293-1321.

[6] Faccioli, E. and Resendiz, D. (1976), "Soil Dynamics: Behavior Including Liquefaction," in **Seismic Risk and Engineering Decisions**, editors: C. Lomnitz and E. Rosenblueth, Elsevier, Amsterdam, 1976, pp.71-140.

[7] Gutenberg, B. (1956), "Effects of Ground on Earthquake Motion, " *Transactions of American Geophysical Union*, Vol. **37**, No.6, 1956, pp. 757-760.

[8] Gutenberg, B. (1957), "Effects of Ground on Earthquake Motion, " *Bulletin of the Seismological Society of America*, Vol. **47**, No.3, 1957, pp. 221-250.

[9] Hays, W. W., Rogers, A. M. and King, K. W. (1979), "Empirical Data about Local Ground Response," *Proceedings of the Second U.S. National Conference on Earthquake Engineering*, Stanford University, 1979, Earthquake Engineering Research Institute, pp. 223-232.

[10] Herrera, I., and Rosenblueth, E. (1965a), "Response Spectra on Stratified Soil," *Proceedings of the Third World Conference on Earthquake Engineering*, New Zealand, 1965, Vol. **I**, pp. I.44-I.60.

[11] Herrera, I., Rosenblueth, E. and Rascon, O. (1965b), "Earthquake Spectrum Prediction for the Valley of Mexico," *Proceedings of the Third World Conference on Earthquake Engineering*, New Zealand, 1965, Vol. **I**, pp. I.61-I.74.

[12] Hudson, D. E. and Housner, G. W. (1958), "An Analysis of Strong-Motion Accelerometer Data from the San Francisco Earthquake of March 22, 1957," *Bulletin of the Seismological Society of America*, Vol. **48**, July 1958, pp. 253-268.

[13] Hudson, D. E. (1972), "Local Distribution of Strong Earthquake Ground Motion," *Bulletin of the Seismological Society of America*, Vol. **62**, No.6, December 1972, pp. 1765-1786.

[14] Idriss, I. M. and Seed, H. B. (1968), "An Analysis of Ground Motions during the 1957 San Francisco Earthquake," *Bulletin of the Seismological Society of America*, Vol. **58**, No.6, December 1968, pp. 2013-2032.

[15] Jennings, P. C. (1962), "Velocity Spectra of the Mexican Earthquakes of 11 May and 19 May, 1962," Earthquake Engineering Research Laboratory, California Institute of Technology, Pasadena, 1962.

[16] Jennings, P. C. (1973), "The Effect of Local Site Conditions on Recorded Strong Earthquake Motions," *Proceedings of the 42nd Annual Convention*, Structural Engineers Association of California, Coronado, October 1973, pp. 120-135.

[17] Jennings, P. C. and Guzman, R. A. (1975), "Seismic Criteria for Nuclear Powerplants," *Proceedings of the U.S. National Conference on Earthquake Engineering*, Ann Arbor, Michigan, Earthquake Engineering Research Institute, June 1975, pp. 474-483.

[18] Jennings, P. C. and Helmberger, D. V. (1978), "Strong-Motion Seismology," *Proceedings of the Second International Conference on Microzonation*, San Francisco, 1978, Vol. **I**, pp. 27-53.

[19] Johnson L.R. and Silva, W. (1981), "The Effects of Unconsolidated Sediments upon the Ground Motion during Local Earthquakes," *Bulletin of the Seismological Society of America*, Vol. **71**, February 1981, pp. 127-142.

[20] Joyner, W. B., Warrick, R. E. and Oliver, A. A. (1976), "Analysis of Seismograms from a Downhole Array in Sediments near San Francisco Bay," *Bulletin of the Seismological Society of America*, Vol. **66**, 1976, pp. 937-958.

[21] Joyner, W. B., Warrick, R. E. and Fumal, T. E. (1981), "The Effect of Quaternary Alluvium on Strong Ground Motion in the Coyote Lake, California, Earthquake of 1979," *Bulletin of the Seismological Society of America*, Vol. **71**, August 1981, pp. 1333-1349.

[22] Kanai, K. (1952), "Relations between the Nature of Surface Layer and the Amplitudes of Earthquake Motions, Part I to IV," *Bulletin of Earthquake Research Institute*, Tokyo University,
(I) Vol. **30**, 1952, pp. 31-37; (II) Vol. **31**, 1953, pp. 219-226;
(III) Vol. **31**, 1953, pp. 276-279; (IV) Vol. **34**, 1956, pp. 167-183.

[23] Lysmer, J. (1978), "Analytical Procedures in Soil Dynamics," Report No. *EERC 78-29*, Earthquake Engineering Research Center, University of California, Berkeley, December 1978.

[24] Rogers, A. M. and Hays, W. W. (1978), "Preliminary Evaluation of Site Transfer Functions Developed from Earthquakes and Nuclear Explosions," *Proceedings of the Second International Conference on Microzonation*, San Francisco, 1978, Vol. **II**, pp. 753-763.

[25] Schnabel, P. B., Lysmer, J. and Seed, H. B. (1972a), "SHAKE - A Computer Program for Earthquake Response Analysis of Horizontally Layered Sites," Report No. *EERC 72-12*, Earthquake Engineering Research Center, University of California, Berkeley, December 1972.

[26] Schnabel, P. B., Seed, H. B. and Lysmer, J. (1972b), "Modification of Seismograph Records for Effects of Local Soil Conditions," *Bulletin of the Seismological Society of America*, Vol. **62**, N0.6, December 1972, pp. 1649-1664.

[27] Seed, H. B. and Idriss, I. M. (1970), "Analysis of Ground Motions at Union Bay, Seattle during Earthquakes and Distant Nuclear Blasts," *Bulletin of the Seismological Society of America*, Vol. **60**, No.1, 1970, pp. 125-136.

[28] Seed, H. B., Ugas, C. and Lysmer, J. (1974), "Site-Dependent Spectra for Earthquake-Resistant Design," Report No. *EERC 74-12*, Earthquake Engineering Research Center, University of California, Berkeley, 1974.

[29] Seed, H. B., Murarka, R., Lysmer, J. and Idriss, I. M. (1976), "Relationships of Maximum Acceleration, Maximum Velocity, Distance from Source and Local Site Conditions for Moderately Strong Earthquakes," *Bulletin of the Seismological Society of America*, Vol. **66**, No.4, 1976, pp. 1323-1342.

[30] Shannon & Wilson, Inc. and Agbabian Associates (SW-AA) (1980), "Geotechnical Data from Accelerograph Stations Investigated During the Period 1975-1979, Summary Report," Prepared for U.S. Nuclear Regulatory Commission, *NUREG/CR-1643*, September 1980.

[31] Shima, E. (1962), "Modifications of Seismic Waves in Superficial Soil Layers as Verified by Comparative Observations on and beneath the Surface," *Bulletin of Earthquake Research Institute*, Tokyo University, Vol. **40**, 1962, pp. 187-259.

[32] Takahasi, R. (1955), "A Short Note on a Graphical Solution of the Spectral Response of the Ground," *Bulletin of Earthquake Research Institute*, Tokyo University, Vol. **33**, 1955, pp. 259-264.

[33] Trifunac, M. D. and Brady, A. G. (1975), "On the Correlation of Seismic Intensity Scales with the Peaks of Recorded Strong Ground Motion," *Bulletin Seismological Society of America*, Vol. **65**, No.1, 1975, pp. 139-162.

[34] Trifunac, M. D. (1976), "Preliminary Analysis of the Peaks of Strong Ground Motion - Dependence of Peaks on Earthquake Magnitude, Epicentral Distance, and Recording Site Conditions," *Bulletin Seismological Society of America*, Vol. **66**, No.1, February 1976, pp. 189-219.

[35] Tsai, N. C. and Housner, G. W. (1970), "Calculation of Surface Motions of a Layered Half-Space," *Bulletin Seismological Society of America*, Vol. **60**, No.5, October 1970, pp. 1625-1651.

[36] Udwadia, F. E. (1972), "Investigation of Earthquake and Microtremor Ground Motions," Report No. *EERL 72-02*, Earthquake Engineering Research Laboratory, California Institute of Technology, Pasadena, 1972.

[37] Udwadia, F. E. and Trifunac, D. M. (1973), "Comparison of Earthquake and Microtremor Ground Motions in El Centro, California," *Bulletin of the Seismological Society of America*, Vol. **63**, No.4, 1973, pp. 1227-1253.

[38] Zeevaert, L. (1964), "Strong Ground Motions Recorded during Earthquakes of May the 11th and 19th, 1962 in Mexico City," *Bulletin of the Seismological Society of America*, Vol. **54**, No.1, February 1964, pp. 209-231.

CHAPTER 2

BODY WAVE PROPAGATION IN MULTILAYERED MEDIA

2.1 Introduction

This chapter provides a basic review of the theory used to calculate the response of a multilayered medium to incident body waves from the underlying half-space. We consider a semi-infinite medium consisting of N parallel, homogeneous layers overlying a half-space. The system is assumed to be linear and the problem is studied in the frequency domain by finding the steady state response. Finding the transfer functions between the free surface and the half-space outcrop is essential in studying the influence of local geology on the frequency content of recorded earthquake ground motions. There exist some different methods for finding the transfer functions, however, the matrix formulation based on the plane wave propagation theory is adopted herein. In this chapter, we will not attempt to describe the historical development of the solutions we will present, but instead we will give a complete analytical method used in the numerical examples and our later local site study.

For readers not familiar with wave propagation theory, a number of texts, e.g., those by Ewing, Jardetzky & Press (1957), Miklowitz (1978), Aki & Richards (1980) and Ben-Menahem & Singh (1981), present the basic formulation of wave propagation problems. To gain an insight into the behavior of plane waves propagating in viscoelastic materials, see the papers by Buchen (1971) and Borcherdt (1973, 1977). Some basic equations and solutions will be used directly without explanations in this chapter. Appendix A gives a list of notations used in this chapter.

For a system consisting of N parallel, homogeneous layers overlying a half-space, there are N+1 boundaries, including the free surface. If a plane harmonic wave (SH, SV or P) approaches from the half-space at a certain angle of incidence, part of the wave is reflected back into the half-space and part is transmitted into the stratified medium above. Each layer has upgoing waves and downgoing waves such that the following boundary conditions are satisfied: continuity of the displacements and stresses at each interface (welded contact), and vanishing of the traction forces at the free surface. These lead to 2N+1 boundary conditions for SH waves and 4N+2 boundary conditions for SV and P waves. This problem is usually solved by the Thomson-Haskell matrix method (Thomson, 1950; Haskell, 1953). However, the matrix formulation can be further simplified for an incident SH wave.

The Thomson-Haskell matrix method was originally derived to compute the phase and group velocities of Rayleigh and Love waves in a layered structure. It involves solving the phase velocity dispersion equations and has been reformulated several times so that it can be efficiently implemented on the digital computer. The method has been extended to study the crustal reflections and transmissions of body waves in the earth crust. It can also be used to study local geology effects. Although this method can be found in the literature, different notations and formulations have been adopted by different researchers. Therefore, the method is reformulated in this chapter. To take into account the attenuation effects of anelastic media, complex wave velocities, complex moduli and complex wavenumbers are used.

In Section 2.2.1 of this chapter, we shall first demonstrate the matrix formulation for the simple case of a vertically incident SH wave from the underlying half-space. Because of its simplicity, this type of analysis is often carried out in the engineering studies. We then consider SH wave incident at a certain angle from the half-space in Section 2.2.2. The Thomson-Haskell matrix formulation for incident P or SV wave at an arbitrary angle is outlined in Section 2.3. The horizontal and vertical transfer functions between the free surface and the underlying half-space outcrop are defined. A numerical computational procedure for the transfer functions of incident P or SV wave, which considers anelastic attenuation effects, is presented.

In Section 2.4, the general features of transfer functions and the effects of material damping and incident angle are investigated in both the frequency and time domains by two numerical examples: a single layered system and a 7-layered system. The transfer functions for different incident angles and for different incident waves are also compared. Finally, in Section 2.5 we shall discuss how to apply the two-dimensional model to evaluate local geology effects on earthquake ground motions. Actual seismic environment in a local geological structure during a strong earthquake is more complex than what the model assumes. Even when surface waves are not considered and the model is appropriate for describing the local geological structure, the transfer function between the free surface response and the half-space outcrop response to multiple incident waves arriving at different times and different angles is not exactly the same as that for a single incident wave at a specified incident angle. Some numerical examples are given to illustrate this.

2.2 Incident SH Wave

2.2.1 Multilayered System with Vertically Incident SH Waves

The system is shown in Fig. 2.1. It consists of N horizontal layers of viscoelastic materials overlying a viscoelastic half-space. We consider the steady-state response of the system excited by vertically incident homogeneous harmonic SH waves. By definition, the wave is said to be homogeneous if its propagation and attenuation vectors are parallel (Borcherdt, 1973). For a homogeneous SH wave approaching vertically, the transmitted and reflected waves are also

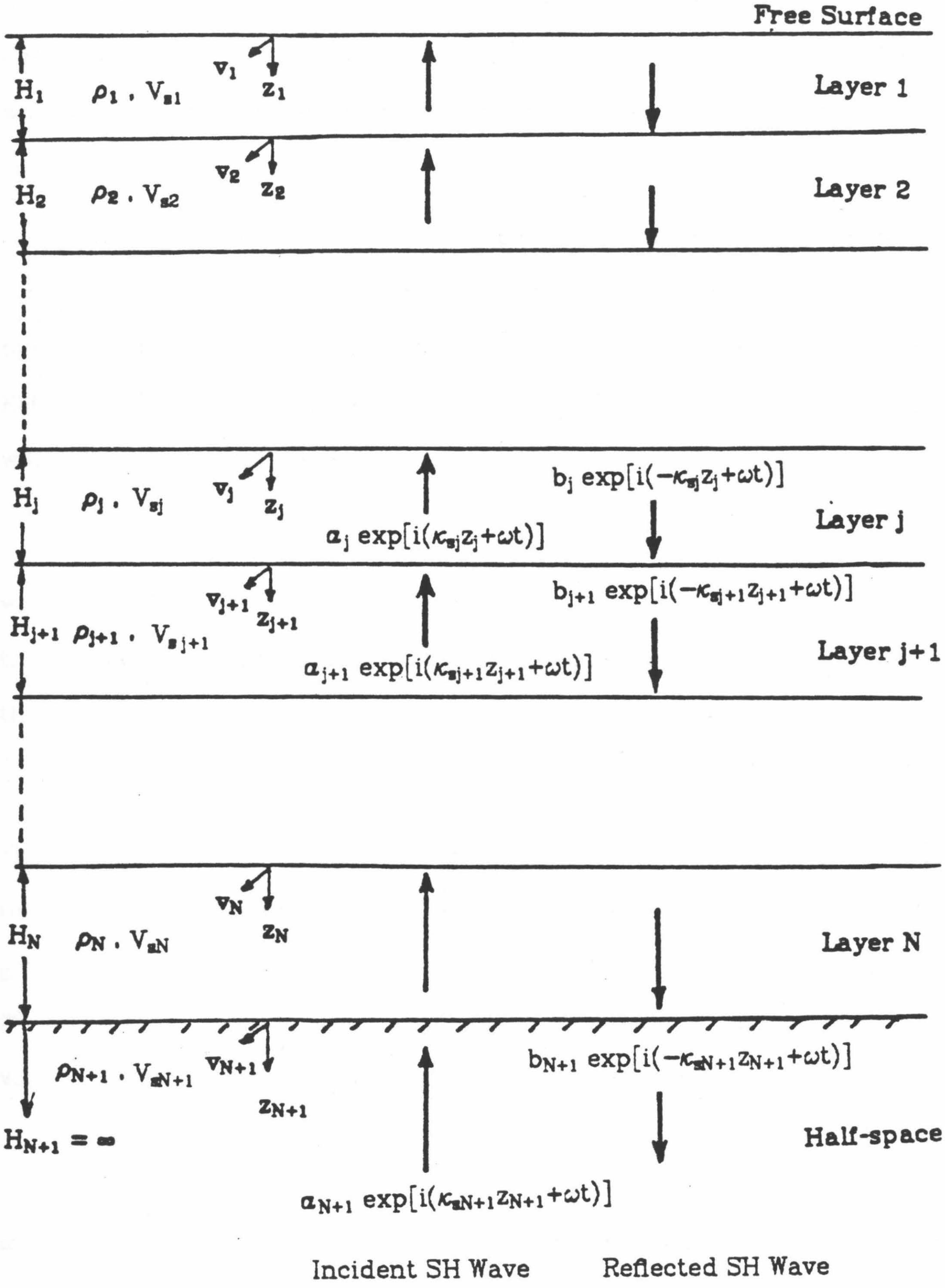

Fig. 2.1 N-layer system with vertically incident SH wave.

homogeneous and vertically propagating. All displacements are horizontal in the y-direction and all the motions at points on the same horizontal plane are in phase and of equal amplitude. Each layer is homogeneous, isotropic and is characterized by the complex shear wave velocity, V, (or by the elastic shear wave velocity, c_s, and the quality factor, Q), the thickness, H, and the mass density, ρ.

The following formulation of this problem is similar to those presented by Tsai (1970), Roesset (1970), and Schnabel *et al.* (1972). However, the viscoelastic model used here is not restricted to any specific type such as the Voigt type. Referring to the coordinate system in Fig. 2.1, we can write the displacements within the jth layer in the form

$$v_j(z_j,t) = [\ \alpha_j\, e^{i\kappa_{sj} z_j} + b_j\, e^{-i\kappa_{sj} z_j}\ ]\, e^{i\omega t} \quad , \quad 0 \le z_j \le H_j \tag{2.2.1}$$

where ω is the frequency, $i = \sqrt{-1}$ and κ_{sj} is the complex shear wavenumber in the jth layer, which is related to the complex shear wave velocity, V_{sj}, through the relation

$$\kappa_{sj} = \omega / V_{sj}\ . \tag{2.2.2}$$

The first term in (2.2.1) represents the superposition of all upgoing waves in the negative z_j-direction and the second term represents the superposition of downgoing waves in the positive z_j-direction. Both terms satisfy the wave equation $\partial^2 v/\partial z^2 = 1/V_s^2\ \partial^2 v/\partial t^2$. The amplitude coefficients α_j and b_j are complex-valued. The shear stresses within the jth layer are given by

$$\tau_j(z_j,t) = \bar{\mu}_j \frac{\partial v_j}{\partial z} = i\, \bar{\mu}_j\, \kappa_{sj}\, [\ \alpha_j\, e^{i\kappa_{sj} z_j} - b_j\, e^{-i\kappa_{sj} z_j}\ ]\, e^{i\omega t} \tag{2.2.3}$$

where $\bar{\mu}_j$ is the complex shear modulus and τ_j represents the shear stress σ_{zy} in the y-direction. By solving the boundary conditions at the interface between the jth and the j+1th layers, i.e.,

$$v_j(H_j,t) = v_{j+1}(0,t) \tag{2.2.4a}$$

and

$$\tau_j(H_j,t) = \tau_{j+1}(0,t)\ , \tag{2.2.4b}$$

the following recursion formulas are obtained:

$$a_{j+1} = \frac{1}{2}(1+\alpha_j)\, a_j\, e^{i\kappa_{sj}H_j} + \frac{1}{2}(1-\alpha_j)\, b_j\, e^{-i\kappa_{sj}H_j} \tag{2.2.5a}$$

$$b_{j+1} = \frac{1}{2}(1-\alpha_j)\, a_j\, e^{i\kappa_{sj}H_j} + \frac{1}{2}(1+\alpha_j)\, b_j\, e^{-i\kappa_{sj}H_j} \tag{2.2.5b}$$

where α_j is the complex impedance ratio between the jth and the j+1th layers and is given by

$$\alpha_j = \frac{\bar{\mu}_j\, \kappa_{sj}}{\bar{\mu}_{j+1}\kappa_{sj+1}} = \frac{\rho_j\, V_{sj}}{\rho_{j+1}V_{sj+1}}\ . \tag{2.2.6}$$

The recursion formulas in (2.2.5) can be written in the following matrix form:

$$\begin{Bmatrix} a_{j+1} \\ b_{j+1} \end{Bmatrix} = [\ \alpha\ ]_j\, [\ H\ ]_j \begin{Bmatrix} a_j \\ b_j \end{Bmatrix},\quad j=1,2,\cdots,N \tag{2.2.7}$$

where

$$[\ \alpha\ ]_j = \begin{bmatrix} \frac{1}{2}(1+\alpha_j) & \frac{1}{2}(1-\alpha_j) \\ \frac{1}{2}(1-\alpha_j) & \frac{1}{2}(1+\alpha_j) \end{bmatrix} \tag{2.2.8a}$$

and

$$[\ H\ ]_j = \begin{bmatrix} e^{i\kappa_{sj}H_j} & 0 \\ 0 & e^{-i\kappa_{sj}H_j} \end{bmatrix}\ . \tag{2.2.8b}$$

At the free surface, the shear stress is zero, hence from equation (2.2.3) we have

$$a_1 = b_1 = \frac{1}{2}a_0 \tag{2.2.9}$$

where a_0 is the total displacement amplitude at the free surface. Beginning with the surface layer, repeated use of (2.2.7), a_{j+1} and b_{j+1} can be expressed in terms of a_1, i.e.,

$$\begin{Bmatrix} a_{j+1} \\ b_{j+1} \end{Bmatrix} = [\ \alpha\ ]_j\,[\ H\ ]_j \cdots [\ \alpha\ ]_1\,[\ H\ ]_1 \begin{Bmatrix} a_1 \\ a_1 \end{Bmatrix}, \quad j=1,2,\cdots,N \tag{2.2.10}$$

or

$$a_{j+1} = A_j(\omega)\, a_1\,,\quad b_{j+1} = B_j(\omega)\, a_1\,,\quad j=1,2,\cdots,N \tag{2.2.11}$$

where

$$\begin{Bmatrix} A_j(\omega) \\ B_j(\omega) \end{Bmatrix} = [\ \alpha\ ]_j\,[\ H\ ]_j \cdots [\ \alpha\ ]_1\,[\ H\ ]_1 \begin{Bmatrix} 1 \\ 1 \end{Bmatrix}, \quad j=1,2,\cdots,N\,. \tag{2.2.12}$$

It is noted that $A_j(\omega)$, $B_j(\omega)$ are complex and functions of frequency ω. The transfer function between the motions at the top of layer j and the top of layer k is defined by

$$TF(j/k) = v_j(z_j=0,t)/v_k(z_k=0,t)\,. \tag{2.2.13}$$

By using (2.2.1) and (2.2.11), TF(j/k) can be written as

$$TF(j/k) = \frac{a_j + b_j}{a_k + b_k} = \frac{A_{j-1}(\omega) + B_{j-1}(\omega)}{A_{k-1}(\omega) + B_{k-1}(\omega)}\,. \tag{2.2.14}$$

The transfer function between the motions at the free surface and the top of the half-space is then given by

$$TF(1/N+1) = \frac{2\,a_1}{a_{N+1} + b_{N+1}} = \frac{2}{A_N(\omega) + B_N(\omega)}\,. \tag{2.2.15}$$

If one considers the case of the half-space without the layered structure on its top, the motion at the free surface of the half-space due to the incident wave of $a_{N+1} \exp(i\,\kappa_{sN+1}\, z_{N+1} + i\omega t)$ will be $2\, a_{N+1} \exp(i\omega t)$. Consequently, we have the following transfer function between the motions at the free surface and the half-space outcrop:

$$\mathrm{TR}(\omega) = \frac{2\,a_1}{2\,a_{N+1}} = \frac{1}{A_N(\omega)}\,. \tag{2.2.16}$$

This transfer function is often used to indicate the influence of local site geology on earthquake ground motions. The modulus of TR(ω) gives the ratio of the amplitude of the motion on the top of the layered soil overlying the bedrock subject to vertically incident SH waves to the amplitude of the motion that would be at the surface of the bedrock if there were no superficial layers. The plot of the modulus of TR(ω) versus frequency ω is called the amplitude ratio spectrum herein.

The explicit expressions for the transfer functions defined above in terms of layer properties are too long and complex. However, the numerical computation of these functions, using the matrix form, is simple on a digital computer. It is seen from the preceding derivation that transfer functions represent the system characteristics, they are the ratios of displacements as well as velocities and accelerations at two different points in the system. The complex shear modulus representing the viscoelastic property of the jth layer is defined by

$$\overline{\mu}_j = \mu_j\,(1 + i\,Q_j^{-1}) \tag{2.2.17}$$

and the complex shear wave velocity in the jth layer is given by

$$V_{sj} = \sqrt{\overline{\mu}_j/\rho_j} = c_{sj}\,\sqrt{1 + i\,Q_j^{-1}} \tag{2.2.18}$$

where μ_j , Q_j are the shear modulus and the quality factor of the jth layer, respectively, and $c_{sj} = \sqrt{\mu_j/\rho_j}$ is the elastic shear wave velocity in the jth layer. The quality factor, Q, is usually assumed to be independent of frequency. Strictly speaking, the Q's are not constant at all frequencies and the velocity must be dispersive in attenuating media because of the causality (Futterman, 1962). However, since the frequency-dependence can be made weak over a finite frequency band of engineering interest, the effect of this assumption is negligible. Furthermore, the quality factor is commonly used in Seismology, while the critical damping ratio, ζ_d, is used by engineers. For small material damping, they can be related through the following equation:

$$Q^{-1} = 2\,\zeta_d\,, \qquad \text{for } Q^{-1} \ll 1\,. \tag{2.2.19}$$

For either the shear wave or the longitudinal wave, we can write the complex wave velocity, V, as

$$V = c\sqrt{1 + i\,Q^{-1}} = V_R + i\,V_I\,, \quad V_R > 0\,,\ V_I \ge 0\,, \tag{2.2.20}$$

and the complex wavenumber, κ_c, as

$$\kappa_c = \omega/V = \kappa_R + i\,\kappa_I\,,\ \ \kappa_R > 0,\ \ \kappa_I \le 0\,, \tag{2.2.21}$$

where $c = c_s = \sqrt{\mu/\rho}$ for the shear wave and $c = c_p = \sqrt{(\lambda+2\mu)/\rho}$ for the longitudinal wave. λ is the Lame's constant. From (2.2.20) and (2.2.21), the real and imaginary parts of V and κ_c are given by

$$V_R^2 = \frac{1}{2}c^2\,[\,1 + (1+Q^{-2})^{1/2}\,]\,,\quad V_I^2 = \frac{1}{2}c^2\,[-\,1 + (1+Q^{-2})^{1/2}\,], \tag{2.2.22}$$

and

$$\kappa_R^2 = \frac{1}{2}\,\frac{\omega^2}{c^2}\,[1+Q^{-2}]^{-1}\,[\,1 + (1+Q^{-2})^{1/2}\,]\,, \tag{2.2.23a}$$

$$\kappa_I^2 = \frac{1}{2}\,\frac{\omega^2}{c^2}\,[1+Q^{-2}]^{-1}\,[-\,1 + (1+Q^{-2})^{1/2}\,]\,. \tag{2.2.23b}$$

The real parts are positive and the signs of imaginary parts should be chosen properly to obtain attenuating waves along the propagation direction. Since we use exp($i\omega t$) to represent the harmonic waves in (2.2.1), V_I is ≥ 0 and κ_I is ≤ 0. On the other hand, the opposite sign should be used if exp($-i\omega t$) is employed. In fact, the transfer functions obtained in two cases are complex conjugate and the amplitude ratios are identical. However, to obtain the transfer function in the time domain, the expression of inverse Fourier transform should be consistent with the time factor employed to derive the transfer function.

2.2.2 Multilayered System with Inclined Incident SH Waves

We now consider the response of a layered system due to an inclined incident SH wave from the half-space at an arbitrary angle Θ_{N+1}. The layered system and the coordinate system are shown in Fig. 2.2. The angle Θ_j is real in an elastic layer except when total reflection occurs. However, total reflection does not occur in a layered structure having larger shear wave velocity at the deeper layer. The angles Θ_j is in general complex in a viscoelastic layer, and we can use the propagation vector, $\vec{P}_j$, and the attenuation vector, $\vec{A}_j$, to interpret Θ_j. The angle formed by the propagation vector in the jth layer with the normal to the layer boundary is denoted by φ_j, while γ_j is the angle between the propagation and attenuation vectors in the jth layer.

Referring to the coordinate system in Fig. 2.2, the displacement field in the jth layer can be written in the form

$$v_j(x,z_j,t) = [\ a_j\, e^{i\,\kappa_{szj}\,z_j} + b_j\, e^{-i\,\kappa_{szj}\,z_j}\ ]\, e^{-i\,\kappa_{sxj}\,x}\, e^{i\omega t} \tag{2.2.24}$$

in which the vertical shear wavenumber, κ_{szj}, and the horizontal shear wavenumber, κ_{sxj}, in the jth layer are defined by

$$\kappa_{szj} = \kappa_{sj} \cos\Theta_j\ , \quad \kappa_{sxj} = \kappa_{sj} \sin\Theta_j \tag{2.2.25a}$$

and

$$[\kappa_{szj}]^2 + [\kappa_{sxj}]^2 = [\kappa_{sj}]^2\ , \quad \kappa_{sj} = \omega / V_{sj}\ . \tag{2.2.25b}$$

The angle Θ_j is not necessary real and is related to Θ_{N+1} through Snell's law. The solution in (2.2.24) is the sum of upward and downward propagating SH waves, both are propagating in the positive x-direction. The shear stresses within the jth layer are given by

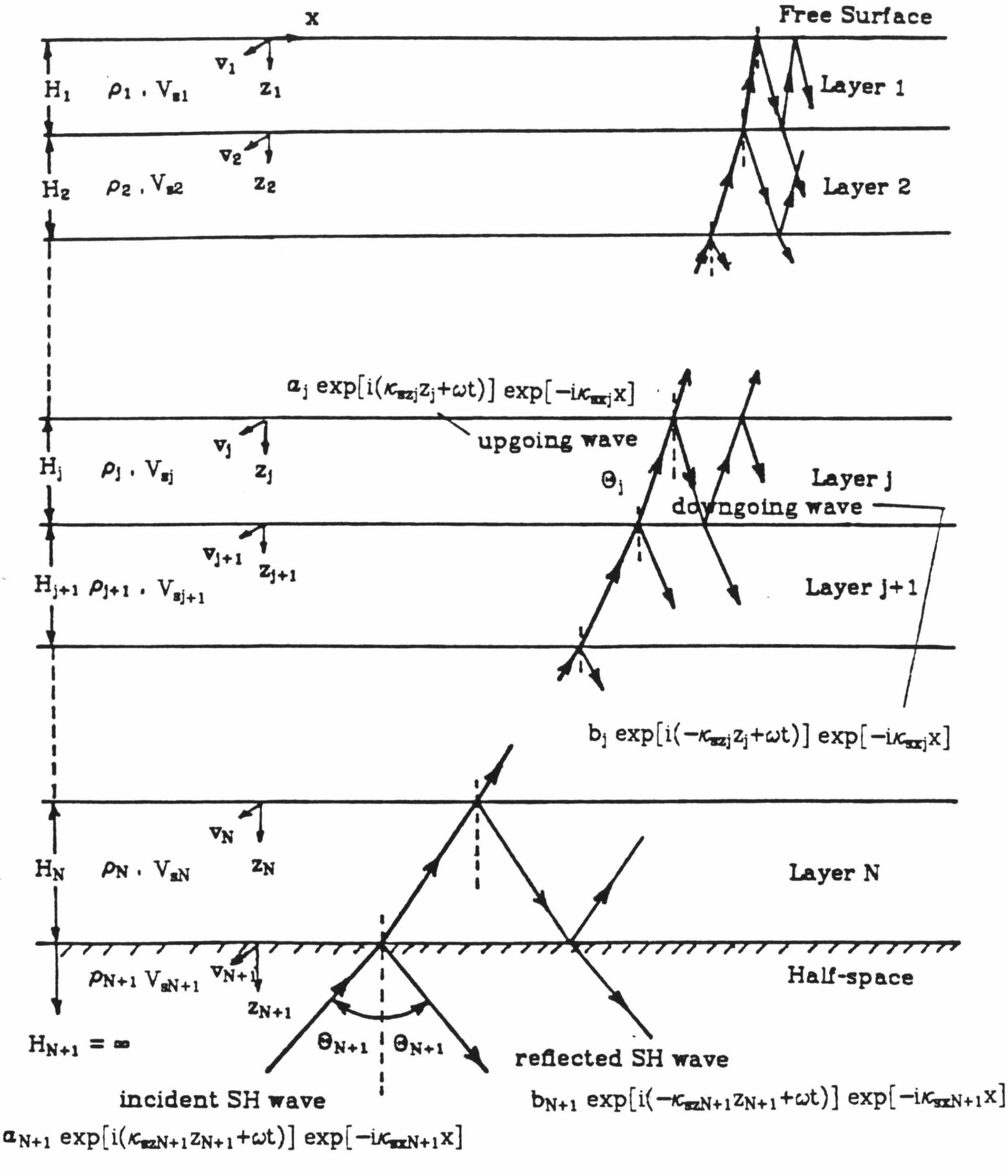

Fig. 2.2 N-layer system with inclined incident SH wave.

$$\tau_j(x,z_j,t) = i\,\bar{\mu}_j\,\kappa_{szj}\,[\,a_j\,e^{i\kappa_{szj}z_j} - b_j\,e^{-i\kappa_{szj}z_j}\,]\,e^{-i\kappa_{sxj}x}\,e^{i\omega t}\,. \tag{2.2.26}$$

By solving the boundary conditions in (2.2.4), we obtain Snell's law, which will be discussed later, and the following recursion formulas:

$$a_{j+1} = \frac{1}{2}(1+\alpha_j)\,a_j\,e^{i\kappa_{szj}H_j} + \frac{1}{2}(1-\alpha_j)\,b_j\,e^{-i\kappa_{szj}H_j} \tag{2.2.27a}$$

$$b_{j+1} = \frac{1}{2}(1-\alpha_j)\,a_j\,e^{i\kappa_{szj}H_j} + \frac{1}{2}(1+\alpha_j)\,b_j\,e^{-i\kappa_{szj}H_j} \tag{2.2.27b}$$

where the complex impedance ratio α_j is defined by

$$\alpha_j = \frac{\bar{\mu}_j\,\kappa_{szj}}{\bar{\mu}_{j+1}\kappa_{szj+1}} = \frac{\rho_j\,V_{sj}\,\cos\Theta_j}{\rho_{j+1}V_{sj+1}\cos\Theta_{j+1}} \tag{2.2.28}$$

which reduces to that in (2.2.6) when $\Theta_j = \Theta_{j+1} = 0$. The recursion formulas in (2.2.27) can be written in the same matrix form as (2.2.7) except that α_j in (2.2.8a) is given by (2.2.28) and the matrix $[\,H\,]_j$ in (2.2.8b) is replaced by

$$[\,H\,]_j = \begin{bmatrix} e^{i\kappa_{szj}H_j} & 0 \\ 0 & e^{-i\kappa_{szj}H_j} \end{bmatrix}. \tag{2.2.29}$$

The transfer functions derived in (2.2.14), (2.2.15) and (2.2.16) are also applicable to this case provided that (2.2.28) and (2.2.29) are used to compute (2.2.12).

Snell's law, obtained by solving the boundary conditions, is

$$\kappa = \kappa_{sxj} = \kappa_{sxN+1}\,, \quad j=1,2,\cdots,N\,. \tag{2.2.30a}$$

From (2.2.25), this can also be written as

$$\sin\Theta_j/V_{sj} = \sin\Theta_{N+1}/V_{sN+1}\,, \quad j=1,2,\cdots,N \tag{2.2.30b}$$

where Θ_j is in general complex for waves in a viscoelastic layer and we can introduce two angles, φ_j and γ_j, to interpret Θ_j. We can write (Borchert, 1973, 1977; Krebes & Hron, 1980)

$$\kappa_{sxj} = P_{xj} - i\,A_{xj}\,,\quad \kappa_{szj} = P_{zj} - i\,A_{zj}\,,\quad j=1,2,\cdots,N+1 \tag{2.2.31}$$

and

$$P_{xj} = |\vec{P}_j|\,\sin\varphi_j\,,\qquad A_{xj} = |\vec{A}_j|\,\sin(\varphi_j - \gamma_j) \tag{2.2.32a}$$

$$P_{zj} = |\vec{P}_j|\,\cos\varphi_j\,,\qquad A_{zj} = |\vec{A}_j|\,\cos(\varphi_j - \gamma_j) \tag{2.2.32b}$$

where $|\vec{P}_j|$ and $|\vec{A}_j|$ are the magnitudes of the propagation vector, $\vec{P}_j$, and the attenuation vector, $\vec{A}_j$, respectively. They can be expressed in terms of Q_j, γ_j and c_{sj}, by

$$|\vec{P}_j|^2 = \frac{\omega^2}{c_{hj}^2}\left[\frac{1+\sqrt{1+Q_j^{-2}/\cos^2\gamma_j}}{1+\sqrt{1+Q_j^{-2}}}\right] \tag{2.2.33a}$$

$$|\vec{A}_j|^2 = \frac{\omega^2}{c_{hj}^2}\left[\frac{-1+\sqrt{1+Q_j^{-2}/\cos^2\gamma_j}}{1+\sqrt{1+Q_j^{-2}}}\right] \tag{2.2.33b}$$

where c_{hj} is defined by

$$c_{hj}^2 = c_{sj}^2\left[\frac{2(1+Q_j^{-2})}{1+\sqrt{1+Q_j^{-2}}}\right]. \tag{2.2.33c}$$

Equations (2.2.30a) and (2.2.31) lead to the viscoelastic form of Snell's law, i.e., A_x and P_x must be continuous across the layer boundary and hence we have

$$|\vec{P}_j|\,\sin\varphi_j = |\vec{P}_{N+1}|\,\sin\varphi_{N+1}\,,\quad j=1,2,\cdots,N \tag{2.2.34a}$$

and

$$|\vec{A}_j|\,\sin(\varphi_j - \gamma_j) = |\vec{A}_{N+1}|\,\sin(\varphi_{N+1} - \gamma_{N+1})\,,\quad j=1,2,\cdots,N\,. \tag{2.2.34b}$$

Given φ_{N+1} and γ_{N+1} in the half-space, $|\vec{P}_{N+1}|$ and $|\vec{A}_{N+1}|$ can be computed from the properties of the half-space by using the relations in (2.2.33). The complex value of κ is obtained from the values of P_x and A_x by (2.2.30a) and (2.2.31). From κ and given layer properties, we can compute κ_{szj} for the jth layer by using (2.2.25b) and (2.2.30a). The values of κ_{szj} for different layers are then used to compute the transfer functions. This procedure does not involve finding the angles φ_j and γ_j in each layer. To obtain φ_j and γ_j, we have to solve two equations in (2.2.34) simultaneously, since $|\vec{P}_j|$ and $|\vec{A}_j|$ are functions of γ_j.

It is interesting to note that the angle Θ_j is real and equal to φ_j, if the waves in the jth layer are homogeneous (i.e., $\gamma_j = 0$). This can be proved as follows: For homogeneous waves, the propagation and attenuation vectors lie in the same direction, from (2.2.32) and $\gamma_j = 0$ we have

$$\tan\varphi_j = \frac{P_{xj}}{P_{zj}} = \frac{A_{xj}}{A_{zj}} \tag{2.2.35}$$

On the other hand, according to (2.2.25a) and (2.2.31), we can write

$$\tan\Theta_j = \frac{\kappa_{sxj}}{\kappa_{szj}} = \frac{P_{xj} - i\,A_{xj}}{P_{zj} - i\,A_{zj}} \tag{2.2.36}$$

It follows from (2.2.35) and (2.2.36) that

$$\tan\Theta_j = \tan\varphi_j \ , \qquad \Theta_j = \varphi_j \ . \tag{2.2.37}$$

It is also noted that SH waves in the layered system are in general inhomogeneous, even though the incident SH wave from the half-space is homogeneous. Furthermore, if any layer has the same quality factor as the half-space and the incident SH wave from the half-space is homogeneous, the SH wave is homogeneous within that layer. Given layer properties of the system, the transfer functions are functions of ω, Θ_{N+1} and γ_{N+1}, and reduce to those for the normal incidence in Section 2.2.1 when $\Theta_{N+1} = \gamma_{N+1} = 0$.

2.3 Incident P or SV Wave

In the case of incident P or SV wave, two potentials which satisfy the wave equation can be used. The displacements and stresses can be expressed in terms of two potentials, Φ and Ψ. The problem of reflection and transmission of P and SV waves at an interface will not be discussed here, but for more detail on this, one can refer to standard texts, e.g., Ewing *et al.* (1957), Miklowitz (1978) and Aki & Richards (1980). We now consider the layered system shown in Fig. 2.3. A plane SV wave is incident from the half-space at an arbitrary angle, Θ_{N+1}. Because of the coupling of SV and P waves, in each layer a pair of P waves (upgoing and downgoing) and a pair of SV waves (upgoing and downgoing) will appear. The following formulation is similar to that presented by Thomson (1950) and Haskell (1953, 1962). However, displacement potentials are used here. A similar formulation using time factor exp(-iωt) and displacement potentials is shown in the texts by Brekhovskikh (1960, 1980). We shall formulate this problem in such a way that the attenuation effect can be taken into account easily in the numerical computations. We shall use time factor exp(iωt). This is analogous to that by Silva (1976). Although Fig. 2.3 only shows incident SV waves from the half-space, in what follows we shall see that the formulation for incident SV waves is also applicable to the problem for incident P waves.

Referring to the notation and the coordinate system in Fig. 2.3, we now consider layer number j. According to plane harmonic wave solutions, the expressions for the potentials of the P and SV waves in the jth layer can be written as (omitting the index j for brevity)

$$\Phi = \Phi_1+\Phi_2 = [\, A_1\, e^{i\kappa_{pz} z} + A_2\, e^{-i\kappa_{pz} z} \,]\, e^{-i\kappa_{px} x}\, e^{i\omega t} \qquad (2.3.1a)$$

$$\Psi = \Psi_1+\Psi_2 = [\, B_1\, e^{i\kappa_{sz} z} + B_2\, e^{-i\kappa_{sz} z} \,]\, e^{-i\kappa_{sx} x}\, e^{i\omega t} \qquad (2.3.1b)$$

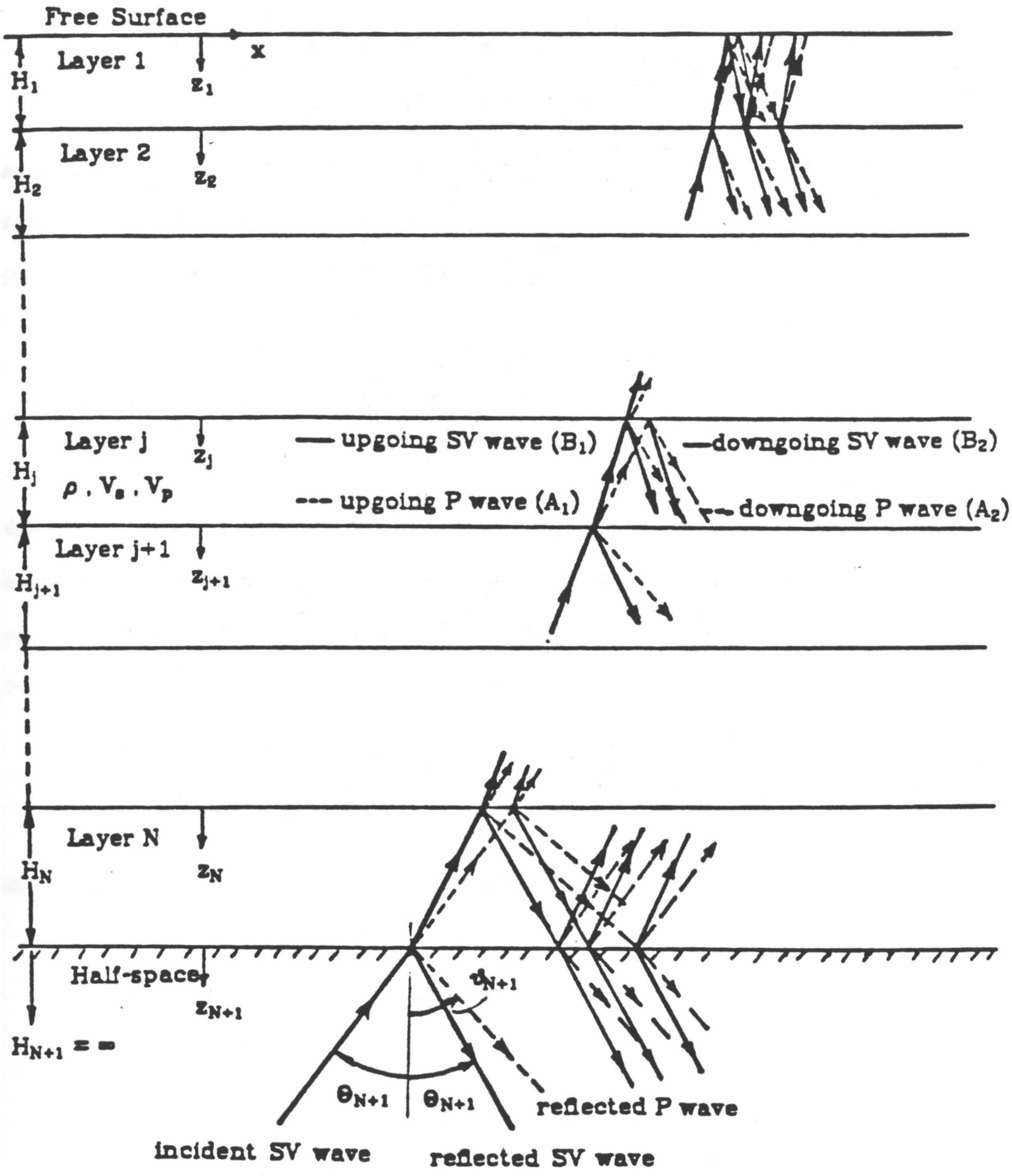

Fig. 2.3 N-layer system with inclined incident SV wave.

where Φ_1, Ψ_1 represent the upgoing waves, Φ_2, Ψ_2 represent the downgoing waves, and

$$\kappa_{px} = \kappa_p \sin\vartheta\,, \quad \kappa_{pz} = \kappa_p \cos\vartheta\,, \quad \kappa_{px}^2 + \kappa_{pz}^2 = \kappa_p^2 \tag{2.3.2a}$$

$$\kappa_{sx} = \kappa_s \sin\Theta\,, \quad \kappa_{sz} = \kappa_s \cos\Theta\,, \quad \kappa_{sx}^2 + \kappa_{sz}^2 = \kappa_s^2 \tag{2.3.2b}$$

κ_p and κ_s are complex wavenumbers associated with the P and SV waves, respectively, and related to frequency, ω, complex P wave velocity, V_p, and complex shear wave velocity, V_s, through the relations

$$\kappa_p = \omega / V_p\,, \; \kappa_s = \omega / V_s \quad \text{or} \quad \omega = \kappa_p V_p = \kappa_s V_s\,. \tag{2.3.3}$$

As in the case of SH waves, Snell's law gives

$$\kappa = \kappa_{px} = \kappa_{sx} = \kappa_p \sin\vartheta = \kappa_s \sin\Theta \tag{2.3.4}$$

where the horizontal wavenumbers, κ_{px} and κ_{sx}, are equal in all layers and a number κ is introduced to represent the common quantity of all layers. Since all the harmonic waves will contain one common factor $\exp[i(-\kappa x+\omega t)]$, we shall omit it for simplicity and rewrite (2.3.1) in the form

$$\Phi = A_1 e^{i\kappa_{pz} z} + A_2 e^{-i\kappa_{pz} z} \tag{2.3.5a}$$

$$\Psi = B_1 e^{i\kappa_{sz} z} + B_2 e^{-i\kappa_{sz} z}\,. \tag{2.3.5b}$$

Also from (2.3.1) we have the following relations:

$$\frac{\partial\Phi}{\partial x} = -i\kappa\Phi\,, \quad \frac{\partial\Phi}{\partial t} = i\omega\Phi \tag{2.3.6a}$$

$$\frac{\partial\Psi}{\partial x} = -i\kappa\Psi\,, \quad \frac{\partial\Psi}{\partial t} = i\omega\Psi \tag{2.3.6b}$$

$$\nabla^2\Phi + \kappa_p^2\Phi = 0\,, \quad \nabla^2\Psi + \kappa_s^2\Psi = 0\,. \tag{2.3.7}$$

Using (2.3.1), (2.3.5), (2.3.6) and (2.3.7), the components of displacement, u and w, are given by

$$u = \partial\Phi/\partial x - \partial\Psi/\partial z = -i\,\kappa\,\Phi - \partial\Psi/\partial z$$

$$= -i\,\kappa\cos\kappa_{pz}z\,(A_1 + A_2) + \kappa\sin\kappa_{pz}z\,(A_1 - A_2)$$

$$-i\,\kappa_{sz}\cos\kappa_{sz}z\,(B_1 - B_2) + \kappa_{sz}\sin\kappa_{sz}z\,(B_1 + B_2) \qquad (2.3.8)$$

and

$$w = \partial\Phi/\partial z + \partial\Psi/\partial x = \partial\Phi/\partial z - i\,\kappa\,\Psi$$

$$= i\,\kappa_{pz}\cos\kappa_{pz}z\,(A_1 - A_2) - \kappa_{pz}\sin\kappa_{pz}z\,(A_1 + A_2)$$

$$-i\,\kappa\cos\kappa_{sz}z\,(B_1 + B_2) + \kappa\sin\kappa_{sz}z\,(B_1 - B_2)\,. \qquad (2.3.9)$$

Similarly, the stress components are given by

$$\sigma_{zz} = \lambda\,\nabla^2\,\Phi + 2\mu\,\partial^2\Phi/\partial z^2 + 2\mu\,\partial^2\Psi/\partial z\partial x$$

$$= \rho\,V_s^2\,(\kappa^2-\kappa_{sz}^2)\,\Phi - i\,2\,\rho\,V_s^2\,\kappa\,\partial\Psi/\partial z$$

$$= \rho V_s^2(\kappa^2-\kappa_{sz}^2)\,[\,\cos\kappa_{pz}z\,(A_1+A_2) + i\sin\kappa_{pz}z\,(A_1-A_2)\,]$$

$$+ 2\rho V_s^2\kappa\,\kappa_{sz}\,[\,\cos\kappa_{sz}z\,(B_1-B_2) + i\sin\kappa_{sz}z\,(B_1+B_2)\,] \qquad (2.3.10)$$

and

$$\sigma_{zx} = 2\mu\,\partial^2\Phi/\partial z\partial x + \mu\,(\,\partial^2\Psi/\partial x^2 - \partial^2\Psi/\partial z^2\,)$$

$$= -i\,2\,\rho\,V_s^2\,\kappa\,\partial\Phi/\partial z - \rho\,V_s^2\,(\kappa^2-\kappa_{sz}^2)\,\Psi$$

$$= 2\rho V_s^2\kappa\,\kappa_{pz}\,[\,\cos\kappa_{pz}z\,(A_1-A_2) + i\sin\kappa_{pz}z\,(A_1+A_2)\,]$$

$$-\rho V_s^2(\kappa^2-\kappa_{sz}^2)\,[\,\cos\kappa_{sz}z\,(B_1+B_2) + i\sin\kappa_{sz}z\,(B_1-B_2)\,]\,. \qquad (2.3.11)$$

The displacements and stresses at the bottom of the jth layer, i.e. at $z_j = H_j$ can be conveniently written in the following matrix form:

$$\begin{Bmatrix} u(H_j) \\ w(H_j) \\ \sigma_{zz}(H_j) \\ \sigma_{zx}(H_j) \end{Bmatrix}_j = \begin{bmatrix} -i\kappa C_p & \kappa S_p & -i\kappa_{sz} C_s & \kappa_{sz} S_s \\ -\kappa_{pz} S_p & i\kappa_{pz} C_p & \kappa S_s & -i\kappa C_s \\ \zeta C_p & i\zeta S_p & \xi \kappa_{sz} C_s & i\xi \kappa_{sz} S_s \\ i\xi \kappa_{pz} S_p & \xi \kappa_{pz} C_p & -i\zeta S_s & -\zeta C_s \end{bmatrix}_j \begin{Bmatrix} A_1+A_2 \\ A_1-A_2 \\ B_1-B_2 \\ B_1+B_2 \end{Bmatrix}_j \tag{2.3.12}$$

where

$$C_p = \cos(\kappa_{pz}\, H_j)\ , \qquad C_s = \cos(\kappa_{sz}\, H_j)\ , \tag{2.3.13a}$$

$$S_p = \sin(\kappa_{pz}\, H_j)\ , \qquad S_s = \sin(\kappa_{sz}\, H_j)\ , \tag{2.3.13b}$$

$$\xi = 2\, \rho\, V_s^2\, \kappa\ , \qquad \zeta = \rho\, V_s^2\, (\, \kappa^2 - \kappa_{sz}^2\,)\ . \tag{2.3.13c}$$

This matrix form may be denoted as

$$\Big\{X(H_j)\Big\}_j = [J(H_j)]_j \Big\{Y\Big\}_j\ , \quad j=1,2,\cdots,N\ . \tag{2.3.14}$$

We may call $\{X(H_j)\}_j$ displacement-stress vector, $\{\,Y\,\}_j$ potential vector and $[J(H_j)]_j$ propagation matrix in the jth layer. The propagation matrix is evaluated from κ and the layer properties of the jth layer. In fact, the matrix form for the displacements and stresses at $z=z_j$ within the jth layer can be written as

$$\Big\{X(z_j)\Big\}_j = [J(z_j)]_j \Big\{Y\Big\}_j\ , \quad 0 \le z_j \le H_j \tag{2.3.15}$$

and (2.3.14) is the value of (2.3.15) at $z_j = H_j$.

The boundary conditions at the interface between the jth and the j-1th layers require continuity of the displacements and stresses, i.e.,

$$\Big\{X(H_{j-1})\Big\}_{j-1} = \Big\{X(0)\Big\}_j = [J(0)]_j \Big\{Y\Big\}_j\ , \ j=1,2,\cdots,N+1\ . \tag{2.3.16}$$

By setting $H_j = 0$ in (2.3.13), $[J(0)]_j$ can be obtained and (2.3.16) is written as

$$\begin{Bmatrix} u(H_{j-1}) \\ w(H_{j-1}) \\ \sigma_{zz}(H_{j-1}) \\ \sigma_{zx}(H_{j-1}) \end{Bmatrix}_{j-1} = \begin{bmatrix} -i\kappa & 0 & -i\kappa_{sz} & 0 \\ 0 & i\kappa_{pz} & 0 & -i\kappa \\ \zeta & 0 & \xi\kappa_{sz} & 0 \\ 0 & \xi\kappa_{pz} & 0 & -\zeta \end{bmatrix}_j \begin{Bmatrix} A_1+A_2 \\ A_1-A_2 \\ B_1-B_2 \\ B_1+B_2 \end{Bmatrix}_j . \qquad (2.3.17)$$

Solving the set of linear equations in (2.3.17), we have

$$\begin{Bmatrix} A_1+A_2 \\ A_1-A_2 \\ B_1-B_2 \\ B_1+B_2 \end{Bmatrix}_j = [J(0)]_j^{-1} \begin{Bmatrix} u(H_{j-1}) \\ w(H_{j-1}) \\ \sigma_{zz}(H_{j-1}) \\ \sigma_{zx}(H_{j-1}) \end{Bmatrix}_{j-1} \qquad (2.3.18a)$$

or

$$\begin{Bmatrix} Y \end{Bmatrix}_j = [J(0)]_j^{-1} \begin{Bmatrix} X(H_{j-1}) \end{Bmatrix}_{j-1} , \quad j=1,2,\cdots,N+1 \qquad (2.3.18b)$$

where $[J(0)]_j^{-1}$ is given by

$$[J(0)]_j^{-1} = \frac{1}{\rho\omega^2} \begin{bmatrix} i\xi & 0 & -1 & 0 \\ 0 & i\zeta/\kappa_{pz} & 0 & \kappa/\kappa_{pz} \\ -i\zeta/\kappa_{sz} & 0 & \kappa/\kappa_{sz} & 0 \\ 0 & i\xi & 0 & 1 \end{bmatrix}_j . \qquad (2.3.19)$$

It is noted that the determinant of $[J(0)]_j$ is $\kappa_{pz}\kappa_{sz}\rho\omega^2$, which is not equal to 0 for $\omega \neq 0$, hence the inverse of $[J(0)]_j$ exists and is given in (2.3.19). Substituting the results in (2.3.18b) into (2.3.14), we obtain the following recurrence formula:

$$\begin{Bmatrix} X(H_j) \end{Bmatrix}_j = [J(H_j)]_j \, [J(0)]_j^{-1} \begin{Bmatrix} X(H_{j-1}) \end{Bmatrix}_{j-1}$$

$$= [\, \mathbf{a} \,]_j \begin{Bmatrix} X(H_{j-1}) \end{Bmatrix}_{j-1} , \qquad j=1,2,\cdots,N \qquad (2.3.20)$$

or

$$\begin{Bmatrix} u(H_j) \\ w(H_j) \\ \sigma_{zz}(H_j) \\ \sigma_{zx}(H_j) \end{Bmatrix}_j = \begin{bmatrix} a_{11} & a_{12} & a_{13} & a_{14} \\ a_{21} & a_{22} & a_{23} & a_{24} \\ a_{31} & a_{32} & a_{33} & a_{34} \\ a_{41} & a_{42} & a_{43} & a_{44} \end{bmatrix}_j \begin{Bmatrix} u(H_{j-1}) \\ w(H_{j-1}) \\ \sigma_{zz}(H_{j-1}) \\ \sigma_{zx}(H_{j-1}) \end{Bmatrix}_{j-1} \qquad (2.3.21)$$

where the matrix $[\mathbf{a}]_j$ is

$$[\ \mathbf{a}\ ]_j = [J(H_j)]_j\, [J(0)]_j^{-1} \ , \quad j=1,2, \cdots ,N\ . \qquad (2.3.22)$$

After a thorough operation of (2.3.22), the elements of $[\ \mathbf{a}\ ]_j$ are given by

$$a_{11} = (2\kappa^2/\kappa_s^2)\ C_p - [(\kappa^2-\kappa_{sz}^2)/\kappa_s^2]\ C_s$$

$$a_{12} = i\kappa\ [(\kappa^2-\kappa_{sz}^2)/(\kappa_{pz}\kappa_s^2)\ S_p + (2\kappa_{sz}/\kappa_s^2)\ S_s]$$

$$a_{13} = i\kappa/(\rho\omega^2)\ [C_p - C_s]$$

$$a_{14} = 1/(\rho\omega^2)\ [(\kappa^2/\kappa_{pz})\ S_p + \kappa_{sz}\ S_s]$$

$$a_{21} = -\ i\kappa\ [(2\kappa_{pz}/\kappa_s^2)\ S_p + (\kappa^2-\kappa_{sz}^2)/(\kappa_{sz}\kappa_s^2)\ S_s]$$

$$a_{22} = -\ (\kappa^2-\kappa_{sz}^2)/\kappa_s^2\ C_p + (2\kappa^2/\kappa_s^2)\ C_s$$

$$a_{23} = 1/(\rho\omega^2)\ [\kappa_{pz}\ S_p + (\kappa^2/\kappa_{sz})\ S_s]$$

$$a_{24} = a_{13}$$

$$a_{31} = i\ 2\rho V_s^2\kappa(\kappa^2-\kappa_{sz}^2)/\kappa_s^2\ [C_p - C_s]$$

$$a_{32} = -\ \rho V_s^2/\kappa_s^2\ [(\ (\kappa^2-\kappa_{sz}^2)^2/\kappa_{pz}\ )\ S_p + 4\kappa^2\kappa_{sz}\ S_s]$$

$$a_{33} = a_{22}$$

$$\alpha_{34} = \alpha_{12}$$

$$\alpha_{41} = -\rho V_s^2/\kappa_s^2\,[4\kappa^2\kappa_{pz}\,S_p + (\,(\kappa^2-\kappa_{sz}^2)^2/\kappa_{sz}\,)\,S_s]$$

$$\alpha_{42} = \alpha_{31}$$

$$\alpha_{43} = \alpha_{21}$$

$$\alpha_{44} = \alpha_{11}\,. \tag{2.3.23}$$

It is interesting to note that the elements of $[\mathbf{a}]_j$ are symmetric with respect to the line drawn from α_{41} to α_{14}.

By applying (2.3.20) repeatedly, the displacement-stress vector at the bottom of the jth layer is related to that at the free surface through the following relation:

$$\left\{X(H_j)\right\}_j = [\,\mathbf{a}\,]_j\,[\,\mathbf{a}\,]_{j-1}\cdots[\,\mathbf{a}\,]_1\left\{X(0)\right\}_1\,,\quad j=1,2,\cdots,N \tag{2.3.24}$$

where $\{X(0)\}_1$ is the displacement-stress vector at the free surface and given by

$$\left\{X(0)\right\}_1 = \begin{Bmatrix} u_0 \\ w_0 \\ 0 \\ 0 \end{Bmatrix}, \tag{2.3.25}$$

u_0 and w_0 being the horizontal and vertical displacements at the free surface, respectively. From (2.3.24) and (2.3.16) for j=N, the displacement-stress vector at the top of the half-space, $\{X(0)\}_{N+1}$, is equal to $\{X(H_N)\}_N$ and given by

$$\left\{X(0)\right\}_{N+1} = [\,\mathbf{a}\,]_N\,[\,\mathbf{a}\,]_{N-1}\cdots[\,\mathbf{a}\,]_1\left\{X(0)\right\}_1 = [\,\bar{A}\,]\left\{X(0)\right\}_1 \tag{2.3.26}$$

where the 4×4 matrix $[\,\bar{A}\,]$ is defined by

$$[\,\bar{A}\,] = [\,\mathbf{a}\,]_N\,[\,\mathbf{a}\,]_{N-1}\cdots[\,\mathbf{a}\,]_1\,. \tag{2.3.27}$$

Denoting u_N and w_N as the displacements at the top of the half-space, from (2.3.26) we have

$$u_N = \bar{A}_{11}\,u_0 + \bar{A}_{12}\,w_0 \tag{2.3.28a}$$

$$w_N = \bar{A}_{21}\,u_0 + \bar{A}_{22}\,w_0\,. \tag{2.3.28b}$$

Equations (2.3.28) show the coupling between the horizontal and vertical displacements. The coefficients in (2.3.28) are dependent on the angle of incidence for incident P waves or incident SV waves.

The potential vector $\{Y\}_{N+1}$ in the half-space are related to the displacement-stress vector $\{X(H_N)\}_N$ at the top of the half-space by (2.3.18), that is

$$\begin{Bmatrix} Y \end{Bmatrix}_{N+1} = [J(0)]_{N+1}^{-1} \begin{Bmatrix} X(H_N) \end{Bmatrix}_N \tag{2.3.29}$$

where

$$\begin{Bmatrix} Y \end{Bmatrix}_{N+1} = \begin{Bmatrix} A_1+A_2 \\ A_1-A_2 \\ B_1-B_2 \\ B_1+B_2 \end{Bmatrix}_{N+1} = \begin{Bmatrix} A_1^{N+1}+A_2^{N+1} \\ A_1^{N+1}-A_2^{N+1} \\ B_1^{N+1}-B_2^{N+1} \\ B_1^{N+1}+B_2^{N+1} \end{Bmatrix}, \tag{2.3.30}$$

A_1^{N+1}, A_2^{N+1}, B_1^{N+1} and B_2^{N+1} being the amplitudes of displacement potentials in the half-space. Substitution of (2.3.26) into (2.3.29) gives the following relation between the potential vector in the half-space and the displacement-stress vector at the free surface:

$$\begin{Bmatrix} Y \end{Bmatrix}_{N+1} = [J(0)]_{N+1}^{-1}\,[\,\bar{A}\,] \begin{Bmatrix} X(0) \end{Bmatrix}_1 = [\,\bar{B}\,] \begin{Bmatrix} X(0) \end{Bmatrix}_1 \tag{2.3.31}$$

where the matrix $[\bar{B}]$ is defined by

$$[\,\bar{B}\,] = [J(0)]_{N+1}^{-1}\,[\,\bar{A}\,]\,. \tag{2.3.32}$$

Expanding (2.3.31) and using the notations in (2.3.30), we have

$$A_1^{N+1} + A_2^{N+1} = \bar{B}_{11}\,u_0 + \bar{B}_{12}\,w_0 \tag{2.3.33a}$$

$$A_1^{N+1} - A_2^{N+1} = \bar{B}_{21}\,u_0 + \bar{B}_{22}\,w_0 \tag{2.3.33b}$$

$$B_1^{N+1} - B_2^{N+1} = \bar{B}_{31}\,u_0 + \bar{B}_{32}\,w_0 \tag{2.3.33c}$$

$$B_1^{N+1} + B_2^{N+1} = \bar{B}_{41}\,u_0 + \bar{B}_{42}\,w_0\,. \tag{2.3.33d}$$

We now deal with the problems of incident P and SV waves separately. For notations, refer to Fig. 2.4.

(a) Incident P Waves: For the case of incident P waves with a potential amplitude A_1^{N+1}, we set $B_1^{N+1} = 0$ in (2.3.33). Then the four unknowns, A_2^{N+1} (reflected P into the half-space), B_2^{N+1} (reflected SV into the half-space) and two components of displacement, u_0 and w_0, at the free surface can be determined in terms of A_1^{N+1} by solving a set of four equations in (2.3.33). Two solutions of them, u_0 and w_0, are given by (using the subscript p to indicate this particular case)

$$u_{0p} = \quad 2\,[\bar{B}_{32} + \bar{B}_{42}]\,A_{1p}^{N+1}/D_p \tag{2.3.34a}$$

$$w_{0p} = -\,2\,[\bar{B}_{31} + \bar{B}_{41}]\,A_{1p}^{N+1}/D_p \tag{2.3.34b}$$

where

$$D_p = (\bar{B}_{11}+\bar{B}_{21})\,(\bar{B}_{32}+\bar{B}_{42}) - (\bar{B}_{12}+\bar{B}_{22})\,(\bar{B}_{31}+\bar{B}_{41})\,. \tag{2.3.35}$$

Knowing the angle of incidence for incident P waves, ϑ_{N+1}, from which the matrix $[\bar{B}]$ is evaluated, and the incident potential amplitude, A_{1p}^{N+1}, we can compute the surface displacements from (2.3.34). It is noted that equations (2.3.34) give two crustal transfer functions relating the output, u_0 or w_0, to the input A_{1p}^{N+1}. These transfer functions depend upon the layered structure and the angle of incidence.

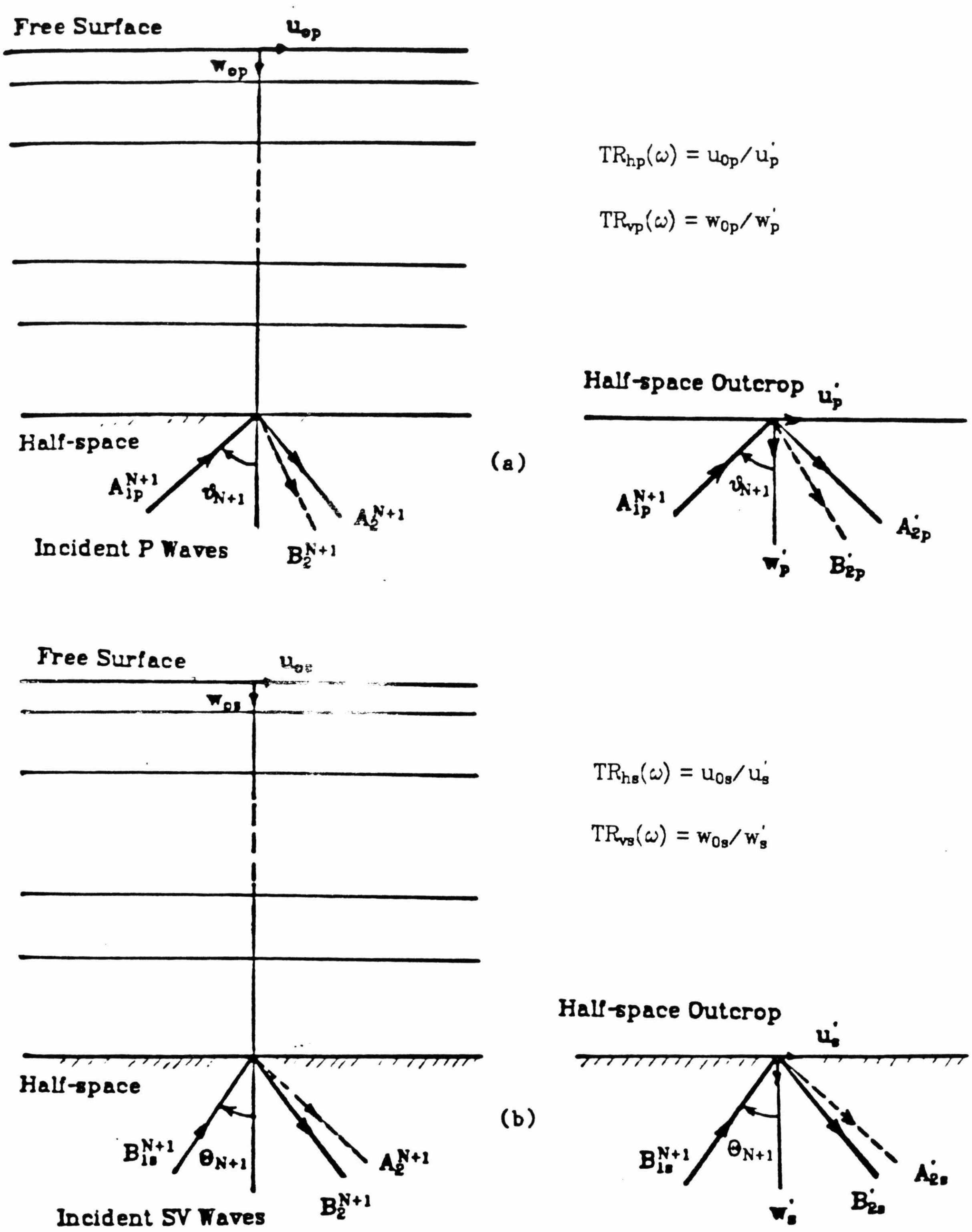

Fig. 2.4 Notation for the derivation of the horizontal and vertical transfer functions between the free surface and the half-space outcrop for (a) incident P waves, and (b) incident SV waves. The wave incident on the half-space outcrop is the same as that at the half-space below the layered medium.

Dividing two crustal transfer functions by each other, we obtain a ratio which is called the crustal transfer function ratio:

$$\mathrm{CTR_p}(\omega) = \frac{w_{0p}}{u_{0p}} = -\frac{\overline{B}_{31} + \overline{B}_{41}}{\overline{B}_{32} + \overline{B}_{42}} . \tag{2.3.36}$$

This ratio is independent of the incident potential and depends on the frequency, the layered structure and the angle of incidence. The crustal transfer ratio spectrum, which is a plot of crustal transfer function ratio versus frequency, has been used by seismologists in the study of crustal structure.

To study the effect of the layered structure on the motions observed at the free surface, let us see what the response would be at the top of the half-space excited by the same incident P wave if there were no superficial layers. Let u_p' and w_p' be the displacements at the half-space outcrop and A_{2p}' , B_{2p}' be the potential amplitudes for the reflected P and SV waves due to the incidence of P wave with A_{1p}^{N+1}, respectively. In this case, we have $B_1^{N+1} = \sigma_{zz} = \sigma_{zx} = 0$ in (2.3.17) and

$$\begin{Bmatrix} u_p' \\ w_p' \\ 0 \\ 0 \end{Bmatrix} = \begin{bmatrix} -i\kappa & 0 & -i\kappa_{sz} & 0 \\ 0 & i\kappa_{pz} & 0 & -i\kappa \\ \zeta & 0 & \xi\kappa_{sz} & 0 \\ 0 & \xi\kappa_{pz} & 0 & -\zeta \end{bmatrix}_{N+1} \begin{Bmatrix} A_{1p}^{N+1}+A_{2p}' \\ A_{1p}^{N+1}-A_{2p}' \\ -B_{2p}' \\ B_{2p}' \end{Bmatrix} . \tag{2.3.37}$$

Solving the four equations in (2.3.37), we have the following solutions:

$$A_{2p}' = \left[\frac{-\zeta^2 + \xi^2\kappa_{sz}\kappa_{pz}}{\zeta^2 + \xi^2\kappa_{sz}\kappa_{pz}} \right]_{N+1} A_{1p}^{N+1} \tag{2.3.38a}$$

$$B_{2p}' = \left[\frac{2\,\zeta\,\xi\kappa_{pz}}{\zeta^2 + \xi^2\kappa_{sz}\kappa_{pz}} \right]_{N+1} A_{1p}^{N+1} \tag{2.3.38b}$$

and

$$u_p' = C_{up}\, A_{1p}^{N+1} \tag{2.3.39a}$$

$$w_p' = C_{wp}\, A_{1p}^{N+1} \tag{2.3.39b}$$

where the coefficients C_{up} and C_{wp} are given by

$$C_{up} = i \left[\frac{2\, \xi\, \kappa_{pz}\, \kappa_{sz}\, (\zeta - \kappa\, \xi)}{\zeta^2 + \xi^2\, \kappa_{sz} \kappa_{pz}} \right]_{N+1} \tag{2.3.40a}$$

$$C_{wp} = i \left[\frac{2\, \zeta\, \kappa_{pz}\, (\zeta - \kappa \xi)}{\zeta^2 + \xi^2\, \kappa_{sz} \kappa_{pz}} \right]_{N+1} \tag{2.3.40b}$$

The subscript N+1 indicates that the corresponding value is evaluated from the properties of the half-space. From (2.3.34) and (2.3.39), the horizontal and vertical transfer functions can then be defined and obtained, they are

$$TR_{hp}(\omega) = u_{0p}/u_p' = \quad 2\, (\overline{B}_{32} + \overline{B}_{42})/(D_p\, C_{up}) \tag{2.3.41}$$

and

$$TR_{vp}(\omega) = w_{0p}/w_p' = -\, 2\, (\overline{B}_{31} + \overline{B}_{41})/(D_p\, C_{wp})\ . \tag{2.3.42}$$

TR_{hp} and TR_{vp} are complex-valued and functions of frequency, they depend on the layered structure and the angle of incidence of P waves.

(b) Incident SV Waves: For the case of incident SV waves, we set AN1 = 0 in (2.3.33). Using the subscript s to indicate this case and following the same derivations as those for incident P waves, we have two components of displacement, u_{0s} and w_{0s}, at the free surface which are given by

$$u_{0s} = -\, 2\, [\overline{B}_{12} + \overline{B}_{22}]\, B_{1s}^{N+1}/D_s \tag{2.3.43a}$$

$$w_{0s} = \quad 2\, [\overline{B}_{11} + \overline{B}_{21}]\, B_{1s}^{N+1}/D_s \tag{2.3.43b}$$

where

$$D_s = (\overline{B}_{11} + \overline{B}_{21})\, (\overline{B}_{32} + \overline{B}_{42}) - (\overline{B}_{12} + \overline{B}_{22})\, (\overline{B}_{31} + \overline{B}_{41})\ . \tag{2.3.44}$$

It is noted that the expression for D_s in (2.3.44) is identical to that for D_p in

(2.3.35). However, they are evaluated in two different cases and hence have different values. The crustal transfer function ratio is given by

$$\mathrm{CTR}_s(\omega) = \frac{w_{0s}}{u_{0s}} = -\frac{\overline{B}_{11} + \overline{B}_{21}}{\overline{B}_{12} + \overline{B}_{22}} \,. \qquad (2.3.45)$$

The displacements u_s' and w_s' at the half-space outcrop and the potential amplitudes A_{2s}' and B_{2s}' of the reflected P and SV waves in the half-space due to incident SV waves with potential B_{1s}^{N+1} are given by

$$B_{2s}' = \left[\frac{-\zeta^2 + \xi^2 \kappa_{sz}\kappa_{pz}}{\zeta^2 + \xi^2 \kappa_{sz}\kappa_{pz}}\right]_{N+1} B_{1s}^{N+1} \qquad (2.3.46a)$$

$$A_{2s}' = \left[\frac{-2\,\zeta\,\xi\kappa_{pz}}{\zeta^2 + \xi^2 \kappa_{sz}\kappa_{pz}}\right]_{N+1} B_{1s}^{N+1} \qquad (2.3.46b)$$

and

$$u_s' = C_{us}\, B_{1s}^{N+1} \qquad (2.3.47a)$$

$$w_s' = C_{ws}\, B_{1s}^{N+1} \qquad (2.3.47b)$$

where the coefficients C_{us} and C_{ws} are defined by

$$C_{us} = i\left[\frac{-2\,\zeta\,\kappa_{sz}\,(\zeta - \kappa\xi)}{\zeta^2 + \xi^2\,\kappa_{sz}\kappa_{pz}}\right]_{N+1} \qquad (2.3.48a)$$

$$C_{ws} = i\left[\frac{2\,\xi\,\kappa_{pz}\,\kappa_{sz}\,(\zeta - \kappa\,\xi)}{\zeta^2 + \xi^2\,\kappa_{sz}\kappa_{pz}}\right]_{N+1} . \qquad (2.3.48b)$$

The horizontal and vertical transfer functions, TR_{hs} and TR_{vs}, are given by

$$\mathrm{TR}_{hs}(\omega) = u_{0s}/u_s' = -2\,(\overline{B}_{12}+\overline{B}_{22})/(D_s\, C_{us}) \qquad (2.3.49)$$

and

$$\mathrm{TR}_{vs}(\omega) = w_{0s}/w_s' = 2\,(\overline{B}_{11}+\overline{B}_{21})/(D_s\, C_{ws})\,. \qquad (2.3.50)$$

To include the anelastic attenuation effect, we should use the appropriate complex layer properties in computing the transfer functions. In viscoelastic media, the wave velocities, V_s and V_p, in (2.3.3) are complex-valued and are given by (2.2.20). As discussed in Section 2.2.2, Snell's law becomes two parts for the wave propagation in viscoelastic media, the complex angles being interpreted by the angles of propagation and attenuation vectors. The half-space can be viscoelastic; the incident P or SV waves may be homogeneous or inhomogeneous within the half-space; the directions of the attenuation and propagation vectors of the incident wave must be specified.

To compute transfer functions, we have to separate the frequency-independent terms from the matrices and calculate these terms first. The following procedure is adopted and built into the computer program:

(1) Input the properties of layered structure, i.e., the elastic P and S wave velocities, the density, the P and S quality factors, and the thickness for each layer. The complex P and S wave velocities are then obtained from (2.2.20) or (2.2.22). Normalized wavenumbers with respect to frequency, i.e., κ_p/ω and κ_s/ω, in each layer can be calculated by using (2.3.3).

(2) Specify incident angles (φ_{N+1} and γ_{N+1}) and the incident wave type (P or SV wave). Normalized horizontal wavenumber κ/ω is then computed from the properties of the half-space by using the relations in (2.2.32) and (2.2.33). The value of κ/ω is complex for a viscoelastic half-space, while it is real for an elastic half-space. From Snell's law in (2.3.4), the normalized horizontal wavenumbers in all layers are equal to κ/ω. Substitution of κ/ω and κ_s/ω , κ_p/ω of each layer into (2.3.2) yields the values of the normalized vertical wavenumbers, κ_{sz}/ω and κ_{pz}/ω, for that layer. The square root is chosen such that the imaginary part of the vertical wavenumber is nonpositive.

(3) Some frequency-independent constants in the elements of $[\mathbf{a}]_j$ for the jth layer in (2.3.23) are computed and stored for the use in the computation of frequency-dependent matrix $[\mathbf{a}]_j$. It is noted from (2.3.34) to (2.3.50) that only 2 columns of $[\bar{B}]$ matrix are necessary for the computation of transfer functions, hence we require to store only eight elements of the product of $[\mathbf{a}]$ matrices in (2.3.27).

(4) For each frequency, starting with the first layer, only ten elements of $[\mathbf{a}]_j$ matrix are calculated because of the symmetry of the matrix. From (2.3.27), eight elements of $[\bar{A}]$ matrix is obtained by N-1 repeated multiplications of a 4×4 matrix $[\mathbf{a}]_j$ by a stored 4×2 matrix which is the product of $[\mathbf{a}]$ matrices of top layers. Once the $[J(0)]_{N+1}^{-1}$ matrix in (2.3.19) for the half-space has been calculated, the first two columns of $[\bar{B}]$ matrix can then be obtained from (2.3.32). It follows from the definitions, the transfer functions are computed for one frequency. Repeat this step over a range of frequencies to obtain the desired spectra.

It is noted that in case of normally incident homogeneous SV or P wave, the computer program for the SH wave can be used to reduce computation time. For the normally incident homogeneous P wave, the vertical transfer function between the free surface and the half-space outcrop can be obtained from similar formulas given in Section 2.2.1 if the shear wave properties are replaced by the P wave properties. Although numerical computation described above is restricted to one type of incident wave, the solution for simultaneously incident P and SV waves at the half-space can be obtained by the superposition principle.

2.4 Numerical Examples

Two computer codes have been written to calculate the transfer functions between the free surface and the half-space outcrop. One considers incident SH waves and the other considers incident P or SV waves at a given incident angle from the half-space. Numerical examples of a single-layered system and a 7-layered system are given herein to illustrate the effects of anelastic attenuation and incident angle on the transfer functions. The incident waves are considered to be homogeneous for simplicity.

2.4.1 Single-Layered System

Consider a single layer overlying a half-space as shown in Fig. 2.5. For SH waves incident at an angle Θ_2 from the half-space, the explicit expression of the transfer function between the free surface and the half-space outcrop is given by (subscript 1 indicates a single-layered system):

$$TR_1(\omega) = \frac{1}{\cos\kappa_{sz1}H + i\,\alpha\,\sin\kappa_{sz1}H} \tag{2.4.1}$$

where κ_{sz1} is the vertical shear wavenumber in the surface layer, H the thickness of the surface layer, and α the impedance ratio between the surface layer and the half-space. κ_{sz1} and α are given by

$$\kappa_{sz1} = \kappa_{s1}\cos\Theta_1 = \frac{\omega}{V_{s1}}\cos\Theta_1 \tag{2.4.2a}$$

and

$$\alpha = \frac{\rho_1 V_{s1}\cos\Theta_1}{\rho_2 V_{s2}\cos\Theta_2}\ . \tag{2.4.2b}$$

The incident angle Θ_2 is complex for inhomogeneous incident waves in a viscoelastic half-space and can be interpreted as two real angles φ_2 and γ_2 (see Fig. 2.5). Here we consider incident SH waves to be homogeneous in the

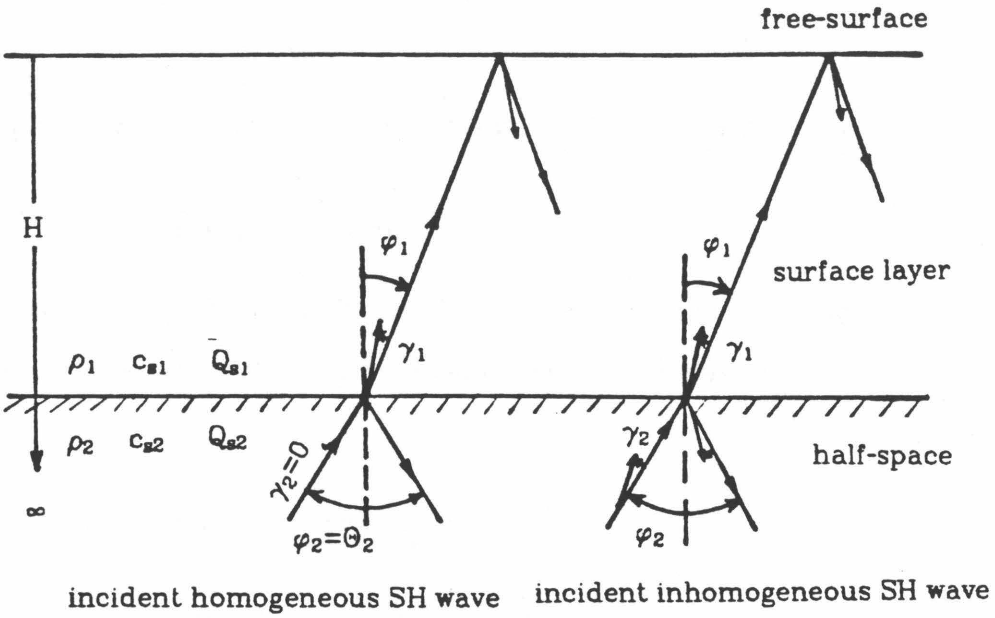

Fig. 2.5 Single layer overlying a half-space.

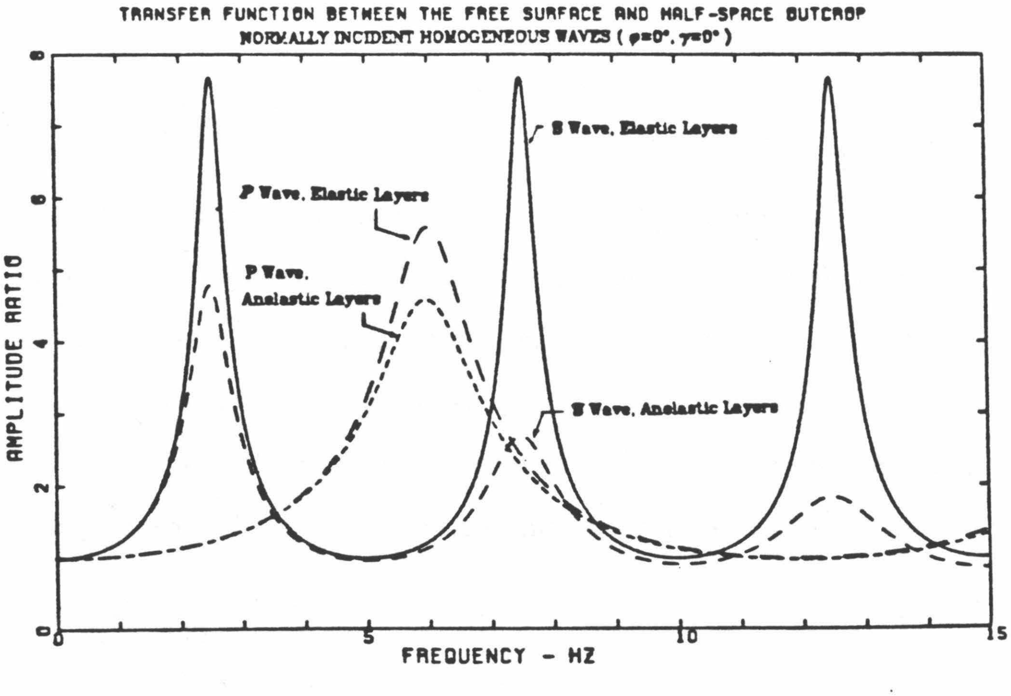

Fig. 2.6 Effect of attenuation on the transfer function of normally incident P and S waves. Single-layered system (Table 2.1).

half-space, hence Θ_2 is real and equal to φ_2, and $\gamma_2 = 0$. In this case, Θ_1 in the surface layer is not necessary real.

The amplitude ratio, which is the absolute value of $TR_1(\omega)$, is given by

$$|TR_1(\omega)| = \frac{1}{|\cos\kappa_{sz1}H + i\ \alpha\ \sin\kappa_{sz1}H|} \ . \tag{2.4.3}$$

The expression in (2.4.3) is applicable to both elastic and viscoelastic wave propagations. However, it can be simplified in the case of elastic wave propagation, i.e.,

$$|TR_{1e}(\omega)| = \frac{1}{\sqrt{1 + (\alpha^2 - 1)\sin^2\kappa_{sz1}H}} \ . \tag{2.4.4}$$

In general when the surface layer is softer than the half-space ($\alpha < 1$), the maxima of $|TR_{1e}(\omega)|$ occur at frequencies given by $\sin\kappa_{sz1}H = 1$, i.e.,

$$\omega_i = \frac{\pi}{2}(2i - 1)\frac{c_{s1}}{H\cos\Theta_1}, \quad i=1,2,\cdots \tag{2.4.5a}$$

or

$$T_i = \frac{2\pi}{\omega_i} = \frac{4H\cos\Theta_1}{c_{s1}(2i-1)}, \quad i=1,2,\cdots \tag{2.4.5b}$$

c_{s1} being the elastic shear wave velocity in the surface layer. The values of $|TR_{1e}(\omega)|$ at these maxima are $1/\alpha$. Therefore, the softer the surface layer, the more significant is the amplification effect. On the other hand, the minima of $|TR_{1e}(\omega)|$ occur at frequencies given by $\sin\kappa_{sz1}H = 0$, and their values at these minima are 1. It also follows from (2.4.5b) that in the case of vertically incident elastic SH waves in which $\Theta_2 = \Theta_1 = 0$, the maxima occur at periods given by

$$T_i = \frac{4\ H}{c_{s1}(2i - 1)}, \quad i=1,2,\cdots \tag{2.4.6a}$$

i.e., at frequencies (which are called the natural frequencies of the system)

$$f_{max} = f_1,\ 3f_1,\ 5f_1,\ \cdots\ ,\quad f_1 = \frac{c_{s1}}{4H}\ , \tag{2.4.6b}$$

and the maximum value of $|TR_{1e}(\omega)|$ is $(\rho_2 c_{s2})/(\rho_1 c_{s1})$. It is noted that the periods in (2.4.6a) are the natural periods of a uniform shear beam with a height H and a shear wave velocity c_{s1}. The fundamental period, $T_1 = 4H/c_{s1}$, is 4 times the travel time for a shear wave to travel vertically across the surface layer.

The time domain transfer function is difficult to obtain analytically. However, for a single-layered and elastic system, it can be evaluated by performing contour integration of the inverse Fourier transform of (2.4.1). For $\alpha < 1$, the transfer function for an elastic single-layered system is given by

$$TR_{1e}(t) = 2\ \left|\frac{\alpha-1}{\alpha+1}\right|^{t/2t_s} \frac{1}{\sqrt{1-\alpha^2}} \sum_{k=0}^{\infty} \delta[t-(2k+1)t_s]\ (-1)^k \tag{2.4.7}$$

where $t_s = \dfrac{H}{c_{s1}}\cos\Theta_1$, $\delta[\ ]$ is the delta function and α is given by (2.4.2b). t_s is the travel time in the vertical direction for inclined SH waves in the surface layer. The transfer function in (2.4.7) consists of a sequence of pulses located at time t_s , $3t_s$, $5t_s$, $\cdots$. The magnitude of the pulse decreases with increase of time. (2.4.7) can also be obtained by using the ray tracing technique and the definition of the transfer function, that is, the impulsive response of the system.

To illustrate the effects of attenuation and incident angle on the transfer function, let us take the single-layered structure in Table 2.1 as an example. The natural frequencies of the system are 2.5, 7.5, 12.5 Hz, $\cdots$ and 6.0, 18.0 Hz, $\cdots$ for normally incident S and P waves, respectively. The term 'anelastic' is used to indicate 'viscoelastic'. We shall only show the amplitudes of the transfer functions, the corresponding phases will not be shown.

Table 2.1 - Physical Parameters for a Single Layered System

Layer No.	c_s (ft/sec)	c_p (ft/sec)	ρg (pcf)	Q_s	Q_p	H (ft)
1	1250	3000	125	10	20	125
half-space	8000	14000	150	100	150	∞

Fig. 2.6 shows the amplitudes of the transfer functions between the free surface and the half-space outcrop for normally incident S and P waves. The curves for the elastic layers (Q's = ∞) and the anelastic layers (Q's are given in Table 2.1) are shown together to illustrate the effects of attenuation. The peaks have the same heights in the elastic case, while the second and third peaks are lower than the first peak in the anelastic case. The troughs of the curves are only slightly affected by the attenuation. Also, it is noted that there is a slight shift of the peaks in the anelastic case. Fig. 2.7 shows the transfer functions for the incident SH waves in elastic layers (top plot) and in anelastic layers (bottom plot) at angles of 0, 15, and 30 degrees from the half-space. Shifting of the peaks is noted; however, the effect of incident angle is insignificant.

To study the transfer functions for incident SV or P waves, we consider 15° and 30° incident angles which are less than the critical angle, 34.85° in this example, of incident SV waves. The vertical and horizontal transfer functions between the free surface and the half-space outcrop are shown in Figs. 2.8 & 2.10 for incident SV waves and in Figs. 2.9 & 2.11 for incident P waves. The results for elastic layers are presented in the top plots and those for anelastic layers are in the bottom plots. For inclined incident SV or P waves, coupling effects occur and both the vertical and horizontal components of the motions are induced. Figs. 2.10 and 2.11 show the horizontal transfer functions for incident SV and P waves, respectively. The transfer functions of normally incident SV waves are also shown in these figures as solid curves. The coupling

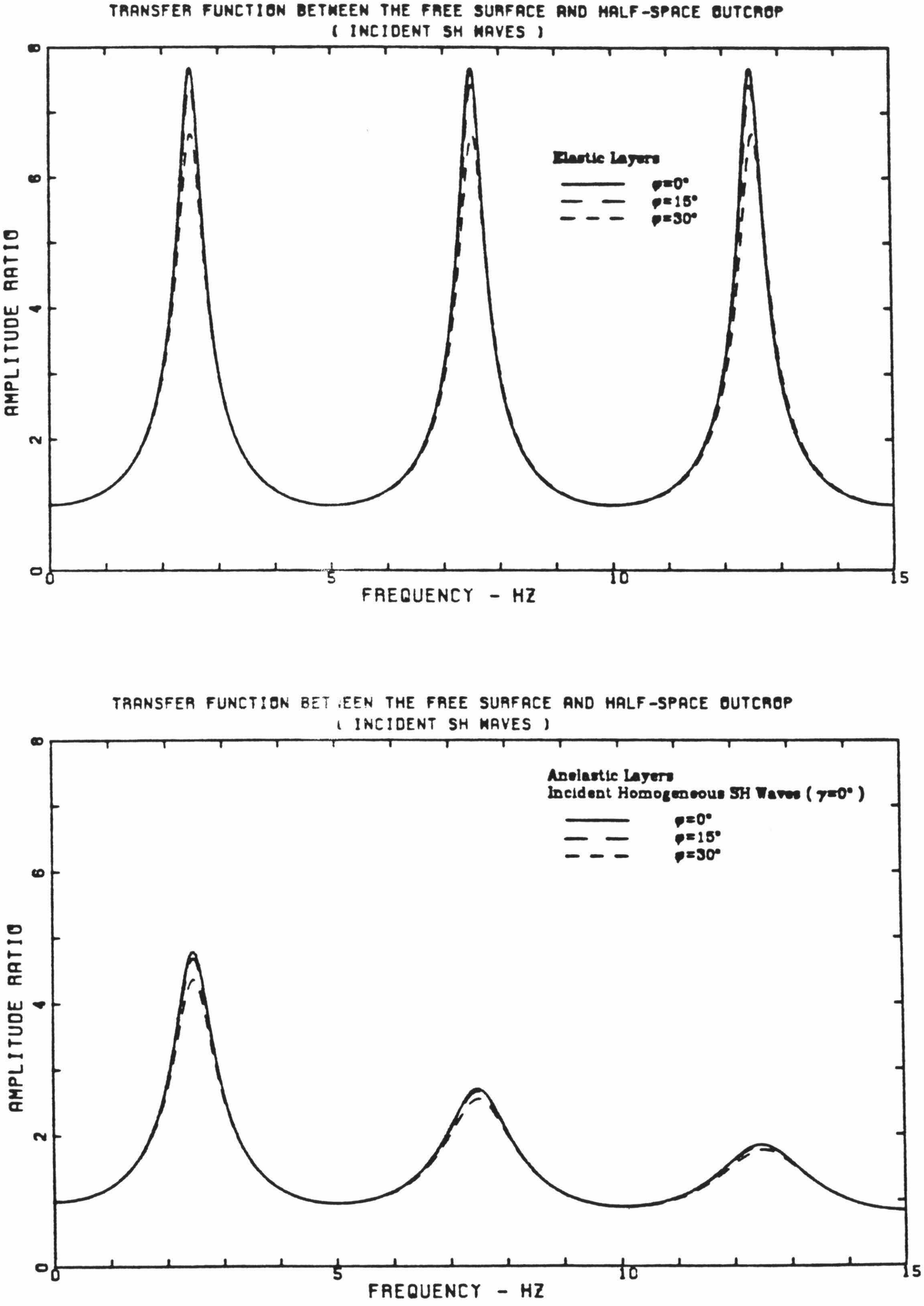

Fig. 2.7 Effects of attenuation and incident angle on the transfer function of incident SH wave. Single-layered system (Table 2.1).

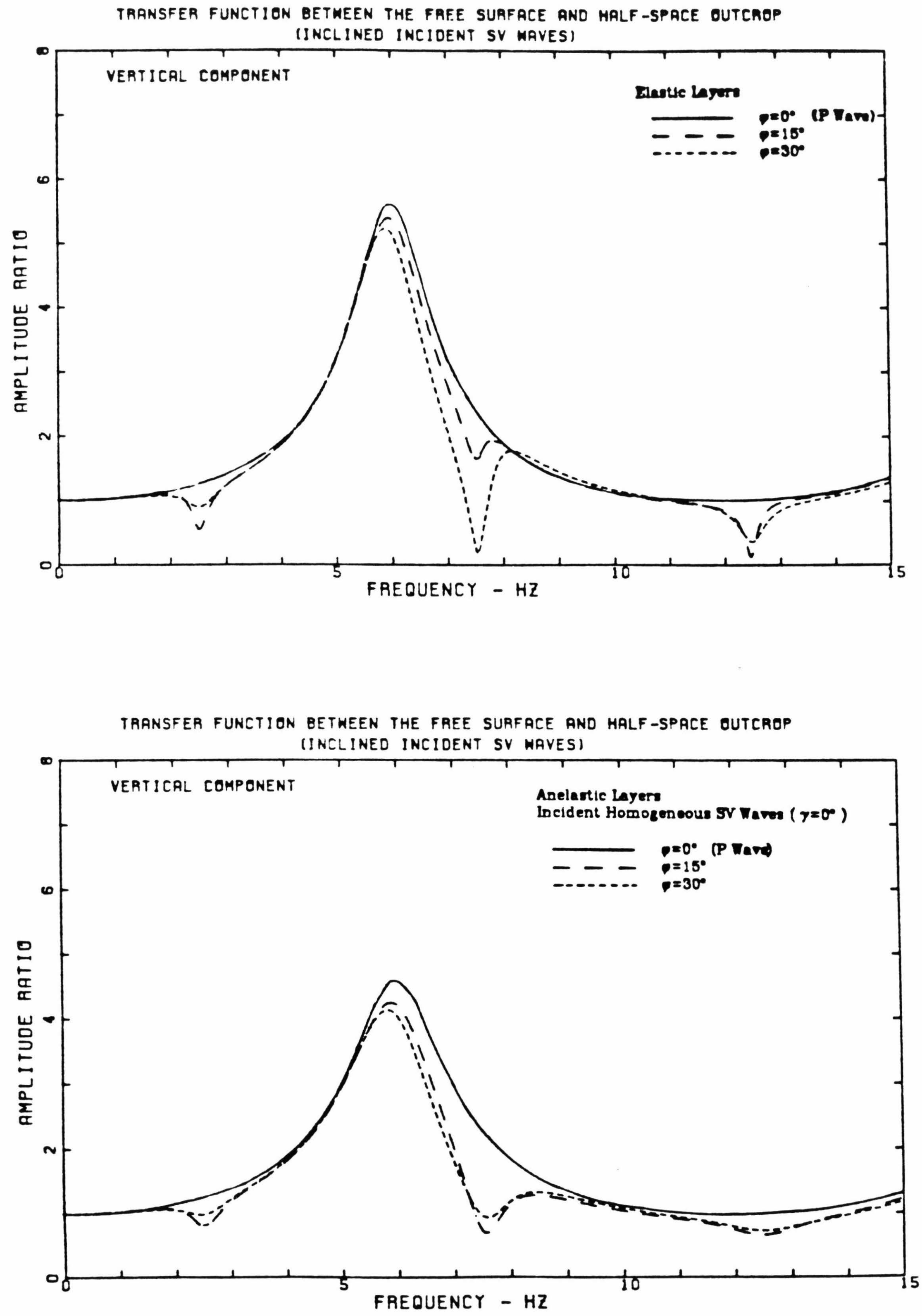

Fig. 2.8 Effects of attenuation and incident angle on the vertical transfer function of incident SV wave. Single-layered system (Table 2.1).

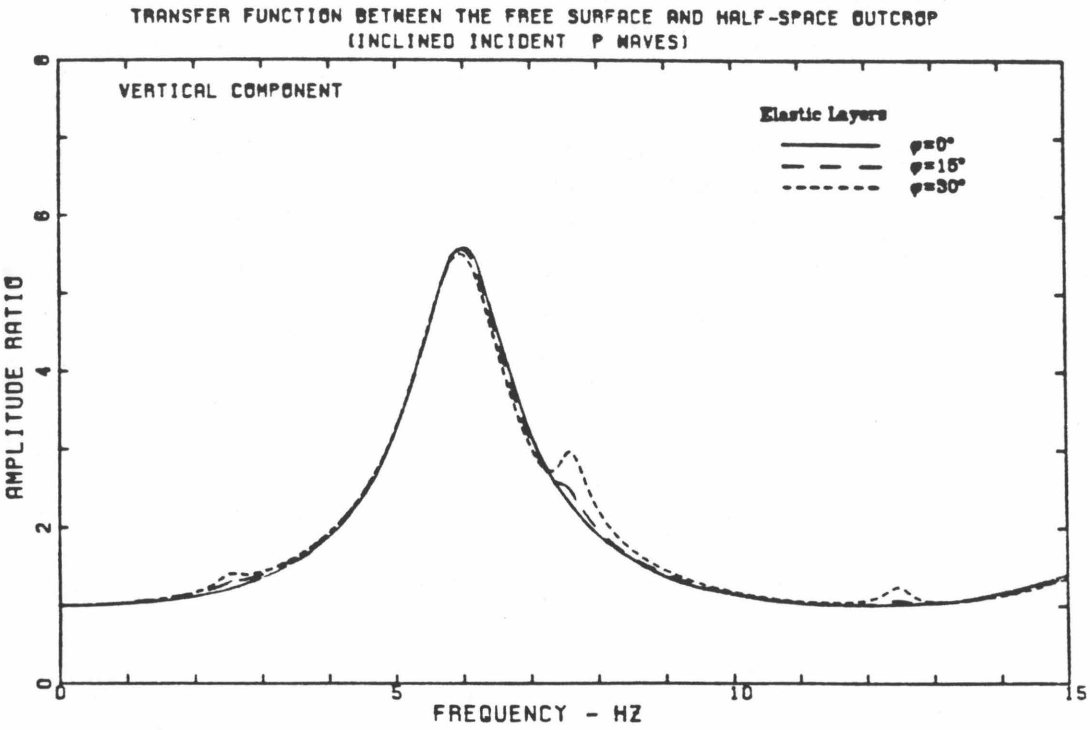

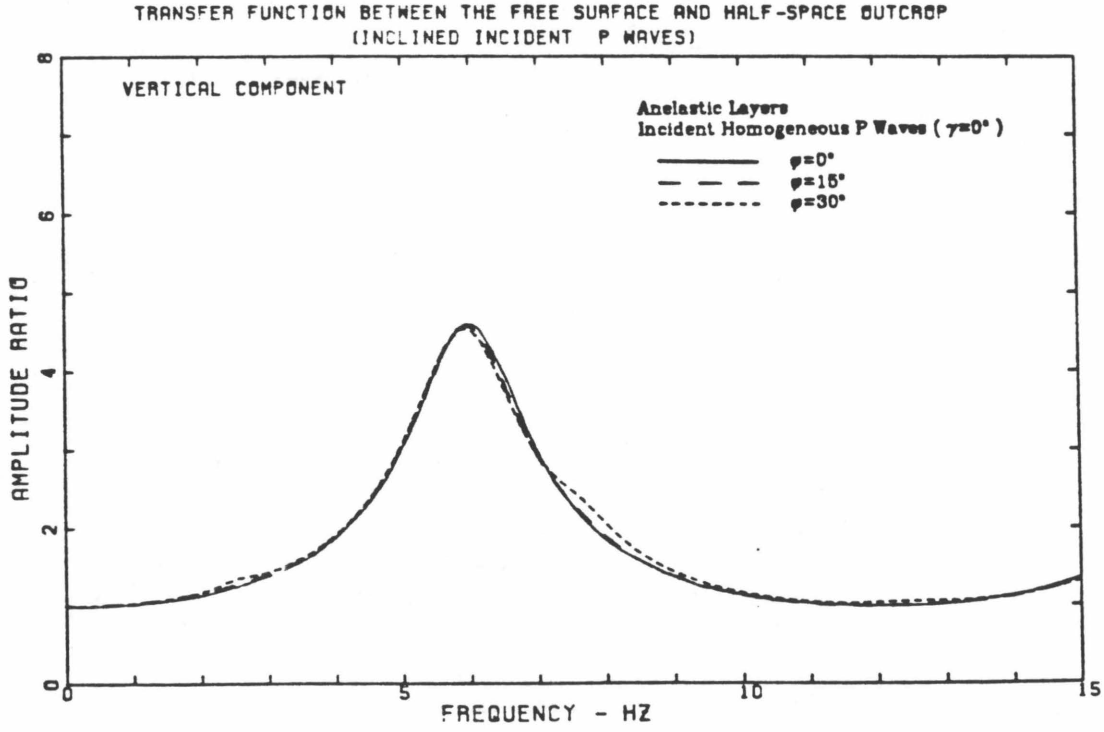

Fig. 2.9 Effects of attenuation and incident angle on the vertical transfer function of incident P wave. Single-layered system(Table 2.1).

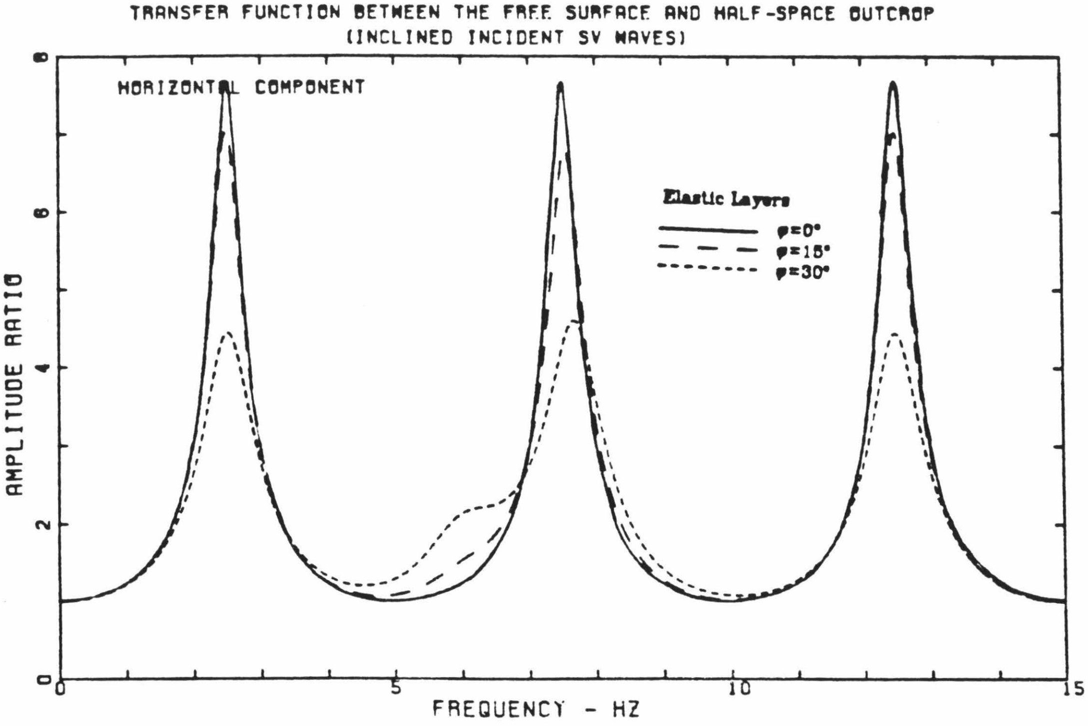

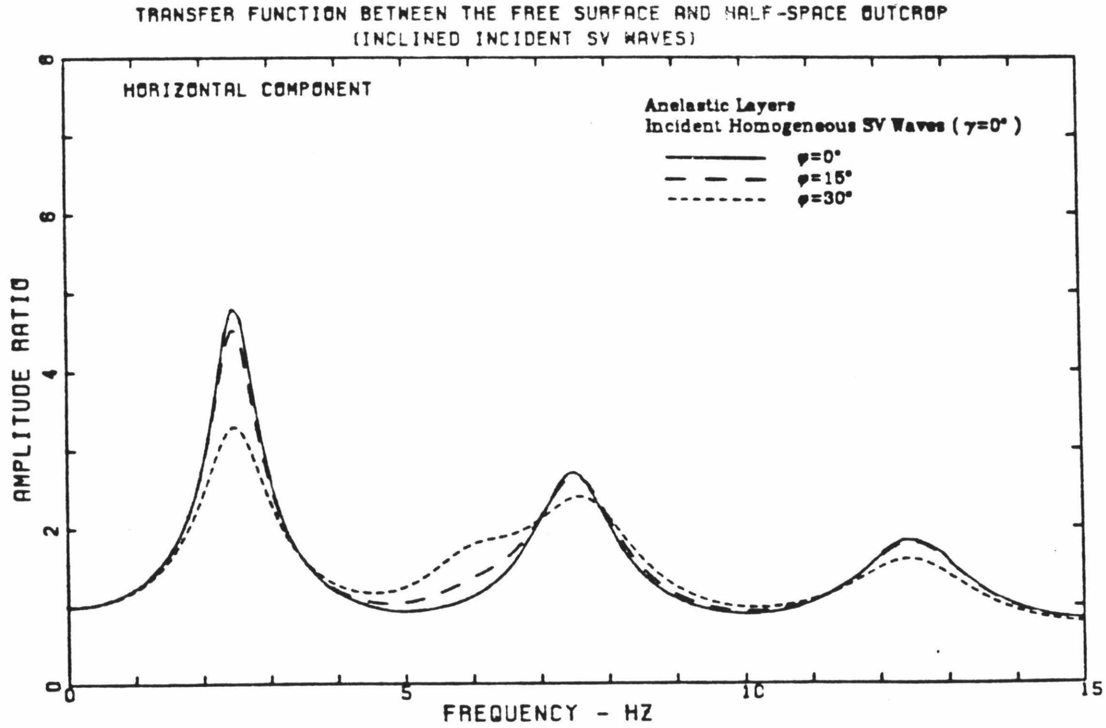

Fig. 2.10 Effects of attenuation and incident angle on the horizontal transfer function of incident SV wave. Single-layered system (Table 2.1).

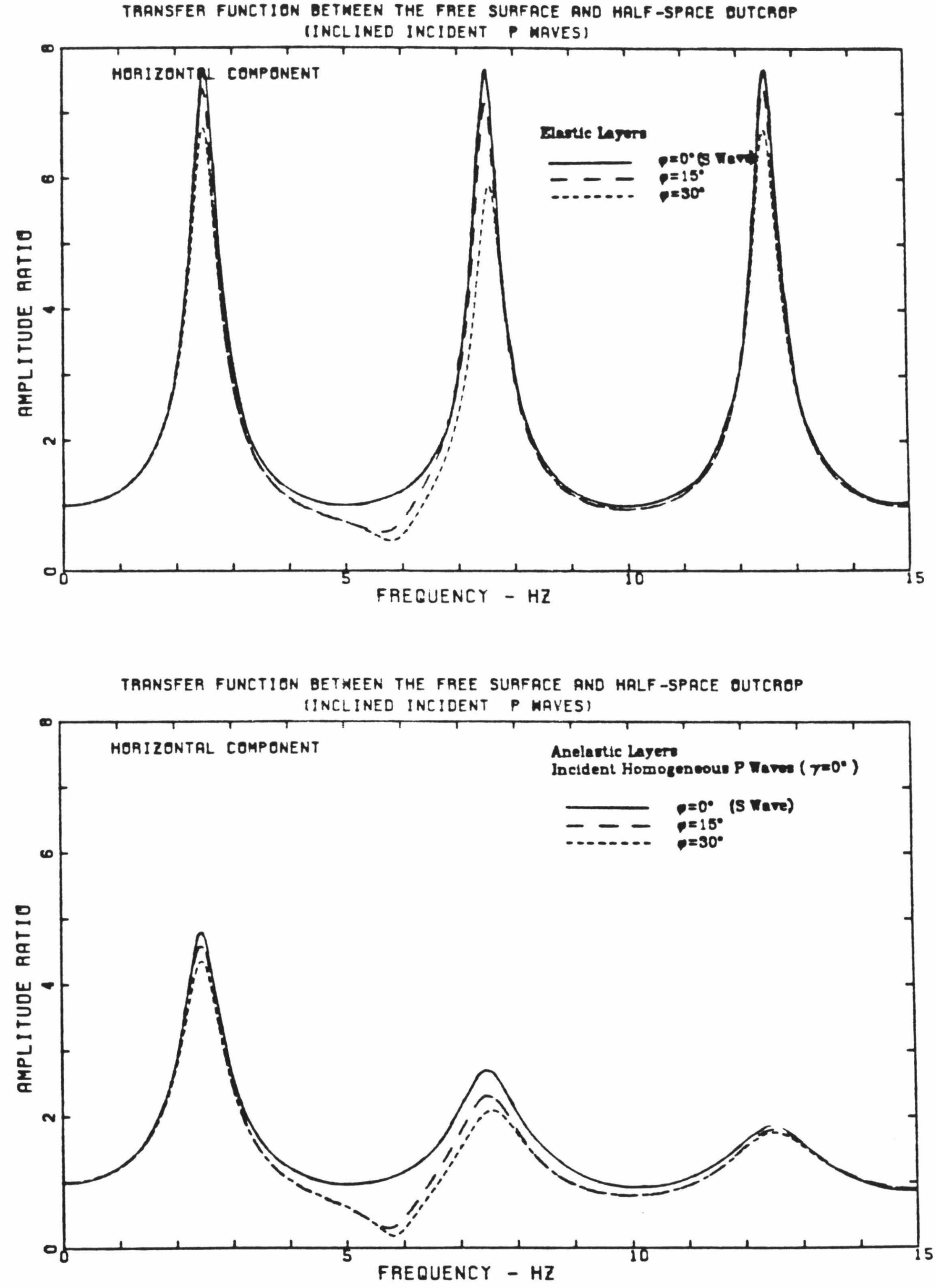

Fig. 2.11 Effects of attenuation and incident angle on the horizontal transfer function of incident P wave. Single-layered system (Table 2.1).

effects may be seen at the frequency near 6 Hz, which is the fundamental frequency of normally incident P waves. Relative to the curves for normally incident SV waves, inclined incident SV waves produce small humps (Fig. 2.10) while inclined incident P waves produce small dips (Fig. 2.11) near the natural frequencies of normally incident P waves. As the incident angle increases, the coupling effect becomes evident and the amplitudes of the peaks decrease. It can also be seen by comparing Fig. 2.10 with Fig. 2.7 that the effect of incident angle on the transfer function is larger for incident SV waves than for incident SH waves. Figs. 2.8 and 2.9 show the vertical transfer functions for incident SV and P waves, respectively. The transfer functions of normally incident P waves are also shown in these figures as solid curves. It is noted that the natural frequencies of normally incident SV waves are 2.5, 7.5 , 12.5 Hz, $\cdots$. The coupling effects are seen near these frequencies. The vertical transfer functions for inclined incident SV waves show dips and those for inclined P waves show humps at these frequencies.

The time domain transfer functions of normally incident SH wave are shown in Fig. 2.12(a) for anelastic layers and in Fig. 2.12(b) for elastic layers. These functions are obtained by inversely Fourier transforming the frequency domain transfer functions in Fig. 2.6. To reduce truncation errors in using finite length of data, the truncation interval is chosen equal to a multiple of the period in the frequency domain transfer function (Brigham, 1974). In this case, the frequency domain transfer functions were truncated at 20 Hz. As seen in Fig. 2.12(b), the transfer function for elastic layers consists of a sequence of isosceles triangles. This is consistent with the analytical function given by (2.4.7); however, the area of each triangle should be interpreted as the magnitude of the corresponding pulse. The effects of material dampings can also be seen in these figures. The viscoelastic surface layer tends to broaden the pulses

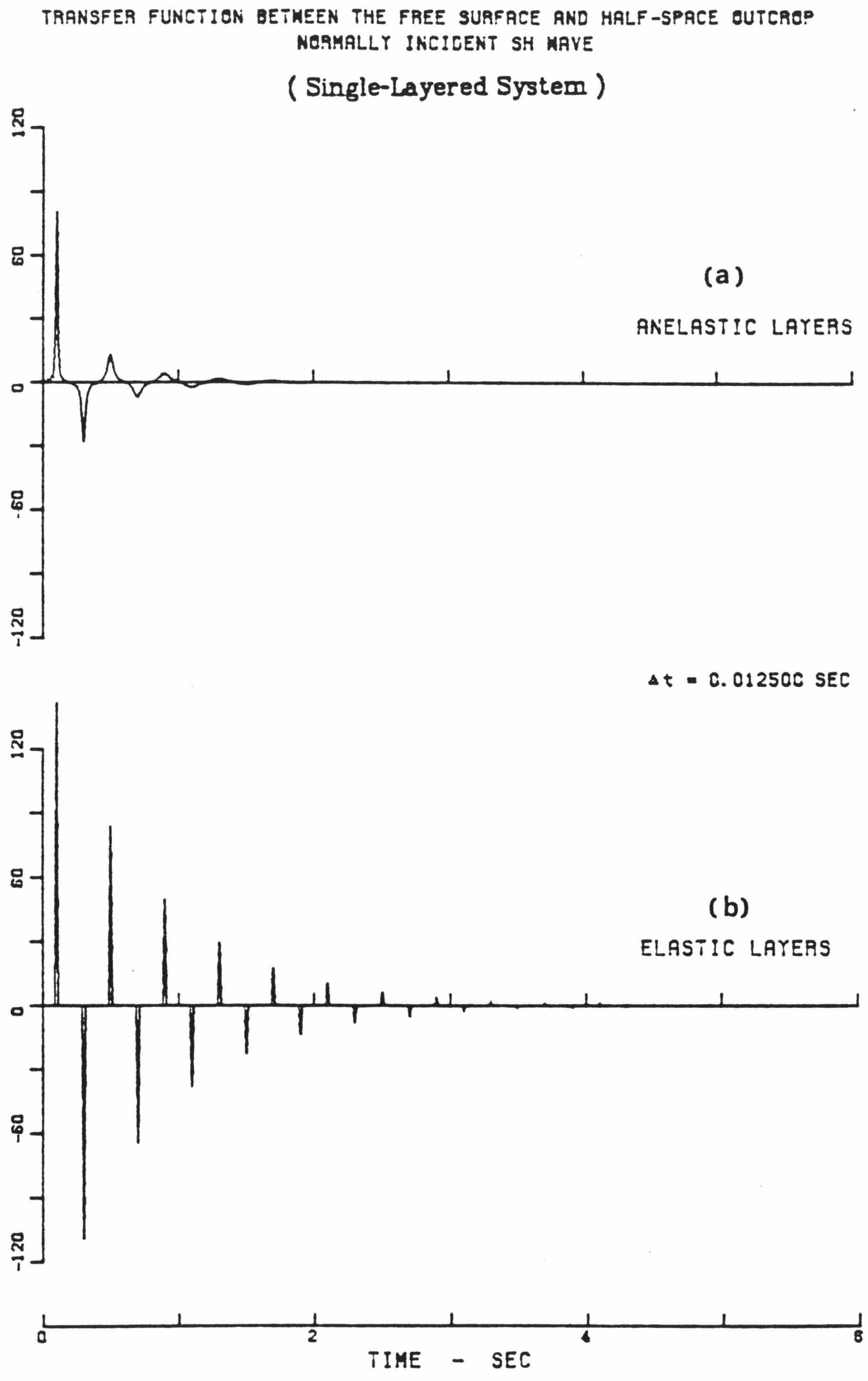
TRANSFER FUNCTION BETWEEN THE FREE SURFACE AND HALF-SPACE OUTCROP
NORMALLY INCIDENT SH WAVE

(Single-Layered System)

Fig. 2.12 The transfer functions of normally incident SH wave in the time domain for the single-layered system(Table 2.1) with (a) anelastic layers, (b) elastic layers.

and decrease their amplitudes.

To give an example of synthetic accelerograms in three components, we consider an incident signal defined as

$$a(t) = k^4 \left[t - kt^2 + k^2 t^3/6 \right] e^{-kt} \;, \qquad t \geq 0 \;, \tag{2.4.8}$$

and $a(t) = 0$, for $t < 0$. k is chosen equal to 10.0. The shape of this signal is shown at the bottom plot of Fig. 2.13. This signal corresponds to the far-field acceleration generated by a point double-couple source with dislocation history $D(t) = 1 - e^{-kt} \left[1+kt+(kt)^2/2+(kt)^3/6 \right]$ (Ebel and Helmberger, 1982). Its Fourier transform is $-k^2\omega^2/(i\omega + k)^4$, which varies as ω^{-2} for $\omega >> k$. We assume the incident angles of P, SV and SH waves are all 30° and incident shear waves arrive at the boundary of the half-space and the layer 4.0-sec later than P wave. The incident waves have the same wave form as that in (2.4.8) and the amplitudes of incident SH, SV and P waves in the half-space are normalized to have 1.0, 1.0 and 0.5, respectively. Fig. 2.13 gives the response at the free surface and at the half-space outcrop in the x-, y- and z-directions. To facilitate comparison, the response of elastic layers is shown on the left-hand plots of the figure while the response of anelastic layers is shown on the right-hand side. The numbers in the figure indicate the peak values. The response $\ddot{v}$ in the y-direction is due to incident SH wave; $\ddot{u}$ and $\ddot{w}$ in the x- and z-directions are due to incident P and SV waves. Since the incident P and SV waves are separated by 4.0-sec, the responses of the system due to P waves and SV waves are also separated in this figure. The response at the half-space outcrop has identical wave form as the incident waves but have different amplitudes. The traces in Fig. 2.13 also show the effects of attenuation, i.e., the amplitudes are reduced, the responses are smoothed out and higher-order reflections do not show up.

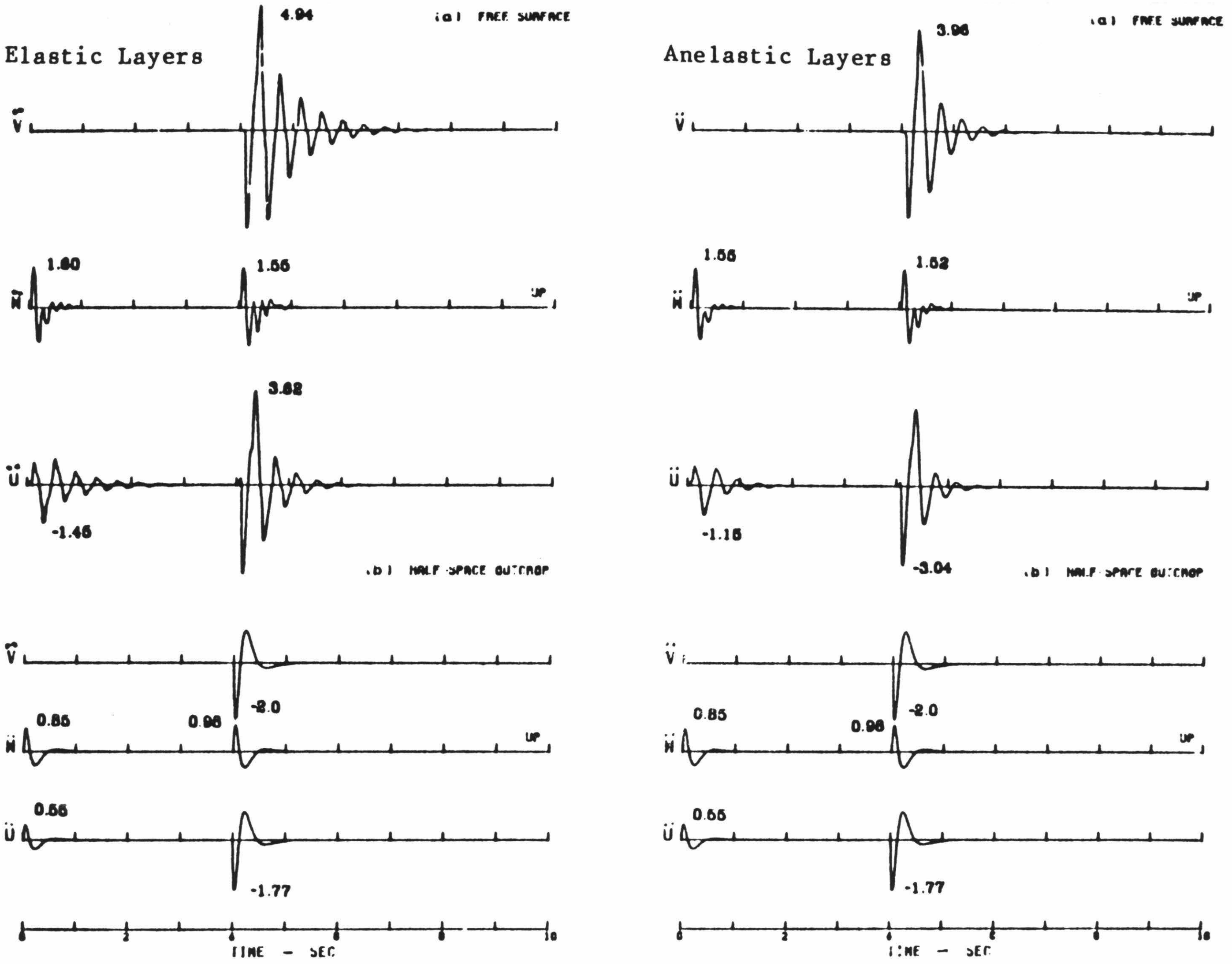

Fig. 2.13 The responses at the free surface and the half-space outcrop to incident SH wave($\ddot{v}$), SV and P waves($\ddot{w}$ and $\ddot{u}$). The amplitudes of incident SH, SV and P waves are 1.0, 1.0 and 0.5, respectively. Single-layered system.

2.4.2 7-Layered System

Consider a system with 7 layers overlying a half-space in Table 2.2.

Table 2.2 - Physical Parameters for a 7-layered System

Layer No.	c_s (ft/sec)	c_p (ft/sec)	ρg (pcf)	Q_s	Q_p	H (ft)
1	620	1400	100	8	8	6
2	1100	2200	108	8	8	17
3	1600	3100	116	10	10	82
4	2000	3800	114	15	15	220
5	2500	4500	120	20	20	53
6	3100	5600	120	25	25	222
7	3600	6400	125	30	30	300
half-space	8000	14000	150	100	150	∞

This describes approximately the subsoil conditions underlying the campus of the California Institute of Technology. The soil profile consists primarily of medium to very dense, silty sands overlying crystalline granite bedrock. The site is a deep alluvial site where the alluvial deposits are about 900 feet thick. Downhole shear wave velocity measurements were made at a location adjacent to the Millikan Library by Shannon & Wilson, Inc. (SW-AA, 1978, 1980a and 1980b). However, only the S wave velocities to a depth of 400 feet were actually measured. The S wave velocities of the lower layers and the bedrock in Table 2.2 are estimated. The corresponding P wave velocities are then estimated by assuming Poission's ratio of soil equal to 0.30 to 0.35. The Q structure has been estimated for illustrative purposes.

Fig. 2.14 shows the transfer functions for normally incident S and P waves. The solid curves are for elastic layers, while the dashed curves are for viscoelastic layers. In the elastic case, the peaks occur at the natural frequencies 0.90, 2.12, 3.66, 4.80, 6.42 Hz, $\cdots$ for incident S waves and at the natural frequencies

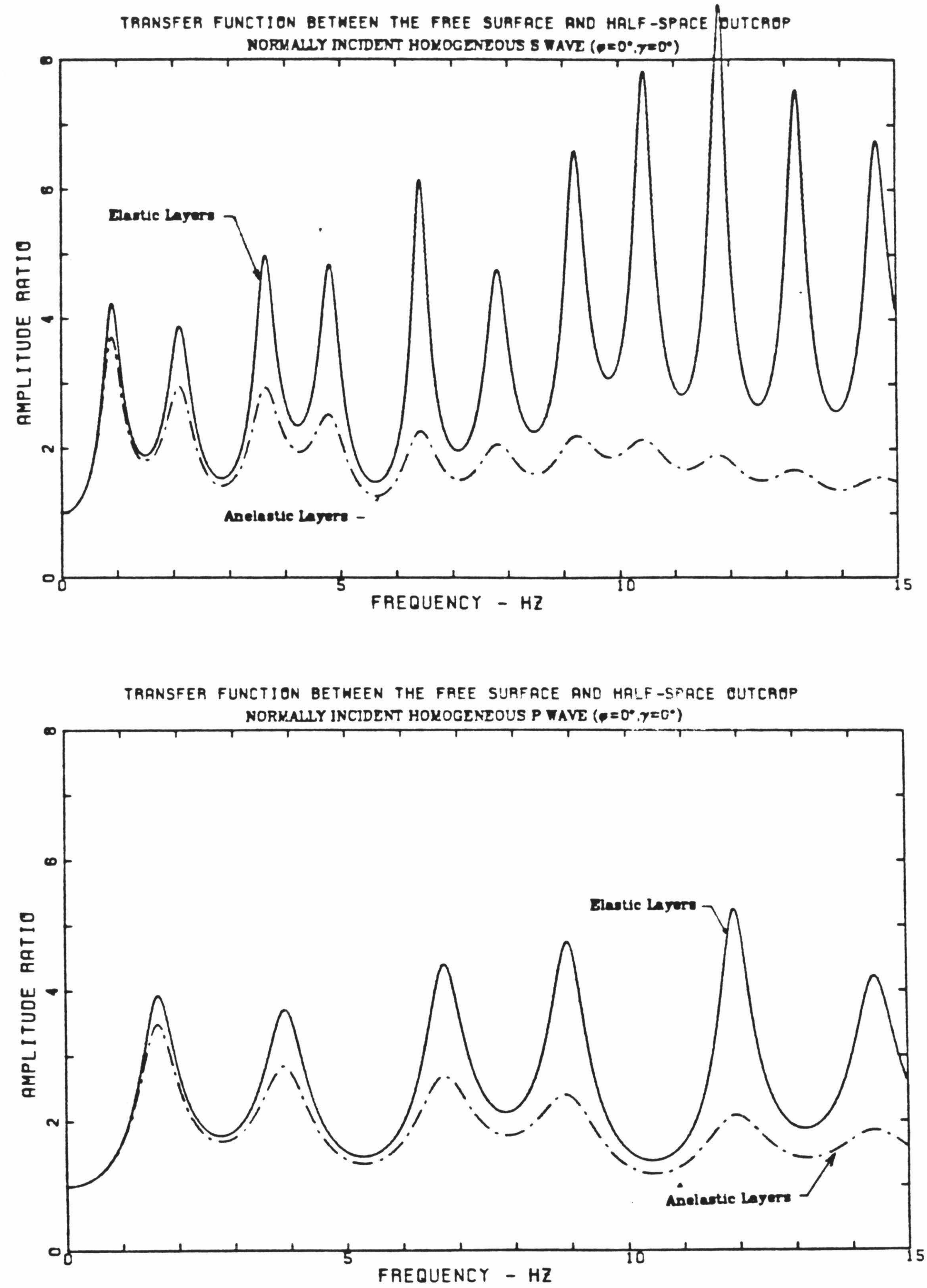

Fig. 2.14 Effect of attenuation on the transfer function of normally incident P and S waves. 7-layered system (Table 2.2).

1.64, 3.92, 6.74 Hz, $\cdots$ for incident P waves. The values of these peaks are consistent with the results predicted by the theory presented by Tsai (1970), namely, the peaks of the transfer function for the normally incident elastic waves in a N-layered system with increasing layer stiffness have an upper bound equal to $1/(\alpha_1\alpha_2 \cdots \alpha_N)$ and a lower bound equal to $1/\alpha_N$, where α_j is the impedance ratio between the jth and the j+1th layers defined by (2.2.6). In this example, we have a lower bound of 2.67 and a upper bound of 19.35 for normally incident S waves, and a lower bound of 2.63 and a upper bound of 15.0 for normally incident P waves. It is noted in the transfer functions of elastic layers that the peaks are not of equal values and larger peaks tend to occur at high frequencies. This is different from the single-layered system where the peaks have the same amplitudes (Fig. 2.6). It is also noted in Fig. 2.14 that the first peak does not have the absolute maximum value in the elastic case. The absolute maximum value occurs at the frequency near 11.8 Hz for incident S waves, while it occurs at the frequency near 12.0 Hz for incident P waves.

It takes 0.3625 seconds for the normally incident S wave at the half-space to reach the free surface. The fundamental period for incident S waves is 1.11 seconds, which is approximately 3.06 times the total travel time. On the other hand, the total travel time for the P waves is 0.195 seconds. The fundamental period for incident P waves is 0.61 seconds, which is about 3.13 times the total travel time. These factors, 3.06 and 3.13 in this example, are dependent on the layered structure and are generally different from the factor of 4 of a single-layered system. It is shown in Fig. 2.14 that the peaks at high frequencies are much more affected by the anelastic attenuation than those at low frequencies. For a system with lower Q's than those in Table 2.2, the curve would become flat at high frequencies.

Fig. 2.15 shows the effect of the incident angle of SH waves on the elastic and anelastic transfer functions. It is noted that when SH waves reach the free surface, the angles are only 1.15° and 2.22° for the incident angles of 15° and 30° in the half-space, respectively. Fig. 2.15 indicates that the effect of incident angle of SH waves is not significant in both the elastic and anelastic cases.

To study the effects of incident angle of SV or P waves on the transfer functions, we consider again the incident angles of 15° and 30°. The results are shown in Figs. 2.16 & 2.18 for incident SV waves and in Figs. 2.17 & 2.19 for incident P waves. The results of normally incident waves are also shown as solid curves in these figures to facilitate comparison, i.e., normally incident P waves are shown in the vertical component and normally incident SV waves are shown in the horizontal component. Some conclusions deduced in the case of the single layered system can also be drawn for the multilayered system. First, the horizontal transfer functions of inclined incident SV or P waves have peaks near the natural frequencies of normally incident SV waves. Secondly, the vertical transfer functions of inclined incident P or SV waves have peaks near the natural frequencies of normally incident P waves. Thirdly, the coupling effects on the transfer functions are shown near the natural frequencies of the system. In the vertical transfer functions, the coupling effects are seen as humps in the case of incident P waves (Fig. 2.17) and as dips in the case of incident SV waves (Fig. 2.16) near the natural frequencies of normally incident SV waves. In the horizontal transfer functions, there are dips in the case of incident P waves (Fig. 2.19) and humps in the case of incident SV waves (Fig. 2.18) near the natural frequencies of normally incident P waves.

The effect of incident angle of P waves is larger on the horizontal transfer functions (Fig. 2.19) than on the vertical transfer functions (Fig. 2.17). On the other hand, for the incident SV waves, the effect is smaller on the horizontal

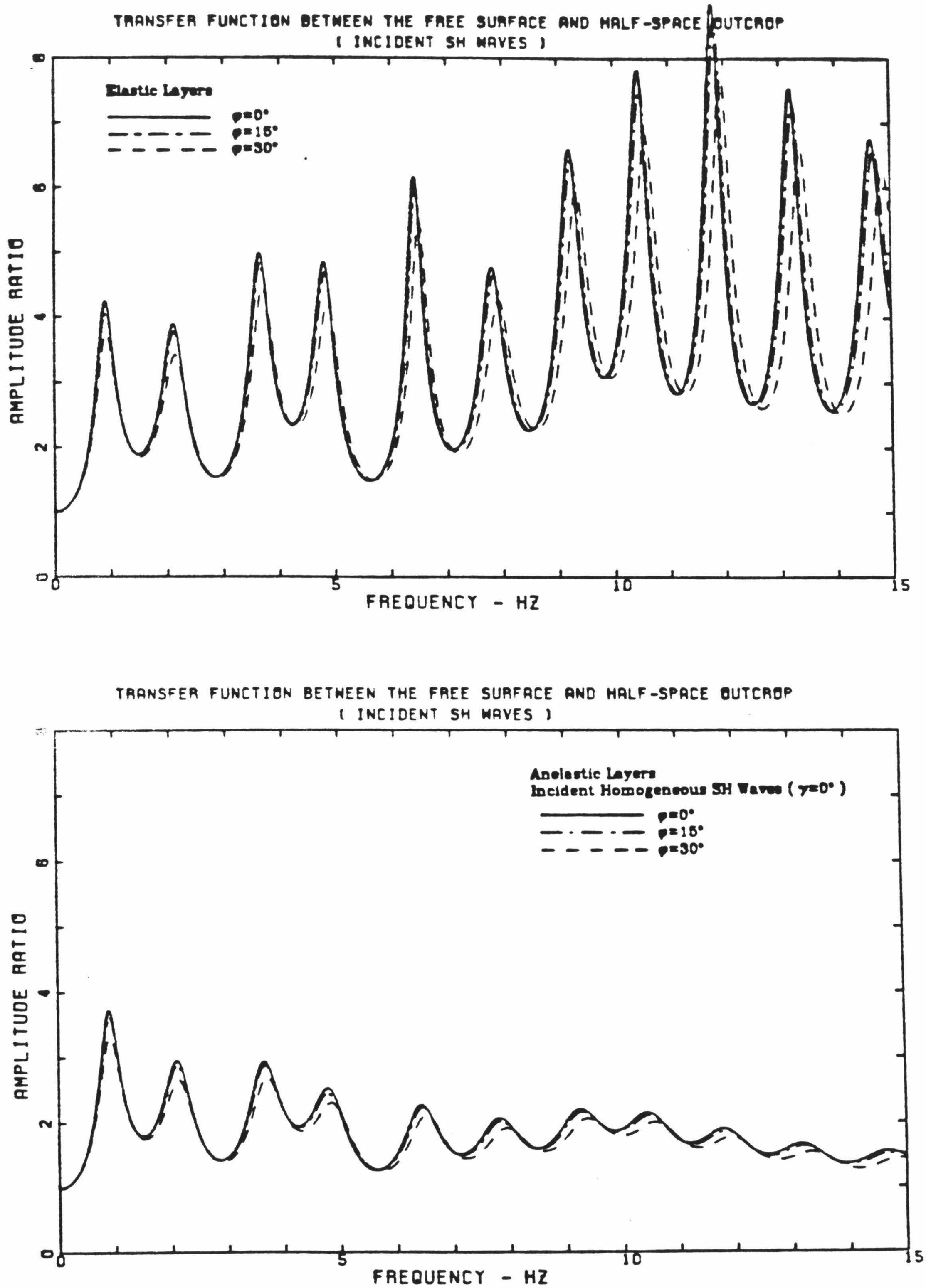

Fig. 2.15 Effects of attenuation and incident angle on the transfer function of incident SH wave. 7-layered system (Table 2.2).

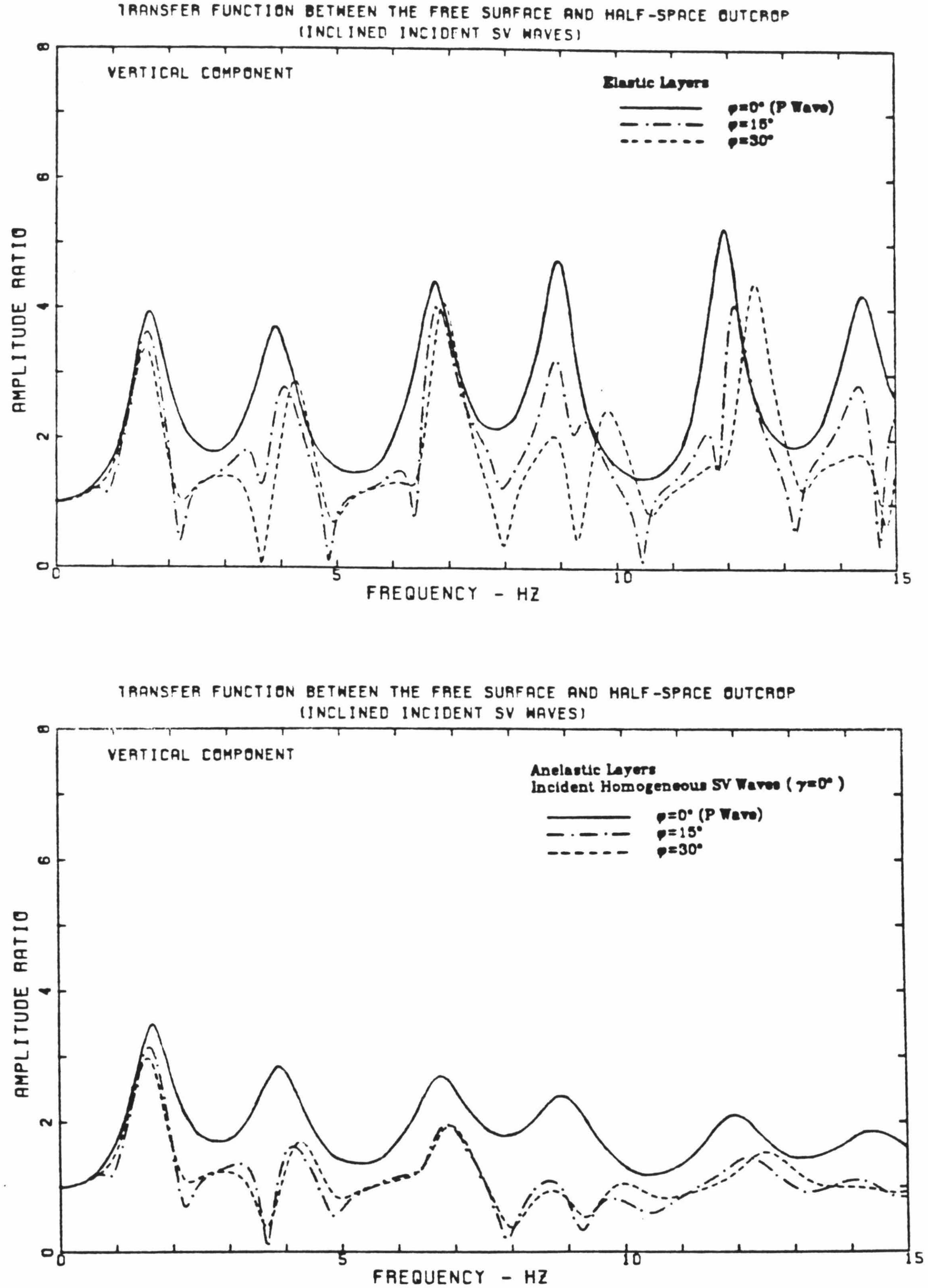

Fig. 2.16 Effects of attenuation and incident angle on the vertical transfer function of incident SV wave. 7-layered system (Table 2.2).

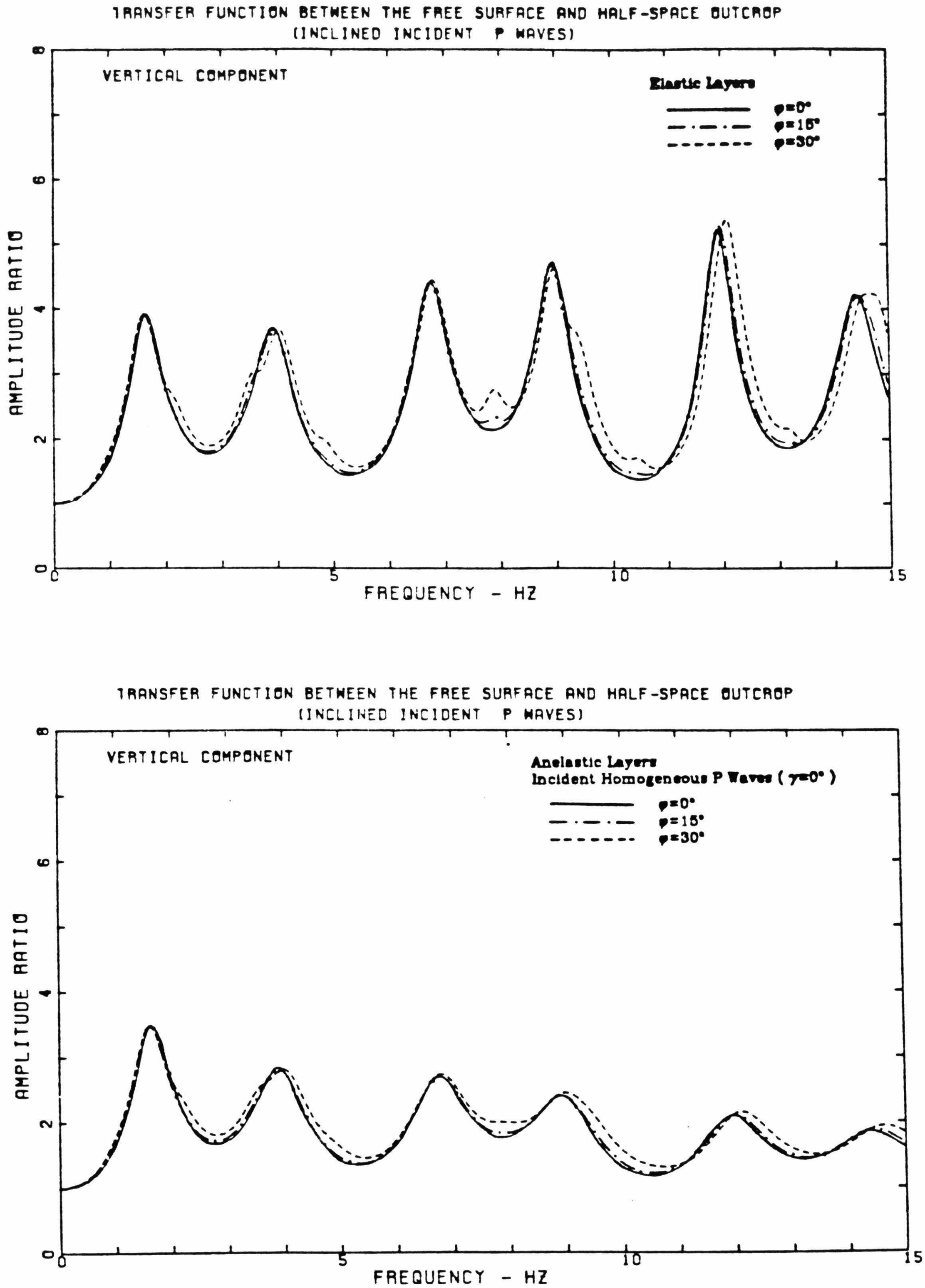

Fig. 2.17 Effects of attenuation and incident angle on the vertical transfer function of incident P wave. 7-layered system (Table 2.2).

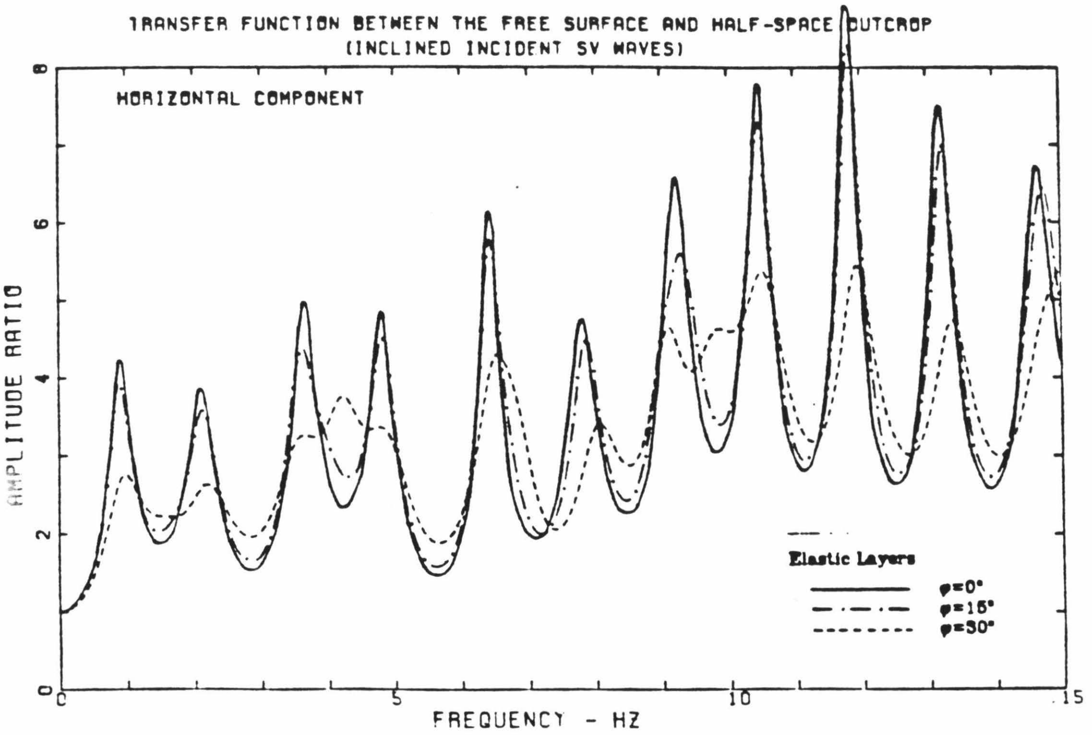

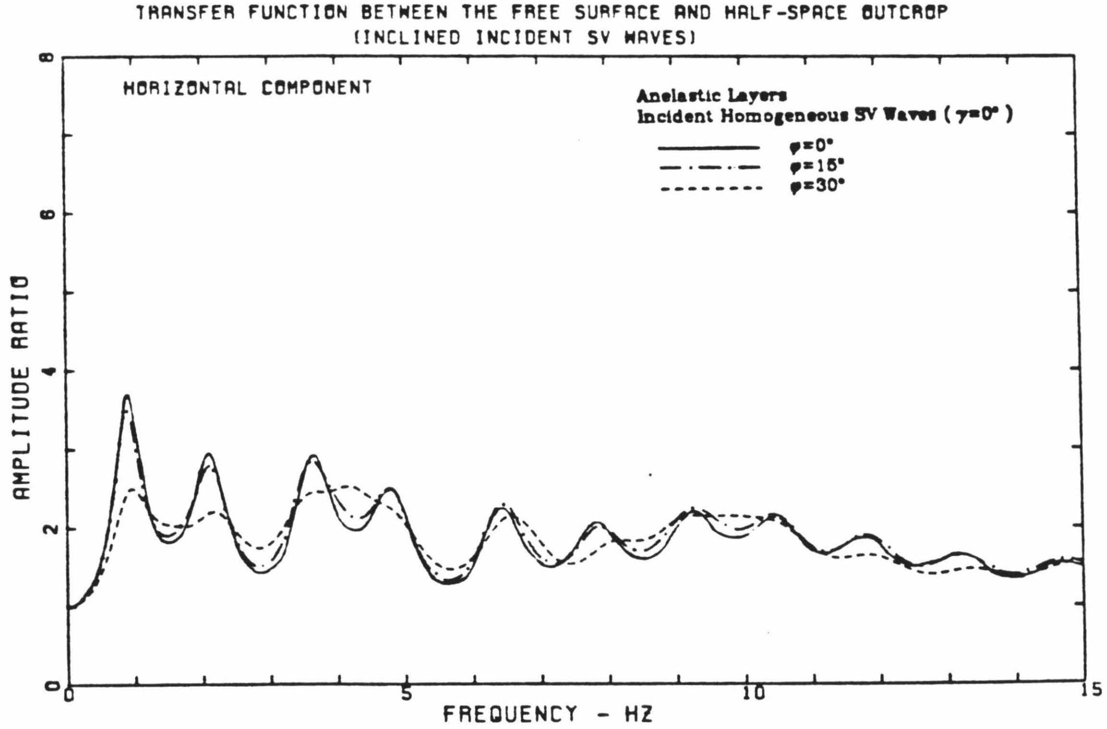

Fig. 2.18 Effects of attenuation and incident angle on the horizontal transfer function of incident SV wave. 7-layered system.

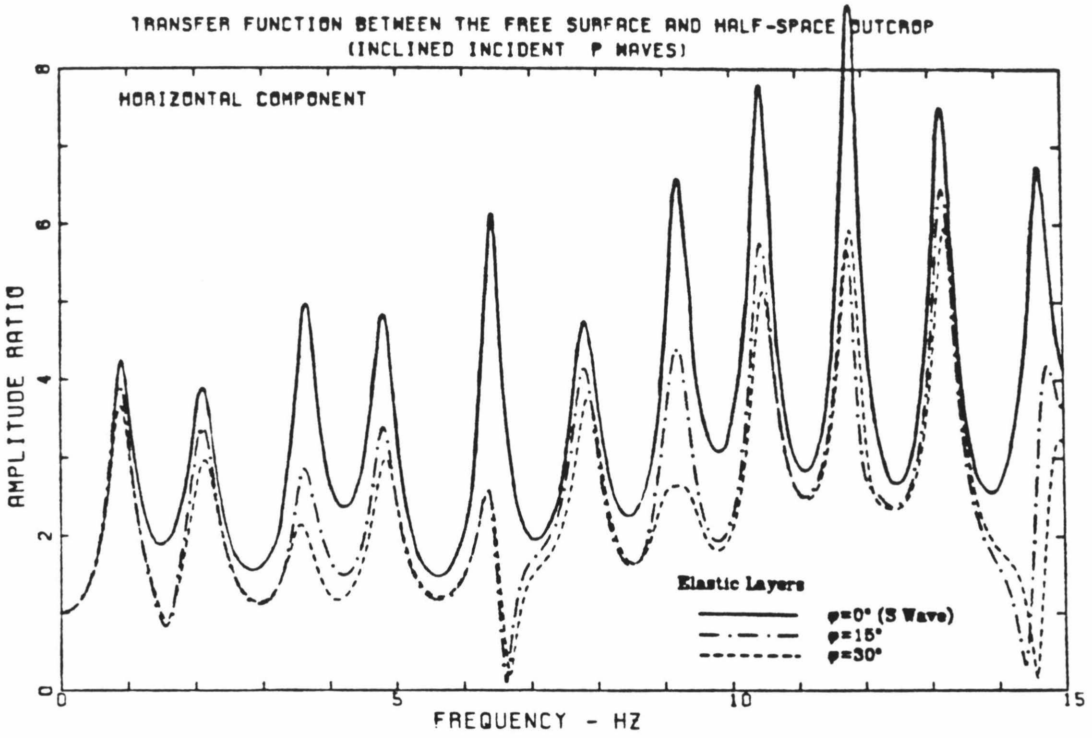

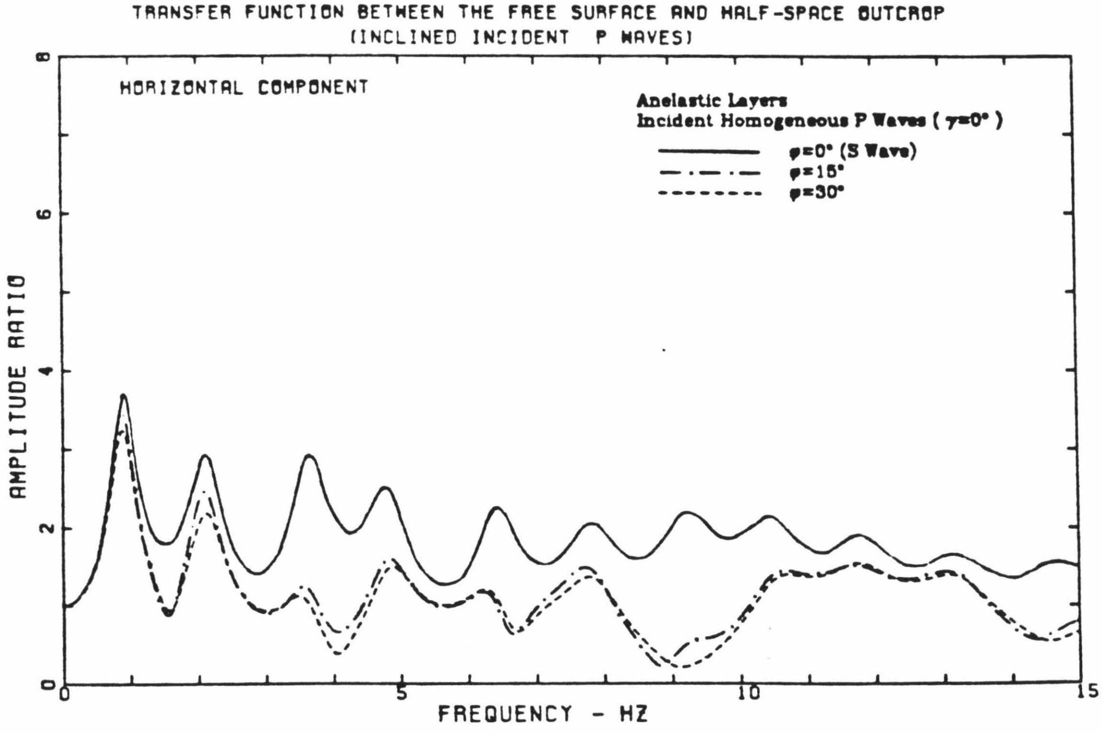

Fig. 2.19 Effects of attenuation and incident angle on the horizontal transfer function of incident P wave. 7-layered system.

transfer functions (Fig. 2.18) than on the vertical transfer functions (Fig. 2.16). It is interesting to note that for the incident angle ranging from 0° to 15°, the transfer functions at frequencies from 0 Hz to the corresponding fundamental frequency are only slightly affected by the anelastic attenuation and the angle of incidence. However, the effects of attenuation and incident angle on the transfer functions are significant at higher frequencies.

Fig. 2.20 gives the time domain transfer functions between the free surface and the half-space outcrop for normally incident SH waves. The corresponding frequency domain transfer functions are those shown in the top plots of Fig. 2.14. Fig. 2.21 shows the synthetic accelerograms at the free surface and at the half-space outcrop. The incident signals to the 7-layered system are the same as those described in Section 2.4.1 for the single-layered system. The notations are similar to those in Fig. 2.13. As seen in Figs. 2.20 and 2.21, the effects of anelastic attenuation reduce the amplitudes, smooth out the response and decrease the higher-order reflections.

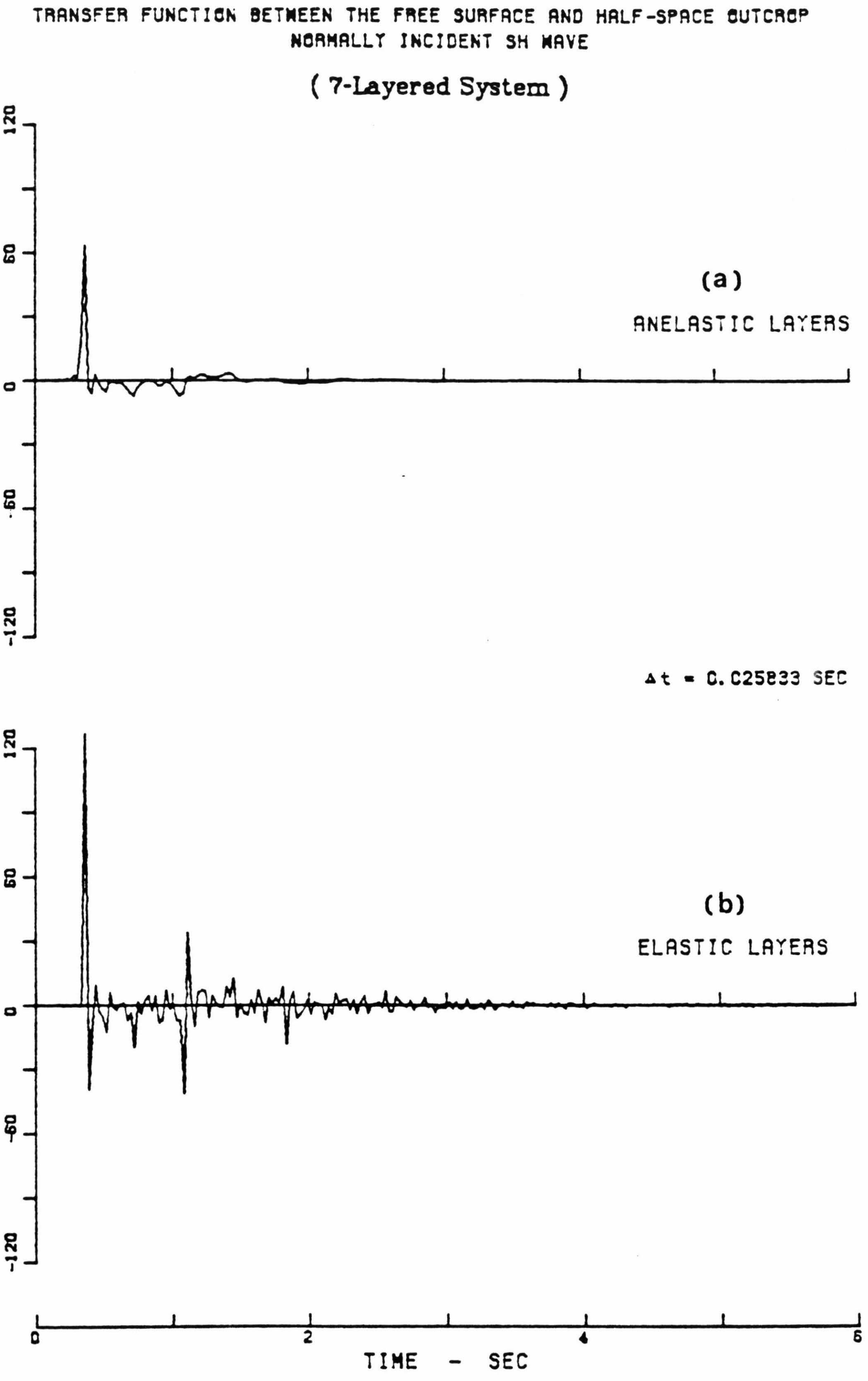

Fig. 2.20 The transfer functions of normally incident SH wave in the time domain for the 7-layered system(Table 2.2) with (a) anelastic layers, (b) elastic layers.

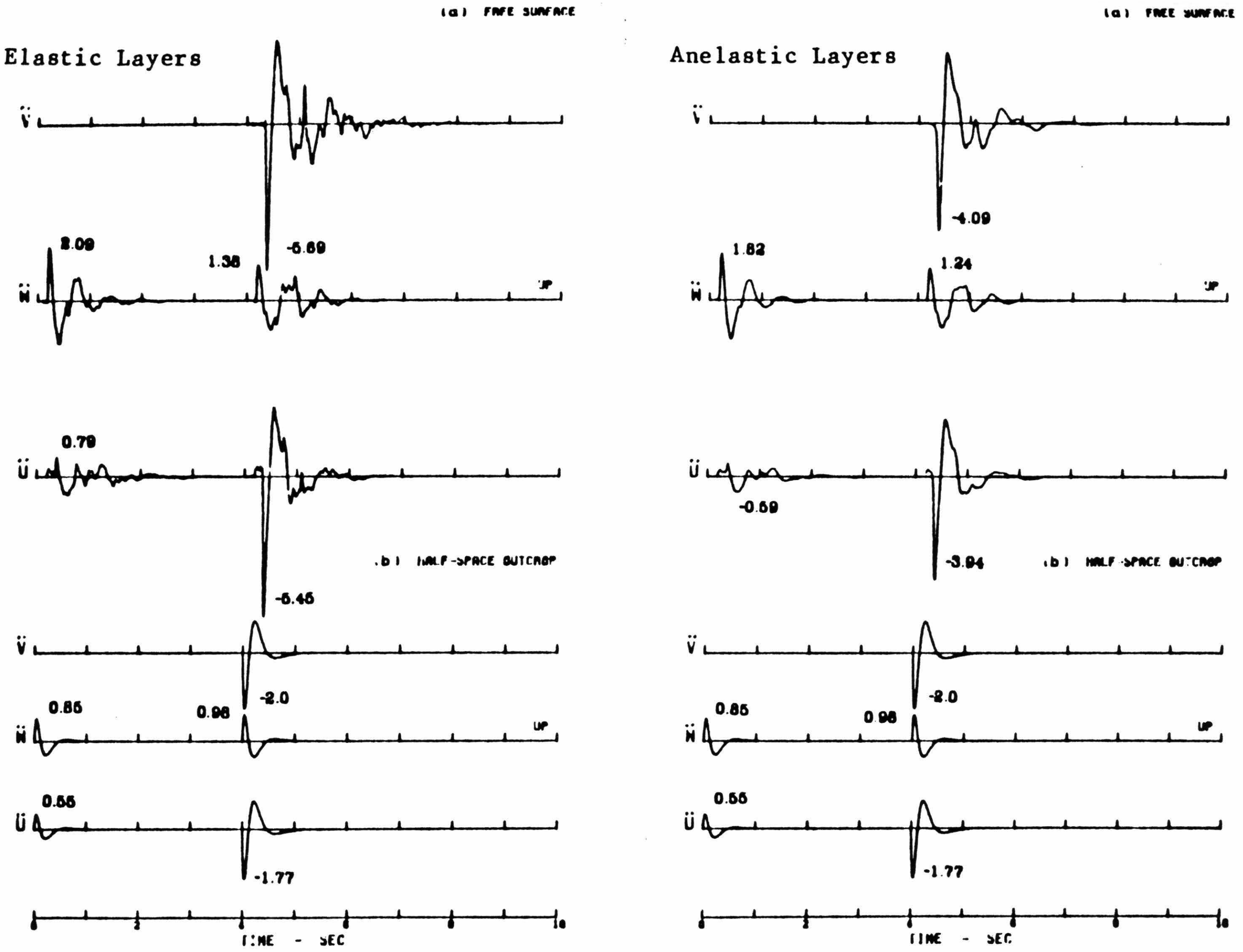

Fig. 2.21 The responses at the free surface and the half-space outcrop to incident SH wave($\ddot{v}$), SV and P waves($\ddot{w}$ and $\ddot{u}$). The amplitudes of incident SH, SV and P waves are 1.0, 1.0 and 0.5, respectively. 7-layered system.

2.5 Discussion

In the previous sections, the transfer function between the free surface and the half-space outcrop was derived for a single incident wave from the half-space at a specified angle. If the type of incident wave and the incident angle are given, the surface response can be computed by means of the linear system theory and the Fourier transform, i.e., the Fourier transform of the output is the product of the Fourier transform of the input and the transfer function. For multiple input, the surface response can be computed by using the superposition principle if the amplitudes, the arrival times and the incident angles of all the incident waves are known. This has been demonstrated by the numerical examples in Figs. 2.13 and 2.21.

In studying the local geology effects on earthquake ground motions, the subsoils overlying the bedrock are modelled by a multilayered structure overlying a half-space. The accelerograms recorded at an alluvium site and a nearby rock site are taken to be the output and the input, respectively, of the layered system. The observed site transfer function is obtained by dividing the Fourier transform of the accelerogram at an alluvium site by that at a nearby rock site. Since a measured accelerogram is composed of body and surface waves arriving at different times, we have to consider the response of the layered structure to a sequence of various wave arrivals having different incident angles. The application of the transfer functions derived in the previous sections to earthquake ground motions is not straightforward, because the relative contributions of P, SV, SH waves and surface waves in an accelerogram are not known. Furthermore, the transfer function for a multiple input, i.e., a sequence of body waves arriving at different times and different angles, is not the same as that for a single input. Therefore, there may be some difficulties in using the transfer function for a single-wave input to compare the observed site transfer function and evaluate local geology effects. In what follows we shall illustrate this by first considering incident SH waves and then incident P and SV waves.

Let a layered structure overlying a half-space be excited by an incident SH wave, $g_1(t)/2$, having an incident angle $\Theta 1$. Then the motions at the half-space outcrop is $g_1(t)$ and the response at the free surface, $f_1(t)$, is given by

$$f_1(t) = \int_{-\infty}^{\infty} g_1(\tau)\, TR_1(t-\tau)\, d\tau \tag{2.5.1}$$

where $TR_1(t)$ is the transfer function in the time domain between the free surface and the half-space outcrop for incident SH waves at $\Theta 1$ incident angle. In the frequency domain, equation (2.5.1) can be written as

$$F_1(\omega) = G_1(\omega)\, TR_1(\omega) \tag{2.5.2}$$

where $F_1(\omega)$ and $G_1(\omega)$ are the Fourier transforms of $f_1(t)$ and $g_1(t)$, respectively, and $TR_1(\omega)$ is the transfer function in the frequency domain which has been derived in Section 2.2.

Suppose a second SH wave, $g_2(t)/2$, is incident from the half-space, having an incident angle $\Theta 2$, t_0 seconds after the first SH wave arrival. The motions at the half-space outcrop is $g_2(t)$. For simplicity, we assume

$$g_2(t) = R\, g_1(t-t_0) \tag{2.5.3}$$

where the constant R is the amplitude ratio of the second wave arrival to the first wave arrival and t_0 is a time delay. The waveforms of two arrivals are assumed to be similar. The relation of $g_2(t)$ and $g_1(t)$ in the frequency domain, by the Fourier time-shift theorem, is given by

$$G_2(\omega) = R\, G_1(\omega)\, e^{-i\omega t_0} \tag{2.5.4}$$

where $G_2(\omega)$ and $G_1(\omega)$ are the Fourier transforms of $g_2(t)$ and $g_1(t)$, respectively.

The surface response to the second incident SH wave is given by

$$f_2(t) = \int_{-\infty}^{\infty} g_2(\tau)\, TR_2(t-\tau)\, d\tau \tag{2.5.5}$$

In the frequency domain, we have

$$F_2(\omega) = G_2(\omega)\, TR_2(\omega) \tag{2.5.6}$$

The transfer function, i.e., the ratio of the Fourier transform of the surface response, $f_1(t)+f_2(t)$, to that of the bedrock outcrop motions, $g_1(t)+g_2(t)$, is given by

$$Tsh(\omega) = \frac{F_1(\omega) + F_2(\omega)}{G_1(\omega) + G_2(\omega)} \tag{2.5.7}$$

From the relations in (2.5.2), (2.5.4) and (2.5.6), we have

$$Tsh(\omega) = \frac{TR_1(\omega) + R\, e^{-i\omega t_0}\, TR_2(\omega)}{1 + R\, e^{-i\omega t_0}} \tag{2.5.8}$$

For the case when $\Theta1=\Theta2$, $Tsh(\omega) = TR_1(\omega) = TR_2(\omega)$ and the transfer function for two inputs is the same as that for single input. This is also true for the case when $\Theta1 = \Theta2$ but the waveforms of two arrivals are different (i.e., the assumption in (2.5.3) is dropped). For the case when $\Theta1 \neq \Theta2$, $Tsh(\omega)$ is not equal to $TR_1(\omega)$ or $TR_2(\omega)$, and is dependent on the time delay t_0 and the amplitude ratio R. To show a numerical example, we consider the 7-layered model with anelastic layers given in Table 2.2 of Section 2.4.2, subjected to two incident SH waves at the angles 10° and 30°, i.e., $\Theta1=10^\circ$ and $\Theta2=30^\circ$. The amplitudes of the transfer functions for $R = 0.5$, $t_0 = 1.0$–sec and $R = 2.0$, $t_0 = 1.0$–sec are shown in Fig. 2.22. As compared to Fig. 2.15, at high frequencies the transfer functions in this figure are not as smooth as those for single incident SH wave. At low frequencies the shape and the locations of the peaks do not differ from those for single incident SH wave. The analysis herein can be extended to consider a number of SH wave arrivals.

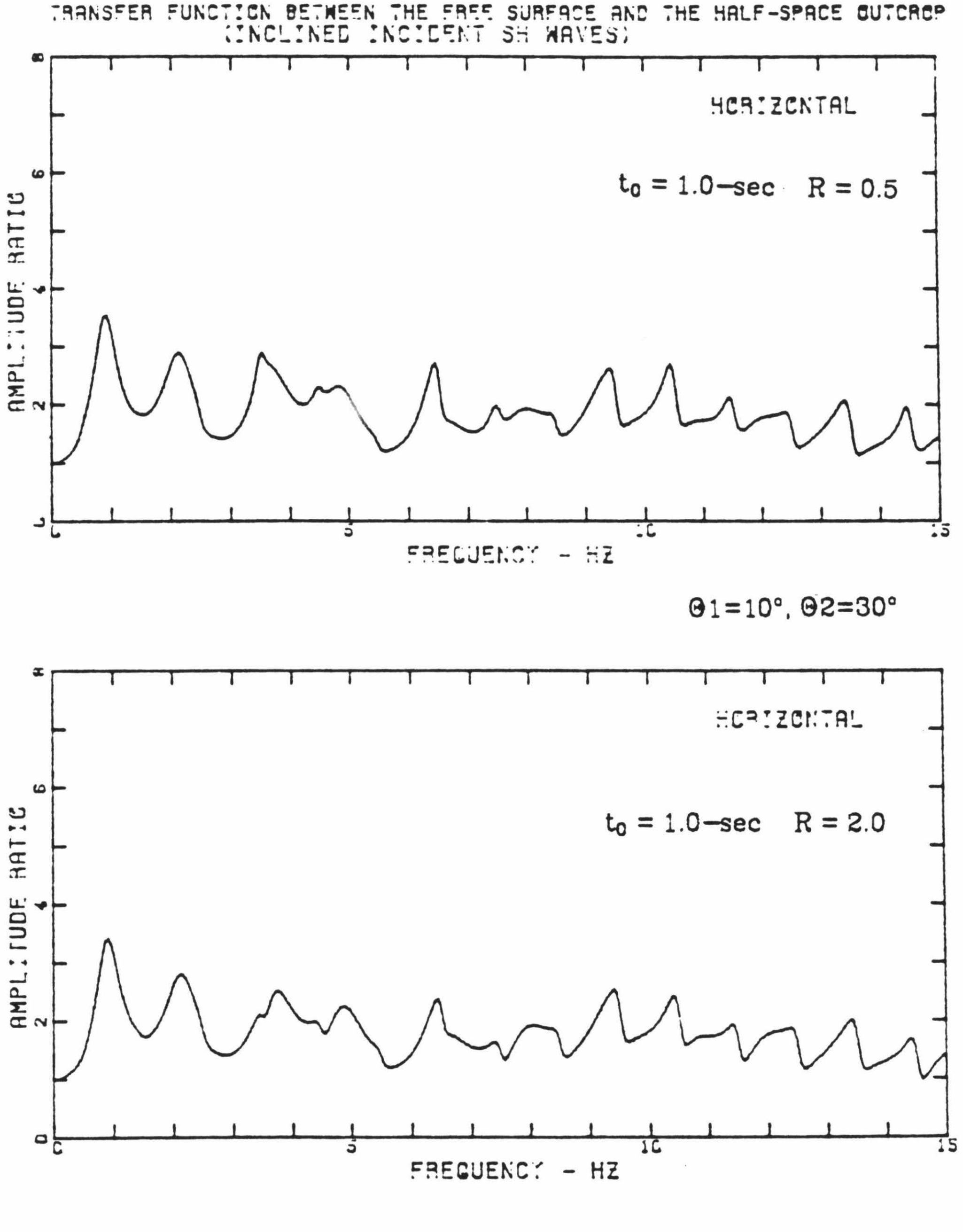

Fig. 2.22 The amplitudes of the transfer function for an incident SH wave at angle 10° and a second incident SH wave at 30° t_0=1.0-sec later. The amplitude of the second incident SH wave is R times that of the first incident SH wave.

Next, we consider a layered system excited by an incident P wave with a potential spectrum, $A(\omega)$, from the half-space at an angle of incidence, ϑ_p. Then by (2.3.39), the Fourier transforms of the horizontal and vertical response at the half-space outcrop are given by (For notations, see Fig. 2.4)

$$u_p'(\omega) = c_{up}(\omega)\, A(\omega) \tag{2.5.9a}$$

and

$$w_p'(\omega) = c_{wp}(\omega)\, A(\omega) \tag{2.5.9b}$$

where the frequency-dependent coefficients, c_{up} and c_{wp}, are given by (2.3.40). From (2.3.41) and (2.3.42), the Fourier transforms of the horizontal and vertical response at the free surface are

$$u_{0p}(\omega) = TR_{hp}(\omega)\, u_p'(\omega) \tag{2.5.10a}$$

and

$$w_{0p}(\omega) = TR_{vp}(\omega)\, w_p'(\omega) \tag{2.5.10b}$$

where $TR_{hp}(\omega)$ and $TR_{vp}(\omega)$ are the horizontal and vertical transfer functions between the free surface and the half-space outcrop, respectively, for an incident P wave at angle ϑ_p.

Let a SV wave with a potential spectrum, $B(\omega)$, be incident from the half-space at an angle Θ_s, t_{sp} seconds after the P wave arrival. Then from (2.3.47) and the Fourier time-shift theorem, the Fourier transforms of the horizontal and vertical response at the half-space outcrop are given by

$$u_s'(\omega) = c_{us}(\omega)\, B(\omega)\, e^{-i\omega t_{sp}} \tag{2.5.11a}$$

and

$$w_s'(\omega) = c_{ws}(\omega)\, B(\omega)\, e^{-i\omega t_{sp}} \tag{2.5.11b}$$

where the coefficients, $c_{us}(\omega)$ and $c_{ws}(\omega)$, are given by (2.3.48). From (2.3.49) and

(2.3.50), the Fourier transforms of the horizontal and vertical response at the free surface are

$$u_{0s}(\omega) = TR_{hs}(\omega)\, u_s'(\omega) \tag{2.5.12a}$$

and

$$w_{0s}(\omega) = TR_{vs}(\omega)\, w_s'(\omega) \tag{2.5.12b}$$

where $TR_{hs}(\omega)$ and $TR_{vs}(\omega)$ are the horizontal and vertical transfer functions, respectively, for an incident SV wave at angle Θ_s.

The horizontal and vertical transfer functions for the combination of both incident P and SV waves are given by

$$Rpsv(\omega) = \frac{u_{0p}(\omega) + u_{0s}(\omega)}{u_p'(\omega) + u_s'(\omega)} \tag{2.5.13a}$$

and

$$Vpsv(\omega) = \frac{w_{0p}(\omega) + w_{0s}(\omega)}{w_p'(\omega) + w_s'(\omega)} \tag{2.5.13b}$$

By the relations from (2.5.9) to (2.5.12), these transfer functions can be written as

$$Rpsv(\omega) = \frac{TR_{hp}(\omega)c_{up}(\omega)A(\omega)+TR_{hs}(\omega)c_{us}(\omega)B(\omega)e^{-i\omega t_{sp}}}{c_{up}(\omega)A(\omega)+c_{us}(\omega)B(\omega)e^{-i\omega t_{sp}}} \tag{2.5.14a}$$

and

$$Vpsv(\omega) = \frac{TR_{vp}(\omega)c_{wp}(\omega)A(\omega)+TR_{vs}(\omega)c_{ws}(\omega)B(\omega)e^{-i\omega t_{sp}}}{c_{wp}(\omega)A(\omega)+c_{ws}(\omega)B(\omega)e^{-i\omega t_{sp}}} \tag{2.5.14b}$$

For simplicity, we assume the potential spectra of incident P wave and incident SV wave differ only by a constant ratio, i.e.,

$$A(\omega) = R_{p/s}\, B(\omega) \tag{2.5.15}$$

where $R_{p/s}$ is a constant and frequency-independent. The transfer functions in

(2.5.14) can then be simplified as

$$\mathrm{Rpsv}(\omega) = \frac{TR_{hp}(\omega)c_{up}(\omega)R_{p/s}+TR_{hs}(\omega)c_{us}(\omega)e^{-i\omega t_{sp}}}{c_{up}(\omega)R_{p/s}+c_{us}(\omega)e^{-i\omega t_{sp}}} \tag{2.5.16a}$$

and

$$\mathrm{Vpsv}(\omega) = \frac{TR_{vp}(\omega)c_{wp}(\omega)R_{p/s}+TR_{vs}(\omega)c_{ws}(\omega)e^{-i\omega t_{sp}}}{c_{wp}(\omega)R_{p/s}+c_{ws}(\omega)e^{-i\omega t_{sp}}} \tag{2.5.16b}$$

To show a numerical example, we again consider the 7-layered structure given in Table 2.2 and assume $\vartheta_p = \Theta_s = 30^\circ$. Fig. 2.23 shows the amplitudes of the horizontal and vertical transfer functions for $R_{p/s} = 0.5$ and $t_{sp} = 2.5$–sec, while Fig. 2.24 shows the results for $R_{p/s} = 0.5$ and $t_{sp} = 1.0$–sec. The amplitude ratios in these figures fluctuate more than those shown in Figs. 2.16 to 2.19 for single incident P or SV wave, and are sensitive to the values of t_{sp} and $R_{p/s}$. The results for different values of $R_{p/s}$ are not shown here; however, it is found that the amplitude of the vertical transfer function has some big spikes when $R_{p/s} = 1.0$.

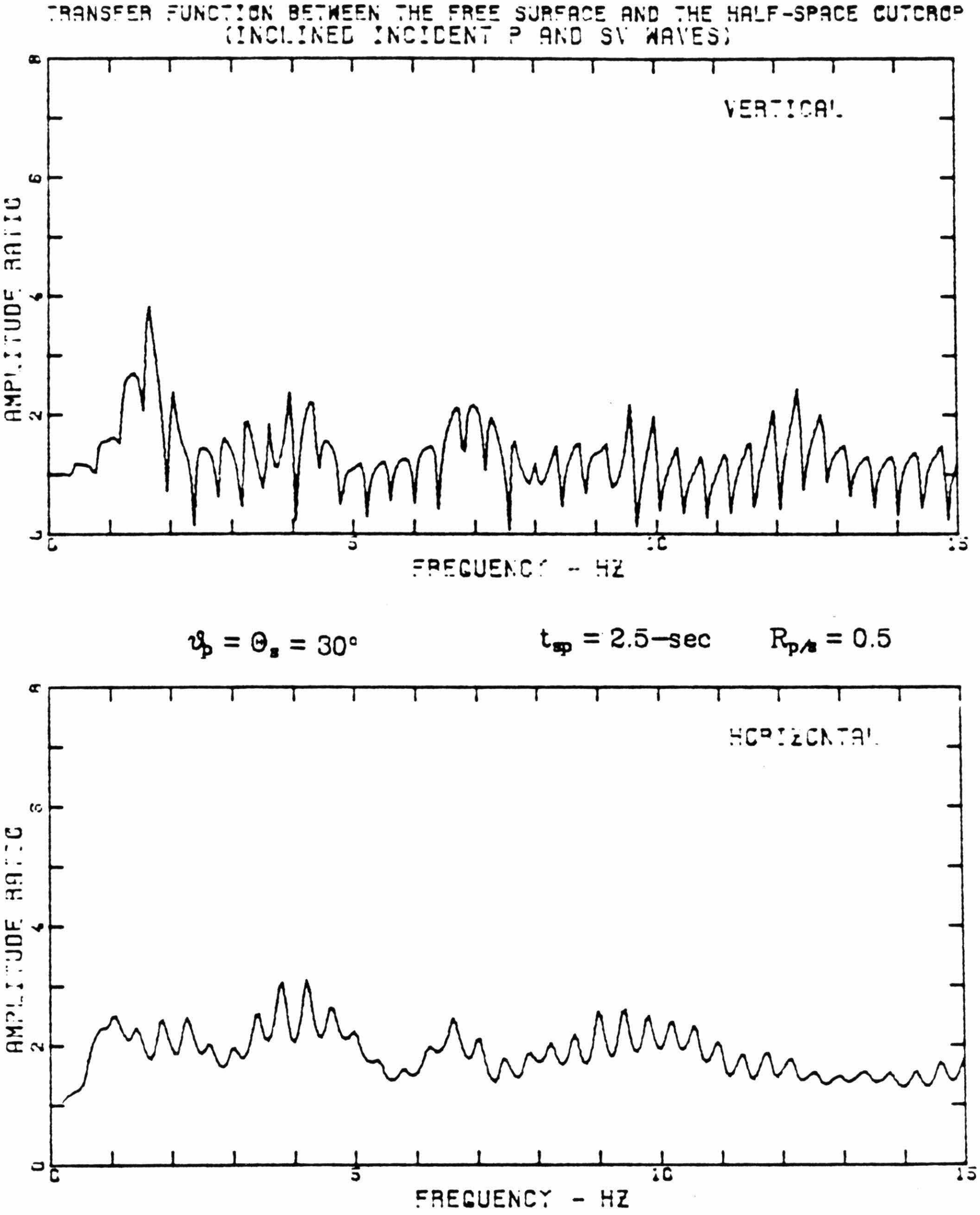

Fig. 2.23 The amplitudes of the horizontal and vertical transfer functions for an incident P wave at 30° and an incident SV wave at 30°. SV-wave arrives t_{sp} -sec after P-wave. The potential of the incident P wave is Rp/s times that of the incident SV wave. Rp/s=0.5 and t_{sp} =2.5-sec.

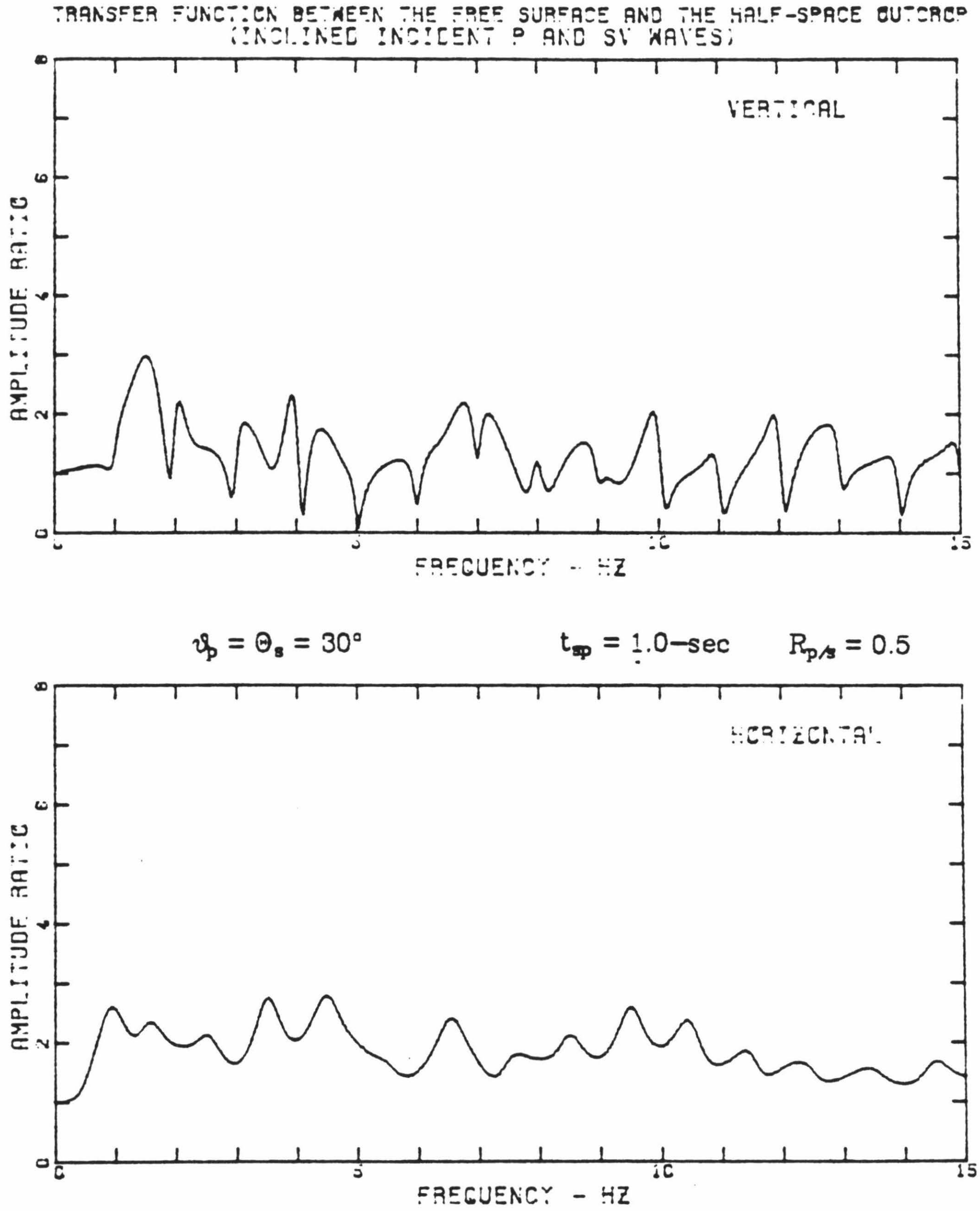

Fig. 2.24 Similar to Fig. 2.23 for Rp/s=0.5 and t_{sp} =1.0-sec.

2.6 References

[1] Aki, K. and Richards, P. G. (1980), **Quantitative Seismology, Theory and Methods,** Two volumes, W. H. Freeman and Company, San Francisco, 1980.

[2] Ben-Menahem, A. and Singh, S. J. (1981), **Seismic Waves and Sources,** Springer-Verlag New York Inc., 1981.

[3] Borcherdt, R. D. (1973), 'Energy and Plane Waves in Linear Viscoelastic Media," *Journal of Geophysical Research*, Vol. **78**, No. 14, 1973, pp. 2442-2453.

[4] Borcherdt, R. D. (1977), 'Reflection and Refraction of Type-II S Waves in Elastic and Anelastic Media," *Bulletin of the Seismological Society of Amercia*, Vol. **67**, No. 1, 1977, pp. 43-67.

[5] Brigham, E. O. (1974), **The Fast Fourier Transform,** Prentice-Hall, Englewood Cliffs, N. J., 1974.

[6] Brekhovskikh, L. M. (1960, 1980), **Waves in Layered Media,** Academic Press, Inc., First Edition, 1960; Second Edition, 1980.

[7] Buchen, P. W. (1971), 'Plane Waves in Linear Viscoelastic Media," *Geophysical Journal of the Royal Astronomical Society*, Vol. **23**, pp. 531-542.

[8] Ebel, J. E. and Helmberger, D. V. (1982), 'P-Wave Complexity and Fault Asperities: The Borrego Mountain, California, Earthquake of 1968," *Bulletin of the Seismological Society of America*, Vol. **72**, No.2, April 1982, pp. 413-437.

[9] Ewing, W. M., Jardetzky, W. S. and Press, F. (1957), **Elastic Waves in Layered Media,** McGraw-Hill Book Company, Inc., New York, 1957.

[10] Futterman, W. I. (1962), 'Dispersive Body Waves," *Journal of Geophysical Research*, Vol. **67**, pp. 5279-5291.

[11] Haskell, N. A. (1953), 'The Dispersion of Surface Waves in Multilayered Media," *Bulletin of the Seismological Society of America*, Vol. **43**, No.1, January 1953, pp. 17-34.

[12] Haskell, N. A. (1960), "Crustal Reflection of Plane SH Waves," *Journal of Geophysical Research*, Vol. **65**, No.13, December 1960, pp. 4147-4150.

[13] Haskell, N. A. (1962), "Crustal Reflection of P and SV Waves," *Journal of Geophysical Research*, Vol. **67**, No.12, November 1962, pp. 4751-4767.

[14] Jones, J. J. and Roesset, J. M. (1970), 'Soil Amplification of SV and P Waves," Research Report R70-3, Department of Civil Engineering, Massachusetts Institute of Technology, Cambridge, January 1970.

[15] Krebes, E. S., and Hron, F. (1980), 'Ray-Synthetic Seismograms for SH Waves in Anelastic Media," *Bulletin of the Seismological Society of America*, Vol. **70**, No. 1, 1980, pp. 29-46.

[16] Miklowitz, J. (1978), **The Theory of Elastic Waves and Waveguides**, North-Holland Publishing Company, Amsterdam, New York, Oxford.

[17] Roesset, J. M. (1970), 'Fundamentals of Soil Amplification," in **Seismic Design for Nuclear Power Plants**, editor; R.J.Hansen, pp. 183-244.

[18] Schnabel, P. B., Lysmer, J. and Seed, H. B. (1972), 'SHAKE - A Computer Program for Earthquake Response Analysis of Horizontally Layered Sites," Report No. *EERC 72-12*, Earthquake Engineering Research Center, University of California, Berkeley, December 1972.

[19] Shannon & Wilson, Inc., and Agbabian Associates (SW-AA) (1978), 'Geotechnical and Strong Motion Earthquake Data from U.S. Accelerograph Stations, Vol. 2, Pasadena, Santa Barbara, Taft, and Hollister, California," *NUREG-0029*, Vol. **2**, NRC-6A, Report to the U.S. Nuclear Regulatory Commission, June 1978.

[20] Shannon & Wilson, Inc., and Agbabian Associates (SW-AA) (1980a), 'Verification of Subsurface Conditions at Selected 'Rock' Accelerograph Stations in California, Vol. 2," *NURE/CR-0055*, Report to the U.S. Nuclear Regulatory Commission, Sepetember 1980.

[21] Shannon & Wilson, Inc., and Agbabian Associates (SW-AA) (1980b), 'Geotechnical Data from Accelerograph Stations Investigated during the Period 1975-1979, Summary Report," *NURE/CR-1643*, Report to the U.S. Nuclear Regulatory Commission, September 1980.

[22] Silva, W. (1976), 'Body Waves in a Layered Anelastic Solid," *Bulletin of the Seismological Society of America*, Vol. **66**, No.5, October 1976, pp. 1539-1554.

[23] Thomson, W. T. (1950), 'Transmission of Elastic Waves through a Stratified Solid Medium," *Journal of Applied Physics*, Vol. **21**, February 1950, pp. 89-93.

[24] Tsai, N. C. (1970), "A Note on the Steady-State Response of an Elastic Half-Space," *Bulletin Seismological Society of America*, Vol. **60**, No.3, June 1970, pp. 795-808.

CHAPTER 3

ANALYSIS OF STRONG MOTION DATA RECORDED IN THE PASADENA AREA

3.1 Introduction

The Pasadena area is situated in the northwestern part of the San Gabriel Valley (Figs. 3.1 and 3.2). This area is bounded on the north side by the San Gabriel Mountains with elevations of over 6000 feet and on the west side by the Verdugo Moutains with low hills in which the crystalline rocks are exposed. The geology of this area consists of Quaternary alluvial deposits overlying granitic and metamorphic rocks. The alluvium is approximately 900 feet thick beneath the campus of the California Institute of Technology (Fig. 3.3) and about 400 feet thick beneath the Jet Propulsion Laboratory. This area has been studied in great detail for small earthquake response by Gutenberg (1957). The local distribution of strong ground motions recorded by 19 seismoscopes and 4 accelerographs during the 1971 San Fernando earthquake has been presented by Hudson (1972).

In this chapter, all the data recorded at four stations in the Pasadena area during four past earthquakes are analyzed to investigate the nature of strong ground motions and local geology effects on recorded ground motions. The data are limited by the availability of digitized accelerograms. Strong motion accelerograms are studied in both the time and frequency domains. Furthermore, the accelerograms of two nearby stations are compared to study the spatial variations of ground motions.

3.2 Stations and Earthquakes Studied

In the Pasadena area, there are four stations, i.e., Jet Propulsion Laboratory (JPL), Seismological Laboratory (SL), Millikan Library (ML) and Athenaeum (ATH), at which strong motion accelerographs are located. The locations of

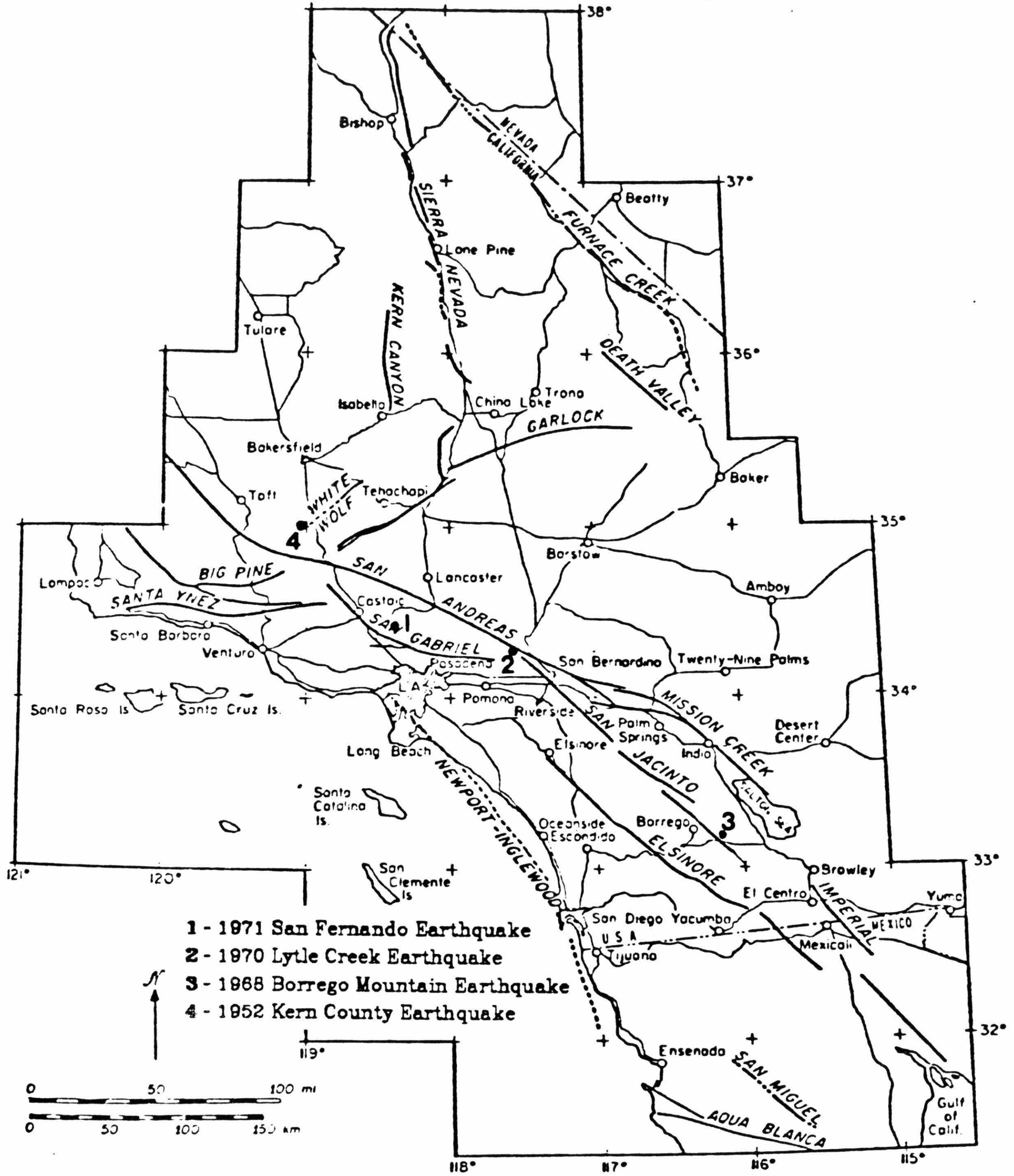

Fig. 3.1 Map indicating the epicenters of four earthquakes recorded in the Pasadena area.

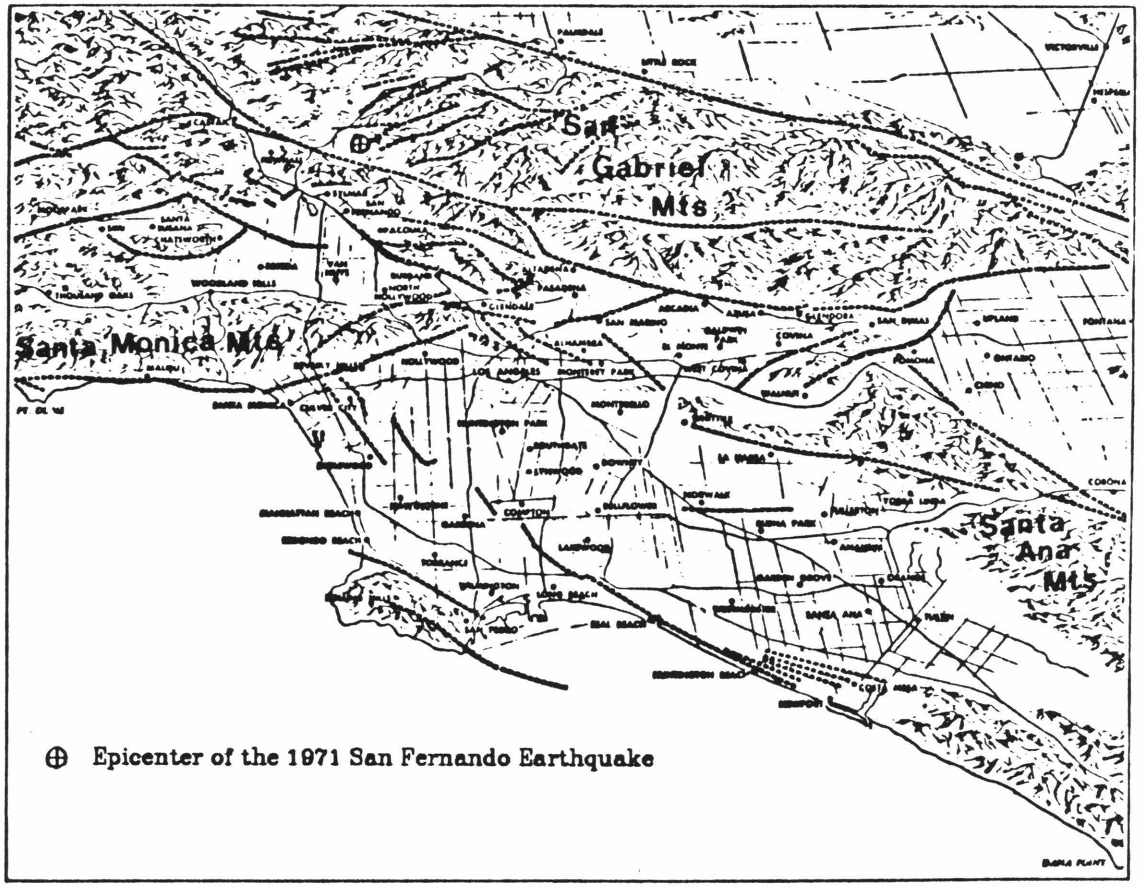

Fig. 3.2 Map indicating location of the Pasadena area. The encircled cross is the epicenter of San Fernando earthquake.

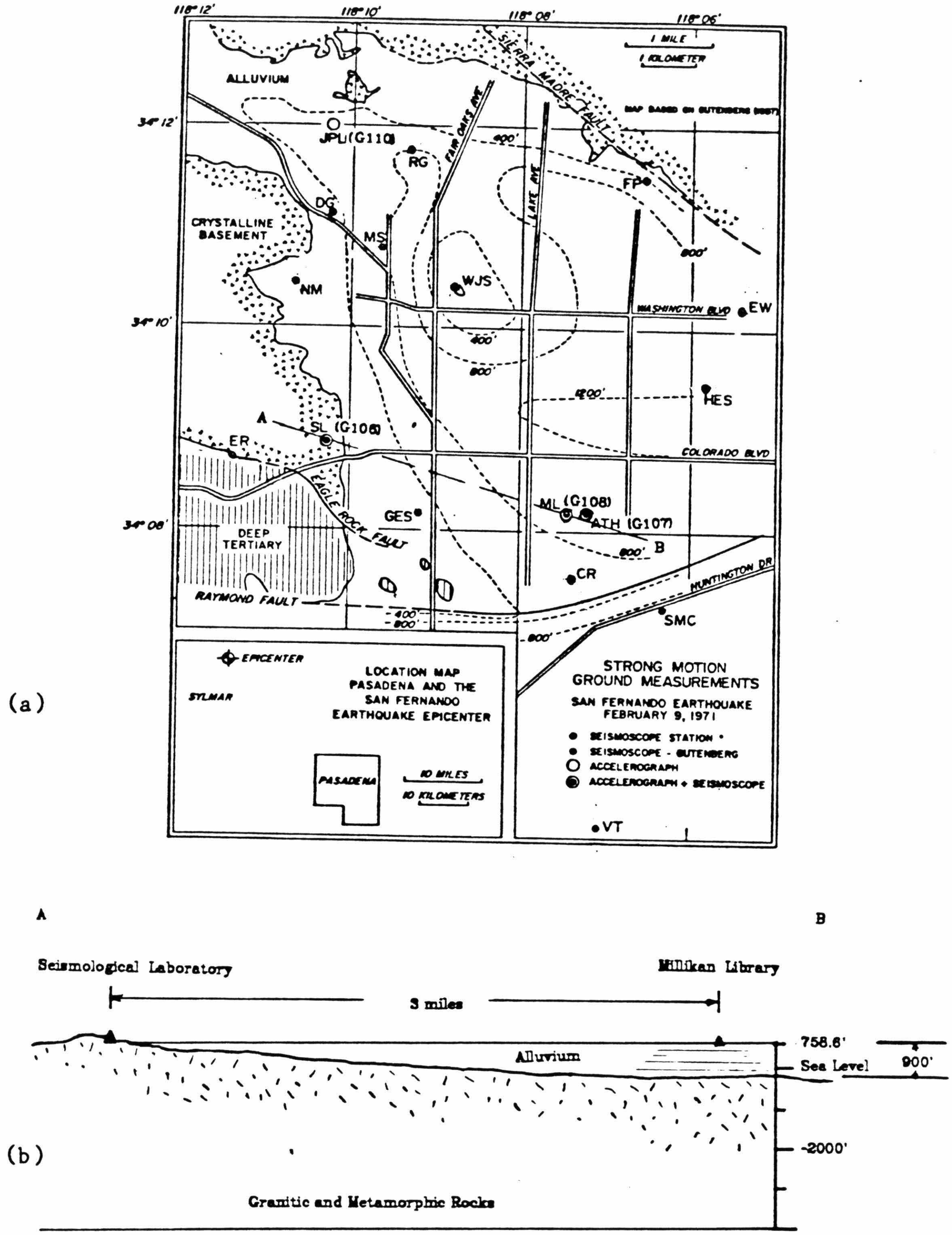

Fig. 3.3 (a) Location of stations in the Pasadena area. Dotted lines indicate the estimated thickness in feet of alluvium overlying crystalline rocks. (modified from Gutenberg, 1957; Hudson, 1972) (b) Profile AB between Seismological Laboratory and Millikan Library.

these stations are shown in Fig. 3.3(a). The Seismological Laboratory, which is about 3 miles from the Millikan Library, is underlain by granitic basement rock. The stations JPL, ML and ATH are located at alluvial sites. A summary of station characteristics is given in Table 3.1. The strong motion data obtained at these stations during four earthquakes are analyzed in this chapter. The earthquakes are the 1971 San Fernando, the 1970 Lytle Creek, the 1968 Borrego Mountain and the 1952 Kern County earthquakes. The epicenters are indicated in Fig. 3.1. The source mechanism of these earthquakes are briefly summarized in Table 3.2.

The 1971 San Fernando earthquake was recorded at all four stations. This set of records has provided data for studying local geology effects on strong ground motions. The 1968 Borrego Mountain earthquake was recorded at JPL, ML and ATH. Although it was recorded at SL, the record was not digitized probably because it was too short (USGS and EERL, 1968). The 1970 Lytle Creek earthquake was recorded at ML and JPL. Only ATH recorded the 1952 Kern County earthquake. The instrument types, epicentral distances and peak recorded accelerations for different records are summarized in Table 3.1. The digital data have been obtained from the Volume II series of magnetic tapes processed at Caltech Earthquake Engineering Research Laboratory. These tapes contain equally spaced accelerograms (corrected for instrument response and band-pass filtered) and integrated velocity and displacement data. The Caltech data reference numbers are also shown in Table 3.1.

Table 3.1 - Station Characteristics and Data References

Station	Seismological Lab. (SL)	Millikan Library (ML)	Athenaeum (ATH)	Jet Propulsion Lab. (JPL)
1971 San Fernando	G106•	G108	G107	G110
instrument	RFT-250	RFT-250	SMA-1	RFT-250
P.G.A.••	19.2%g	20.2%g	10.9%g	21.2%g
Δ #	36 km	39 km	40 km	32 km
1970 Lytle Creek	————	W342	————	W344
instrument		RFT-250		RFT-250
P.G.A.		2.0%g		2.5%g
Δ		56 km		59 km
1968 Borrego Mountain	————	Y375	Y376	Y373
instrument		AR-240	USGS SM 7D	AR-240
P.G.A.		1.0%g	1.0%g	0.8%g
Δ		216 km	215 km	223 km
1952 Kern County	————	————	A003	————
instrument			USGS	
P.G.A.			5.3%g	
Δ			128 km	
Site Characteristics	granite crystalline rock.	900 ft alluvium. basement of 9-story R.C. bldg.	900 ft alluvium. basement of 2½-story R.C.bldg.	400 ft alluvium. basement of 9-story steel frame bldg.

• Caltech reference number.

•• P.G.A. (%g) - peak ground acceleration which is the largest in three components.

Δ (km) - epicentral distance.

Table 3.2 - Earthquake Characteristics

Parameters	San Fernando Earthquake Feb. 9, 1971 6:00 PST	Lytle Creek Earthquake Sept. 12, 1970 6:30 PST	Borrego Mountain Earthquake April 8, 1968 18:30 PST	Kern County Earthquake July 21, 1952 4:53 PDT
Epicenter	34°24'00"N 118°23'42"W	34°16'12"N 117°32'24"W	33°11'24"N 116°07'42"W	35°00'00"N 119°02'00"W
Focal Depth	13 km	8 km	9 km	16 km
Magnitude •				
Local, M_L	M_L=6.3	M_L=5.7	M_L=6.8	M_L=7.2
Surface-wave, M_s	M_s=6.6	- - -	M_s=6.7	M_s=7.7
Seiemic Moment M_0 (dyne-cm)	1.4×10^{26}	0.01×10^{26}	0.7×10^{26}	20.0×10^{26}
Focal Mechanism	thrust	- - -	right-lateral strike-slip	left-lateral, thrust
strike	~ N64°W	- - -	~ N48°W	~ N50°E
dip	~ 52°NE	- - -	~ vertical	~ 60-66°SE

• Kanamori and Jennings (1978).

3.3 Data of the 1971 San Fernando Earthquake

3.3.1 Strong Motion Accelerograms

The accelerograms obtained at SL, ML, ATH and JPL during the 1971 San Fernando earthquake have been corrected for instrument response and were bandpassed between 0.125 and 25 Hz. The 40-sec portions of the accelerograms are shown in Figs. 3.4a, b and c. To facilitate comparison, the records were shifted relative to each other along the time axis so that the first shear wave arrivals at four stations were lined up approximately. An aftershock was recorded at SL, ML and JPL between 30 and 35 seconds. This aftershock was also recorded at the Pacoima Dam which was in the epicentral region. The vertical motions have distinctly higher frequencies and lower amplitudes than horizontal motions which is typical. The duration of strong shaking was approximately 8 seconds, this being the same as the duration of the slipping process of the fault.

These four stations are located in almost the same azimuth with respect to the epicenter and the distance attenuation effect should be a minor factor in the variation of ground shaking in this area. Comparisons of the accelerograms in Fig. 3.4 show the following aspects:

(1) Strongly polarized motions in the east-west direction are observed at SL. Slightly polarized motions in the S82E direction are also observed at JPL. On the other hand, the motions at ML and ATH are equally intense in both horizontal directions. It is noted that SL is situated on the edge of the Verdugo Mountains and JPL is near the San Gabriel Mountains. The variation is attributed to the change of seismic wave ray paths resulting from the irregular sedimentary basin in the area. It indicates the influences of 3-dimensional local geology features on the recorded surface motions. As will be seen in the next section, the motions at SL are equally intense in the

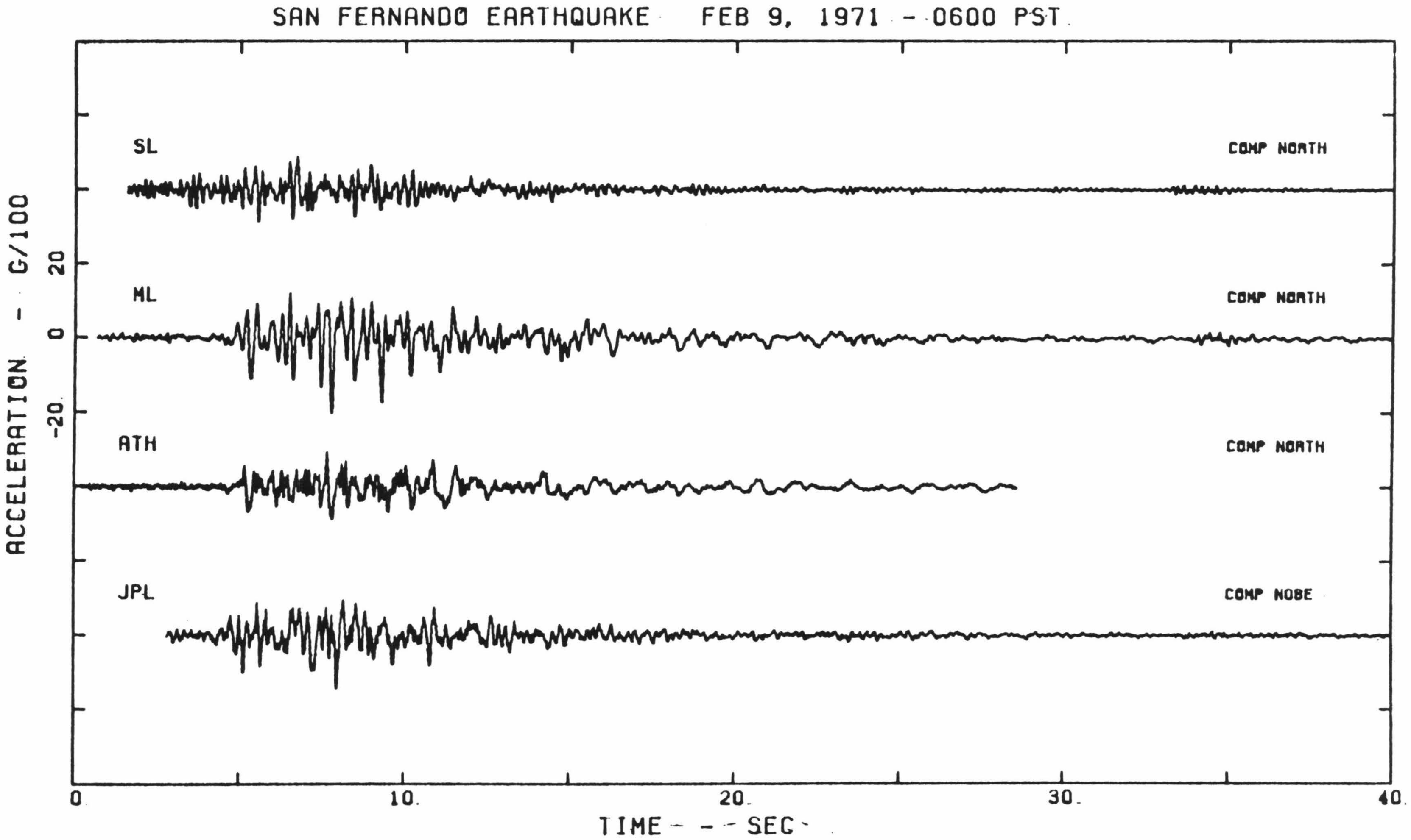

Fig. 3.4a Recorded accelerations at SL, ML, ATH and JPL in the Pasadena area during the 1971 San Fernando earthquake - north component.

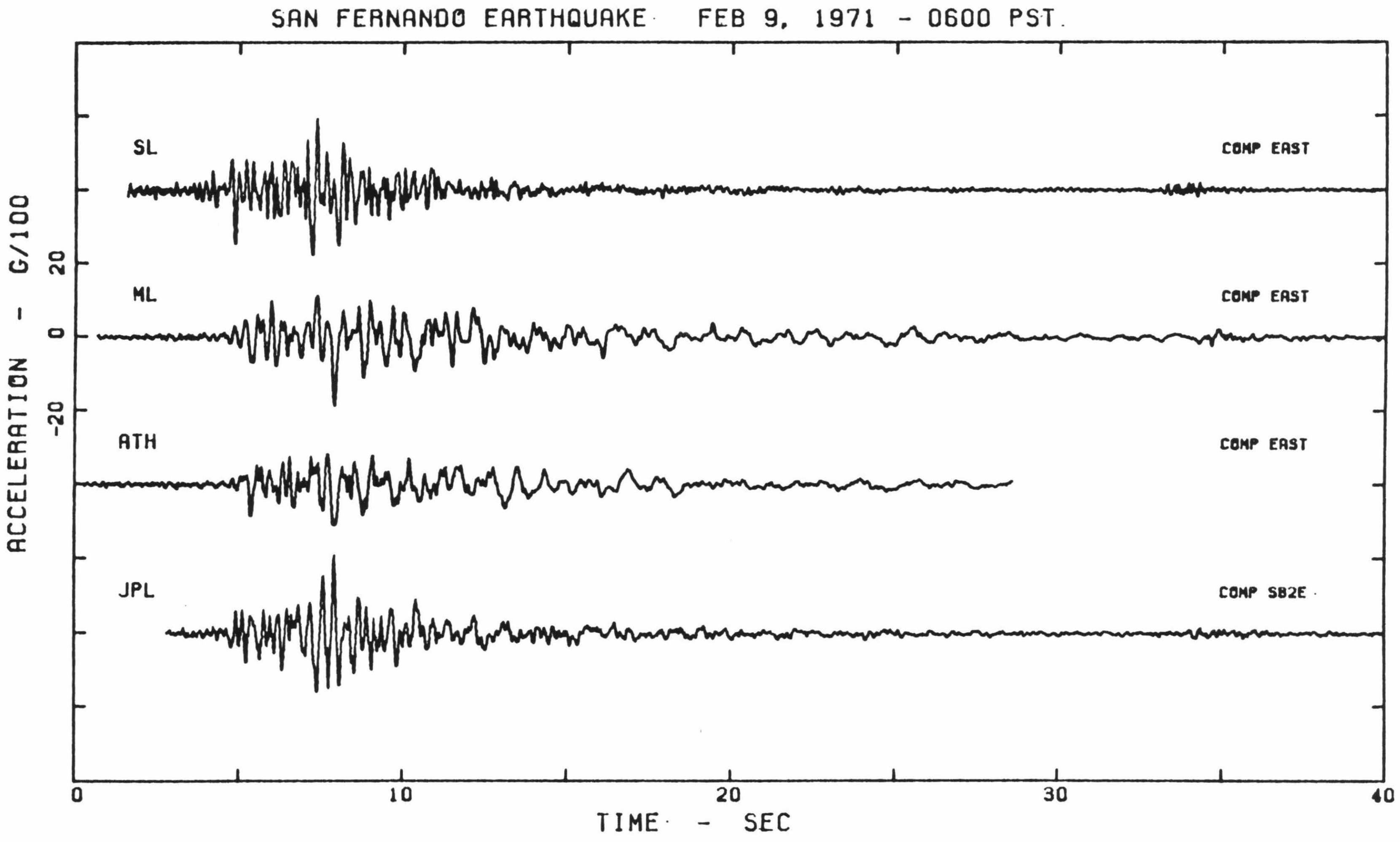

Fig. 3.4b Recorded accelerations at SL, ML, ATH and JPL in the Pasadena area during the 1971 San Fernando earthquake - east component.

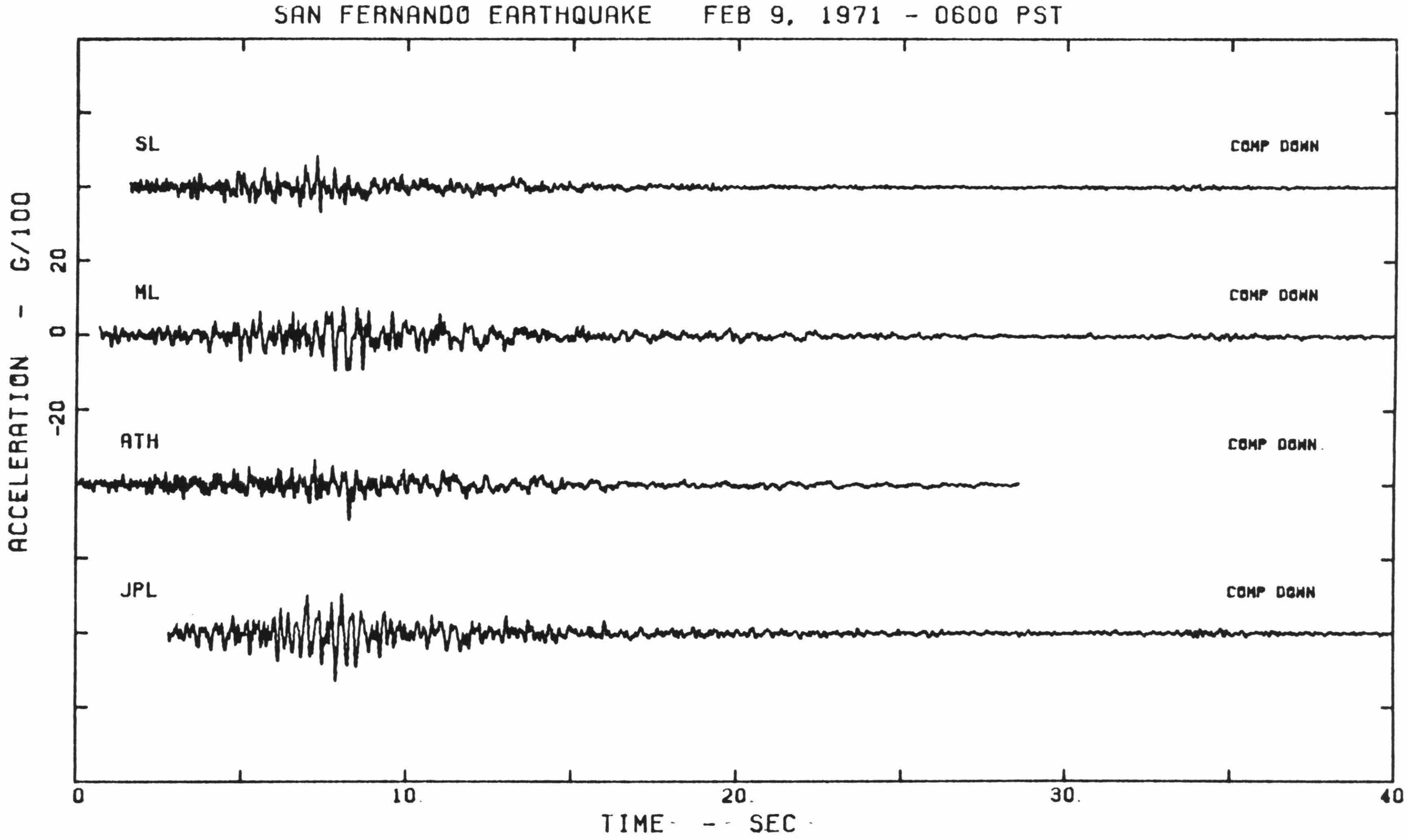

Fig. 3.4c Recorded accelerations at SL, ML, ATH and JPL in the Pasadena area during the 1971 San Fernando earthquake - vertical component.

transverse and radial directions. In Section 3.3.3, we shall investigate the 2-dimensional characteristics of ground motions recorded at these stations in the frequency domain.

(2) Comparison of the first part of the accelerograms shows that the arriving P waves are mainly seen in the vertical component at ML and ATH, while the motions of incoming P waves at SL are equally seen in three components. This implies that at SL seismic body waves emerged at some angles other than vertically. On the other hand, seismic body waves might have arrived at ML and ATH nearly vertically because of the bending of the rays in the low velocity sediments underlying the stations. The early motions at JPL are not predominantly vertical because the station is near the San Gabriel Mountains and the underlying alluvium is not as deep as those at ML and ATH.

(3) The shakings at ML, ATH and JPL are not significantly greater than those at SL. This observation is inconsistent with the conclusion drawn by Gutenberg (1956, 1957) in the study of local geology effects on very small earthquake motions. In that study, Gutenberg found that the motions on the Caltech campus were several times larger than those recorded at the Seismological Laboratory. It should be noted that Gutenberg's measurements were of extremely weak ground motions that were far below the threshold of human sensibility. His findings are not directly applicable to strong ground motions.

(4) Detailed comparison of the accelerograms in Fig. 3.4 indicates that relative to SL, the ground accelerations at other stations are dominated by waves of longer periods not only in the strong-shaking part but in the trailing part, although obscure long-period motions also exist at SL between 10 and 30

seconds. The change of dominant frequencies from high frequency at a rock site to low frequency at alluvial sites was also observed in the records of the 1957 San Francisco earthquake (Hudson and Housner, 1958; or see Fig. 1.3). The variation of the frequency content of the motions at SL and other stations are partly due to the local geology effect. The frequency content of these motions will be investigated in Section 3.3.3.

(5) The duration of the shakings at ML and ATH was longer than that at SL. This is due to larger amplitudes of the trailing motions at ML and ATH. The trailing motions are characterized by relatively long-period waves and are constituted by the surface waves, indirect body waves and reverberating body waves in the sediment basin.

3.3.2 Interpretation of the Ground Motion Data

To investigate the data in more detail, the horizontal accelerograms were rotated to the transverse and radial components. They are presented in Figs. 3.5a and b. Positive radial motion is in the direction radially away from the earthquake epicenter, and positive transverse motion is normal to positive radial motion in the counterclockwise direction. As seen in these figures, the motions at SL are no longer polarized in either the transverse or the radial component. On the other hand, the SL motions are polarized in the east-west direction which is approximately parallel to the fault rupture trace on the ground surface. Figs. 3.6a, b, and c present the integrated velocities for the transverse, radial and vertical components, respectively, at these stations.

Based on both the acceleration and velocity curves, the approximate arrival time for the first shear wave from the hypocenter is marked with an arrow s in these figures. For the San Fernando earthquake, the first shear wave arrival at ML and ATH can be identified by a visual inspection of the accelerograms. Since

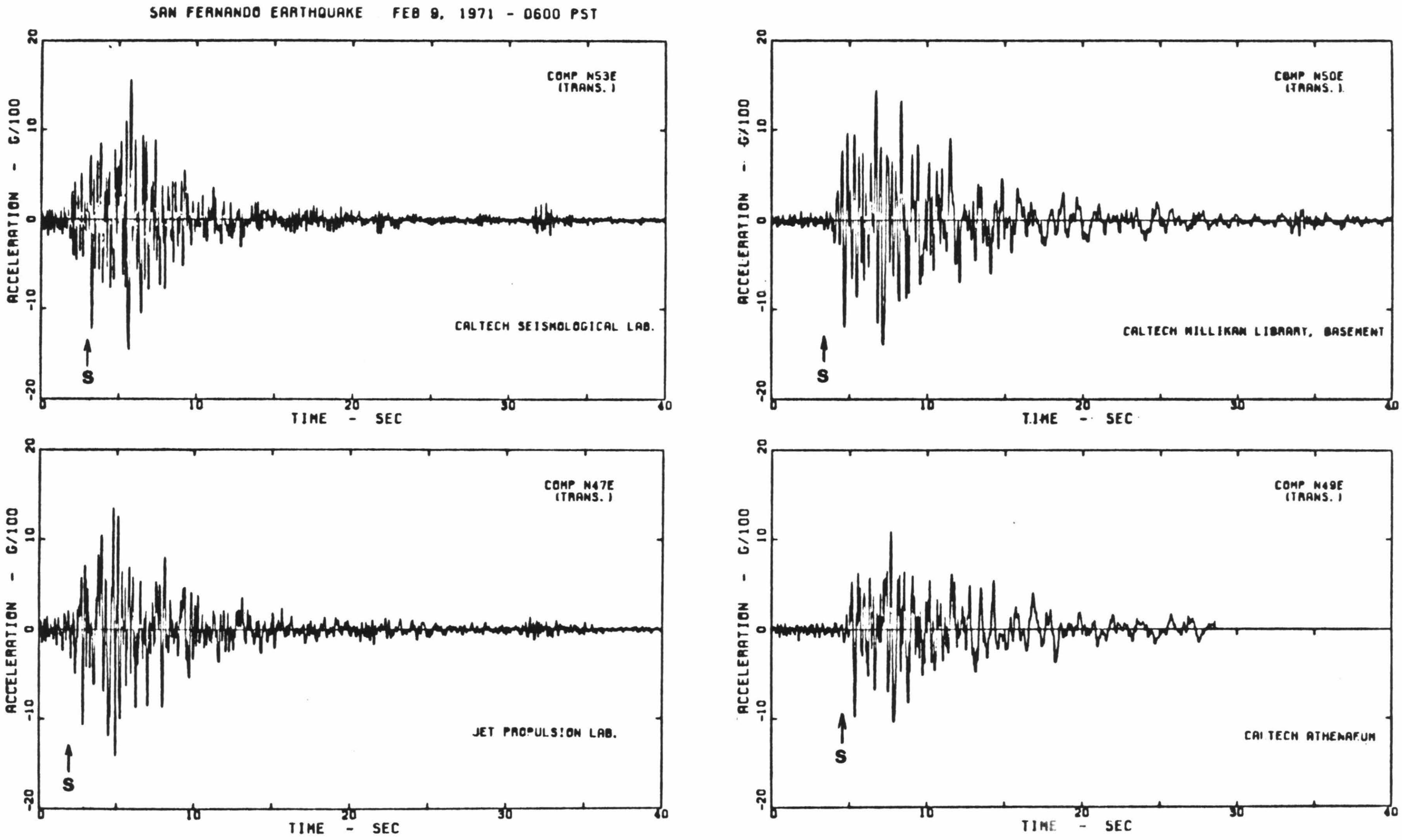

Fig. 3.5a Ground accelerations at SL, ML, ATH and JPL - transverse component, San Fernando earthquake. The first shear wave arrival is marked with the arrow s.

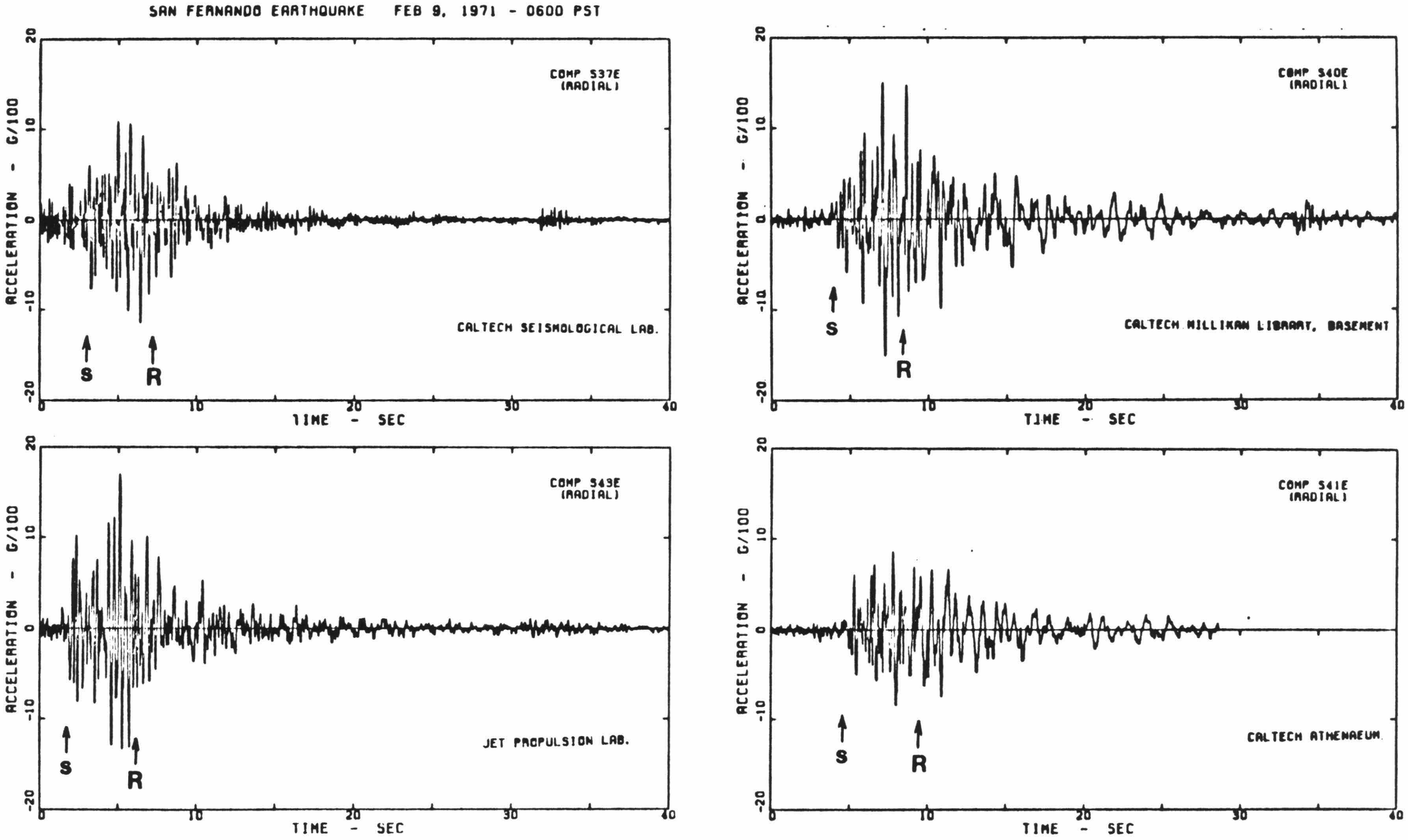

Fig. 3.5b Ground accelerations at SL, ML, ATH and JPL - radial component, San Fernando earthquake. The first shear wave arrival is marked with the arrow s, while the first Rayleigh wave arrival is marked with the arrow R.

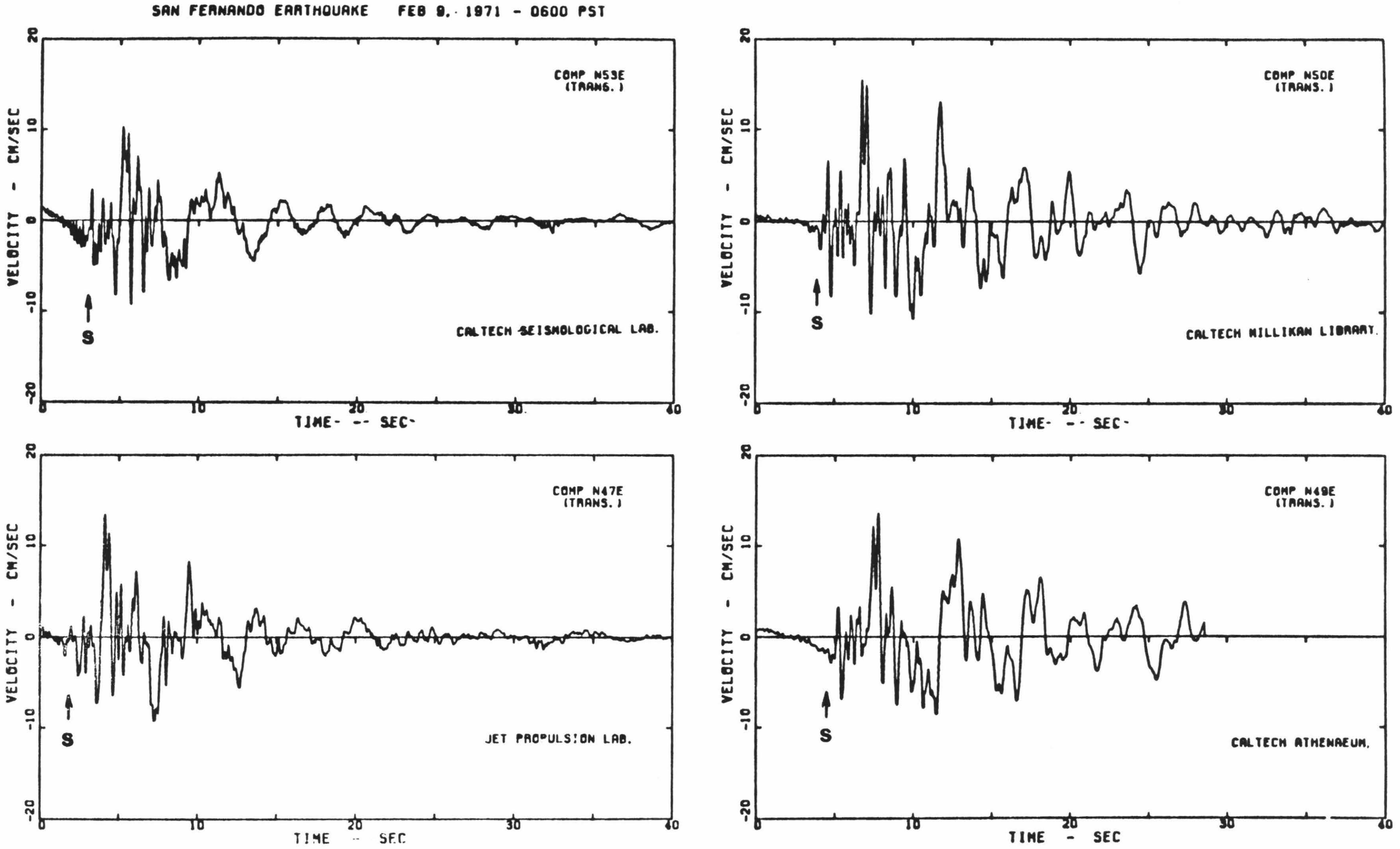

Fig. 3.6a Ground velocities at SL, ML, ATH and JPL - transverse component, San Fernando earthquake. The first shear wave arrival is marked with the arrow s.

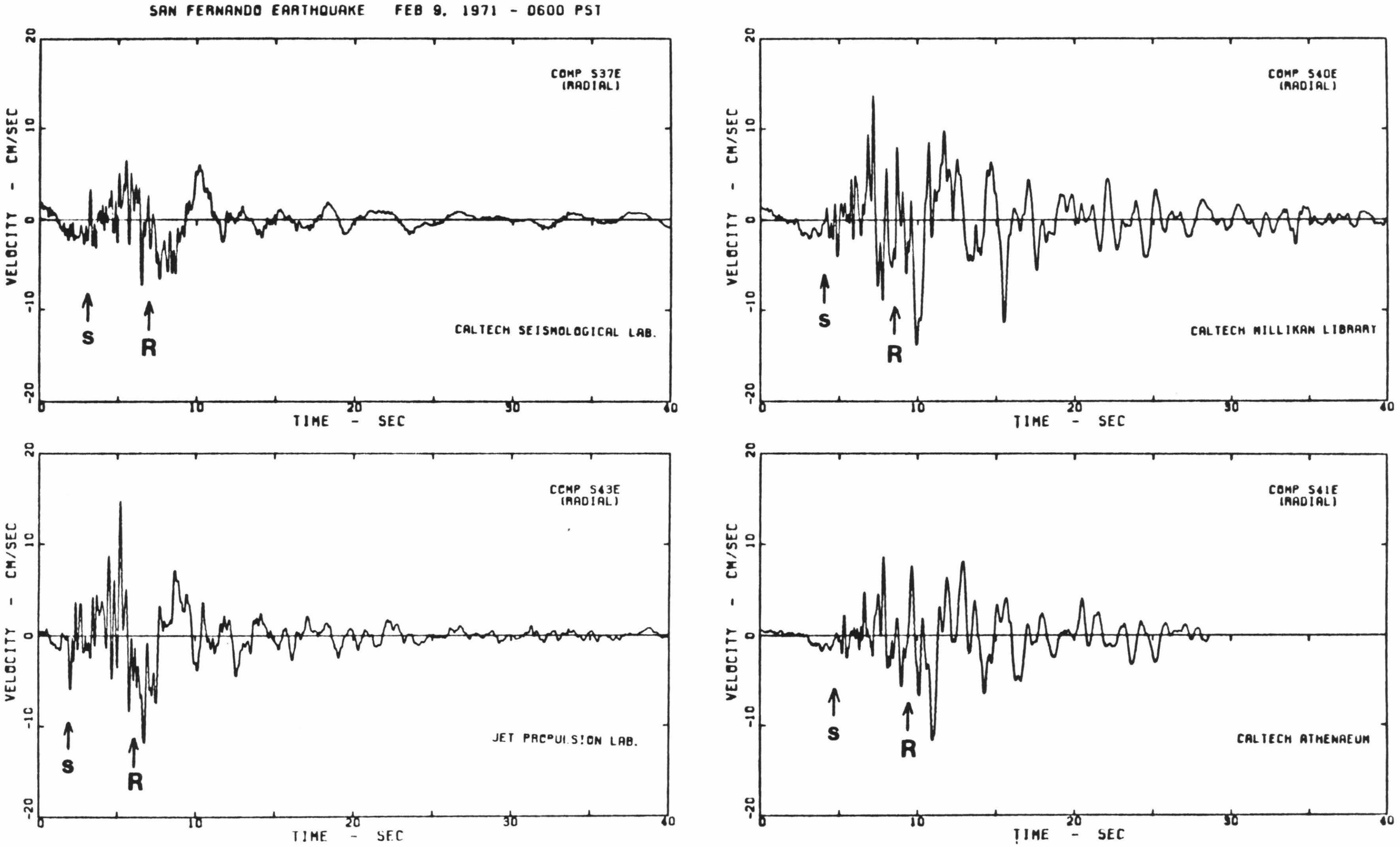

Fig. 3.6b Ground velocities at SL, ML, ATH and JPL - radial component, San Fernando earthquake. The first shear wave arrival is marked with the arrow s, while the first Rayleigh wave arrival is marked with the arrow R.

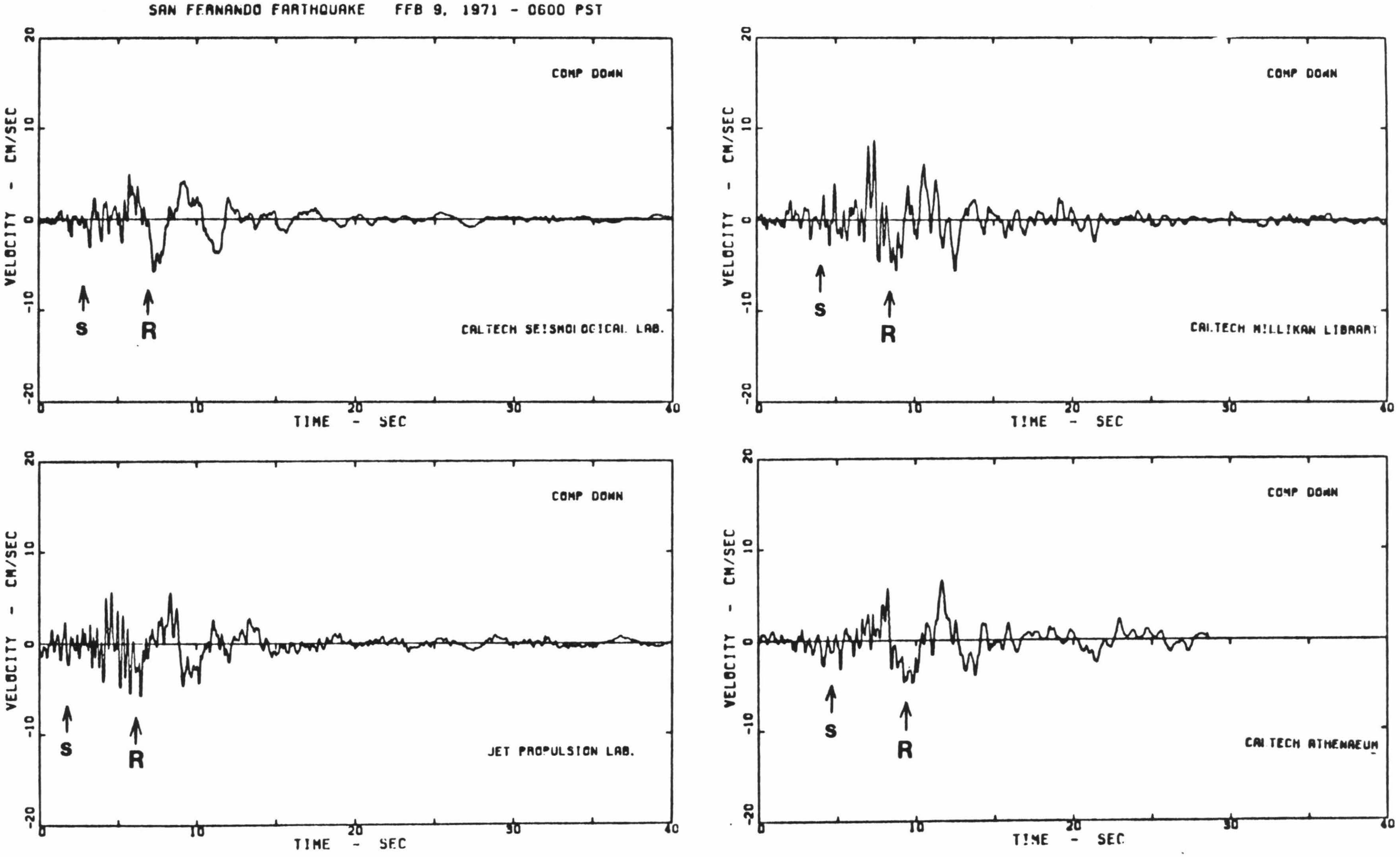

Fig. 3.6c Ground velocities at SL, ML, ATH and JPL - vertical component, San Fernando earthquake. The first shear wave arrival is marked with the arrow s, while the first Rayleigh wave arrival is marked with the arrow R.

the bending of seismic wave paths by the low-velocity sediment underlying ML and ATH, the first larger horizontal motion is associated with the first shear wave arrival. On the other hand, it is not so clear about the first shear wave arrival in the SL and JPL accelerograms. The integrated velocity curves were used to facilitate identification. The first shear wave arrival is approximately estimated when the first distinct velocity pulse appears. It is noted that the accelerographs at ML, JPL and SL were interconnected by a telephone line (Hudson, 1971). The instruments were presumably triggered at about the same time. Furthermore, the first shear wave should arrive at JPL first, then SL and then ML. The ATH accelerograph, which was not on the interconnected network, started by a vertical starter before the network instruments.

Following the first shear wave arrival, there will be shear waves arriving from other parts of the rupturing fault, which will be mixed with P waves and surface waves. Although it is impossible to separate each wave type arriving at a station, the surface wave arrival can be tentatively identified by using three components of ground displacement. In Figs. 3.7a, b, c and d, the particle displacement trajectories are plotted on the plane consisting of the vertical and radial directions. This is similar to the method used by Hanks (1975) in studying the surface wave propagations and dispersions during the 1971 San Fernando earthquake. Arrows indicate the direction of particle motion as time increases. The particle motions are presented by three separate plots for the time intervals of 0- to 10-sec, 10- to 20-sec and 20- to 30-sec. The numbers indicate the points at every 2 seconds. In general, at these stations a large displacement of shear waves is seen in the positive radial direction, then it is followed by a large retrograde loop of Rayleigh waves with duration of 4- to 5-sec. The large retrograde particle motion suggests that ground displacements in the vertical and radial components are largely composed of Rayleigh waves with 4- to 5-sec period traveling

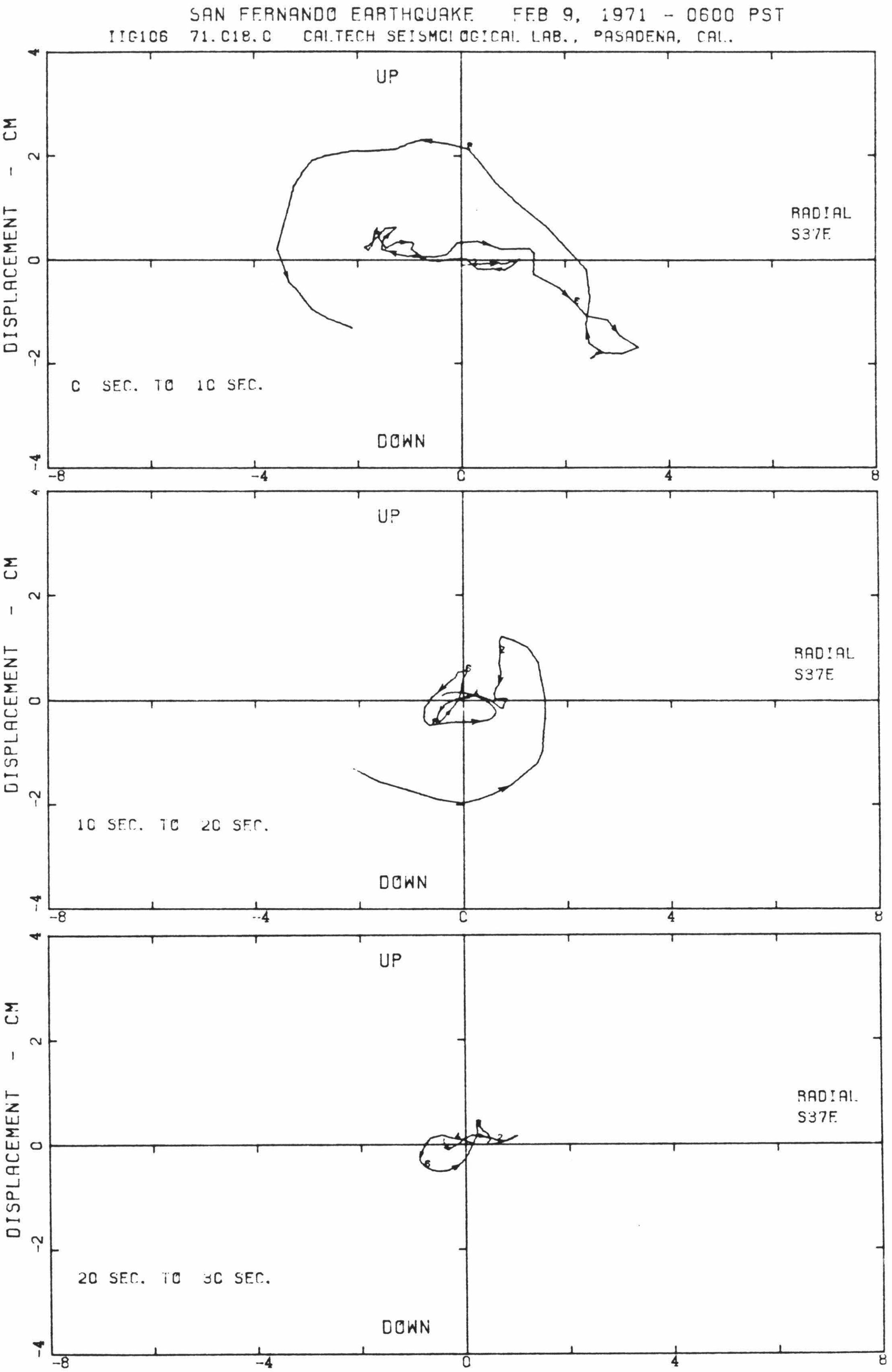

Fig. 3.7a Particle displacement trajectories on the plane consisting of the vertical and radial directions - SL.

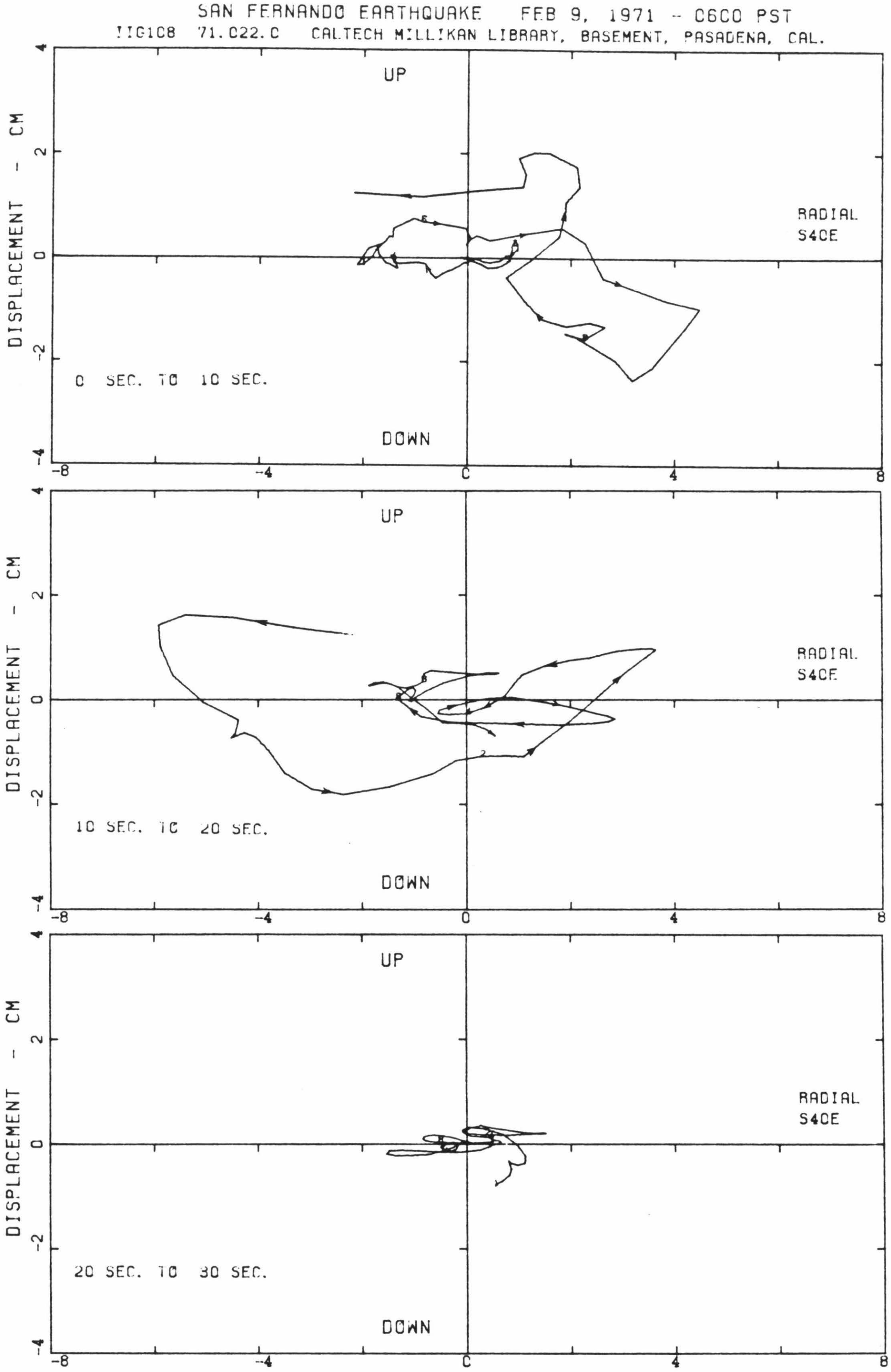

Fig. 3.7b Particle displacement trajectories on the plane consisting of the vertical and radial directions - ML.

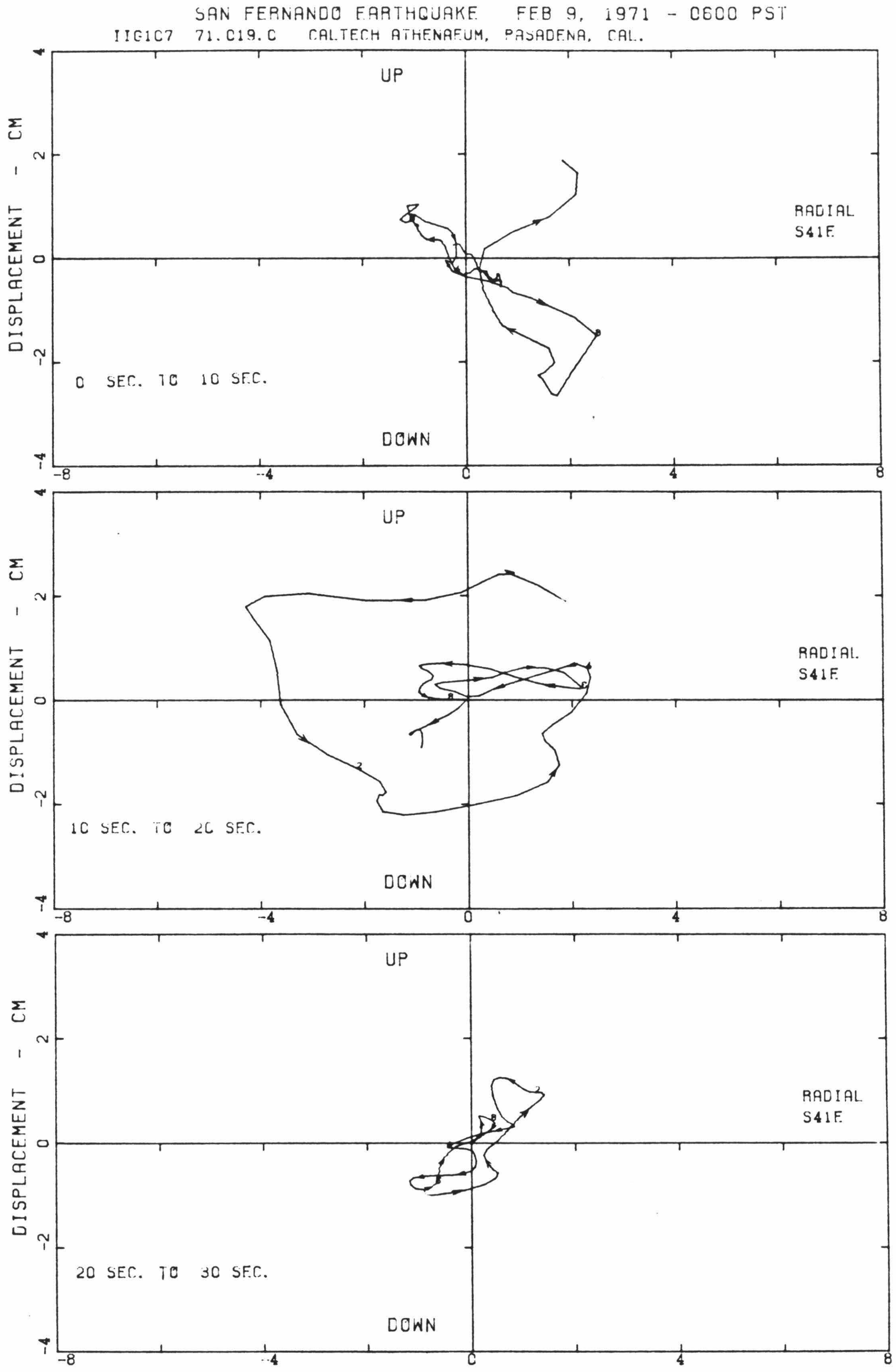

Fig. 3.7c Particle displacement trajectories on the plane consisting of the vertical and radial directions - ATH.

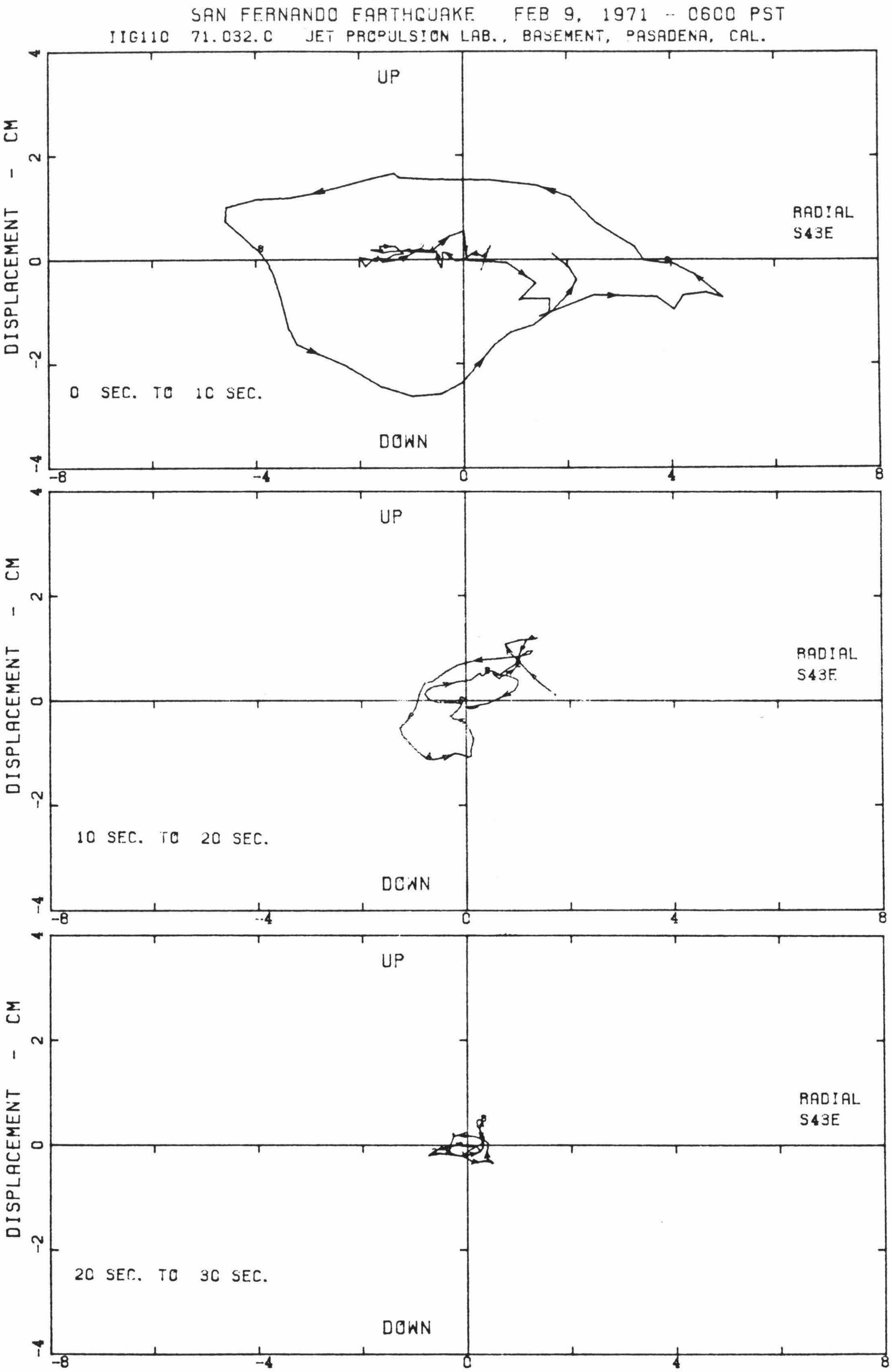

Fig. 3.7d Particle displacement trajectories on the plane consisting of the vertical and radial directions - JPL.

through the area. It is noted that the displacement curves were not filtered and the retrograde loops shown in these figures are not smooth ellipses. This is due to the fact that high-frequency body waves are superimposed on surface waves in these figures. To show the relative arrival to the shear waves, the arrival time of Rayleigh waves is approximately estimated and marked R in Figs. 3.5 and 3.6. It is interesting to note that long-period Rayleigh waves are also visible in the SL accelerograms, although in general the amplitudes of long-period Rayleigh waves in the acceleration curves are relatively smaller than those of high frequency waves.

When ground velocities at these stations are compared in Fig. 3.6, it shows a high degree of coherence in the wave forms. For example, a large velocity pulse with duration of about 0.68-sec is seen in the velocity curves at all stations. The only significant difference that can be found is the trailing part of the velocities between 12- and 30-sec. At SL, this part of ground velocities were dominated by waves of longer period than about 2.0 seconds. However, additional waves with shorter period than 2.0-sec are present in the JPL, ML and ATH records. The trailing motions are constituted by later arriving surface waves, indirect body waves from the source and reverberating waves in the basin. However, the amplification of the weak rock motions in the trailing part by the soil may be due to the surface waves propagating across the nonhorizontal layered structures in the area. This part of ground motions may contain important information related to the local geology. We shall investigate this in the next chapter.

3.3.3 2-Dimensional Characteristics of Ground Motions

To study the frequency content of these motions and the variation of Fourier amplitudes on the horizontal plane with the orientation of the accelerograph, the Fourier transforms of the horizontal accelerograms were computed. The first 20.48-sec portions of the accelerograms were used and tapered at the leading and trailing 10% ends using the data window suggested by Bingham *et al.* (1967) to reduce truncation errors. This part of the accelerogram consists of P, S and surface waves. The Fourier amplitude spectra corresponding to two recorded horizontal components are shown as dashed curves in Figs. 3.8a, b, c and d. Solid curves give the maximum and minimum Fourier amplitude spectra of horizontal components, which are computed from the Fourier transforms of two recorded horizontal components. It is noted that the maximum and minimum amplitudes are the upper and lower bounds of all possible Fourier amplitudes, respectively, on the horizontal plane. For more details on this, see Huang (1982). The spectra are presented from 0 to 15 Hz only, since the Fourier amplitudes are negligible for higher frequencies.

As seen in Fig. 3.8a, for most frequencies at SL, the maximum amplitudes occur in the E-W direction and the minimum amplitudes in the N-S direction. This is a special case when the maximum Fourier amplitudes of most frequencies concentrate in one geographical direction resulting in the strongly polarized motions in the E-W direction (Fig. 3.4). At JPL, three prominent peaks in the maximum amplitude spectrum are nearly in the S82E direction (Fig. 3.8d) resulting in the slightly polarized motions in the accelerograms (Fig. 3.4). In Figs. 3.8b and c for ML and ATH, the amplitudes of recorded components lie between the maximum and minimum amplitudes for most frequencies, hence the corresponding accelerograms do not show any strong polarization. It is noted that the maximum or minimum Fourier amplitude does not, in general, occur in the same direction at different frequencies.

To compare the frequency content of the motions recorded at these stations, the total power of three components and the total power of two horizontal components for each station are shown in Fig. 3.9. The total power is the sum of the

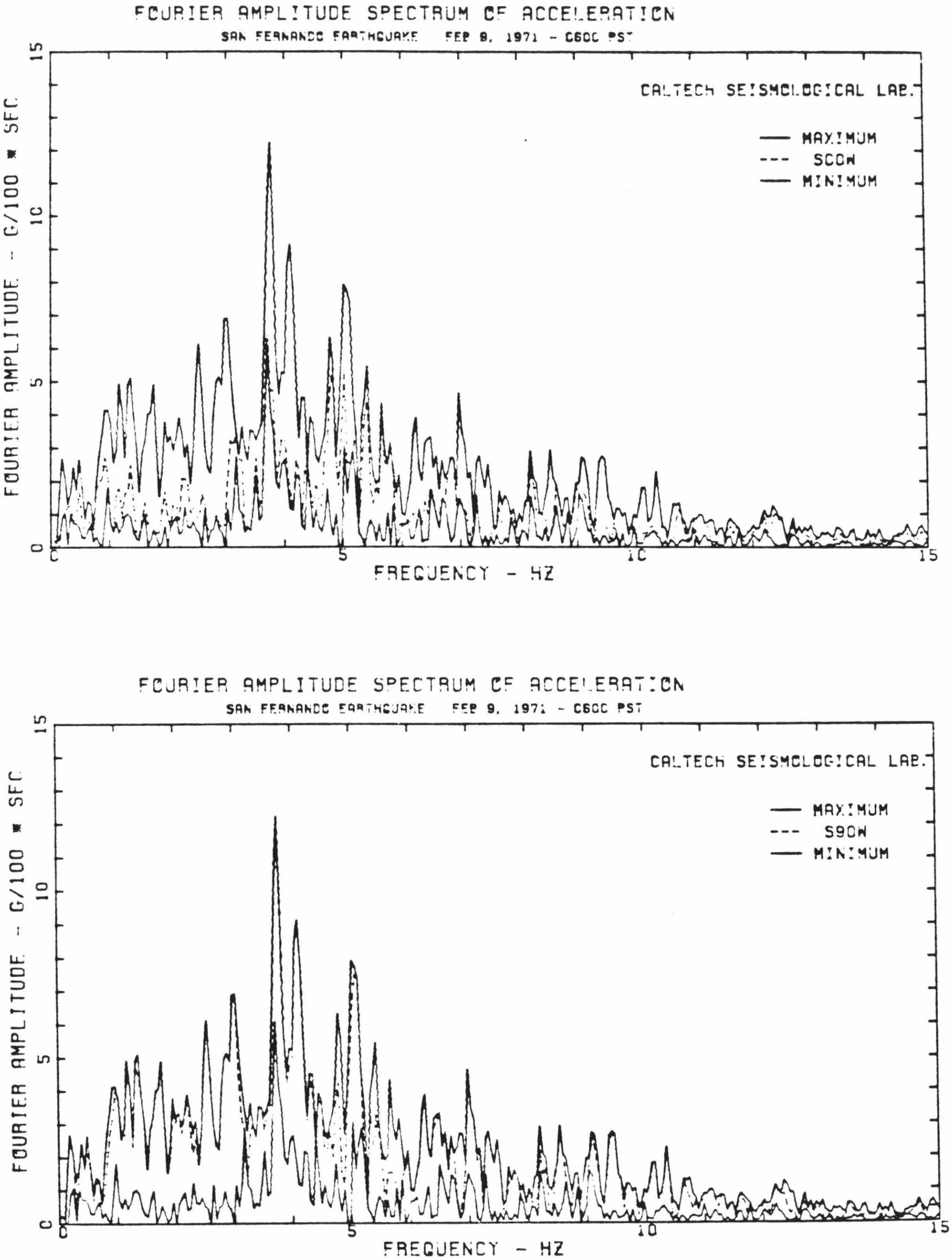

Fig. 3.8a Fourier amplitude spectra for two recorded horizontal components and the corresponding maximum and minimum Fourier amplitude spectra - SL. San Fernando earthquake.

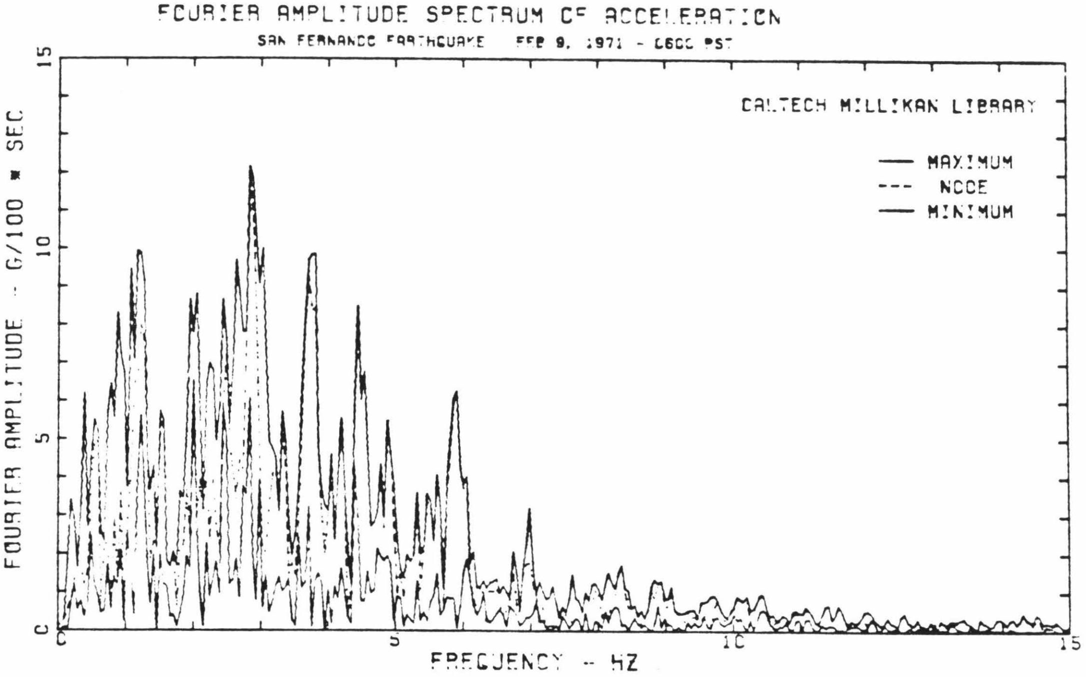

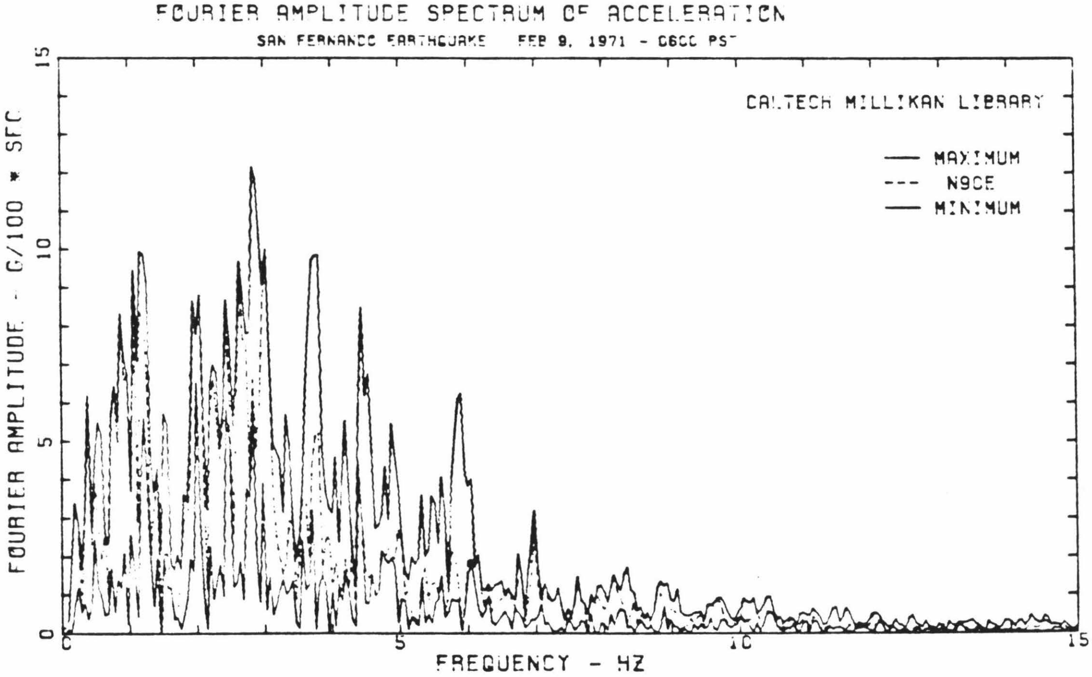

Fig. 3.8b Fourier amplitude spectra for two recorded horizontal components and the corresponding maximum and minimum Fourier amplitude spectra - ML. San Fernando earthquake.

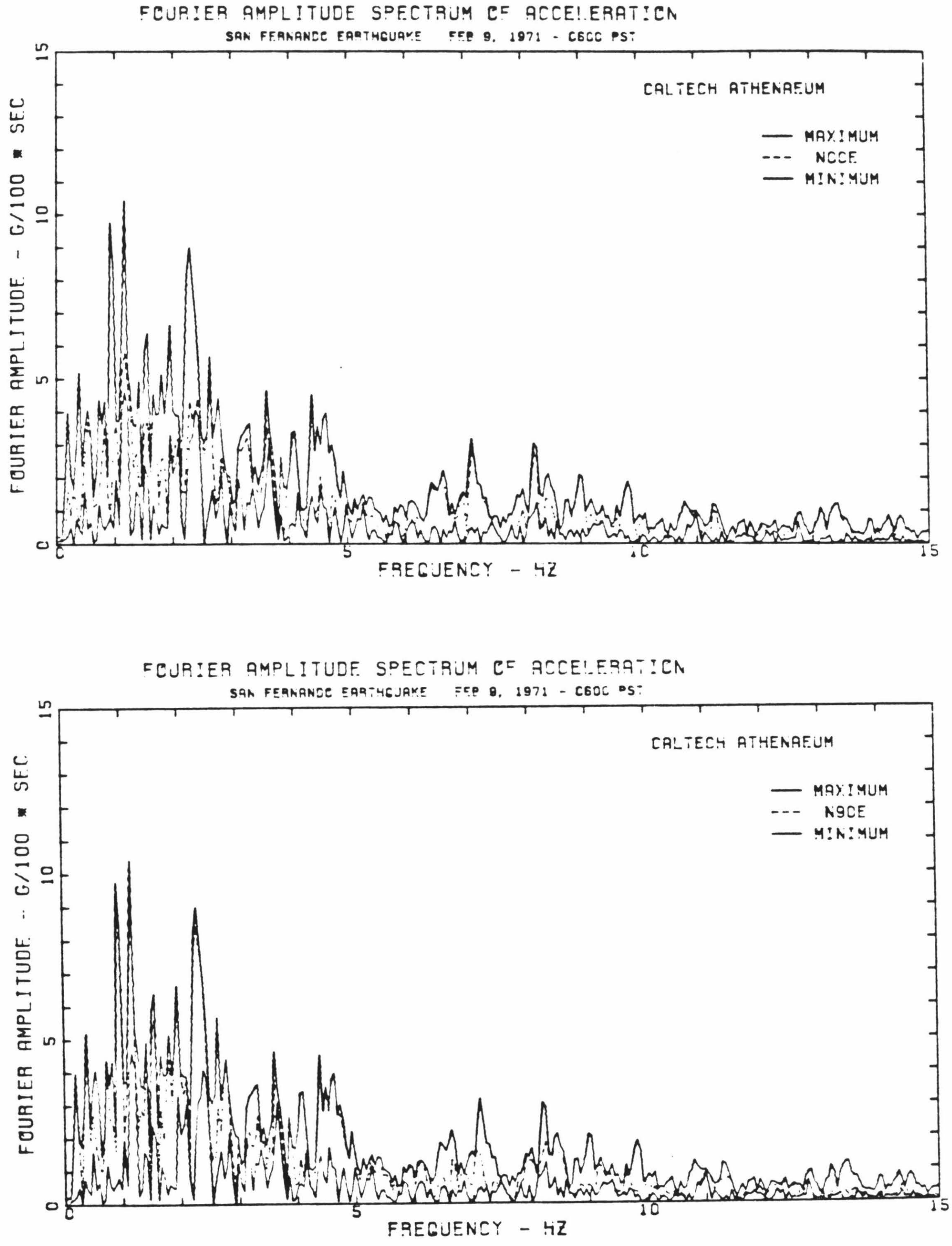

Fig. 3.8c Fourier amplitude spectra for two recorded horizontal components and the corresponding maximum and minimum Fourier amplitude spectra - ATH. San Fernando earthquake.

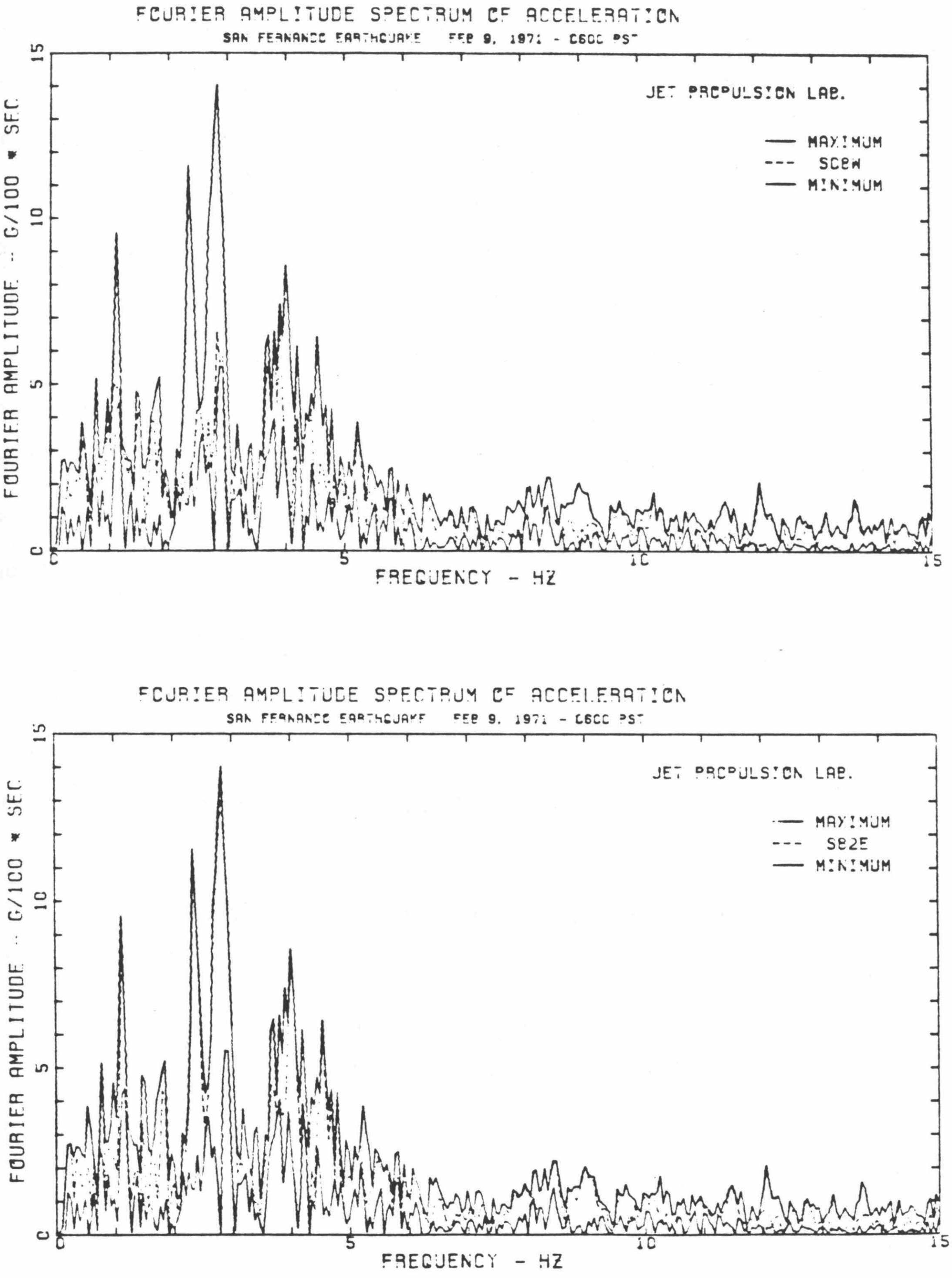

Fig. 3.8d Fourier amplitude spectra for two recorded horizontal components and the corresponding maximum and minimum Fourier amplitude spectra - JPL. San Fernando earthquake.

Fourier amplitude squares of two or three components, which is independent of the orientation of the recording axes. The total power spectra are computed from the Fourier amplitudes shown in Fig. 3.8 and the Fourier amplitudes for the vertical component. The powers have been smoothed once by a window weighted ¼, ½, and ¼. Since the total power contributed from the vertical component is relatively smaller than that from two horizontal components, the peaks in two total power spectra are located at the same frequencies. A comparison of the total power spectra in Fig. 3.9 shows that the total powers at frequencies ranging from 0.8 to 1.3 Hz and from 2.0 to 3.0 Hz are larger at ML, ATH and JPL than at SL. On the other hand, three peaks located at 3.8, 4.1 and 5.1 Hz in the SL spectrum are greater than the corresponding values in other spectra. By comparison with the SL spectrum, the dominant frequencies at ML, JPL and ATH are altered to lower frequencies. This has been observed in the accelerograms (Fig. 3.4).

In Fig. 3.9, the locations of some peaks are different in different spectra. For example, a prominent peak is located at 2.83 Hz in the ML and JPL spectra, but is not seen in the SL and ATH spectra. The peaks shown in the ML spectrum at 2.0 and 5.9 Hz do not appear in other spectra. Two peaks can be seen near 1.20 and 2.35 Hz in the JPL, ML and ATH spectra, but not in the SL spectrum. Different peaks in the total power spectra have been picked by eye and their positions are indicated by the bars in Fig. 3.10. To search for the possibility of significant soil-structure interaction effect on the ML and JPL spectra, the modal frequencies of the ML and JPL buildings during the San Fernando earthquake are also indicated in this figure. It is well known that the inertia forces generated by the structural vibration tend to produce large peaks in the basement spectra at frequencies which are close to the modal frequencies of the superstructure. A comparison of the peaks in Fig. 3.10 shows no evidence of

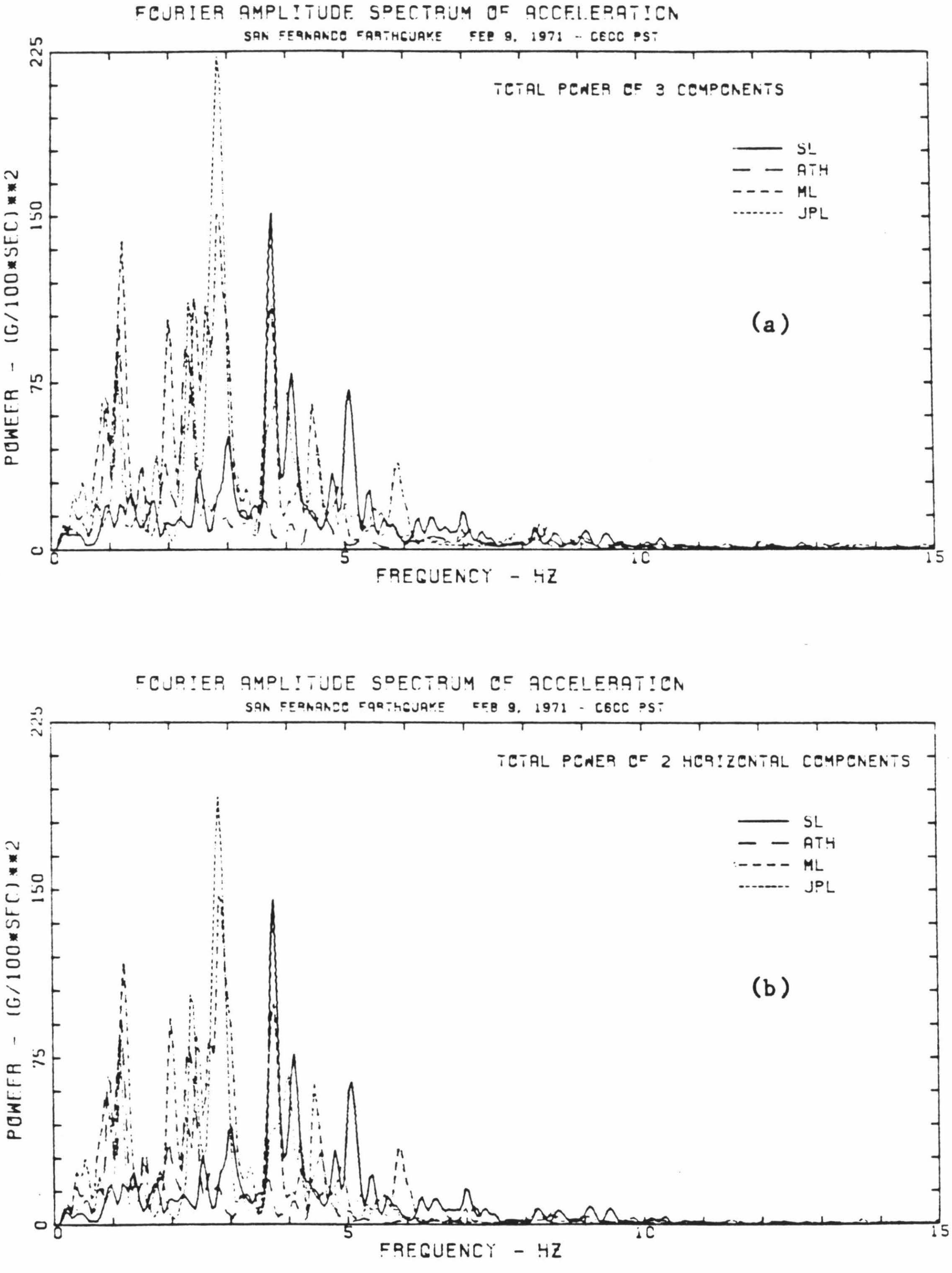

Fig. 3.9 Comparisons of the total power spectra of (a) 3 components, (b) 2 horizontal components, for SL, ML, ATH and JPL. San Fernando earthquake.

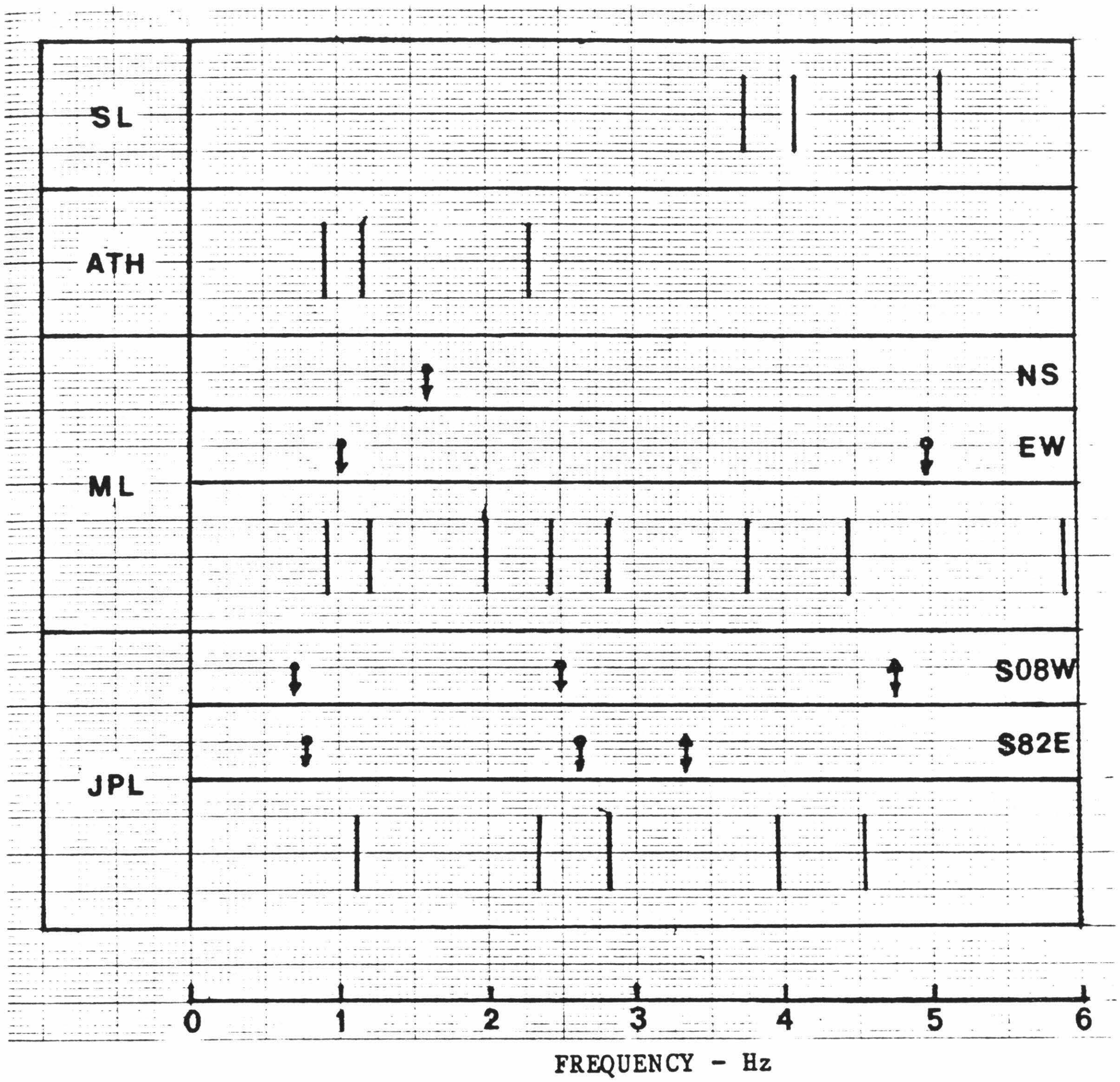

| --- locations of the peaks in the total power spectra in Fig. 3.9.

↓ --- 1st modal frequency
⇣ --- 2nd modal frequency
↕ --- 3rd modal frequency (from McVerry, 1979).

Fig. 3.10 Barchart showing the locations of peaks in the total power spectra and the modal frequencies of ML and JPL buildings during the 1971 San Fernando earthquake.

significant inertia soil-structure interaction at ML and JPL. Although the differences between the spectra of two nearby stations, i.e., ML and ATH, need to be investigated, it is concluded that the accelerograms at ML, ATH and JPL consist mainly of lower frequencies than 3.0 Hz while the SL accelerograms are dominated by waves with higher frequencies than about 3.5 Hz.

3.3.4 Comparisons of Millikan Library and Athenaeum Records

The Millikan Library and the Athenaeum are located on the campus of the California Institute of Technology (Fig. 3.11). The Athenaeum is approximately 1200 feet due east of the Millikan Library. The accelerograph of ML was located in the basement of a 9-story reinforced concrete building, whereas the accelerograph of ATH was in the basement of a 2½-story reinforced concrete building. The dissimilarity in the accelerograms recorded so close together was widely noted soon after the records became available and has been discussed several times in the literature.

It has been suggested that the difference may have been caused by the soil-structure interaction; however, the spectra of the accelerograms discussed in the previous section do not support this. Crouse and Jennings (1975) made an analysis and indicated no evidence of significant inertia soil-structure interaction for the Millikan Library and the Athenaeum. They explained that some of the observed differences may be attributable to the size of building foundation, i.e., kinematic soil-structure interaction. The foundation may act as a low-pass filter which will filter out seismic waves with wavelength smaller than the size of the foundation. The Athenaeum with larger foundation is more effective at suppressing waves of higher frequency than is the Millikan Library. However, this explanation fails if seismic waves were incident upon the building foundation vertically. In Section 3.3.1, we have seen the accelerograms from which we

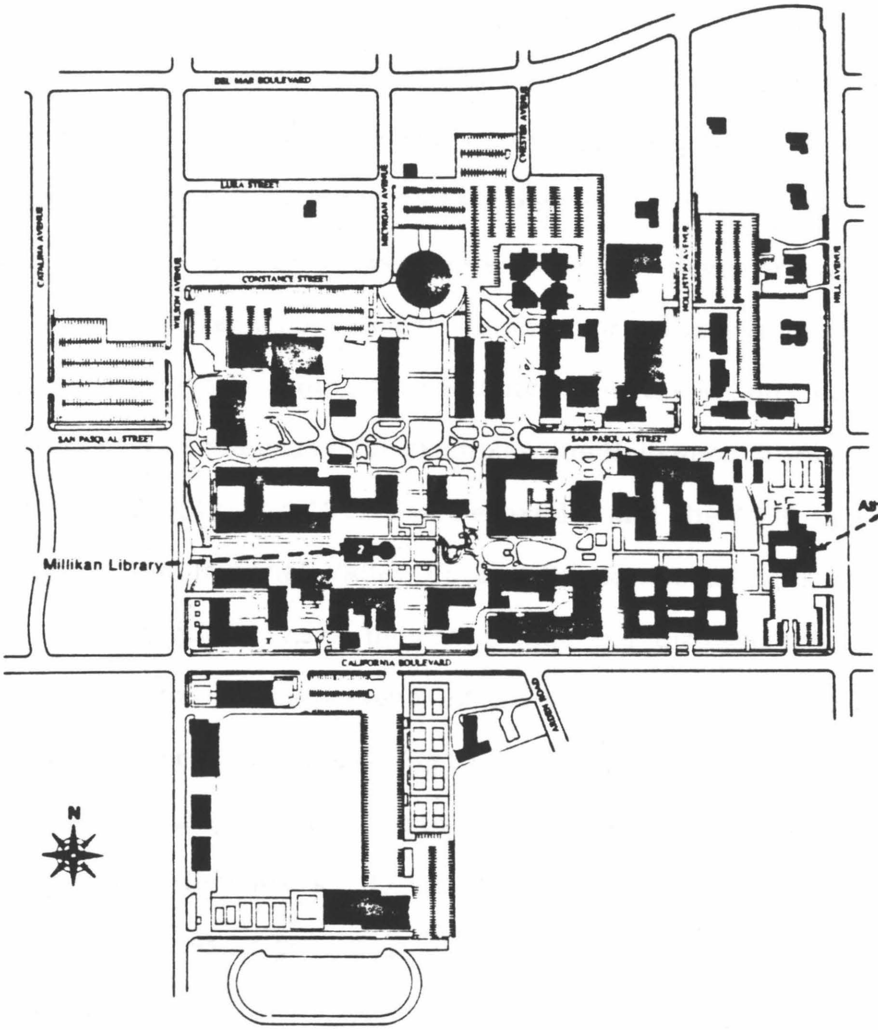

Fig. 3.11 Map indicating the relative locations of Millikan Library and Athenaeum on the Caltech campus. Note that the distance between these two stations is about 1200 feet.

found that seismic body waves corresponding to the earliest parts of the records emerged nearly vertically at the ML and ATH.

It is not clear how the local geological irregularities, the foundation slab flexibility, the embedment of the foundation and other nearby structures can affect the recorded motions. However, it is well known that for a seismic wave to see an inhomogeneity its wavelength has to be comparable to or shorter than the size of the inhomogeneity. Hence, low frequency seismic waves propagate more coherently than high frequency waves. Furthermore, the motions recorded simultaneously within the building foundation and in the vicinity outside the buildings during past earthquakes, for examples, the Hollywood Storage building in the 1952 Kern County, the 1971 San Fernando, and the 1970 Lytle Creek earthquakes, and the Imperial Valley County Services building in the 1979 Imperial Valley earthquake, have indicated that the displacement and the velocity are less affected by the presence of the building than the acceleration. As we compare the accelerograms in Fig. 3.4, the pulses in the ATH accelerograms tend to be less sharp than those in the ML accelerograms and hence the amplitudes of acceleration are smaller at ATH. Despite the difference in the accelerations, we have seen a good degree of similarity between the velocities at ML and ATH in Fig. 3.6.

To facilitate comparison, Fig. 3.12 shows the velocities plotted on the same diagram. The instruments were not triggered at the same time, hence the origin of the records for one of the stations has to be shifted. It is assumed that body waves were incident on the Caltech campus nearly vertically, the velocities corresponding to body wave arrivals are expected to be in phase at ML and ATH. By approximately matching the wave forms between the first shear wave and surface wave arrivals, the ATH record was shifted by t_s of 0.68-sec. The error of t_s should be within ±0.04-sec. The first shear wave arrival is marked by s and

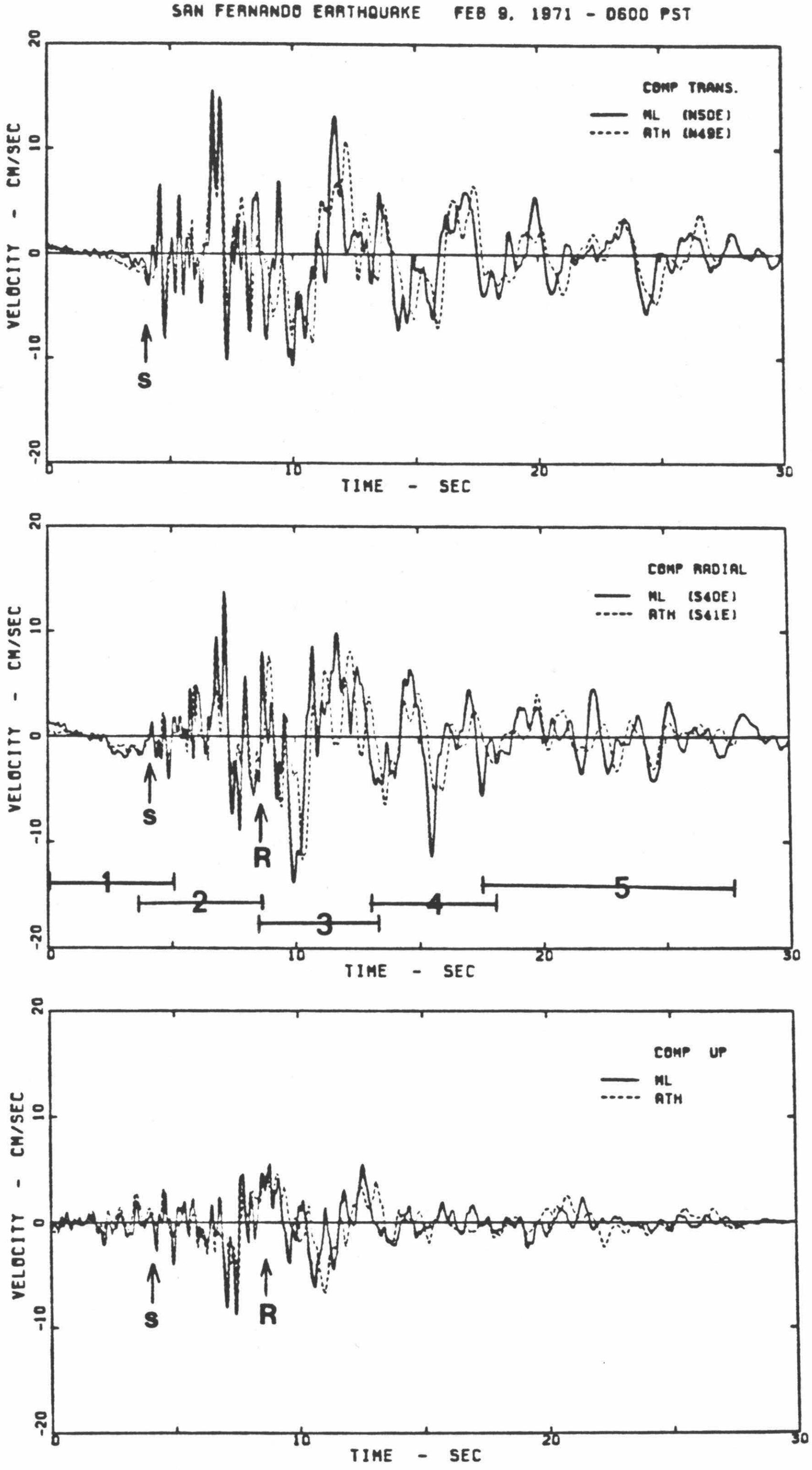

Fig. 3.12 Comparison of ground velocities at Millikan Library and Athenaeum. San Fernando earthquake. The windows indicate the truncated data for computing the Fourier transforms.

the Rayleigh wave arrival at ML by R in the plots. In general the body wave phases are well matched, although the peaks at ML tend to be of greater amplitudes than those at ATH and sometimes ML and ATH have velocities in the opposite directions. The surface waves arrived at ATH about 0.15- to 0.25-sec later than at ML. This is consistent with the distance of 1200 feet between these two stations and the surface wave velocity. Due to dispersion, long period surface waves travel faster than the short period waves. The phase differences between ML and ATH in the trailing motions are frequency-dependent.

So far we have used the displacements to identify the surface wave arrivals and the velocities to adjust the origins of two nearby records. Although we are not able to separate different wave types exactly, we know approximately where they are in the records. Having shifted the origin of the ATH records, we compare the frequency contents of the ML and ATH accelerograms by performing moving window analyses to see whether the differences are related to different wave arrivals. The accelerograms are divided into five parts, i.e., 0.0- to 5.12-sec, 3.6- to 8.72-sec, 8.2- to 13.32-sec, 13.0- to 18.12-sec and 17.5- to 27.74-sec. The windows are indicated in Fig. 3.12. The first part contains P waves and early arriving S waves. The second part consists mainly of S waves in the horizontal components and of P waves in the vertical component. The third part includes surface waves and late arriving body waves. The last two parts consist mainly of surface waves. The first four windows are 10.24-sec wide and the last one is 20.48-sec. The truncated data of each part were tapered at the leading and trailing 10% ends. The Fourier amplitude spectra of accelerations for three components are presented in Figs. 3.13a, b, c, d, and e. The amplitudes have been smoothed once by passing the corresponding power spectra by a window weighted ¼, ½, and ¼. The amplitude ratios were obtained by dividing the once-smoothed ML amplitudes by the once-smoothed ATH amplitudes and smoothing

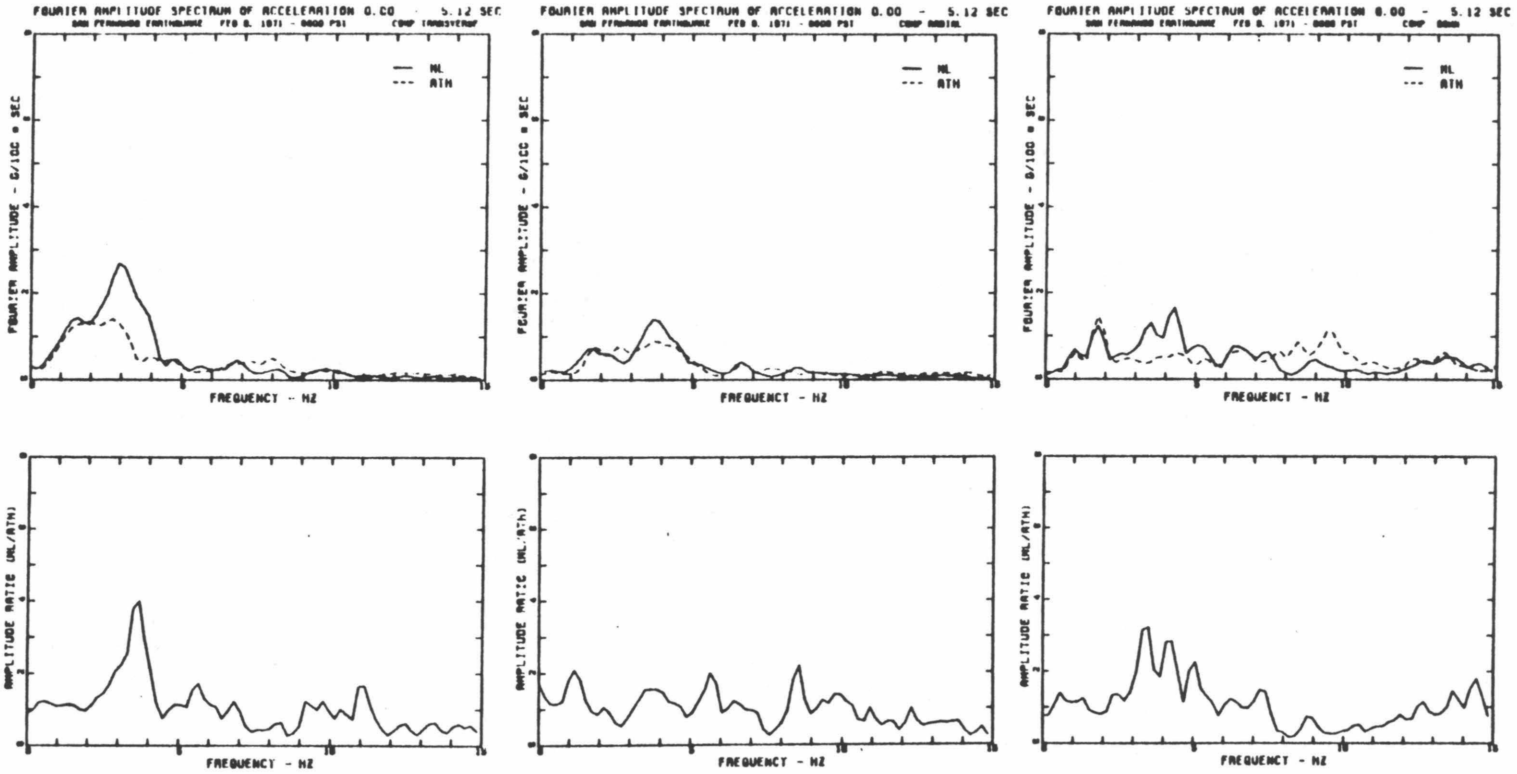

Fig. 3.13a Comparison of Fourier amplitude spectra of recorded accelerations at ML and ATH from 0.00- to 5.12-sec. (first window indicated in Fig. 3.12).

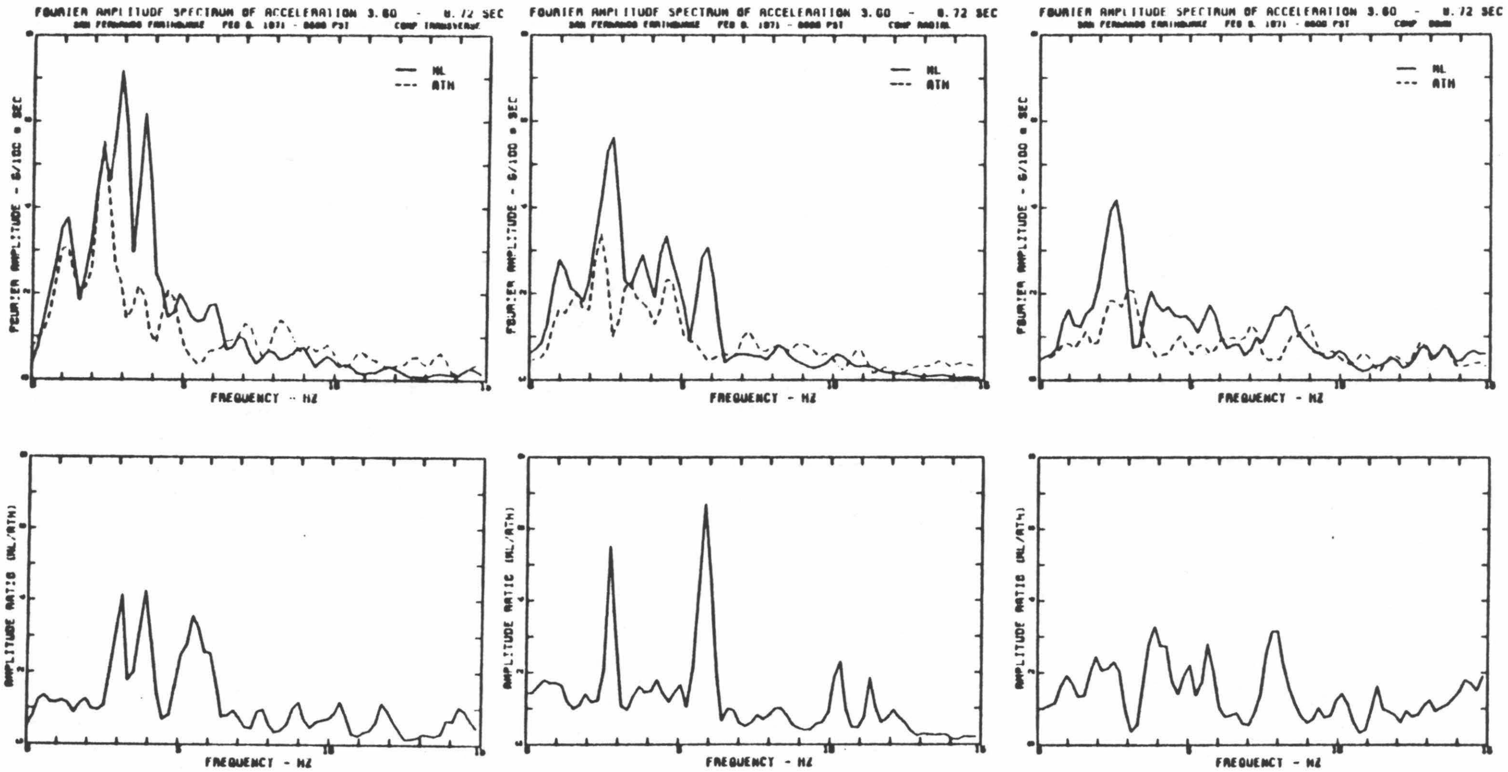

Fig. 3.13b Similar to Fig. 3.13a for the accelerations from 3.60- to 8.72-sec. (second window indicated in Fig. 3.12).

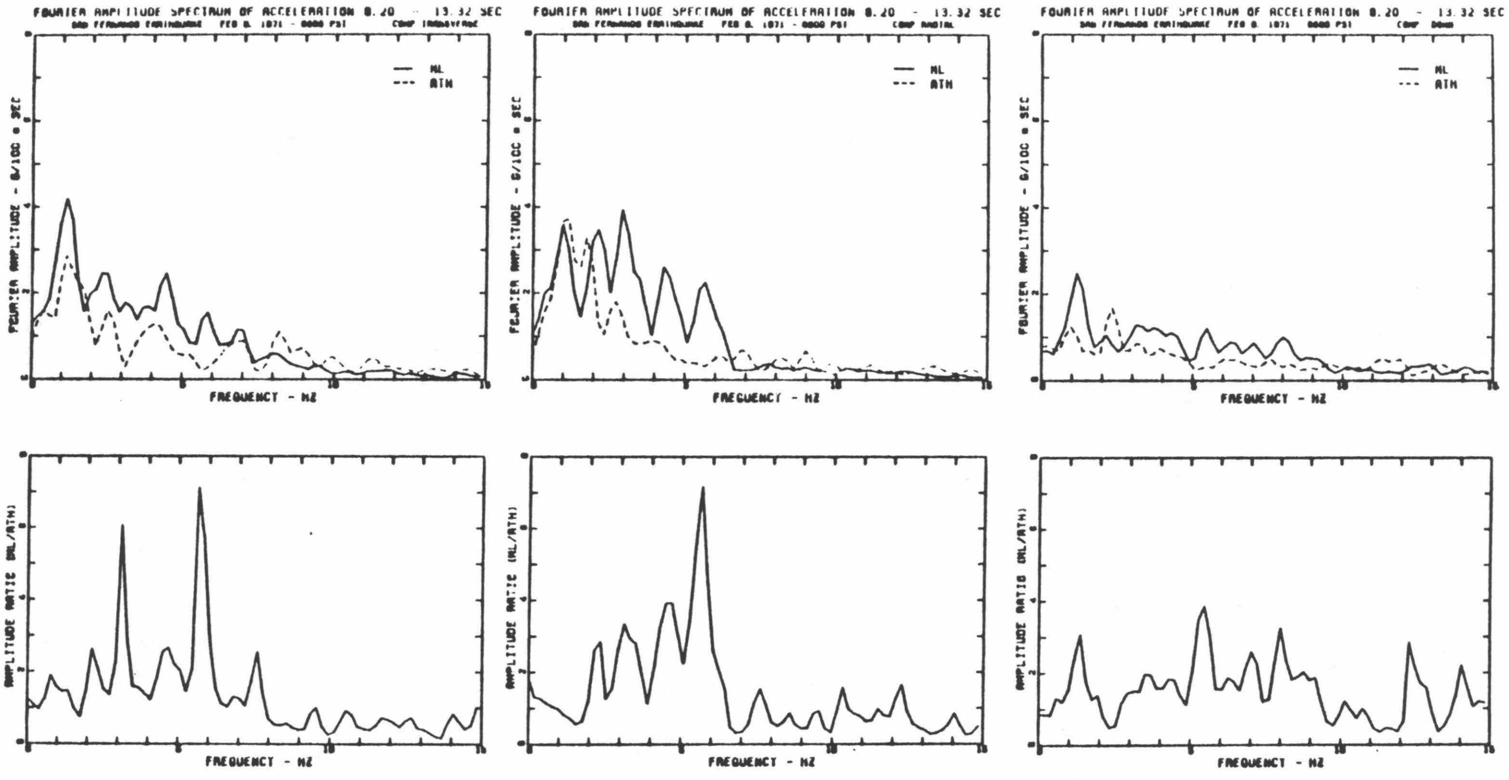

Fig. 3.13c Similar to Fig. 3.13a for the accelerations from 8.20- to 13.32-sec. (third window indicated in Fig. 3.12).

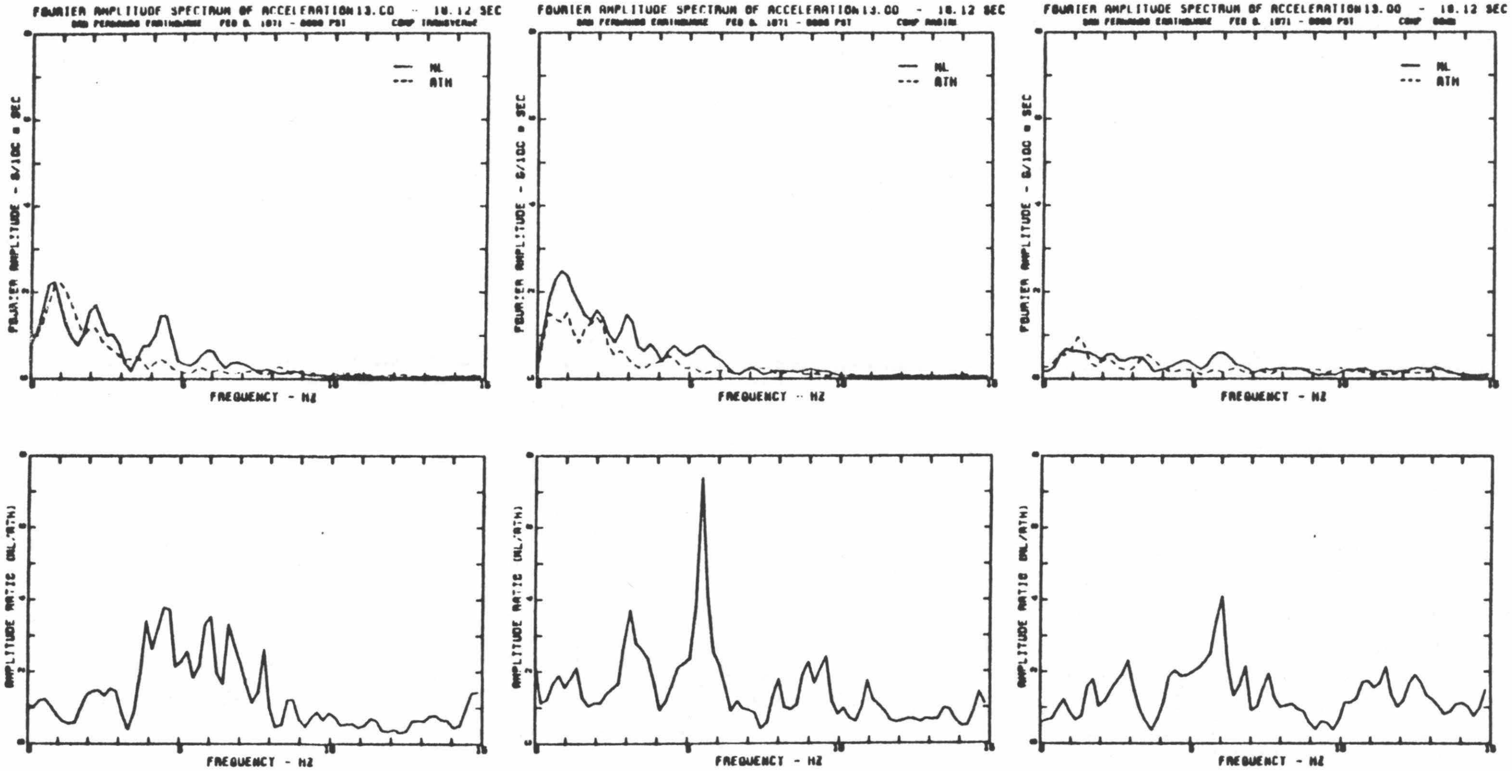

Fig. 3.13d Similar to Fig. 3.13a for the accelerations from 13.00- to 18.12-sec. (fourth window indicated in Fig. 3.12).

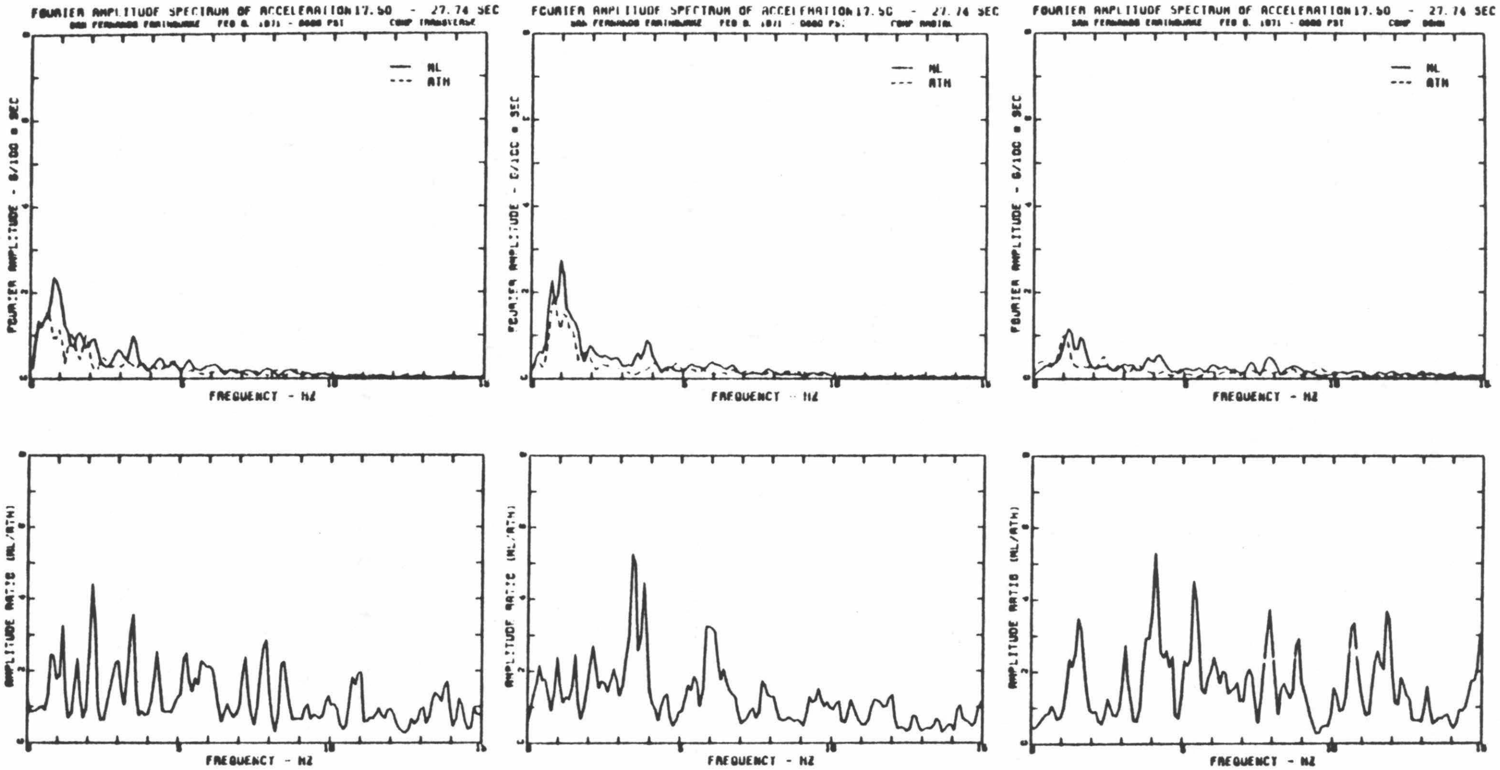

Fig. 3.13e Similar to Fig. 3.13a for the accelerations from 17.50- to 27.74-sec. (fifth window indicated in Fig. 3.12).

these ratios once. They are shown on the bottom plots in Fig. 3.13. It is noted that the peaks in the ratio spectra corresponding to low amplitudes are insignificant. The amplitude ratios fluctuate more in Fig. 3.13e because the frequency spacing there is one half of those for other plots in Fig. 3.13. The vertical scales are fixed for all the plots so that the change of frequency content with increasing time can be seen in these plots. The second part corresponding to the strongest shaking during the earthquake has largest amplitudes (Fig. 3.13b). The shift of dominant frequencies from between 2 and 4 Hz for the early parts to about 1.0 Hz for the later parts is noted in these spectra. The change of frequency content from high frequency to low frequency as time increases can also be observed in the accelerograms (Fig. 3.5). In general the spectra of ML and ATH agree well up to 2 Hz, although some spectra only agree well to some lower frequencies than 2 Hz. The significant differences occur at frequencies between 2 and 6 Hz where the ML spectra have larger amplitudes than the ATH spectra. For higher frequencies than 6 Hz, the amplitudes are small and the difference is insignificant; however, in this frequency range the ML amplitudes are not always larger than the ATH amplitudes.

Further comparisons are made in some invariant quantities with respect to the instrument orientation. The maximum and the minimum horizontal amplitude spectra and the total power spectra for each segment of the accelerograms are shown in Figs. 3.14a and b. They are obtained from unsmoothed Fourier transforms and have been smoothed once. It should be noted that the vertical scales in the total power spectra in the bottom plots of Fig. 3.14 are different for different windows. At frequencies between 2 and 6 Hz where the dissimilarity is prominent, the differences between the maximum and the minimum amplitudes tend to be smaller at ATH than at ML. In other words, the variations of Fourier amplitudes in different horizontal directions are larger at ML than at ATH in this

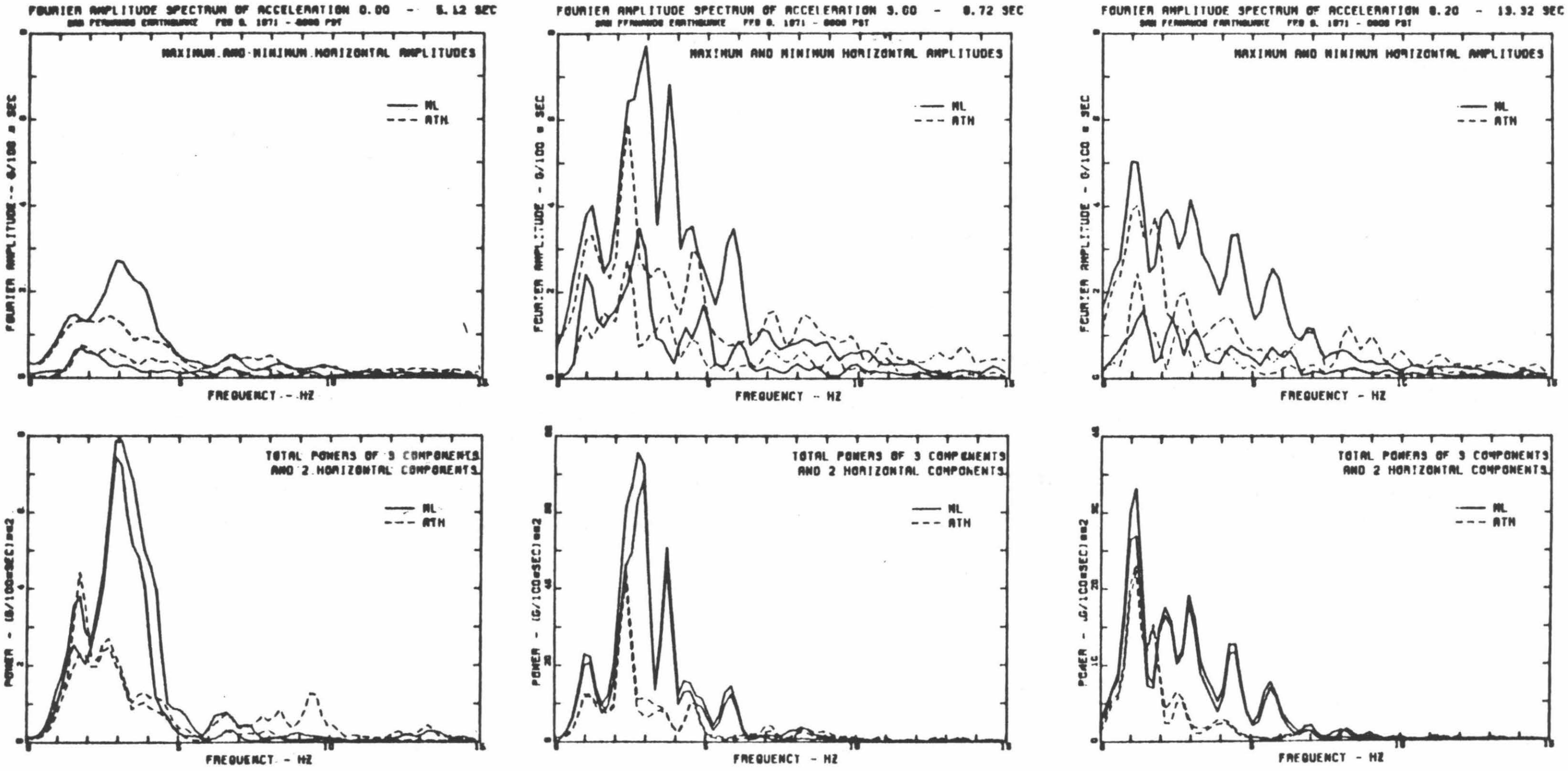

Fig. 3.14a Comparison of the maximum, minimum Fourier amplitude spectra, total power spectra for ML and ATH - first, second and third windows indicated in Fig. 3.12.

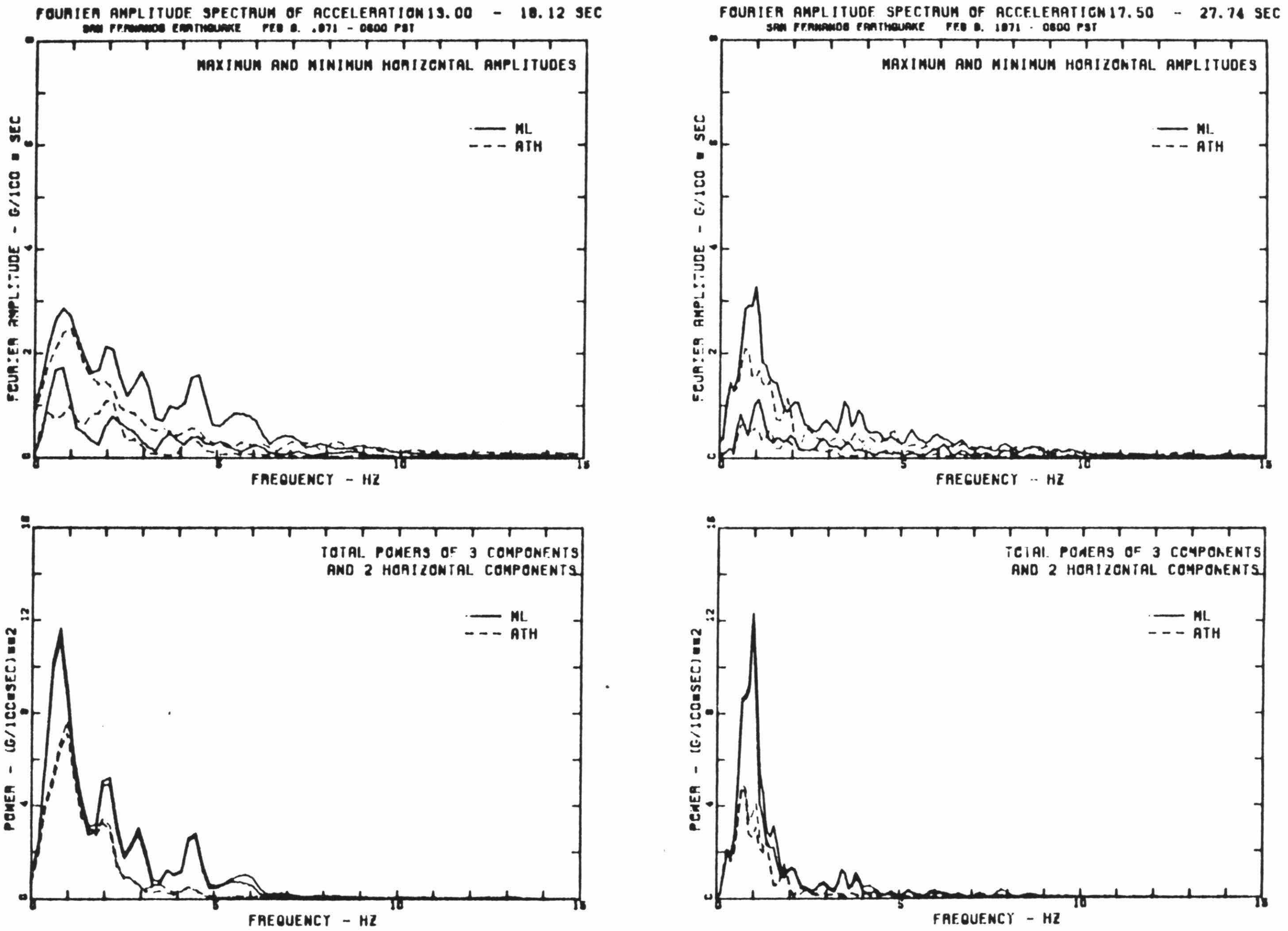

Fig. 3.14b Similar to Fig. 3.14a for the fourth and fifth windows in Fig. 3.12.

frequency range. Comparisons of the total power spectra for ML and ATH also show a good agreement up to 2 Hz and a disagreement between 2 and 6 Hz. The frequency ranges over which the similarity and dissimilarity ocur do not seem to be affected by different wave arrivals. It is noted that in the second, third and fourth total power spectra, ML has larger amplitudes than ATH at the first peak located near 1.0 Hz which is the fundamental frequency of the ML building in the E-W direction. However, this should not be attributed to the soil-structure interaction effect of the ML building, since the total power spectra for ML and ATH are about equal at 1.6 Hz which is the fundamental frequency of the ML building in the N-S direction. It is also noted in the last total power spectrum that two peaks near 1.0- and 1.6-Hz are larger in the ML spectrum than the ATH spectrum. These spectra correspond to the trailing part of the basement motions and the time when roof motions were still strong and consisted essentially of fundamental mode vibrations. The inertia soil-structure interaction effects might have contributed to the basement motions in the trailing part.

3.4 Data of the 1970 Lytle Creek Earthquake

The accelerograms obtained at ML and JPL during the 1970 Lytle Creek earthquake are shown in Figs. 3.15a and b. These accelerograms have been corrected and were band-pass filtered between 0.07 and 25 Hz. The instruments were triggered after the first shear wave arrival, hence the early P wave motions were not recorded. Although the records continued to about 60 seconds, the records were only digitized to about 23.4 seconds. The motions were weak and hence the integrated displacements are very sensitive to the long period data processing errors. No attempt was made to identify the surface wave arrivals by using the particle displacement or velocity trajectory. Theoretically the particle acceleration trajectory can also be used; however, it is not easy to identify the retrograde ellipses because of the high-frequency fluctuations in the accelerograms.

To study the frequency content of these motions, the 20.48-sec portions of the accelerograms were tapered and transformed to obtain the Fourier transforms. The Fourier amplitude spectra for two horizontal components as well as the maximum and the minimum amplitude spectra are shown in Figs. 3.16a and b. The amplitudes for this earthquake are about one-tenth of those for the San Fernando earthquake not only because this earthquake had a smaller source dimension but also because of the larger epicentral distances of these stations from this earthquake (Tables 3.1 & 3.2). It is noted that this earthquake was located about 57 km away, but the recorded motions contained relatively large amplitude high-frequency waves. The source spectrum would be expected to have prominent high-frequency content. The total powers of three components and two components are shown in Fig. 3.17 to compare the frequency contents of the motions recorded at ML and JPL. In general for frequencies higher than 2.5 Hz the total powers are larger at ML than at JPL. The

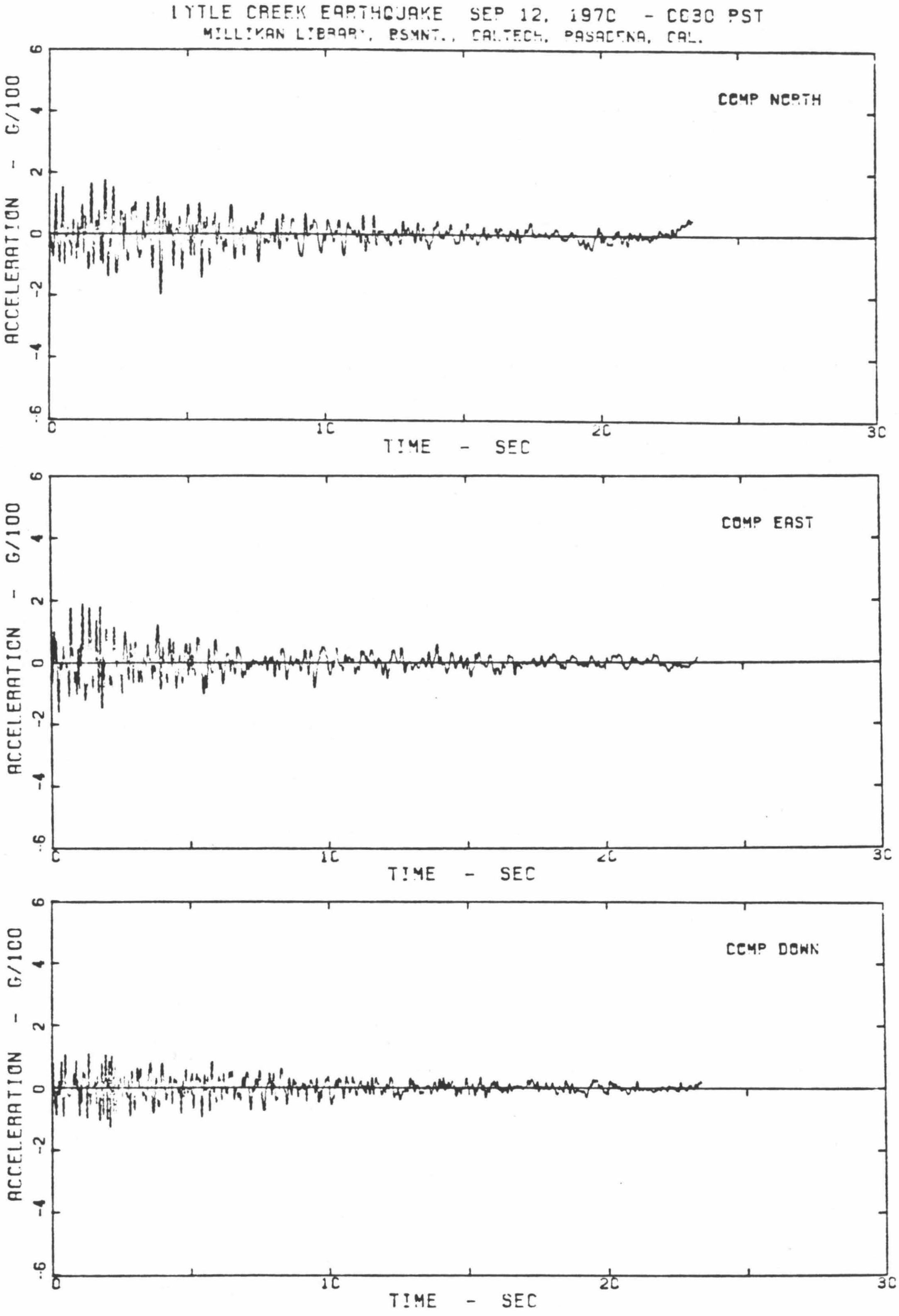

Fig. 3.15a Recorded accelerations at Millikan Library during the 1970 Lytle Creek earthquake.

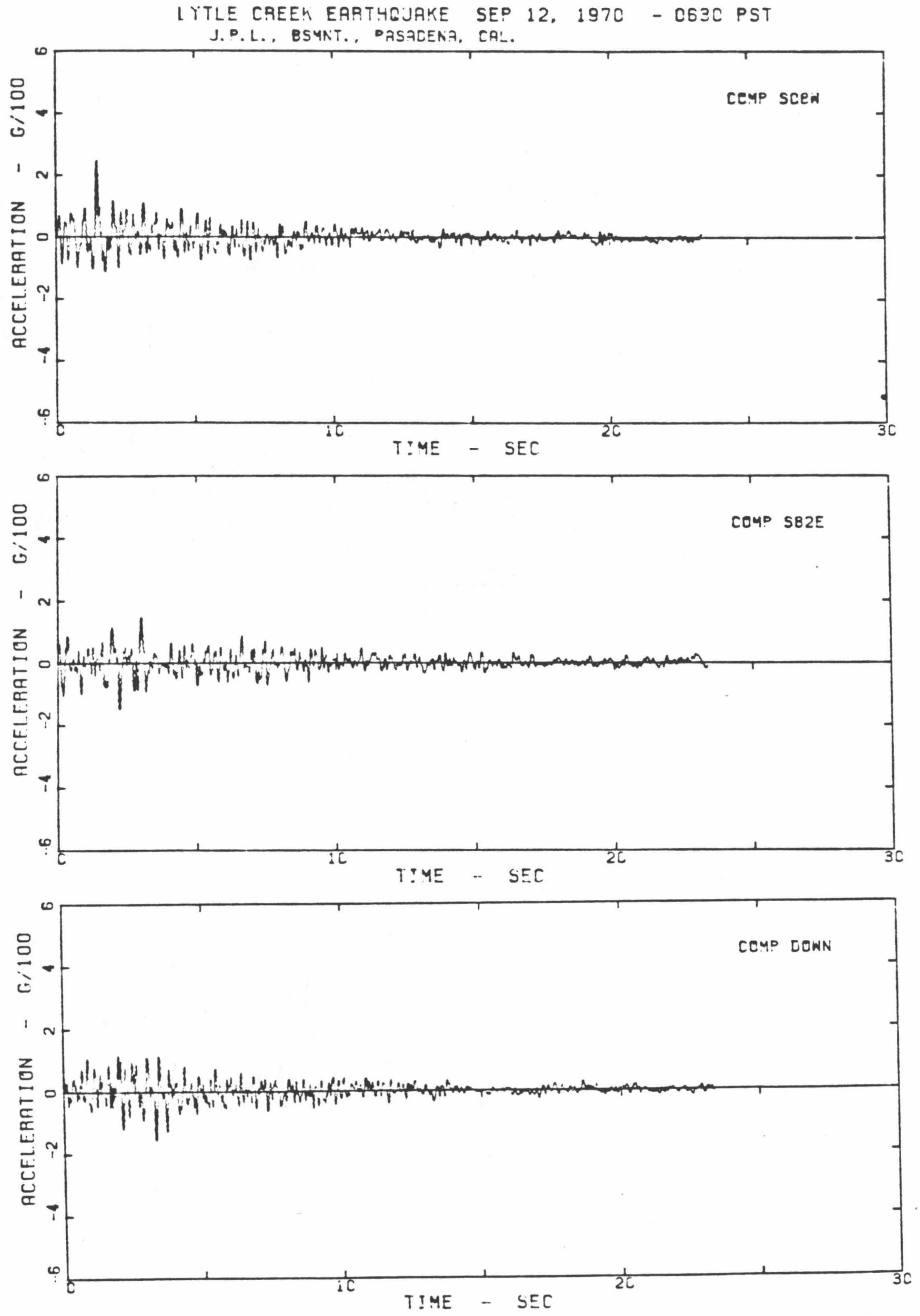

Fig. 3.15b Recorded accelerations at Jet Propulsion Laboratory during the 1970 Lytle Creek earthquake.

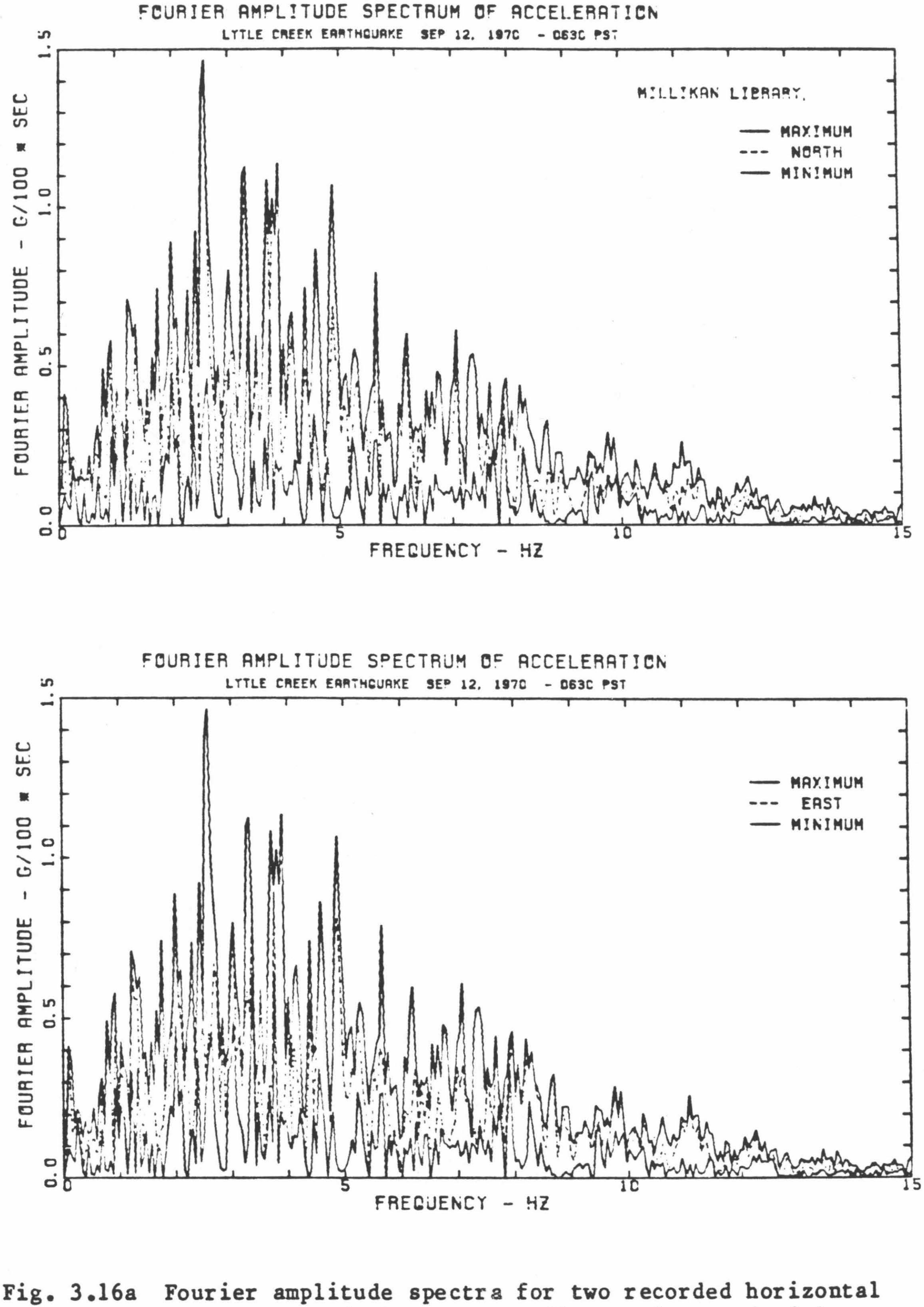

Fig. 3.16a Fourier amplitude spectra for two recorded horizontal components and the corresponding maximum and minimum Fourier amplitude spectra - ML. Lytle Creek earthquake.

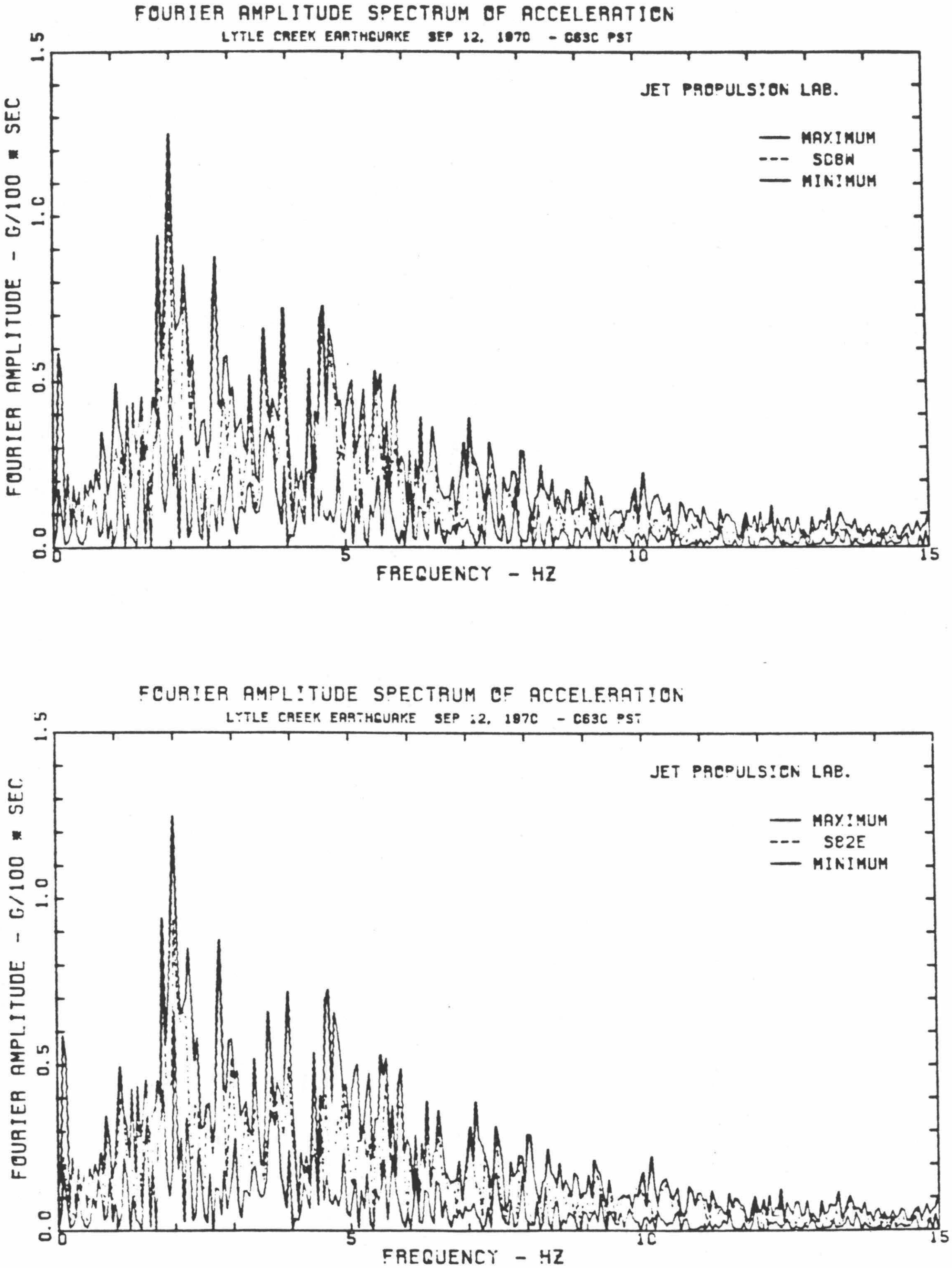

Fig. 3.16b Fourier amplitude spectra for two recorded horizontal components and the corresponding maximum and minimum Fourier amplitude spectra - JPL. Lytle Creek earthquake.

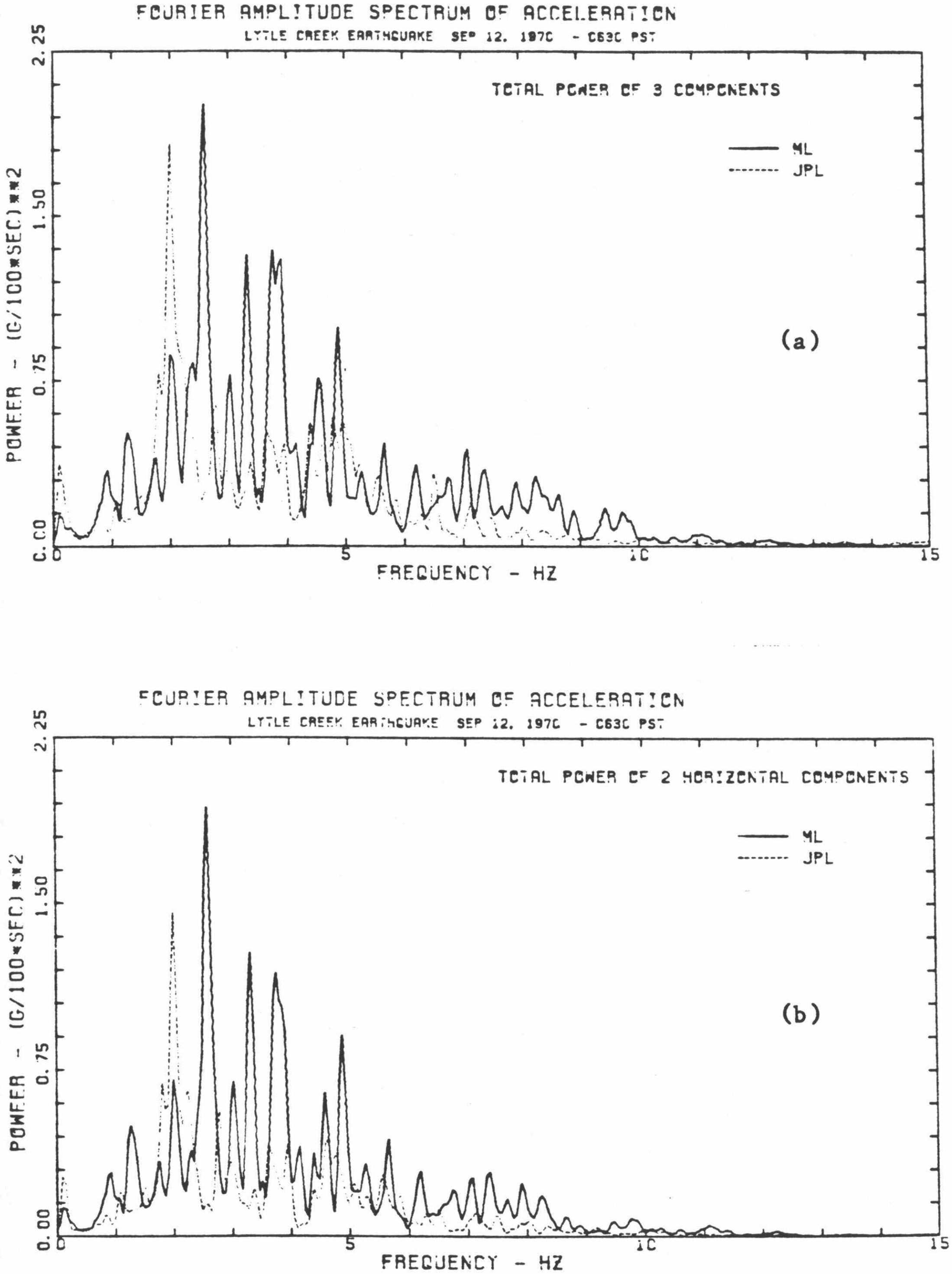

Fig. 3.17 Comparisons of the total power spectra of (a) 3 components, (b) 2 horizontal components, for ML and JPL. Lytle Creek earthquake.

predominant peak is located at 2.59 Hz in the ML spectra, whereas it is located at 1.98 Hz in the JPL spectra. The fundamental frequencies of the ML building during this earthquake were about 1.94 Hz in the NS direction and about 1.41 Hz in the EW direction. The first two modal frequencies of the JPL building were about 0.89, 2.99 Hz in the S08W direction and 0.98, 3.10 Hz in the S82E direction. Detailed analysis of these spectra shows no evidence of significant inertia soil-structure interaction during this earthquake for the ML and JPL buildings. The first peak near 0.1 Hz could be related to long period data processing errors.

3.5 Data of the 1968 Borrego Mountain Earthquake

The accelerograms obtained at ML, ATH and JPL during the 1968 Borrego Mountain earthquake are shown in Fig. 3.18. To facilitate comparison, the Athenaeum record was shifted to the right by 2.28-sec to approximately match the wave forms of the Millikan Library record, and the JPL record was approximately lined up in this figure. These accelerograms were band-pass filtered between 0.07 and 25 Hz. The ML and ATH instruments started before the shear wave arrivals, whereas the JPL instrument started after the first shear wave arrival. Both records lasted more than 60 seconds, but only the early part of the records were digitized. In fact, the RFT-250 accelerograph at the Seismological Laboratory was triggered during this earthquake (USGS & EERL, 1968); however, the record was not digitized probably because of its short length. A comparison of the raw records shows that the amplitudes of the motions at SL were not smaller than those at other stations. This is in good agreement with the observations in the 1971 San Fernando earthquake. As seen in Fig. 3.18, the accelerograms recorded in this area consist of surface waves which have amplitudes comparable to shear waves. Because of the low signal-to-noise ratio in the records, we do not attempt to identify the surface wave arrivals by using the

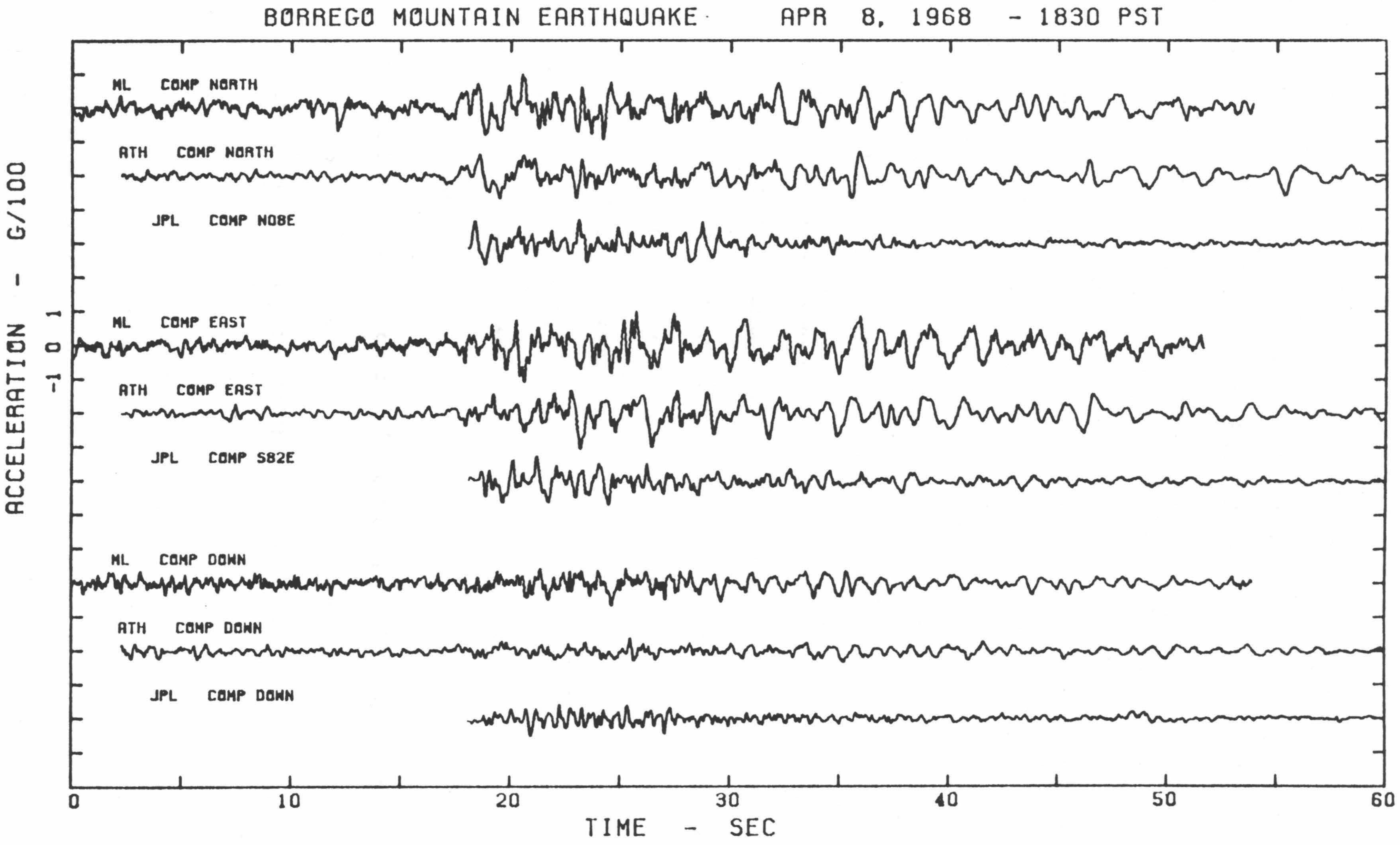

Fig. 3.18 Recorded accelerations at ML, ATH and JPL during the 1968 Borrego Mountain earthquake.

particle displacement trajectory. It is noted that the motions in the trailing part of the accelerograms at JPL were smaller than those at ML and ATH, although the difference in the epicentral distances is only 7 to 8 km which is very small as compared to the distance to the earthquake source. This might be the effect of local geology on the surface wave propagations across the Pasadena area.

A comparison of the ML and ATH accelerograms indicates several aspects. First, the motions between 0- and 17-sec corresponding to the P wave arrivals in the vertical component are comparable to those in two horizontal components, which indicates that body waves were incident to these stations nonvertically. This is different from the observations in the San Fernando earthquake during which body waves arrived at ML and ATH nearly vertically (Fig. 3.4). Secondly, the accelerograms at ML contain some high frequency motions which do not appear in the ATH accelerograms. This difference is attributable to the low-pass filter effects of the larger size of the Athenaeum foundation. Thirdly, the difference in amplitudes between ML and ATH motions is smaller during this earthquake than during the 1971 San Fernando earthquake. It is noted that the motions for this earthquake were much smaller than those for the 1971 San Fernando earthquake.

To compare the frequency content of the motions at ML and ATH, the 40.96-sec portions from 10.0- to 50.96-sec of the accelerograms in Fig. 3.18 were Fourier transformed. The thrice-smoothed Fourier amplitude spectra for three components are shown in Fig. 3.19. Solid curves give the ML spectra and dashed curves are for the ATH spectra. Fig. 3.20 shows the thrice-smoothed maximum, minimum horizontal amplitude spectra and the total power spectra. In general the ML spectra have greater amplitudes than the ATH spectra, especially at the peaks near 0.59, 1.0 and 3.8 Hz. However, the shapes of the spectra are quite

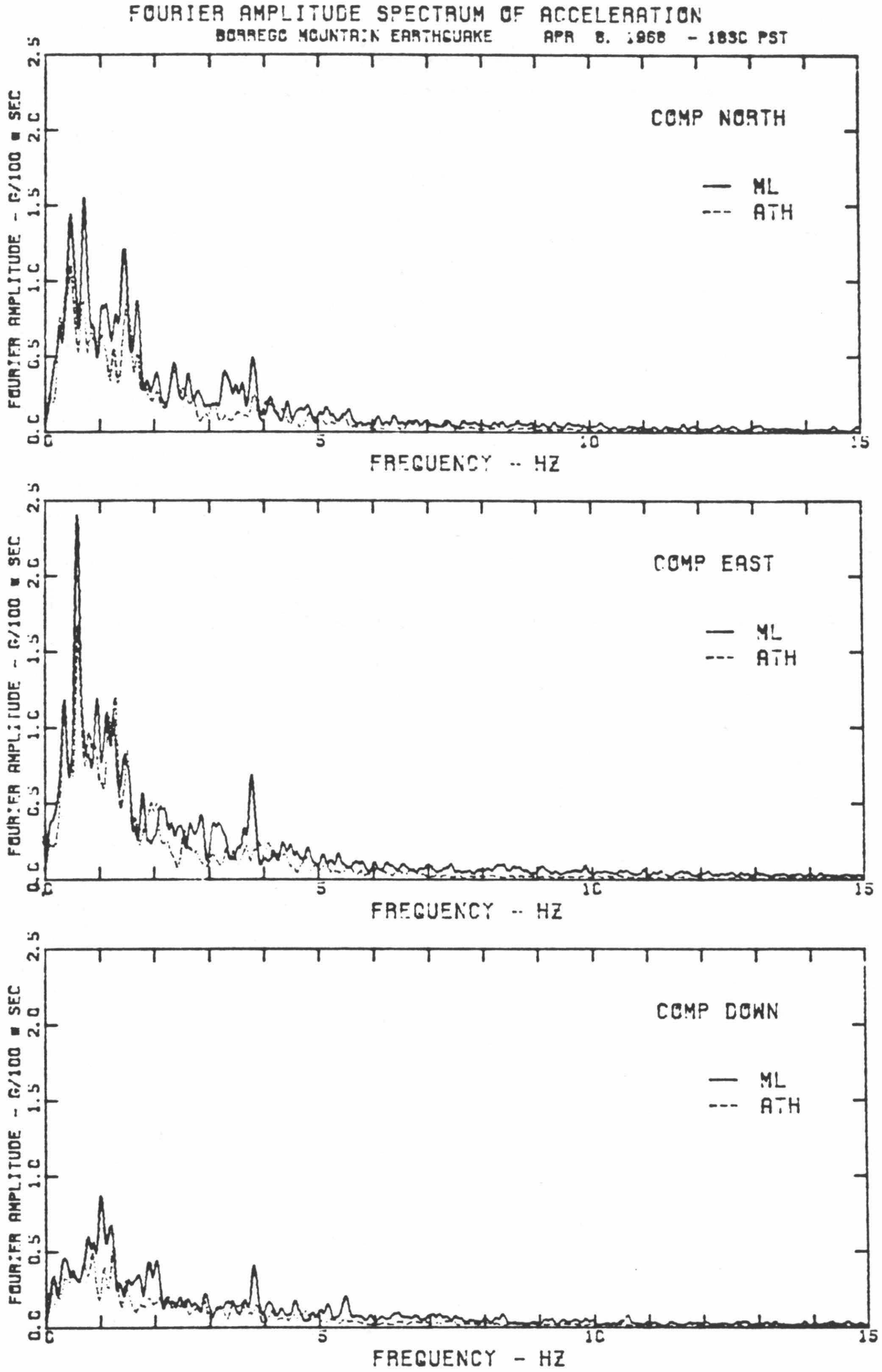

Fig. 3.19 Comparison of Fourier amplitude spectra for ML and ATH. Borrego Mountain earthquake.

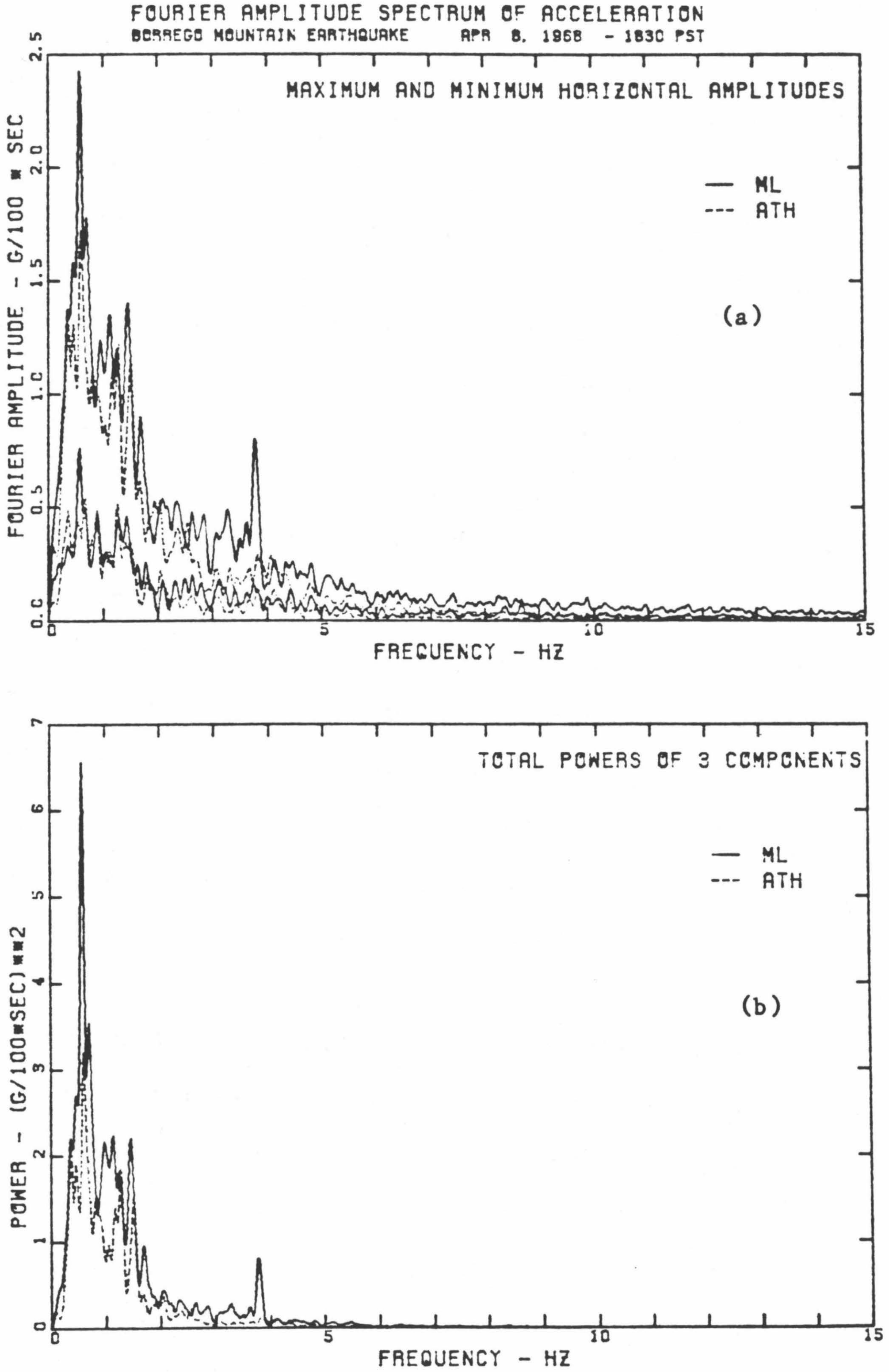

Fig. 3.20 Comparisons of (a) maximum, minimum Fourier amplitude spectra, (b) total power spectra of 3 components, for ML and ATH. Borrego Mountain earthquake.

similar and the difference is relatively small. It is noted that a prominent peak located near 3.8 Hz is found in all three components of the ML spectra, but is not shown in the ATH spectra. The common feature of these spectra is that the Fourier amplitudes decrease exponentially toward the high frequencies. This is due to the fact that this earthquake occurred more than 200 km away, a distance over which high-frequency waves would die out and long-period waves would become dominant. On the other hand, the source spectrum might itself have much low-frequency content because this earthquake was generated by strike-slip faulting

3.6 Data of the 1952 Kern County Earthquake

The accelerograms obtained at the Athenaeum during the 1952 Kern County earthquake are shown in Fig. 3.21. These accelerograms were band-pass filtered between 0.07 and 25 Hz. This earthquake was the largest earthquake in California since the 1906 San Francisco earthquake. The source mechanism of this earthquake involved both the thrusting and left-lateral strike-slip on the White Wolf fault (Fig. 3.1). The duration of the faulting slipping process was about 25 to 30 seconds. The motions for the first part of the accelerograms corresponding to the P wave arrivals were larger in the vertical component than in the horizontal components. It is noted that the early part motions at ATH during the San Fernando earthquake were mainly concentrated in the vertical component (Fig. 3.4). Although this earthquake was located along almost the same direction from this station as was the San Fernando earthquake, the arriving angles of seismic body waves at ATH were different for these two earthquakes. The complete accelerograms of 81.92-sec were Fourier transformed. Fig. 3.22 shows the thrice-smoothed Fourier amplitude spectra for three components. Large amplitudes are mainly at the frequencies between 0.5 and 2.0 Hz.

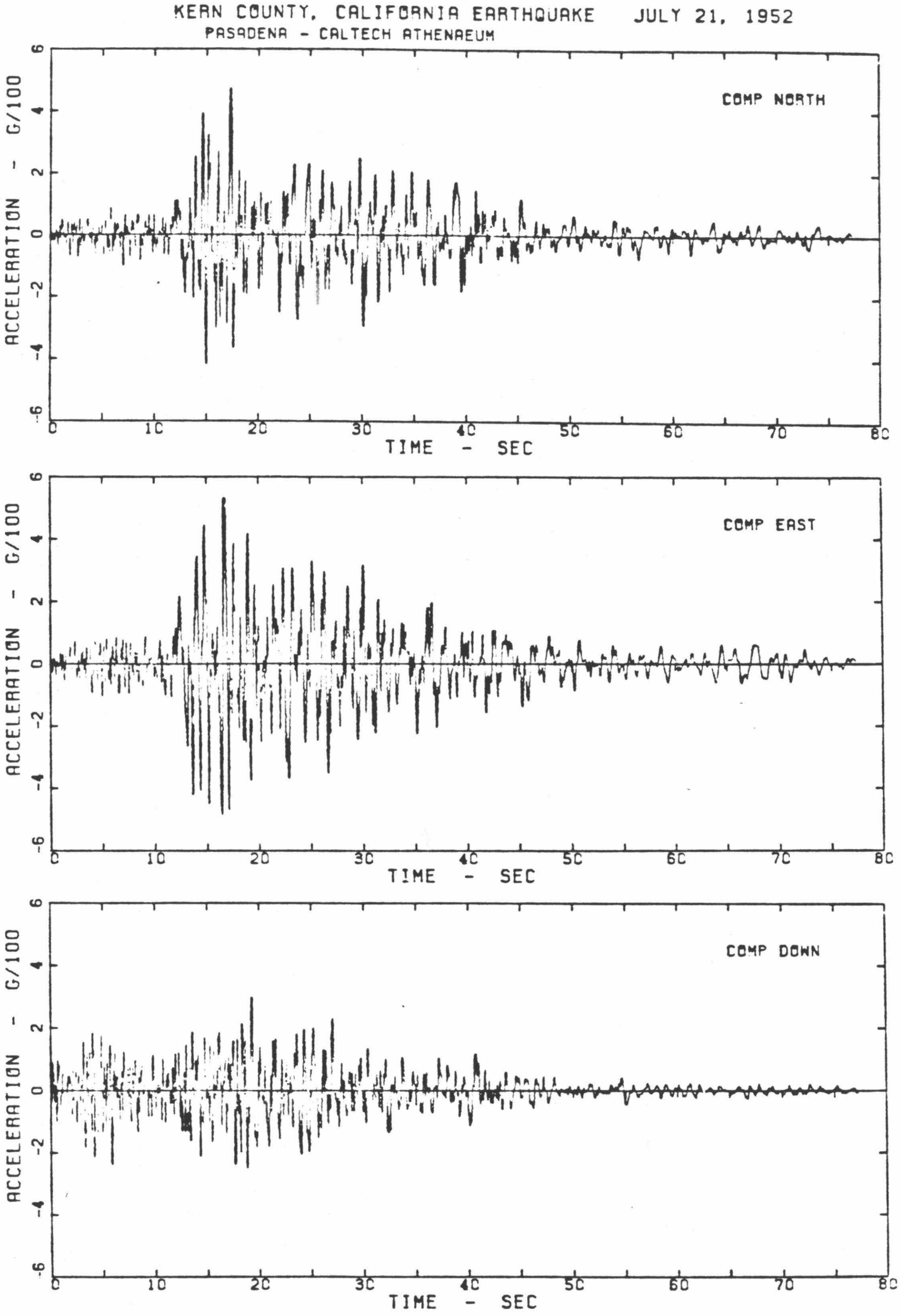

Fig. 3.21 Recorded accelerations at Athenaeum during the 1952 Kern County earthquake.

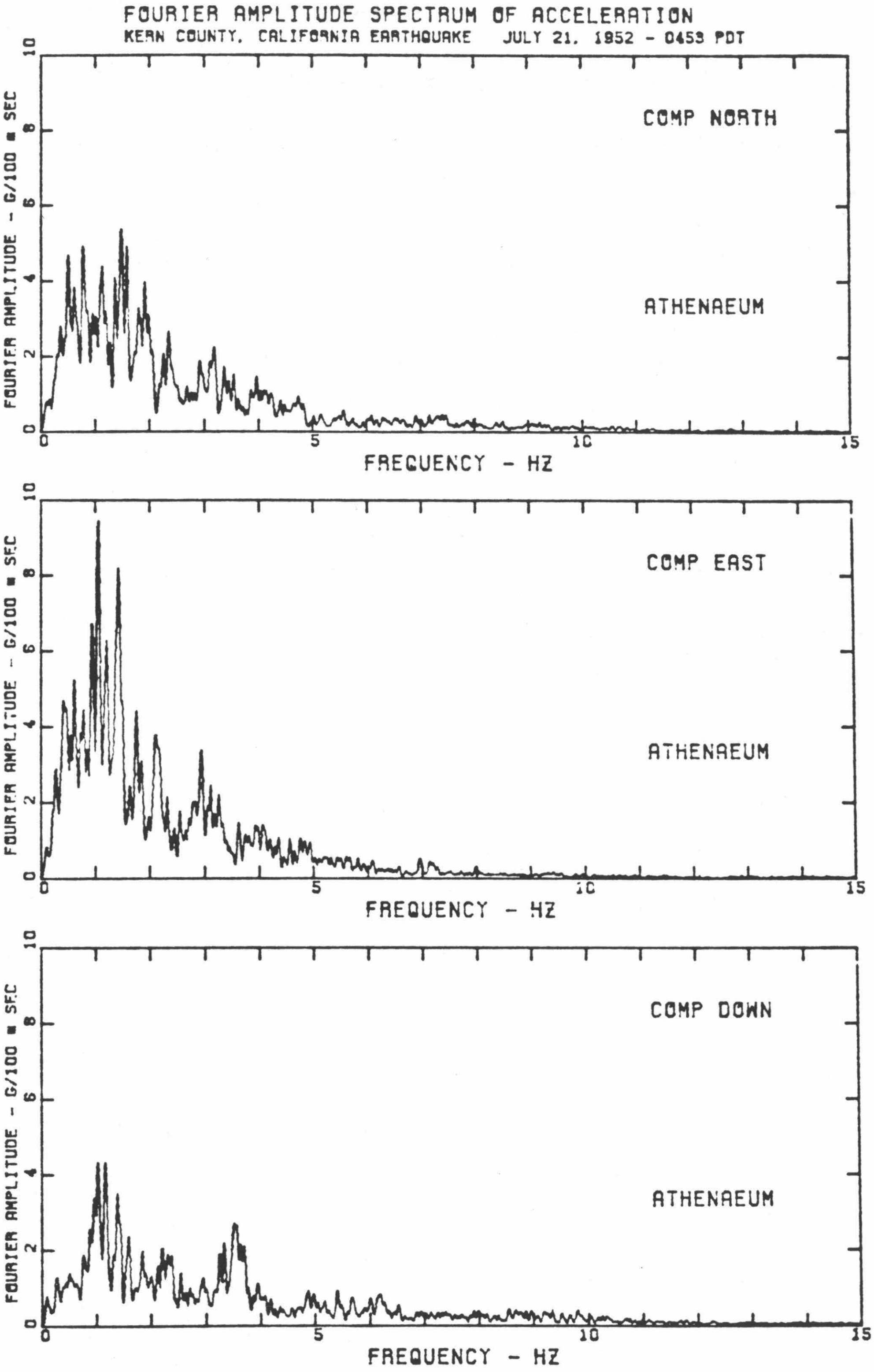

Fig. 3.22 Fourier amplitude spectra of the accelerograms in Fig. 3.21.

3.7 Investigation of Possible Site Periods

It is well known that the ground motions caused by the local geology effects depend on the three-dimensional nature of the local geology configuration and the direction of the arriving seismic waves. If the local geology conditions modify the incoming seismic waves in a significant and simple way as the simplified model predicts, we would see repeated peaks in the Fourier amplitude spectra for different earthquakes regardless of the earthquake source mechanism and the propagation path effects. The period at which a repeated peak is located is sometimes called the site period which should be a characteristic of a local site if it exists. Several studies, for examples, at a El Centro strong-motion accelerograph site in the Imperial Valley (Udwadia and Trifunac, 1973), four sites in the Los Angeles area (Trifunac and Udwadia, 1974) and several nearby sites in Los Angeles (Crouse, 1976), have indicated that no significant peaks in the spectra can be identified as site periods and the local geology effects have been overshadowed by the source mechanism and travel path effects. The data recorded in the Pasadena area provide another opportunity to investigate possible site periods. The unsmoothed Fourier amplitudes derived in the previous sections are smoothed several times, i.e., twice for the San Fernando and the Lytle Creek spectra, 4 times for the Borrego Mountain spectra and 9 times for the Kern County spectra, so that the smoothing bandwidth is about 0.25 Hz for all spectra. The amplitude spectra are compared in Figs. 3.23a, b and c for ML, JPL and ATH, respectively. To show the relative strength of the motions recorded in different earthquakes, the records obtained at each station are plotted on the same diagram in Figs. 3.24a, b and c. Solid lines indicate the windows in which the Fourier transforms were computed. Each window includes the motions of both body and surface waves.

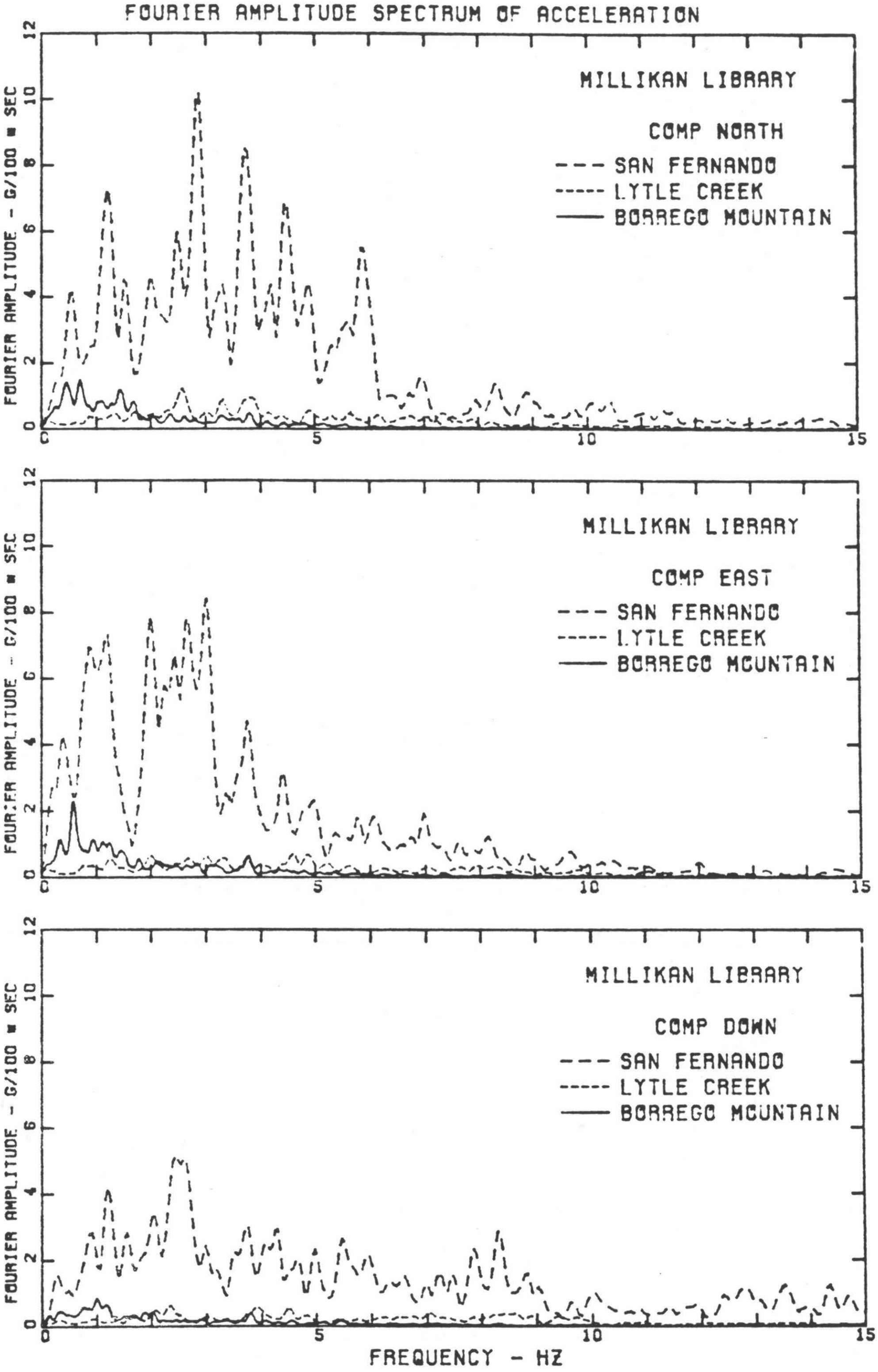

Fig. 3.23a Smoothed Fourier amplitude spectra - ML.

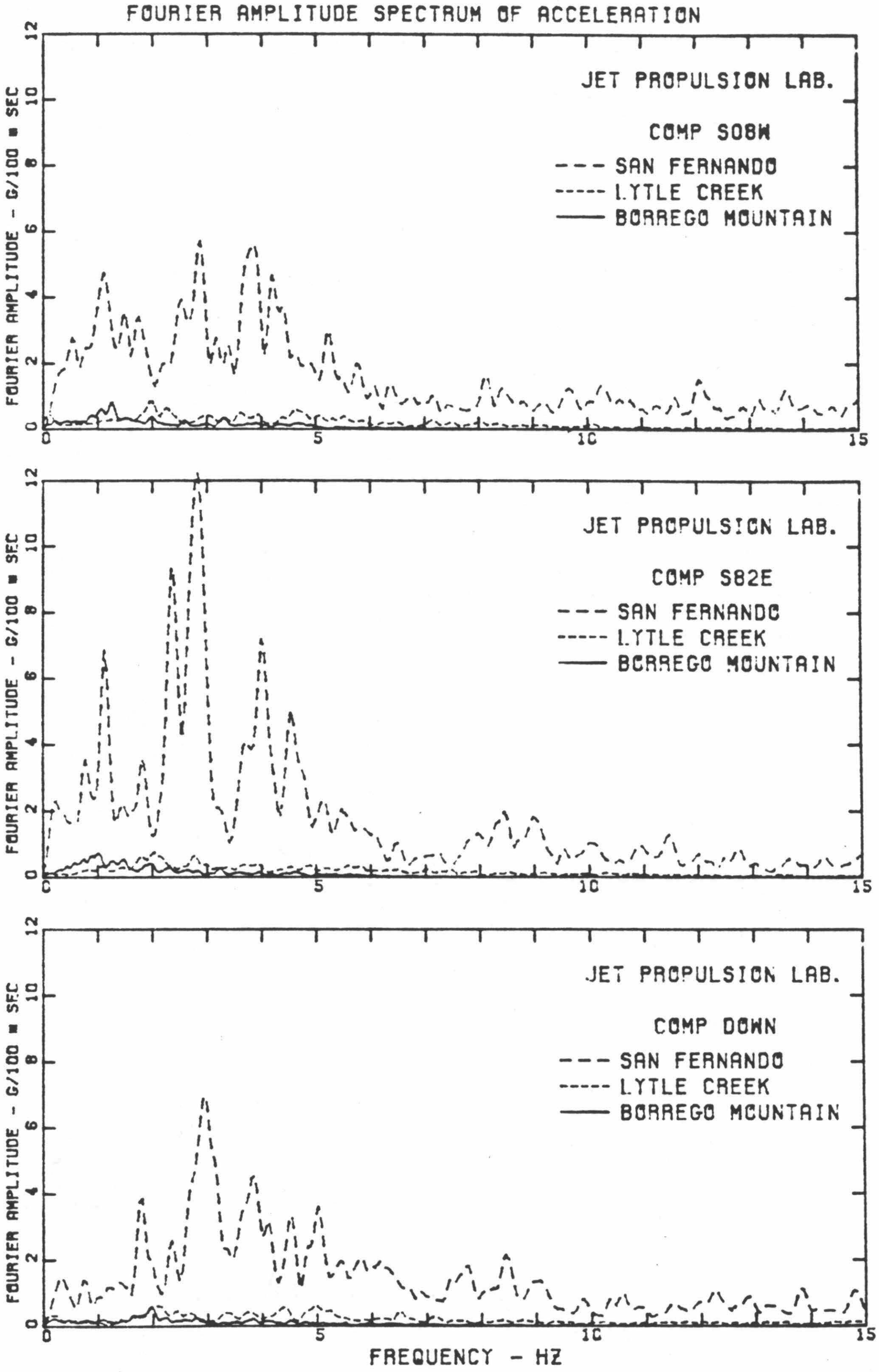

Fig. 3.23b Smoothed Fourier amplitude spectra - JPL.

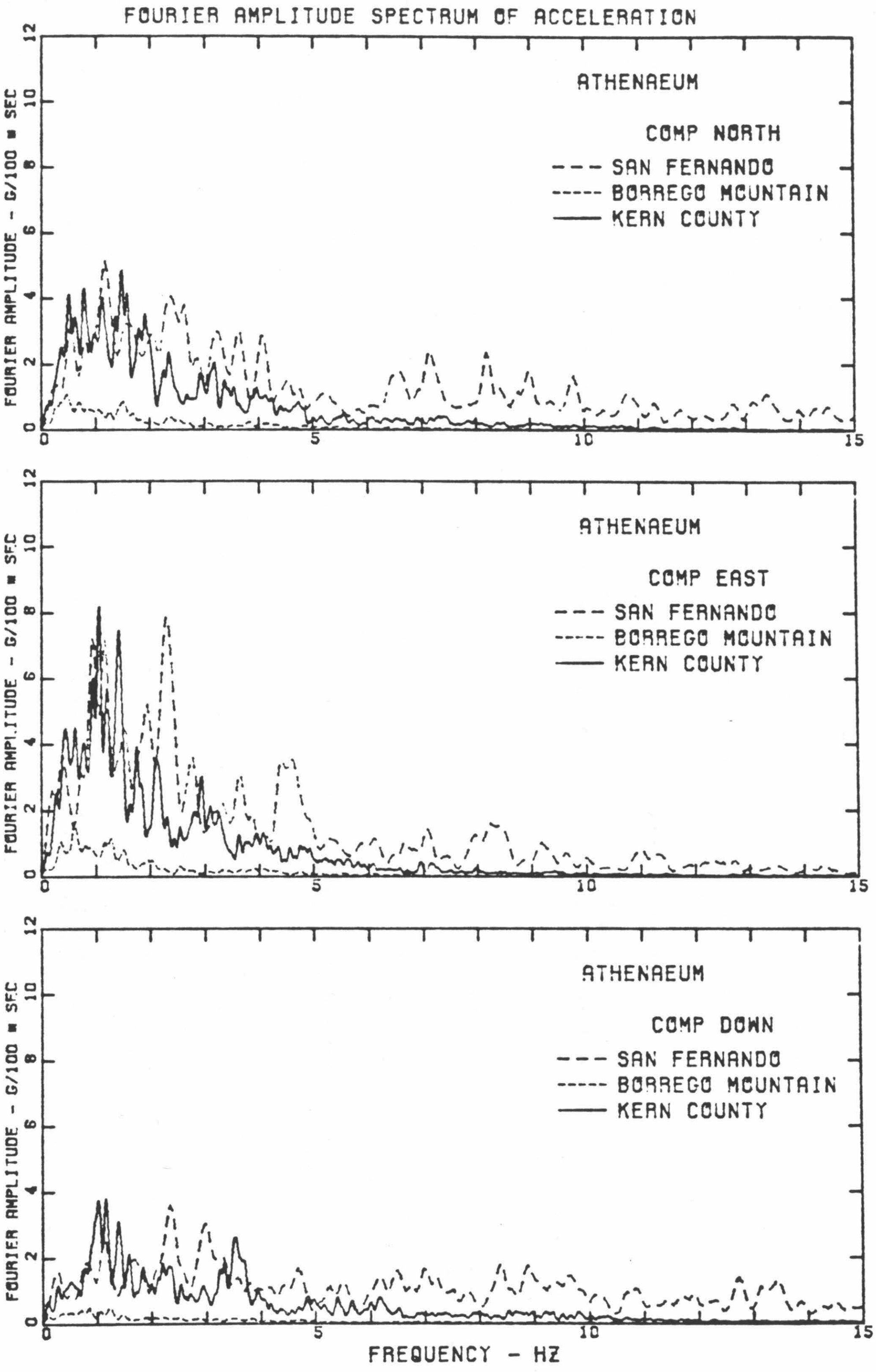

Fig. 3.23c Smoothed Fourier amplitude spectra - ATH.

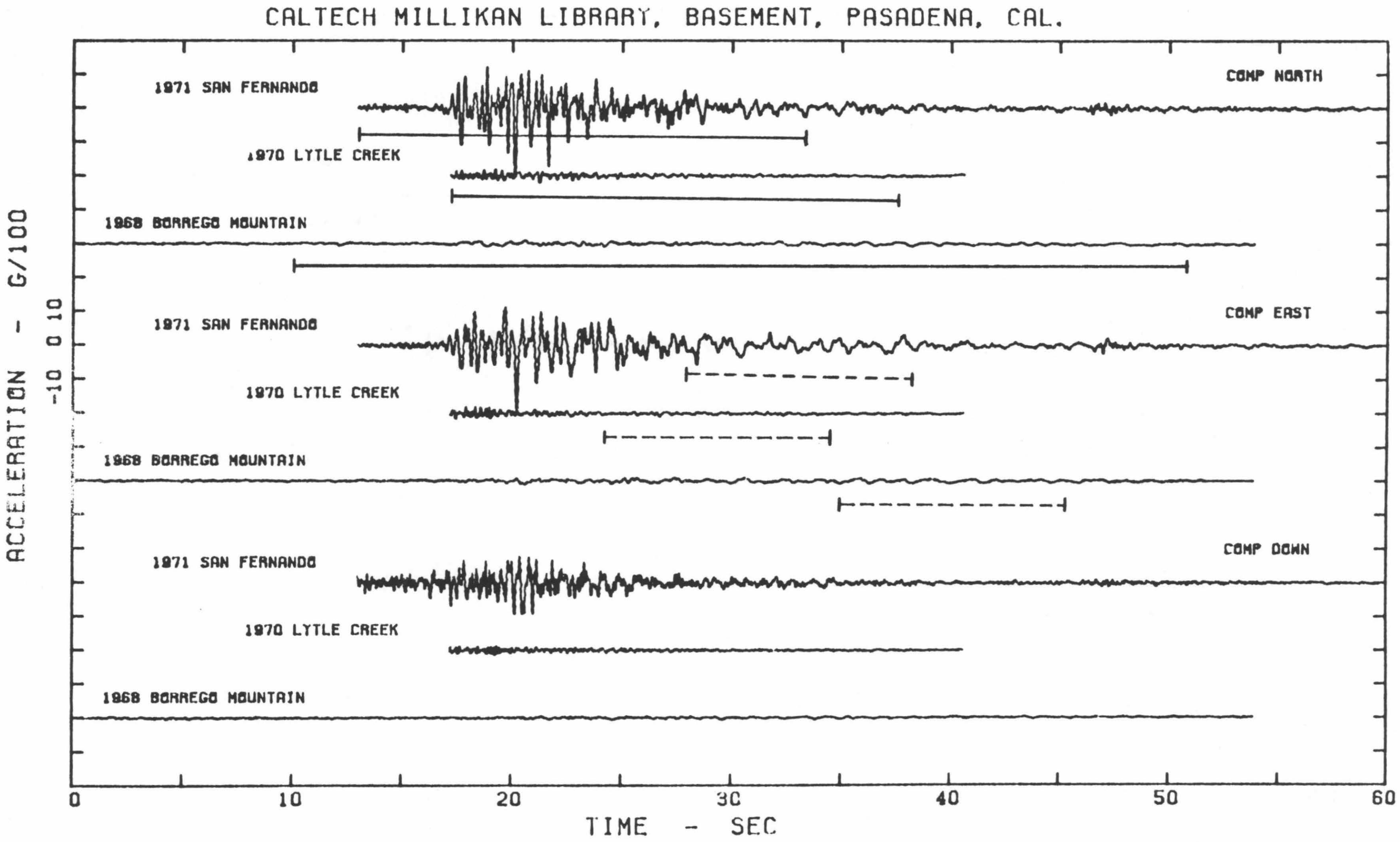

Fig. 3.24a Recorded accelerations from the San Fernando, the Lytle creek and the Borrego Mountain earthquakes at Millikan Library. (solid windows indicate the data from which the spectra in Fig. 3.23a are computed, while dashed windows are for Fig. 3.25a)

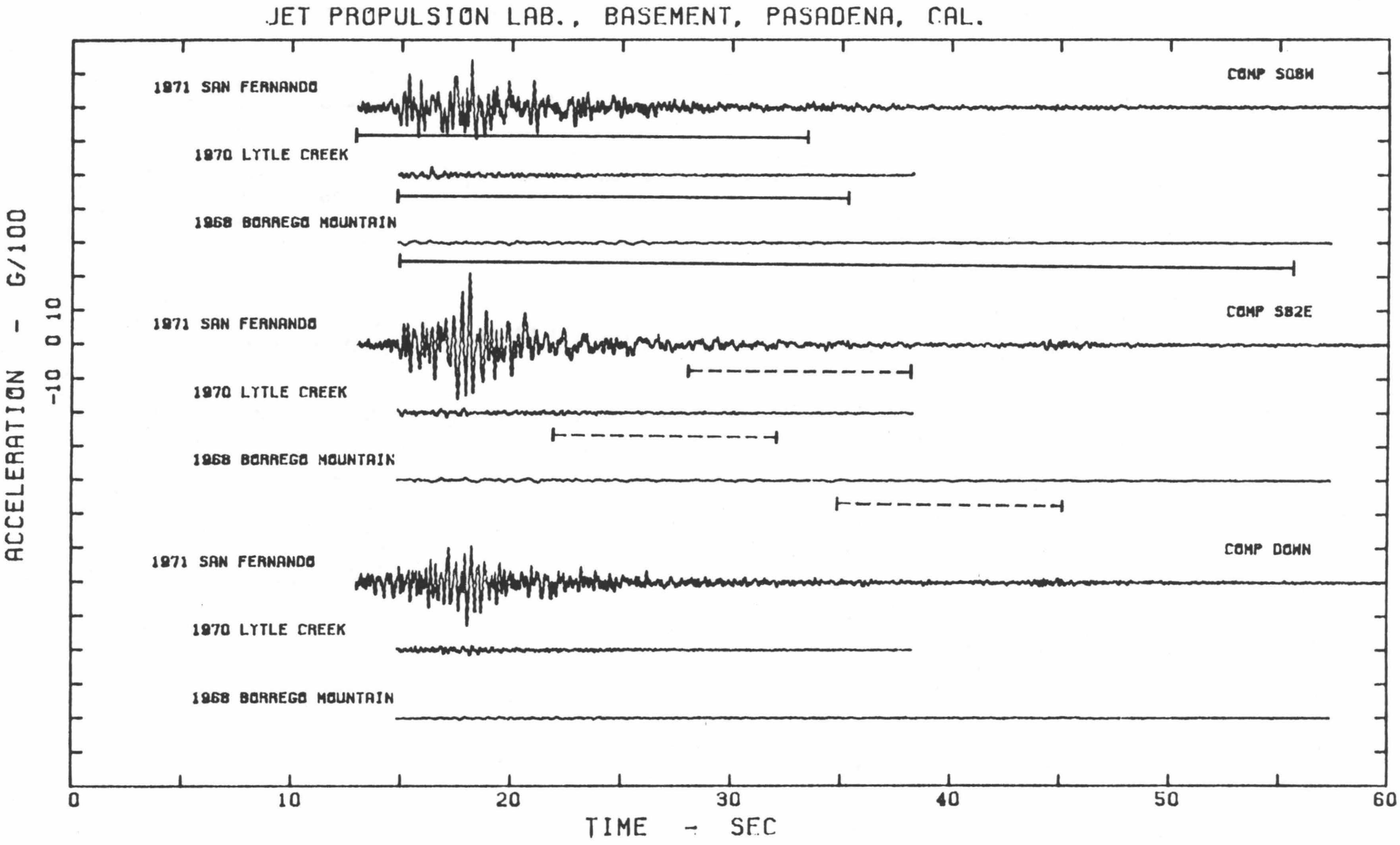

Fig. 3.24b Recorded accelerations from the San Fernando, the Lytle creek and the Borrego Mountain earthquakes at Jet Propulsion Laboratory. (solid windows indicate the data from which the spectra in Fig. 3.23b are computed, while dashed windows are for Fig. 3.25b)

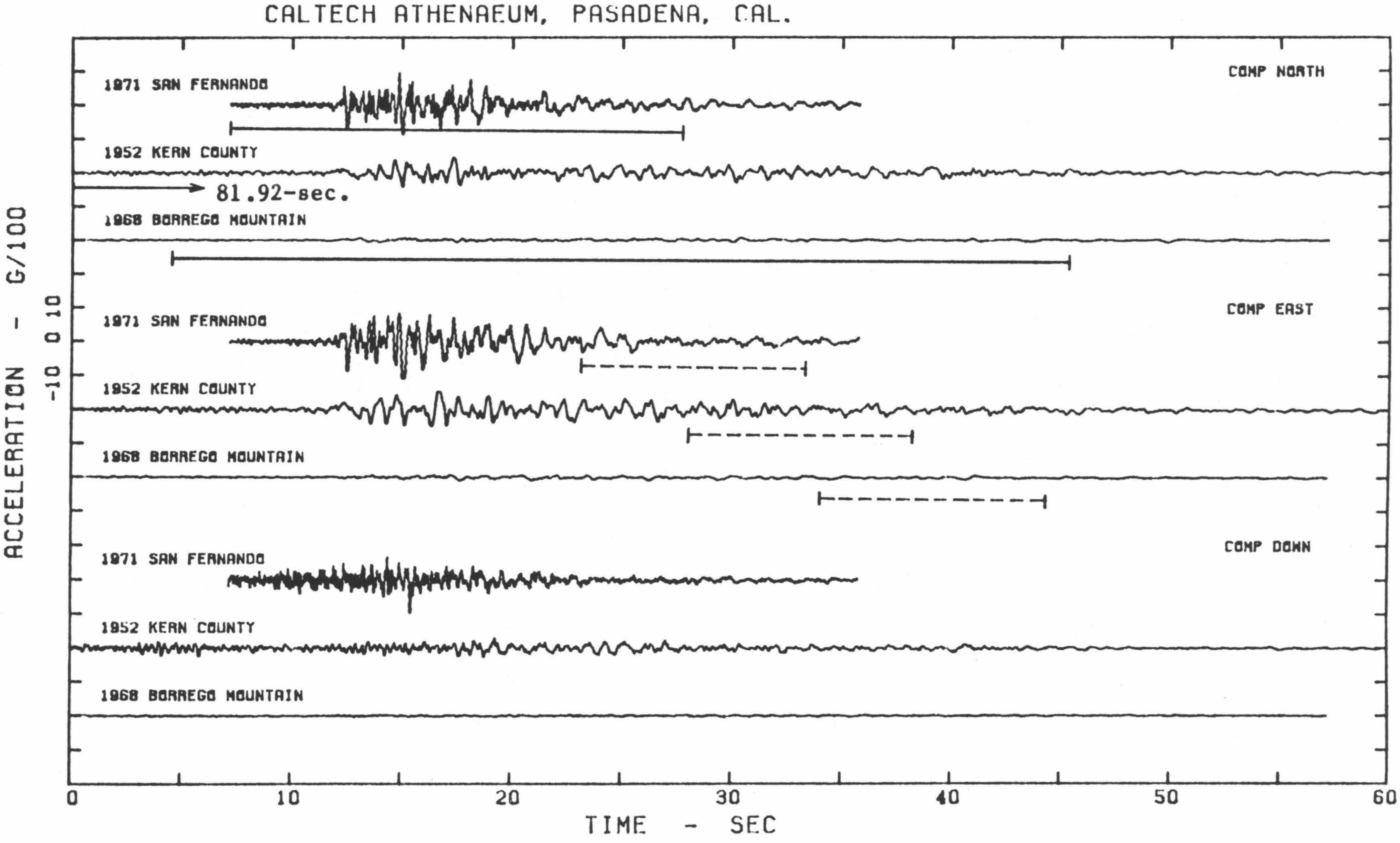

Fig. 3.24c Recorded accelerations from the San Fernando, the Kern County and the Borrego Mountain earthquakes at Athenaeum. (solid windows indicate the data from which the spectra in Fig. 3.23c are computed, while dashed windows are for Fig. 3.25c)

The amplitude spectra for ML and JPL in Figs. 3.23a and b show no detectable predominant peaks that repeated during the San Fernando, the Lytle Creek and the Borrego Mountain earthquakes. Fig. 3.23c shows the amplitude spectra at ATH for the San Fernando, the Borrego Mountain and the Kern County earthquakes. At low frequencies between 0- and 2-Hz, the spectra for the Kern County earthquake are comparable to those for the San Fernando earthquake, although the Kern County earthquake was located about thrice as far as the San Fernando earthquake. This is because the Kern County earthquake had a big seismic moment; the source spectrum would have large low-frequency content. Despite the distance attenuation effect, in such a distance the low-frequency motions are still as large as those generated by a smaller and closer event. It is interesting to note that a peak located near 1.2 Hz is seen in the San Fernando spectra as well as in the Kern County spectra, but it is not seen in the Borrego Mountain spectra. Since this peak is also seen in the ML spectra for the San Fernando earthquake, one might attempt to interpret this peak as a site period. However, this peak is also located at the same frequency in the vertical spectra. This is inconsistent with the results predicted by the simplified model that peaks produced by local geology effects would be expected to be at higher frequency in the vertical component than in any horizontal component. The seismic waves generated by the Kern County and the San Fernando earthquakes were arriving at this area from about the same direction, while the seismic waves of the Borrego Mountain earthquake were arriving from another direction.

It is also interesting to see whether the trailing parts of these ground motions, which consist essentially of surface waves, have been dominated by the same period of motions during different earthquakes. A 10.24-sec window was applied to all the records and the dashed lines in Fig. 3.24 show the windows where the data were Fourier transformed. The once-smoothed Fourier amplitude spectra for ML, JPL and ATH are shown in Figs. 3.25a, b and c, respectively. To facilitate comparison, the spectra of the trailing motions at SL for the San Fernando earthquake are shown as solid curves in these figures. Detailed comparison of all spectra in these figures shows that there are no frequencies which dominate in all earthquake motions. For all earthquakes recorded in this area, the amplitudes in the JPL spectra are smaller than those in the ML and ATH spectra. This is also seen in the accelerograms shown in the previous sections. The trailing motions at ML and ATH were mainly in the frequency range from 0- to 2-Hz for all earthquakes except for the Lytle Creek earthquake. Relative to SL for the San Fernando earthquake, the trailing motions at ML and ATH in this frequency range were larger. It is noted that the peaks located near 1.6 Hz in the NS component and near 0.3 Hz and 1.0 Hz in the EW component are shown in both the ML and ATH spectra for the San Fernando earthquake. However, the peaks near 1.0 and 1.6 Hz, which are fundamental frequencies of the ML building in the NS and EW directions, respectively, are of larger amplitudes at ML than at ATH. It is likely that inertia soil-structure interaction effects have contributed to the trailing basement motions of the ML building.

It is well known that the frequency content of surface waves generated by the earthquake is dependent on the depth of the source. Surface waves could be affected by the low-velocity sediments as they travel from a rock site to an alluvial site. The effects may increase with increase of frequency because the high frequency surface wave does not penetrate deeply and most of its energy is contained in the upper layers near the surface. However, the effects are dependent on the 3-dimensional configuration of local geology and hence the direction of arriving waves. The propagation of surface waves in laterally varying media is a problem which can not generally be solved analytically; one must rely on the recorded data to assess these effects. The data presented here indicate that

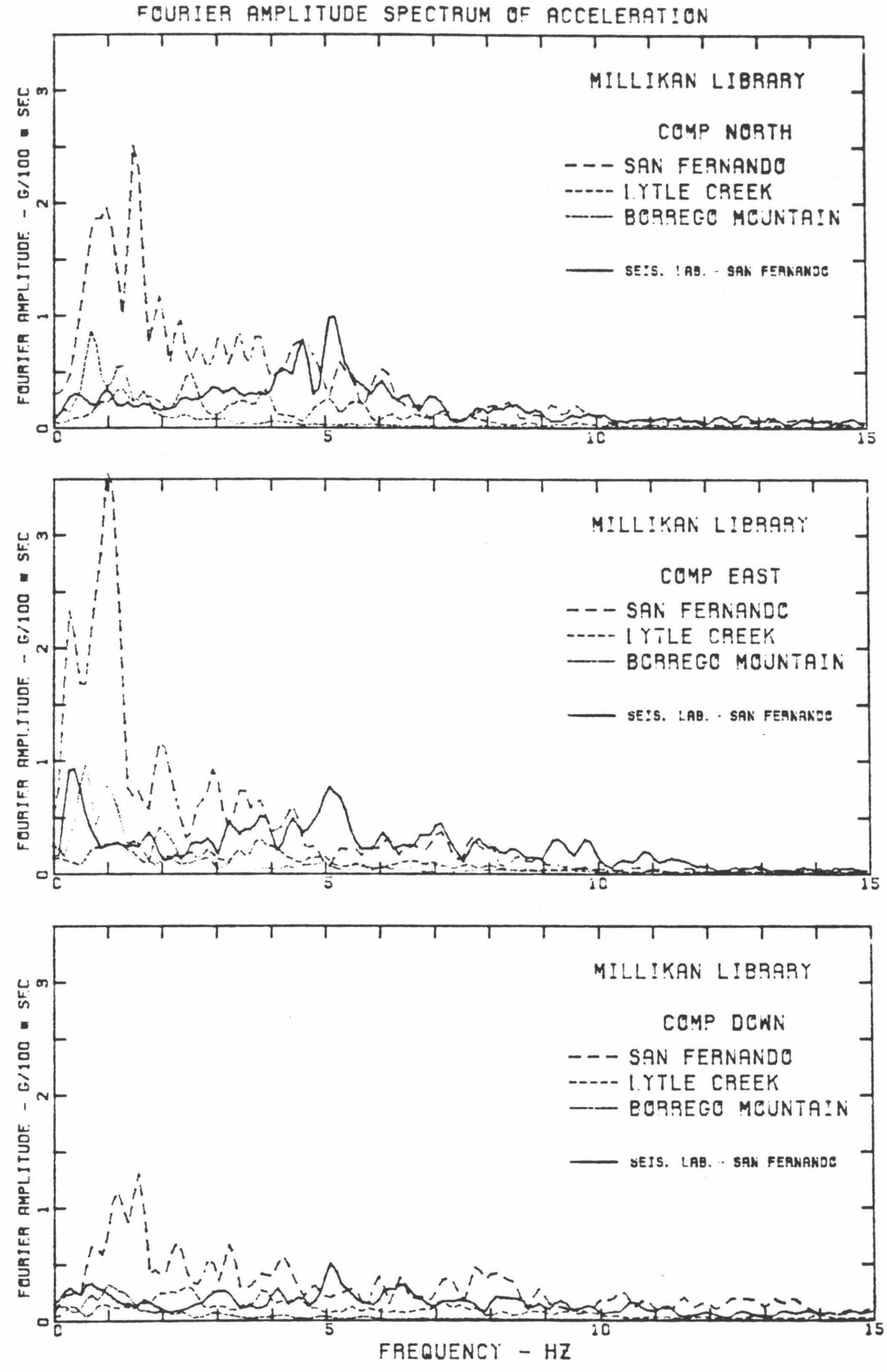

Fig. 3.25a Smoothed Fourier amplitude spectra of the selected trailing accelerations in Fig. 3.24a - ML.

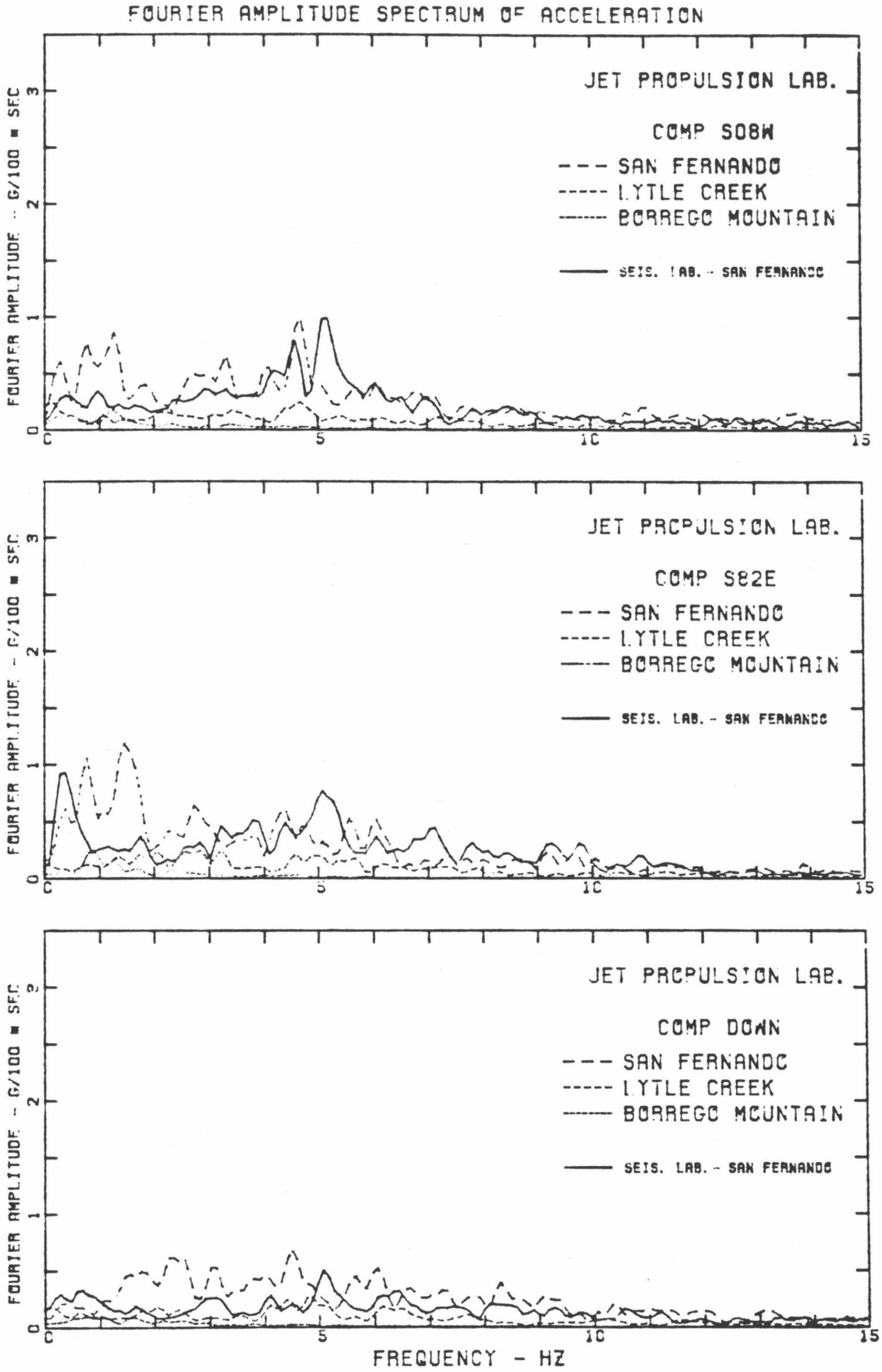

Fig. 3.25b Smoothed Fourier amplitude spectra of the selected trailing accelerations in Fig. 3.24b - JPL.

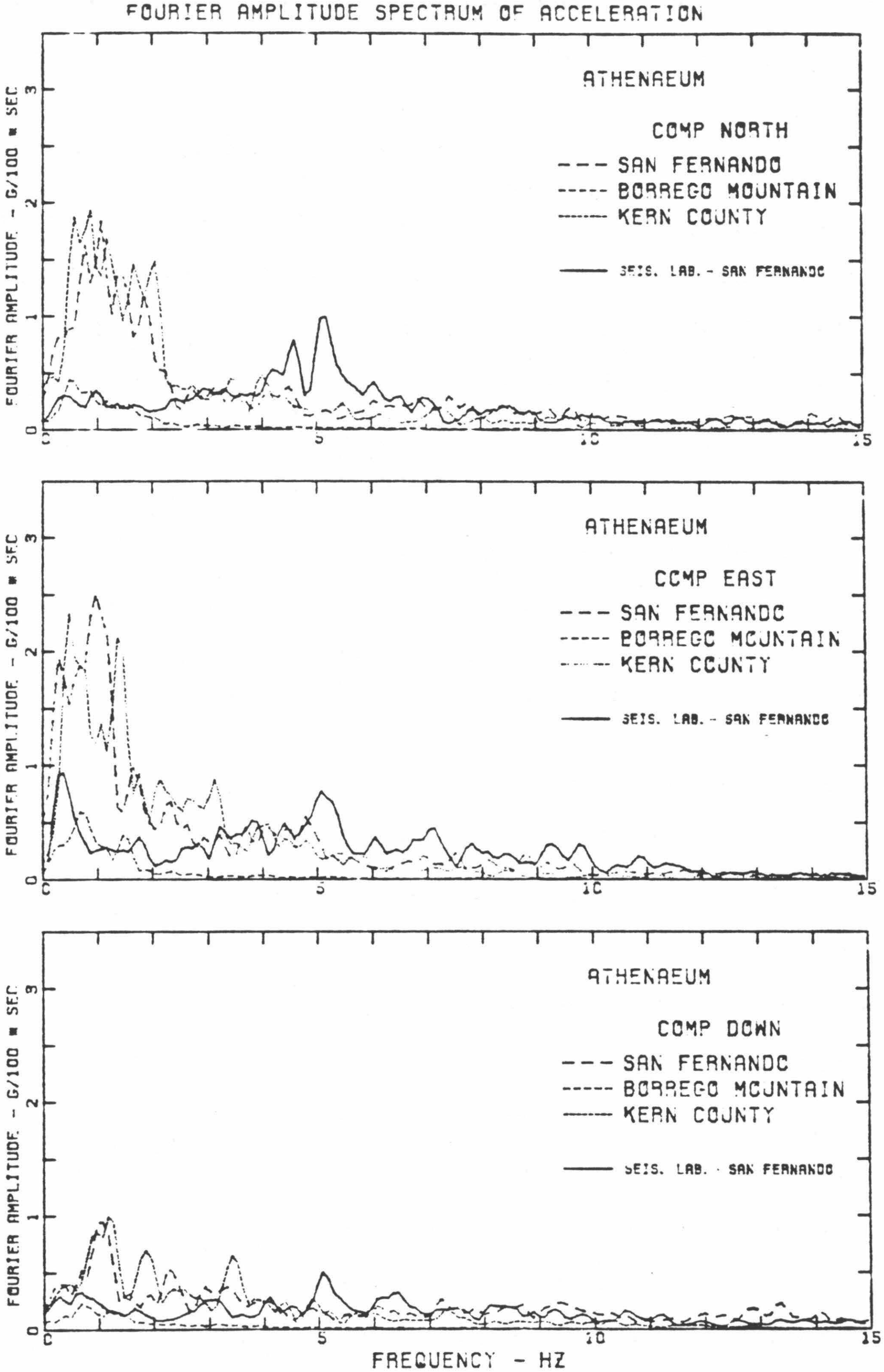

Fig. 3.25c Smoothed Fourier amplitude spectra of the selected trailing accelerations in Fig. 3.24c - ATH.

local geology effects on surface wave propagations are dependent on the directions of arriving waves.

3.8 Spatial Variations of Ground Motions

Spatial variations of ground motions are of particular interest to engineers in designing extended structures such as suspension bridges, long-span highway bridges, dams and pipelines. In analyzing the response of such structures to earthquake ground motions, one may involve in considering multiple support excitations. The records obtained at ML and ATH during the 1971 San Fernando and the 1968 Borrego Mountain earthquakes have provided data for studying spatial variations of ground motions. Since the motions for the San Fernando earthquake were stronger than those for the Borrego Mountain earthquake, only the results for the San Fernando earthquake are presented and discussed herein.

Because the instruments were triggered independently, some efforts were made to synchronize the time reference on these two stations. As shown in Section 3.3.4, we have aligned the records by matching two velocity curves and assuming that body waves arrived simultaneously and hence in phase at these stations. The match was done by eye; it is possible that small errors in the time synchronization remain. To be more precise, a least square fit of the motions corresponding to body waves was made. The differences in acceleration and velocity between the ML and ATH records were computed for each component and their squares were integrated from 0- to 7.2-sec. As shown in Fig. 3.12, 7.2-sec is the time before surface wave arrivals. The results for different values of t_s which is the shift of ATH records along the time axis, are shown in Fig. 3.26. The markers indicate the points where numerical values were evaluated. Since the sample interval is 0.02-sec for the acceleration and is 0.04-sec for the velocity, t_s

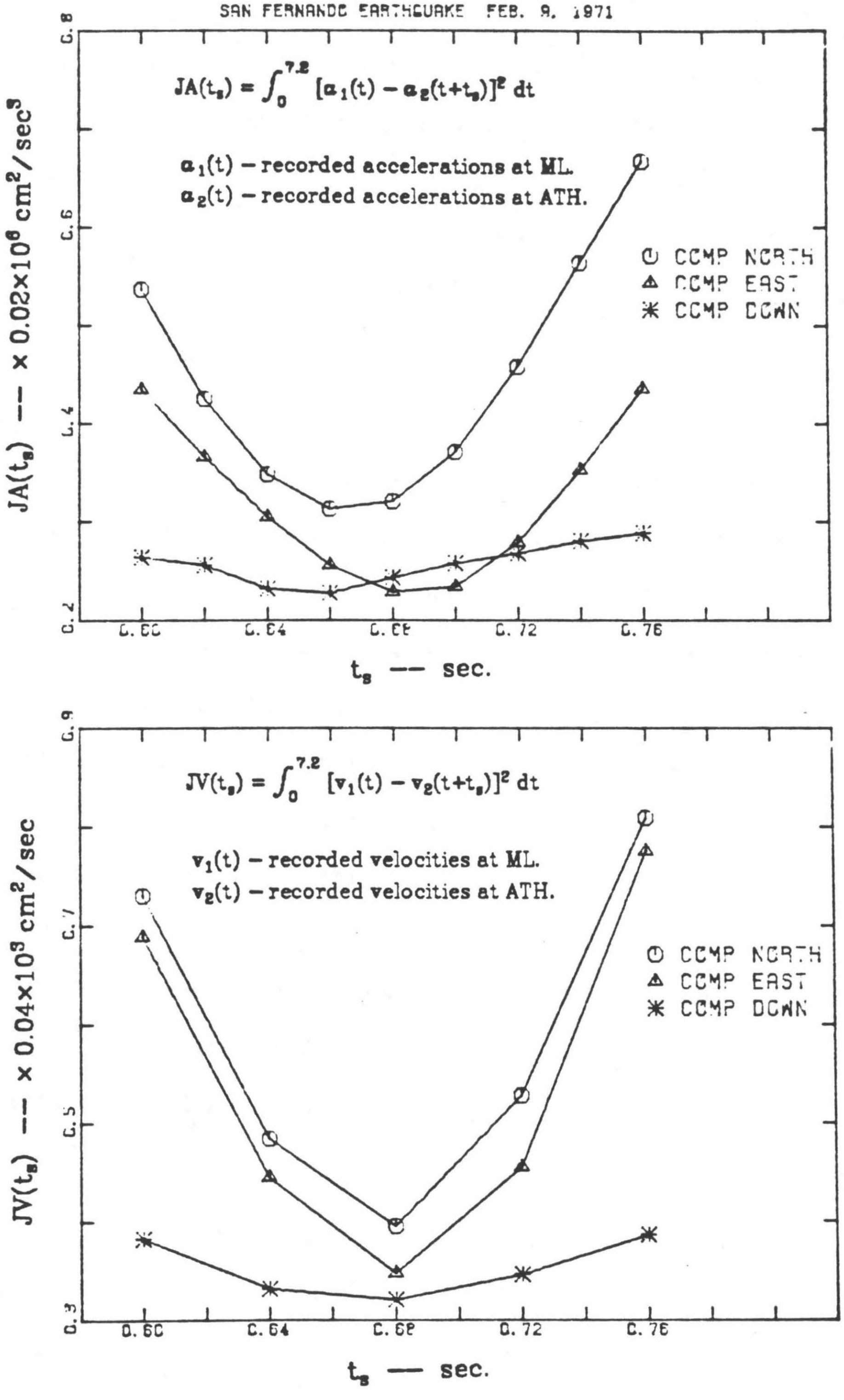

Fig. 3.26 Optimal estimate of the shift, ts, of the Athenaeum records along the time axis to least-squares fit the Millikan Library records between 0.0 and 7.2-sec.

is chosen as a multiple of the corresponding time interval. In the velocity fit, the optimal value of t_s is 0.68-sec, which agrees with the match done by eye in Fig. 3.12. On the other hand, in the acceleration fit, the optimal t_s is 0.66-sec for the north and the vertical components and is 0.68-sec for the east component. As a result, all the analyses performed here have been repeated for two different values of t_s, i.e., 0.66- and 0.68-sec. Since the differences in the results are found insignificant, only the results for t_s=0.66-sec are presented here.

Fig. 3.27 shows the relative displacements between ML and ATH in three components. The peak values are 3.02-, 2.77- and 1.70-cm for the NS, the EW and the vertical components, respectively. All these peaks occurred during the surface wave arrivals. It is noted that the distance between ML and ATH is about 1200 feet. The longitudinal relative displacement in the EW component is of interest to bridge or pipeline engineers. For instance, if a 1200 feet span bridge is to be built at this site, then the structure must be designed to tolerate or allow a 2.77 centimeters longitudinal relative displacement between two piers. Another important parameter in designing the oil or gas pipelines is the ground strain developed during strong earthquakes. The average longitudinal strain between ML and ATH can be estimated as the ratio obtained by dividing the relative longitudinal displacement by the distance between ML and ATH. If a pipe had been buried along the line between ML and ATH, the maximum axial strain of the pipe would have been about 7.6×10^{-5}.

In analyzing the linear response of a structure to earthquake excitations at two supports, the input motions can be separated into the in-phase and out-of-phase components. Furthermore, for a symmetric structure with two supports, the in-phase motions could excite the symmetric modes but not antisymmetric modes, whereas the contrary is true for the out-of-phase motions. Let $a_1(t)$ and $a_2(t)$ be the recorded ground accelerations at stations 1 and 2, respectively, in a

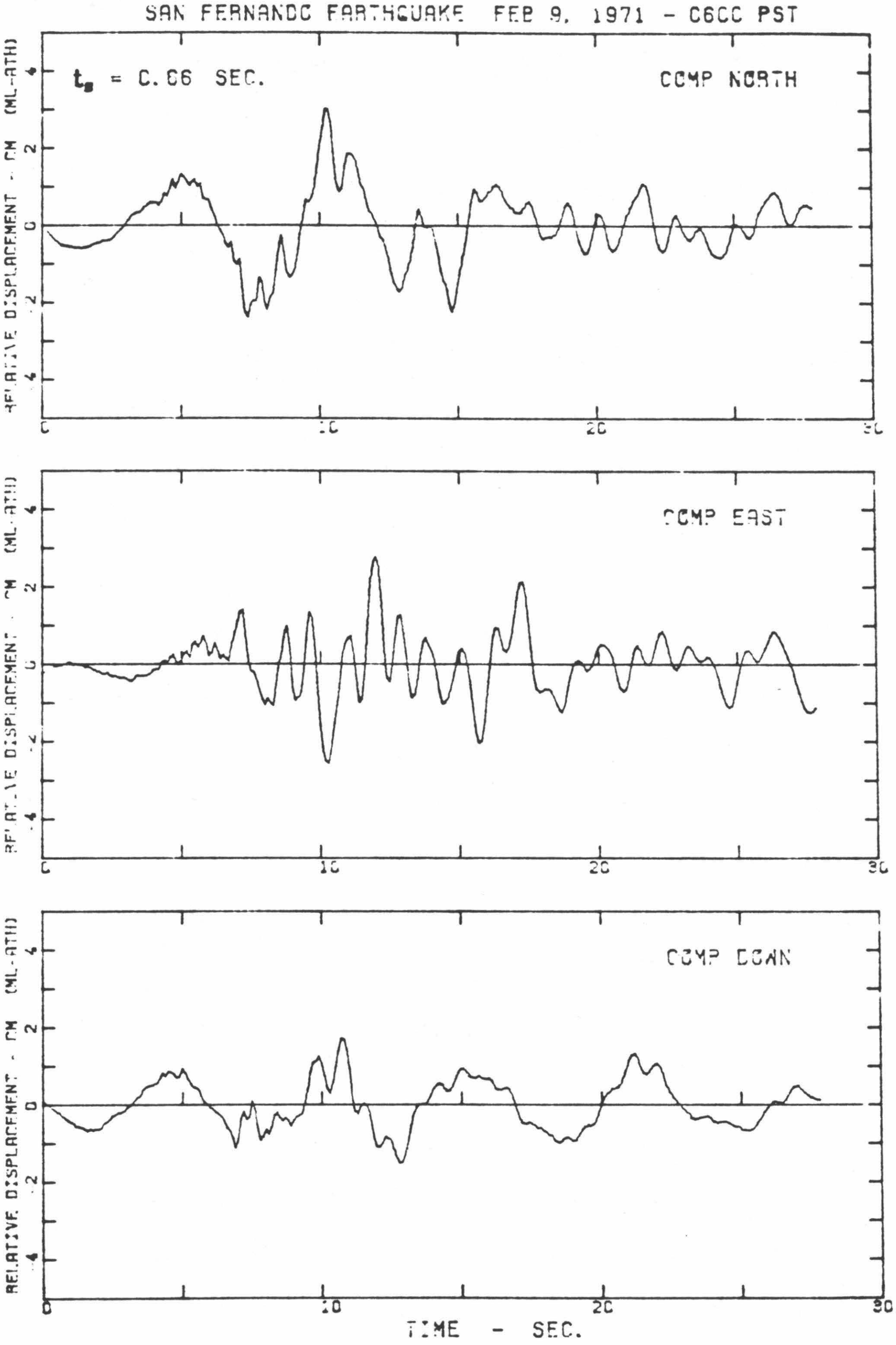

Fig. 3.27 Estimated relative displacements between Millikan Library and Athenaeum. San Fernando earthquake.

given direction, the in-phase component, $a_{in}(t)$, and the out-of-phase component, $a_{out}(t)$, are given by

$$a_{in}(t) = \frac{a_1(t) + a_2(t)}{2} , \quad a_{out}(t) = \frac{a_1(t) - a_2(t)}{2} .$$

To compare the frequency content of these two components for the ML and ATH motions recorded during the San Fernando earthquake, Fig. 3.28 shows the Fourier amplitude spectra for the in-phase and the out-of-phase components in the NS, EW and vertical directions. The Fourier transforms were computed from the 20.48-sec portions of the in-phase and the out-of-phase accelerations. The data were tapered and the Fourier amplitudes have been smoothed once. The relative frequency content of in-phase and out-of-phase motions are dependent upon wave periods and apparent velocities of waves propagating across two stations. For example, for a monochromatic wave train of period T traveling across the stations with an apparent velocity, C_a, two stations would have the same motions if the distance of two stations is sufficiently smaller than or is equal to a multiple of the apparent wavelength, $\lambda_a = C_a T$. As we have indicated in the previous sections that body waves were incident nearly vertically at these stations during the San Fernando earthquake, hence $C_a \approx \infty$ and the in-phase motions would be expected to have been stronger than the out-of-phase motions. However, because the amplitudes of the motions at two stations differ significantly (Fig. 3.4), the amplitudes of the out-of-phase motions are comparable to those of the in-phase motions. For the surface waves traveling across these stations, their periods must be sufficiently long so that the out-of-phase motions are considerably smaller than the in-phase motions. Comparison of the in-phase and out-of-phase spectra in Fig. 3.28 indicates that in dynamic analysis of a 1200 feet span bridge with fundamental period longer than 2 seconds, the assumption that the same motions act simultaneously at two supports would be

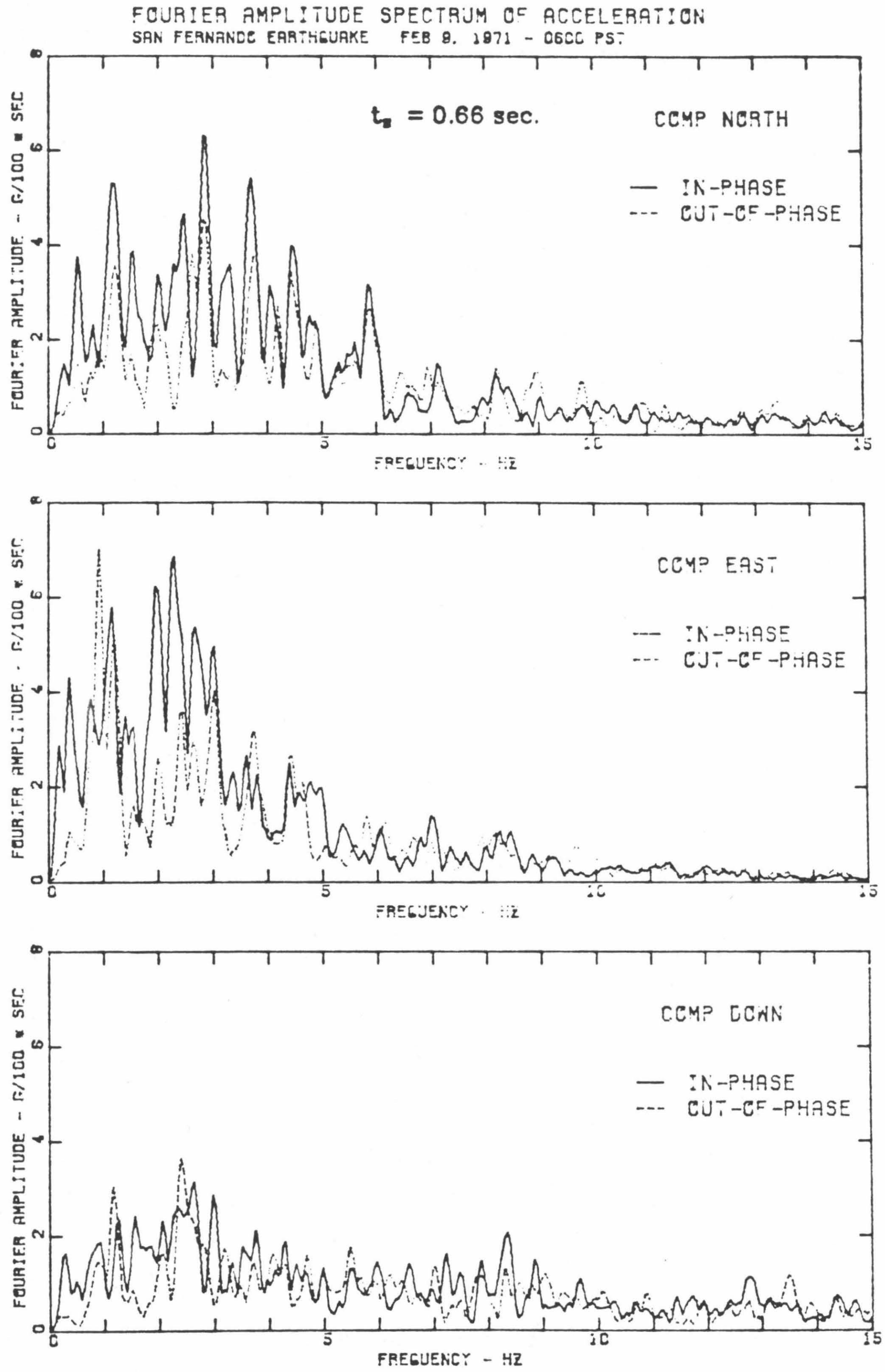

Fig. 3.28 Fourier amplitude spectra of in-phase and out-of-phase components of the motions at Millikan Library and Athenaeum. San Fernando earthquake.

acceptable for the fundamental mode response. On the other hand, the out-of-phase motions are not negligible in the response of higher modes.

3.9 Summary

Accelerograms recorded at four stations in the Pasadena area during the 1971 San Fernando, the 1970 Lytle Creek, the 1968 Borrego Mountain and the 1952 Kern County earthquakes have been studied. The nature of strong ground motions in this area was investigated in both the time and frequency domains. The first shear wave and surface wave arrivals were approximately identified in some of the accelerograms.

The 1971 San Fernando earthquake was recorded at SL, ML, ATH and JPL. Comparisons of the accelerograms obtained from this earthquake have showed the following features: (1) Strongly polarized motions in the east-west direction are observed at SL but are not at ML or ATH. Slightly polarized motions in the S82E direction are observed at JPL. (2) Seismic body waves arrived at ML and ATH stations nearly vertically, while they arrived at SL at some angles other than zero. (3) The shakings at ML, ATH and JPL are not significantly greater than those at SL. (4) Relative to SL, the ground accelerations at ML, ATH and JPL are dominated by longer period waves. (5) The duration of strong shaking in the area was approximately 8 seconds, which is the same as the duration of the slipping process of the fault. (6) The trailing motions at ML and ATH are dominated by relatively long period waves and have larger amplitudes than the trailing motions at SL.

Analysis of the accelerograms obtained from the San Fernando earthquake indicated that the first surface wave arrived at the area approximately 4.5 seconds after the first shear wave. Ground displacements at all stations are dominated by the surface wave of 4- to 5-sec period. A high degree of coherence in the wave forms of ground velocities has been observed at all stations. However, there are differences of the frequency content in the trailing motions between SL and other stations. The variation of the frequency content of the ground motions on the horizontal plane with the orientation of the accelerograph was shown by the maximum and the minimum Fourier amplitude spectra. The total power spectra indicated that the motions at ML, ATH and JPL during the San Fernando earthquake consist mainly of waves with lower frequencies than 3.0 Hz, while the SL motions are dominated by waves with frequencies between 3.5 and 5.5 Hz.

The 1970 Lytle Creek earthquake was recorded at ML and JPL. Most energy of the recorded motions is concentrated at frequencies between 1.7 and 5.0 Hz. The accelerograms obtained at ML, ATH and JPL during the 1968 Borrego Mountain earthquake consist of surface waves whose amplitudes are comparable to shear waves. The motions are dominated by waves having frequencies lower than 2.0 Hz. The 1952 Kern County earthquake was recorded at ATH. The recorded motions consist mainly of long-period waves having frequencies lower than 2.0 Hz. The duration of ground shaking was about 25 to 30 seconds.

The Fourier amplitude spectra for the overall motions as well as for the selected trailing motions recorded during different earthquakes at the same station are compared. The comparison indicates that there are no repeated spectral peaks which can be identified as site periods. Moreover, local geology effects are less evident on the leading parts of the accelerograms than on the trailing parts, and depend on the 3-dimensional configuration of local geology and the direction of arriving seismic waves.

The San Fernando records obtained at ML and ATH on the Caltech campus are compared to investigate their differences. The ATH records are approximately shifted with respect to the ML records. Despite the marked difference in the ground accelerations between ML and ATH, a good degree of similarity in the velocity curves has been observed. The Fourier amplitude spectra for different parts of the accelerograms were compared. In general the ML and ATH spectra agree well up to 2.0 Hz. At frequencies between 2.0 and 6.0 Hz the ML spectra are of larger amplitudes than the ATH spectra. The difference does not seem to be related to different wave arrivals. The inertia soil-structure interaction of the ML building might have occurred in the trailing motions, although no significant soil-structure interaction was observed in the early part of the motions. The difference of the recorded motions at ML and ATH during the 1968 Borrego Mountain earthquake, which is smaller in amplitudes than the difference in the San Fernando earthquake, is attributable to the low-pass filter effects of the larger size of the ATH building foundation.

By approximately adjusting the origin of the ATH records, spatial variations of the ground motions at ML and ATH, which are about 1200 feet apart, during the 1971 San Fernando earthquake have been studied. The Fourier amplitude spectra of the in-phase and the out-of-phase components of the differential motions were obtained. Relative displacements between ML and ATH were also presented.

3.10 References

[1] Bingham, C., Godfrey, M. D., and Tukey, T. W. (1967), "Modern Techniques of Power Spectrum Estimation," *IEEE Transactions on Audio and Electroacoustics*, AU-**15**, pp. 56-66.

[2] Crouse, C. B. and Jennings, P. C. (1975), "Soil-Structure Interactions during the San Fernando Earthquake," *Bulletin of the Seismological Society of America*, Vol. **65**, No.1, 1975, pp. 13-36.

[3] Crouse, C. B. (1976), "Horizontal Ground Motions in Los Angeles during the San Fernando Earthquake," *Earthquake Engineering and Structural Dynamics*, Vol. **4**, 1976, pp. 333-347.

[4] Gutenberg, B. (1956), "Effects of Ground on Earthquake Motion, " *Transactions of American Geophysical Union*, Vol. **37**, No.6, 1956, pp. 757-760.

[5] Gutenberg, B. (1957), "Effects of Ground on Earthquake Motion, " *Bulletin of the Seismological Society of America*, Vol. **47**, No.3, 1957, pp. 221-250.

[6] Hanks, T. C. (1975), "Strong Ground Motion of the San Fernando, California Earthquake: Ground Displacements," *Bulletin of the Seismological Society of America*, Vol. **65**, No.1, 1975, pp. 193-225.

[7] Huang, M. J. (1982), "On the Characteristics of 3-Dimensional Earthquake Ground Motion," *Proceedings of the 3rd International Earthquake Microzonation Conference*, Seattle, June 28 - July 1, 1982, pp. 435-446.

[8] Hudson, D. E. and Housner, G. W. (1958), "Analysis of Strong-Motion Accelerometer Data from the San Francisco Earthquake of March 22, 1957," *Bulletin of the Seismological Society of America*, Vol. **48**, No. 3, 1958, pp.253-268.

[9] Hudson, D. E. (1971), "Strong-Motion Instrumental Data on the San Fernando Earthquake of February 9, 1971," D. E. Hudson, editor, Earthquake Engineering Research Laboratory and Seismological Field Survey, September, 1971.

[10] Hudson, D. E. (1972), "Local Distribution of Strong Earthquake Ground Motion," *Bulletin of the Seismological Society of America*, Vol. **62**, No.6, December 1972, pp. 1765-1786.

[11] Kanamori, H and Jennings, P. C. (1978), "Determination of Local Magnitude, M_L, from Strong Motion Accelerograms," *Bulletin of the Seismological Society of America*, Vol. **68**, No.2, 1978, pp. 471-485.

[12] McVerry, G. H. (1979), "Frequency Domain Identification of Structural Models from Earthquake Records," Report No. *EERL* 79-2, October, 1979, California Institute of Technology, Pasadena, California.

[13] Trifunac, D. M. and Udwadia, F. E. (1974), "Variations of Strong Earthquake Ground Shaking in the Los Angeles Area," *Bulletin of the Seismological Society of America*, Vol. **64**, No.5, 1974, pp. 1429-1454.

[14] Udwadia, F. E. and Trifunac, D. M. (1973), "Comparison of Earthquake and Microtremor Ground Motions in El Centro, California," *Bulletin of the Seismological Society of America*, Vol. **63**, No.4, 1973, pp. 1227-1253.

[15] USGS and EERL (1968), "Strong-Motion Instrumental Data on the Borrego Mountain Earthquake of 9 April, 1968," Joint Report by the Seismological Field Survey, Environmental Science Services Administration, U. S. Dept. of Commerce, and the Earthquake Engineering Research Laboratory, California Institute of Technology, August, 1968.

CHAPTER 4

STUDY OF LOCAL GEOLOGY EFFECTS ON THE STRONG GROUND MOTIONS IN THE PASADENA AREA

4.1 Introduction

The accelerogram recorded by an accelerograph is the result of many complex processes which transfer seismic energy from the earthquake source to the recording instrument. As the earthquake fault ruptures over a finite area of the fault, seismic waves are radiated from different points on the fault. Before the seismic waves arrive at the station, the energy is absorbed by anelastic wave propagation and scattered by random heterogeneities along the travel path. Finally, the local geology underlying the station and the instrument modify the signal further. Each process, as a first approximation, can be represented by a linear filter. The recorded signal can then be viewed as the convolution of each filter. In other words, regarding the earthquake source as the input, the effect of each process can then be represented by a transfer function and the recorded signal is the output. If we denote the Fourier transform of an earthquake source as I(f), the effect of travel path as T(f), the effect of local geology as S(f) and the instrument response function as R(f), the Fourier transform of the recorded ground motions, F(f), is then given by

$$F(f) = R(f)\, S(f)\, T(f)\, I(f) \tag{4.1}$$

where f is the frequency.

To derive the transfer function S(f) for the local geology, it is necessary to choose an idealized model for the subsoil profile and assume the type of incident wave. For a subsoil profile in which the material properties do not vary significantly in the horizontal direction and the effect of the curvature of layer boundaries can be neglected, a semi-infinite layered system consisting of horizontally stratified layers overlying a homogeneous half-space is the simplest and most widely used model. The bedrock underlying an alluvium site is modeled by the half-space. Surface waves are usually not considered in the study of local geology effect because of the difficulty in considering the irregular boundary between the alluvium and the bedrock. We then make a simplifying assumption that the curvature of the spherical wavefronts is small for body waves whose wavelengths are much smaller than the distance traveled and consider the propagating body waves to be plane waves. The transfer function is derived by finding the steady state response of the layered system to incident plane harmonic body waves from the bedrock. The incident body waves can be P, SV or SH waves, and the incident angle at the half-space can be nonzero. The analytical methods and numerical examples for deriving the transfer function have been given in Chapter 2. The transfer function representing the effect of the layered system is defined as the ratio of the Fourier transform of the response at the free-surface divided by that at the bedrock, or divided by that at the bedrock outcrop if there were no superficial layers on the top.

The effect of local geology on recorded ground motions can be examined by considering the ratio of the Fourier amplitude spectrum of ground motions recorded at an alluvium site to that from the same source recorded at a nearby surface rock site, provided that both sites are in the same azimuthal direction and have nearly equal epicentral distances. This ratio, denoted by $E(f)$, is given by $E(f) = |F_a(f)| / |F_r(f)|$ where the subscripts a and r indicate the alluvium and rock sites, respectively, and $|\ |$ represents the Fourier amplitude. We shall call it the observed amplitude ratio or the observed site transfer function. The observed site transfer functions from nuclear explosion data have been used to empirically evaluate local geology effects (e.g., Borcherdt, 1970; and Rogers & Hays, 1978).

Since the downhole records at the bedrock are usually not available, The suggestion has been made to evaluate local geology effects by assuming that the earthquake motions at a nearby surface rock site are the same as the motions that would have been recorded at the surface of the bedrock if there were no soils on the top. The motions at the rock site are taken as input to the subsoil profile for a local site, the response at the free surface is then computed from the transfer function between the free surface and the half-space outcrop of an analytical model (e.g., Schnabel *et al.*, 1972; and Joyner *et al.*, 1981). The computed time history response can then be used to compute response spectra. If downhole records are available, they can be the input to the subsoil profile (Tsai & Housner, 1970; Joyner *et al.*, 1976; and Johnson & Silva, 1981).

During the 1971 San Fernando earthquake, strong motion records were obtained at the Seismological Laboratory (SL, rock site), the Millikan Library and the Athenaeum (ML and ATH, alluvium sites) of the California Institute of Technology. In Section 4.3, the observed site transfer functions are computed for the overall motions and for the trailing motions. The features of observed site transfer functions are discussed.

The approximate subsoil conditions underlying the Caltech campus are available. These data provide an opportunity to test the adequacy of the assumptions described above and the analytical models given in Chapter 2. In Section 4.4, we assess how much of the local geology effects can be evaluated by analytical methods, having available geotechnical data, by comparing the observed amplitude ratios between ML, ATH and SL with the computed amplitude ratios from the subsoil profile. To investigate how well a simple model predicts the observations, a systematic frequency domain identification technique is employed to find the optimal model parameters which produce a least-squares match between the observed amplitude ratios and the theoretical results from the model.

4.2 The Site and the Data from the 1971 San Fernando Earthquake

In Chapter 3, we have described the local geology in the Pasadena area and analyzed the strong motion accelerograms recorded during the 1971 San Fernando earthquake. The local subsoil conditions underlying the Caltech campus were investigated by Shannon & Wilson, Inc. (SW-AA, 1978). The boring, which extended to a depth of 400 feet below the ground surface, was drilled in 1975 at a location about 200 feet southwest of the Millikan Library. The shear wave velocities at low levels of strain were measured by using the downhole method. The alluvium consists primarily of medium to very dense, silty sands with the water table standing about 240 feet below the surface (SW-AA, 1978). The P-wave and S-wave velocities of the subsoil profile are shown schematically in Fig. 4.1. The in situ shear wave velocities of the subsoil to a depth of 400 feet below the ground surface are adopted from the report by Shannon & Wilson, Inc. and Agbabian Associates (SW-AA, 1978, 1980). Other wave velocities of the 900 feet subsoil profile are estimated and indicated by the dashed lines in Fig. 4.1. The Seismological Laboratory, which is about 3 miles from the Caltech campus, is underlain by granitic basement rock.

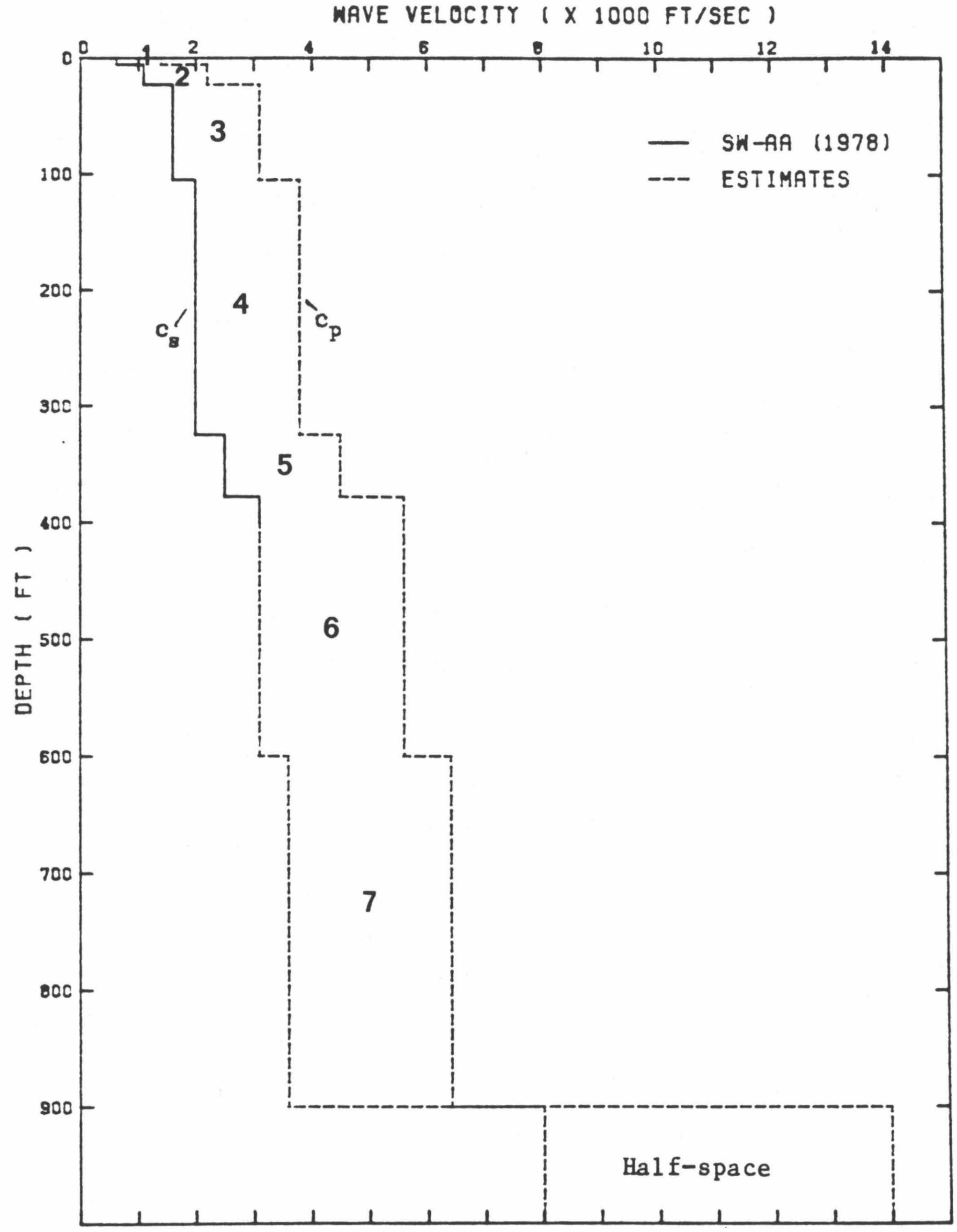

Fig. 4.1 P and S wave velocities of the subsoil profile underlying the Caltech campus. The solid lines are adopted from the report by SW-AA(1978), while the dashed lines are estimated.

4.3 Observed Site Transfer Functions

4.3.1 The First 20.48-sec Portion of the Accelerogram

The Fourier amplitude spectra of selected 20.48-sec portions of the accelerograms recorded at the Seismological Laboratory(SL), the Millikan Library(ML) and the Athenaeum(ATH) were calculated. For each station, the Fourier amplitude spectra for the transverse and radial components as well as for the three recording components were computed. The truncated acceleration data were tapered at the leading and trailing 10% ends. Each Fourier amplitude spectrum was smoothed by passing the corresponding power spectrum by the Hanning window (¼, ½, ¼ weights) two times. The observed site transfer functions between ML (or ATH) and SL in corresponding directions were then obtained by dividing the twice-smoothed ML (or ATH) Fourier amplitude spectra by the twice-smoothed SL amplitude spectra. The ratios are then smoothed twice with the Hanning window. The results are shown in Figs. 4.2a, b and c for the north, east and vertical components, respectively, and shown in Figs. 4.3a and b for the transverse and radial components, respectively. The accelerograms as well as the twice-smoothed Fourier amplitude spectra and the twice-smoothed amplitude ratios are shown in these figures.

Based on the analysis in Chapter 3, the ML and ATH accelerograms have been aligned so that they have approximately the same time origin. The SL accelerograms were also aligned approximately with the ML and ATH accelerograms. The shift of the accelerogram in the time axis does not affect the values of Fourier amplitudes. To facilitate comparison, the observed amplitude ratios between ATH and SL are plotted on the same diagram as those between ML and SL. It should be noted that the peak amplitude ratios at the low and the high frequency ends corresponding to small amplitudes in the SL spectra are

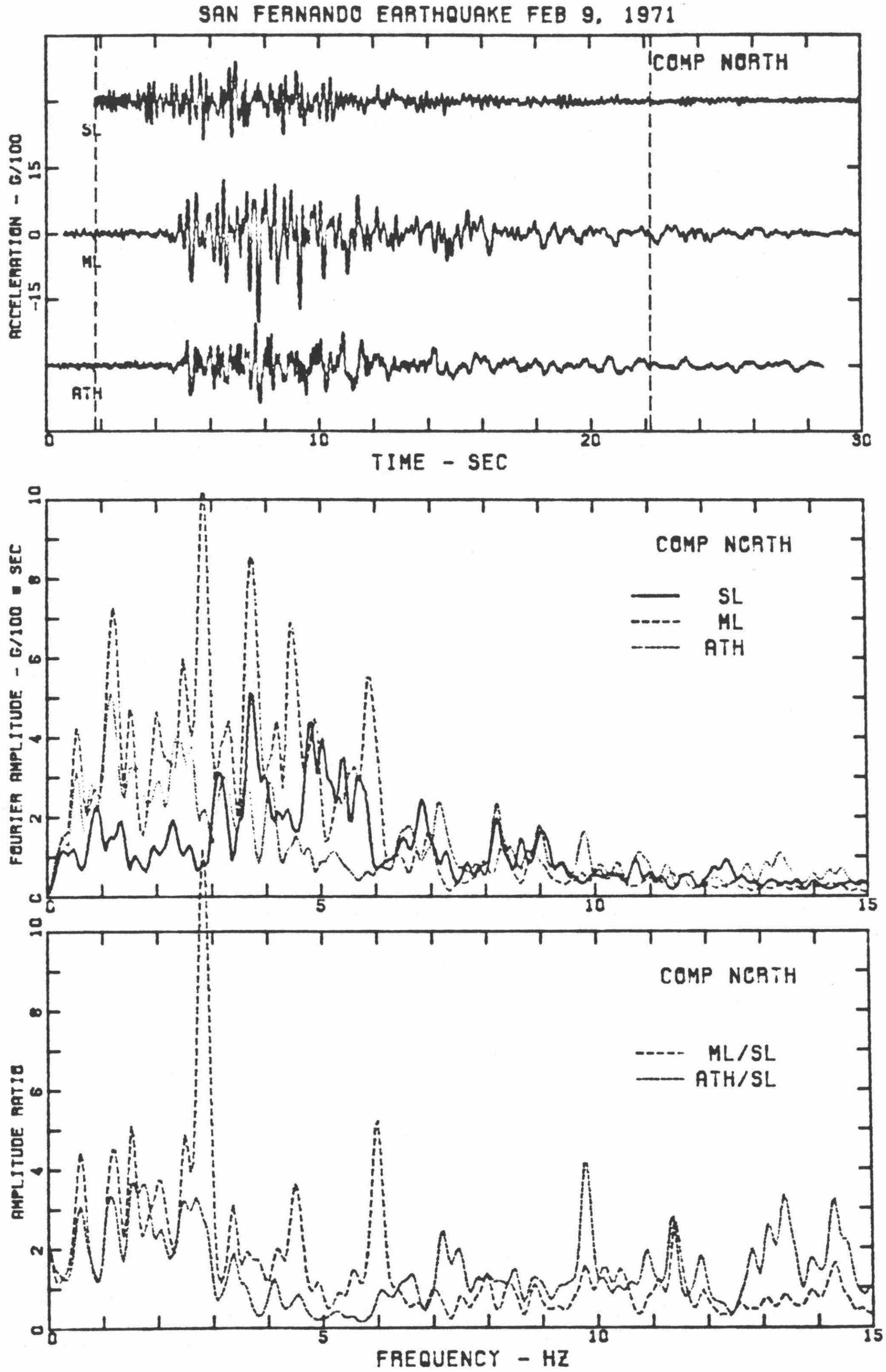

Fig. 4.2a Accelerograms, Fourier amplitude spectra and Observed amplitude ratios for ML, ATH and SL - north component, San Fernando earthquake. Dashed lines indicate the data from which the Fourier transforms are computed.

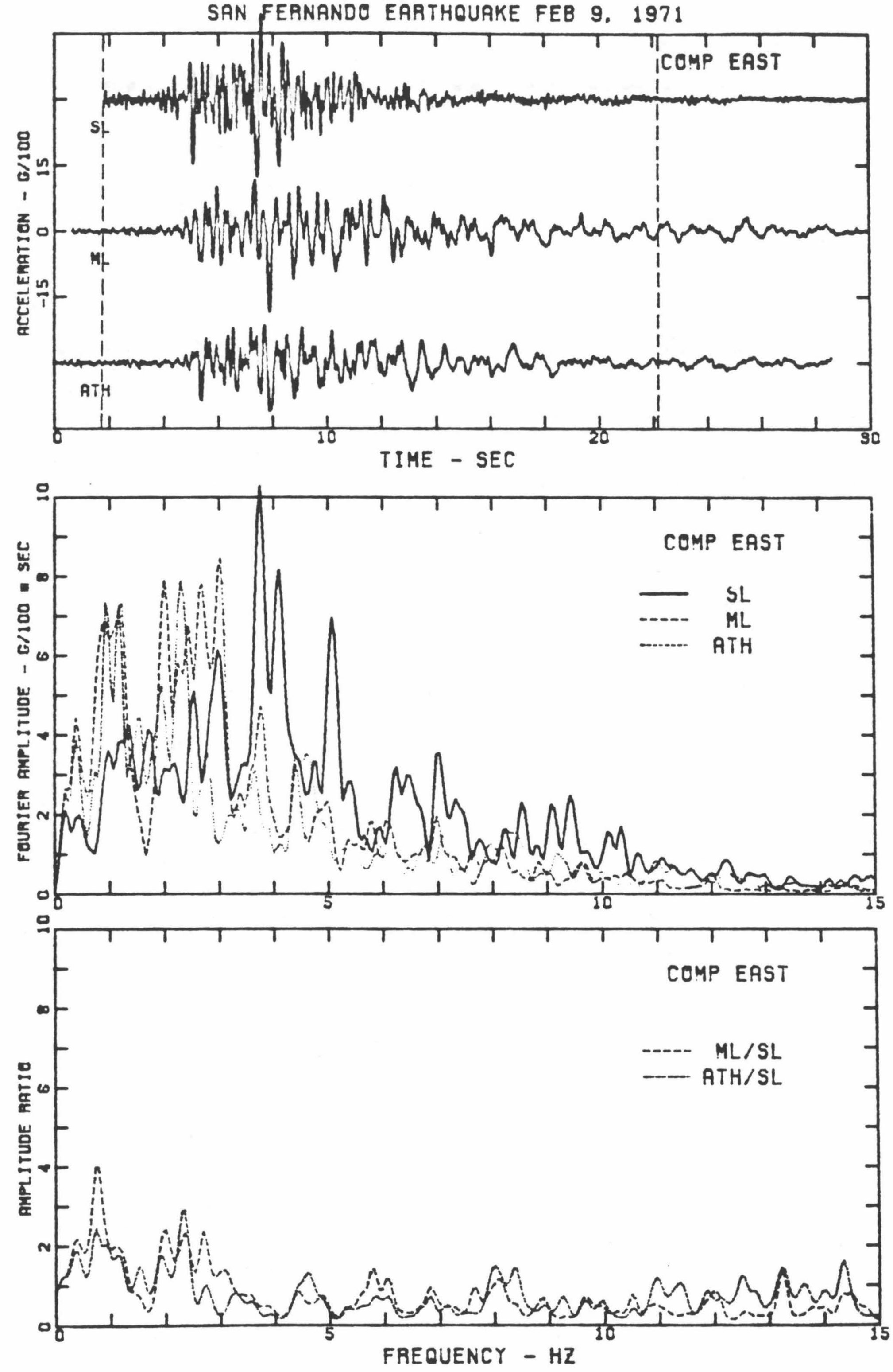

Fig. 4.2b Similar to Fig. 4.2a for the east component.

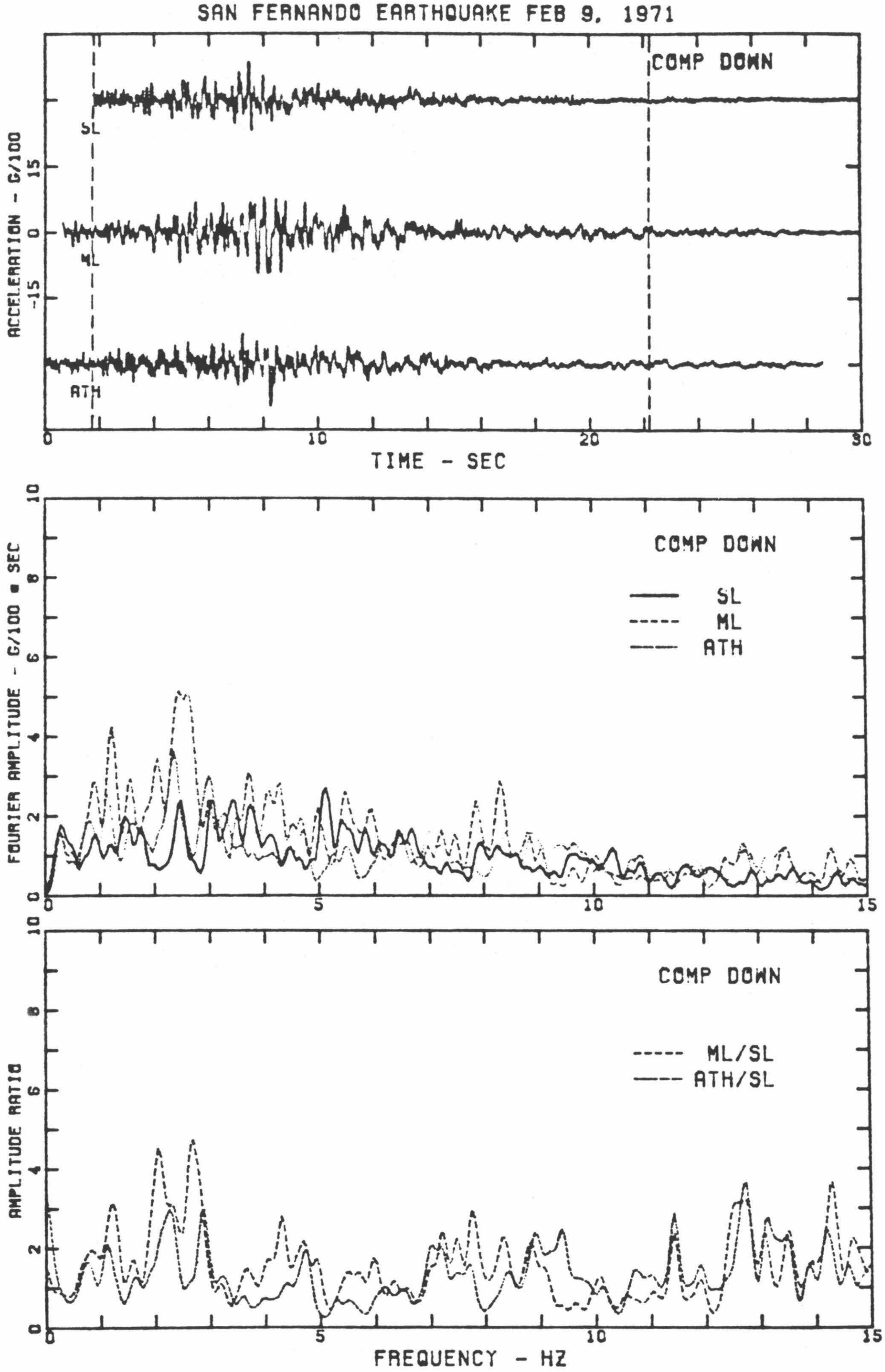

Fig. 4.2c Similar to Fig. 4.2a for the vertical component.

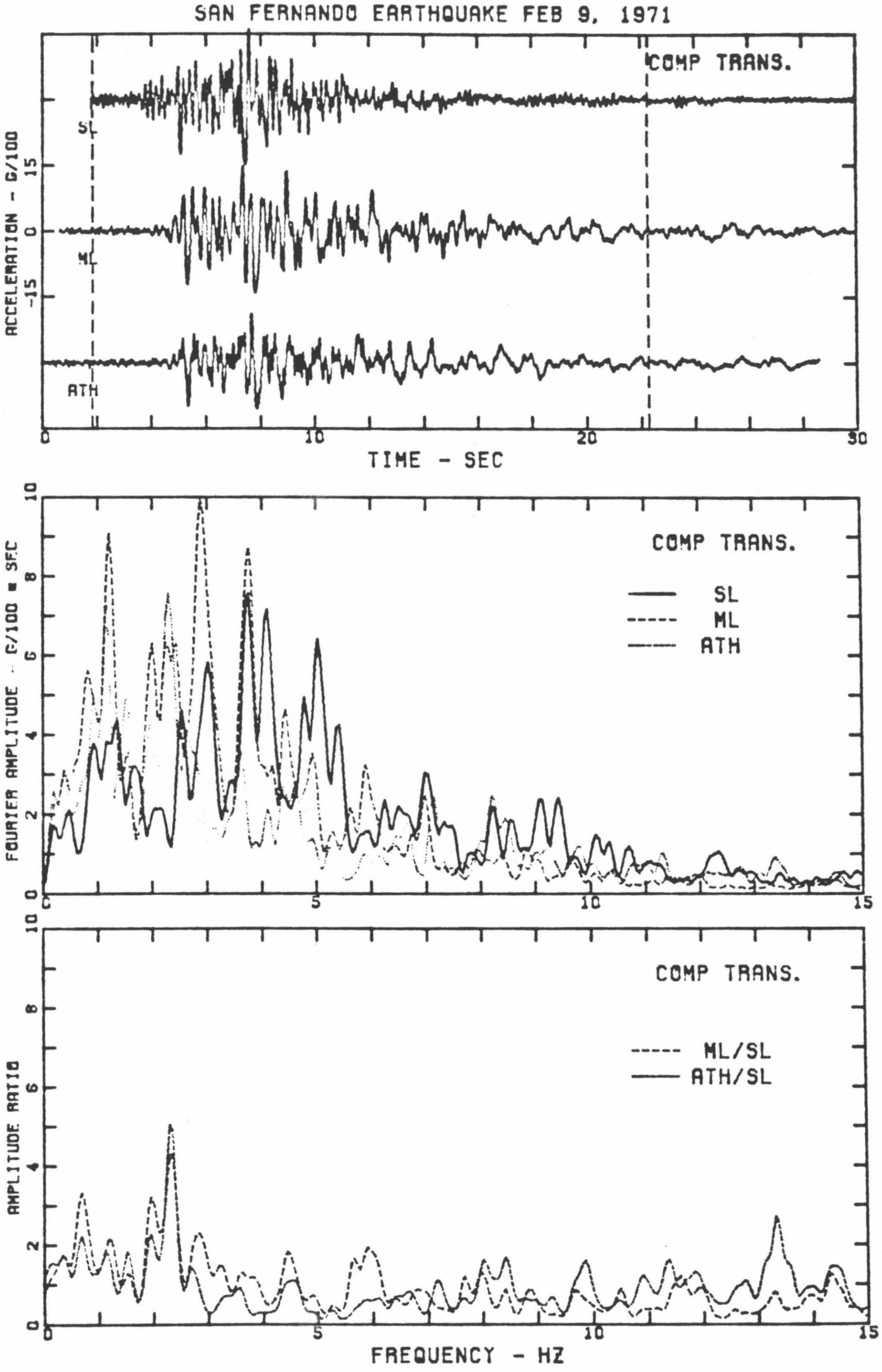

Fig. 4.3a Similar to Fig. 4.2a for the transverse component.

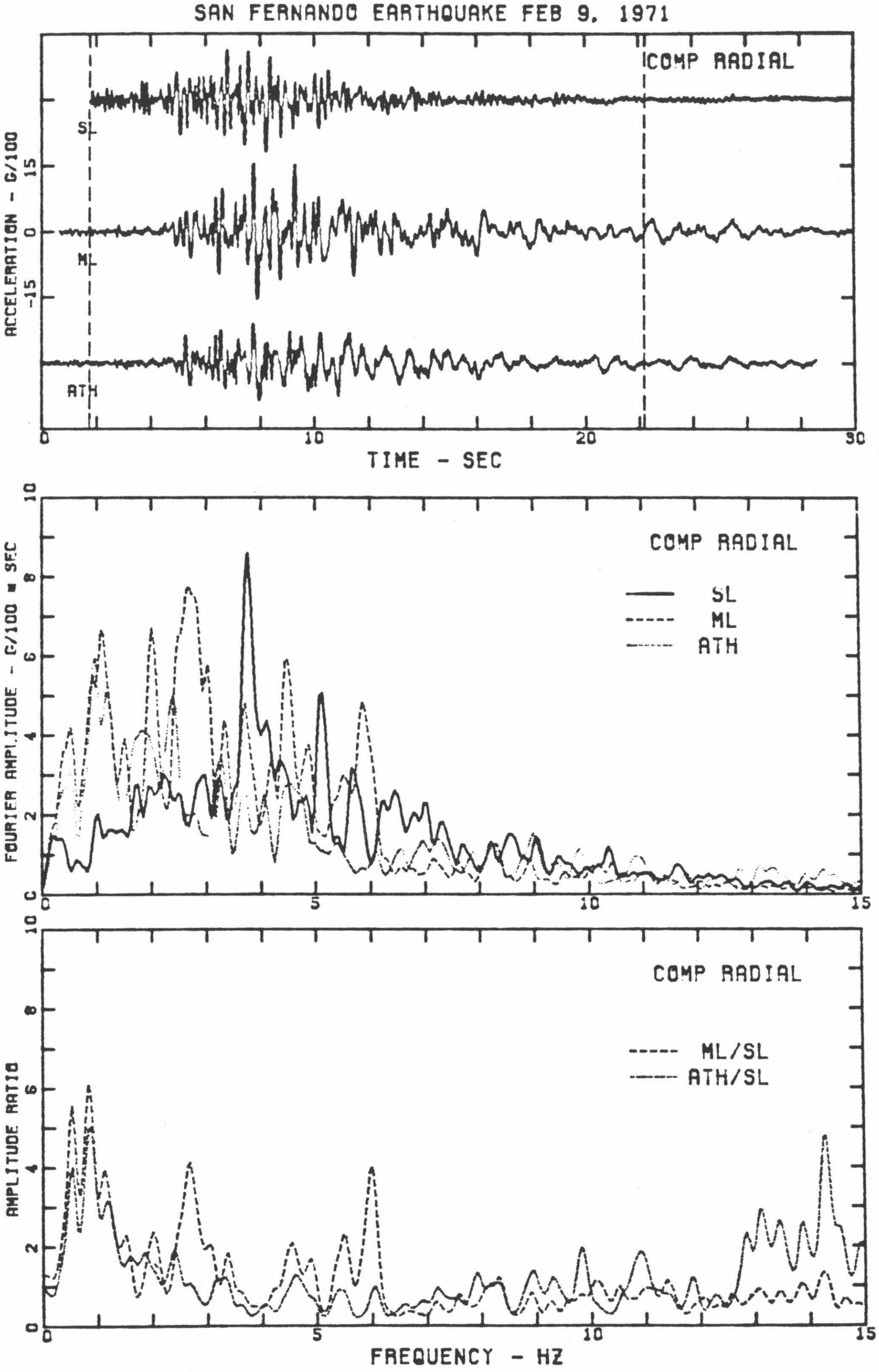

Fig. 4.3b Similar to Fig. 4.2a for the radial component.

insignificant. The dashed lines in the top plot indicate the portion of the accelerogram from which the Fourier transfrom was computed. According to the analysis in Chapter 3, this portion of the accelerogram consists of P, S and surface waves.

There are several significant features of the observed site transfer functions in these figures:

(1) The observed amplitude ratios between ATH and SL are different from those between ML and SL. This is because of the dissimilarity in the accelerograms recorded at ML and ATH, which has been discussed in more detail in Section 3.3.4. The locations of the peak amplitude ratios differ significantly at frequencies higher than 2.5 Hz, especially in the north and radial components. However, for frequencies lower than 2.5 Hz the peaks in two observed amplitude ratio spectra are located at the same frequency, although their amplitudes are not exactly equal. It is unlikely that the subsoil profile underlying ML and ATH could differ significantly enough to cause the difference of the ground motions at these two stations.

(2) At the frequency where the dominant peak amplitude ratio occurs, the Fourier amplitudes are not necessarily predominant in the ML and ATH spectra. For example, in the east component of the observed amplitude ratios between ML and SL (Fig. 4.2b) the dominant peak is located at 0.76 Hz whereas the Fourier amplitude in ML spectra at this frequency is not prominent. This is different from the dynamic response of a building where the spectrum of roof motions shows prominent peaks at the first few modal frequencies of building vibration. To illustrate this, Fig. 4.4 gives an example of the dynamic response of a nine-story steel frame building at the Jet Propulsion Laboratory(JPL) in Pasadena during the 1971 San Fernando earthquake.

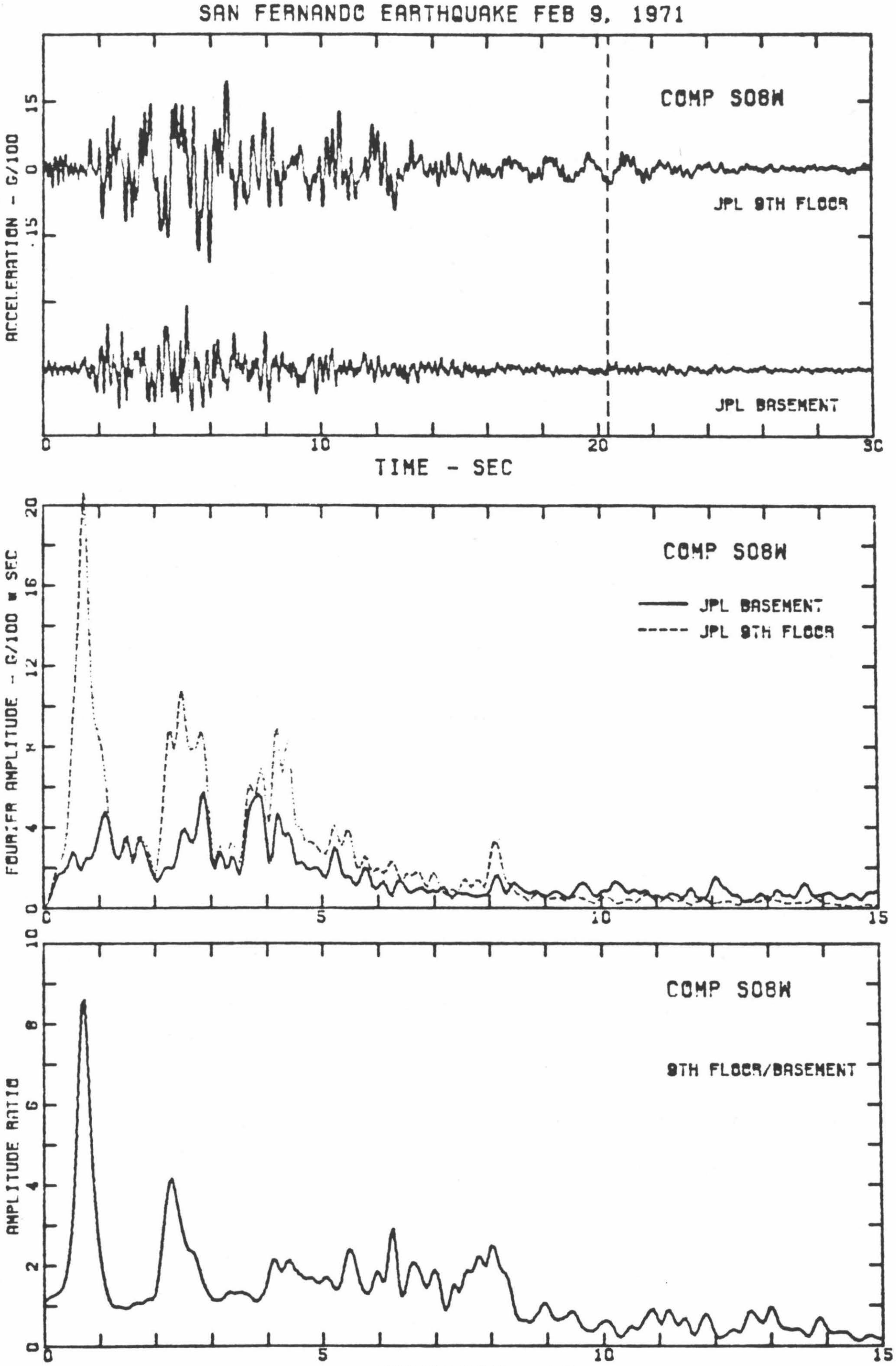

Fig. 4.4 Accelerograms recorded at the basement and the 9th floor of JPL building - S08W component. Fourier amplitude spectra and the amplitude ratios between the 9th floor and the basement. Fourier transforms are computed from the data between 0.0-sec and the dashed line.

Data reduction for the accelerograms in this figure was identical to the process for Figs. 4.2 and 4.3. As shown in Fig. 4.4, the amplitude spectrum of roof motions shows prominent peaks at the first and second modal frequencies, and the amplitude ratios at low frequencies are much smoother than those in Figs. 4.2 and 4.3. It has been demonstrated that the earthquake response of this building can be modelled by considering shear beam type motions. If the soil column had vibrated in the same way as the building, the amplitude spectrum of the surface motions would have prominent peaks at the modal frequencies of the shear vibration of soil column. However, the observations here do not indicate this, so a simplified model of vertically propagating shear waves will not predict the behavior of local subsoils as well as it does for the building. This is to be expected from the fact that the earthquake motions of such a building are vertically traveling shear waves, whereas the motions of the soil column are not all from vertically traveling waves.

(3) The transfer functions are quite different in different directions, whereas a simplified model of vertically propagating shear waves predicts no difference between the transfer functions of individual components in the horizontal directions. It does not appear that these differences are predictable by the 2-dimensional model of considering inclined incident SH, P and SV waves. In Chapter 3, we have seen that strongly polarized motions were observed in the east-west direction at SL but were not at ML or ATH. The change of seismic wave ray paths resulting from the irregular 3-dimensional local geology in the area might have caused this. On the other hand, the data might have indicated the inadequacy of the assumption that the SL motions represent the underlying bedrock outcrop motions beneath the ML and ATH. To use the recorded data at an alluvium site and a nearby rock site to empirically

characterize the local geology effect, a more realistic empirical site transfer function, which is independent of recording axis, is desirable. In what follows we shall define and examine a direction-independent observed site transfer function.

Let $|F_x(f)|$ and $|F_y(f)|$ be the Fourier amplitude spectra for two perpendicular recording horizontal axes, x- and y-axes, at a station, we note that the total power of the horizontal components, i.e.,

$$|F_x(f)|^2 + |F_y(f)|^2 = \text{constant}(f) \tag{4.2}$$

is an invariant quantity of the orientation of recording axes. For more details on this, see Huang (1982). We may define an average Fourier amplitude as

$$|F(f)| = \sqrt{(|F_x(f)|^2 + |F_y(f)|^2)/2} \tag{4.3}$$

to represent the Fourier amplitude spectra in all the horizontal directions. Obviously, it is not the same as the arithmetic average of $|F_x(f)|$ and $|F_y(f)|$. The observed amplitude ratios can then be defined by

$$E_a(f) = \frac{|F(f)|_{ML}}{|F(f)|_{SL}} \quad \text{or} \quad = \frac{|F(f)|_{ATH}}{|F(f)|_{SL}} \tag{4.4}$$

where the subscripts ML, ATH and SL indicate the Millikan Library, the Athenaeum and the Seismological Laboratory, respectively. $E_a(f)$ can be interpreted as the square root of the ratio of the total power spectrum of ML or ATH divided by the total power spectrum of SL, and is a function of frequency. It is called the average observed amplitude ratio in this report. Fig. 4.5 gives the average Fourier amplitude spectra for ML, ATH and SL, and the average observed amplitude ratios. The amplitude ratios are all smaller than 4.0.

4.3.2 The Trailing Part of the Accelerogram

As analyzed in Chapter 3, significant differences of ground motions between

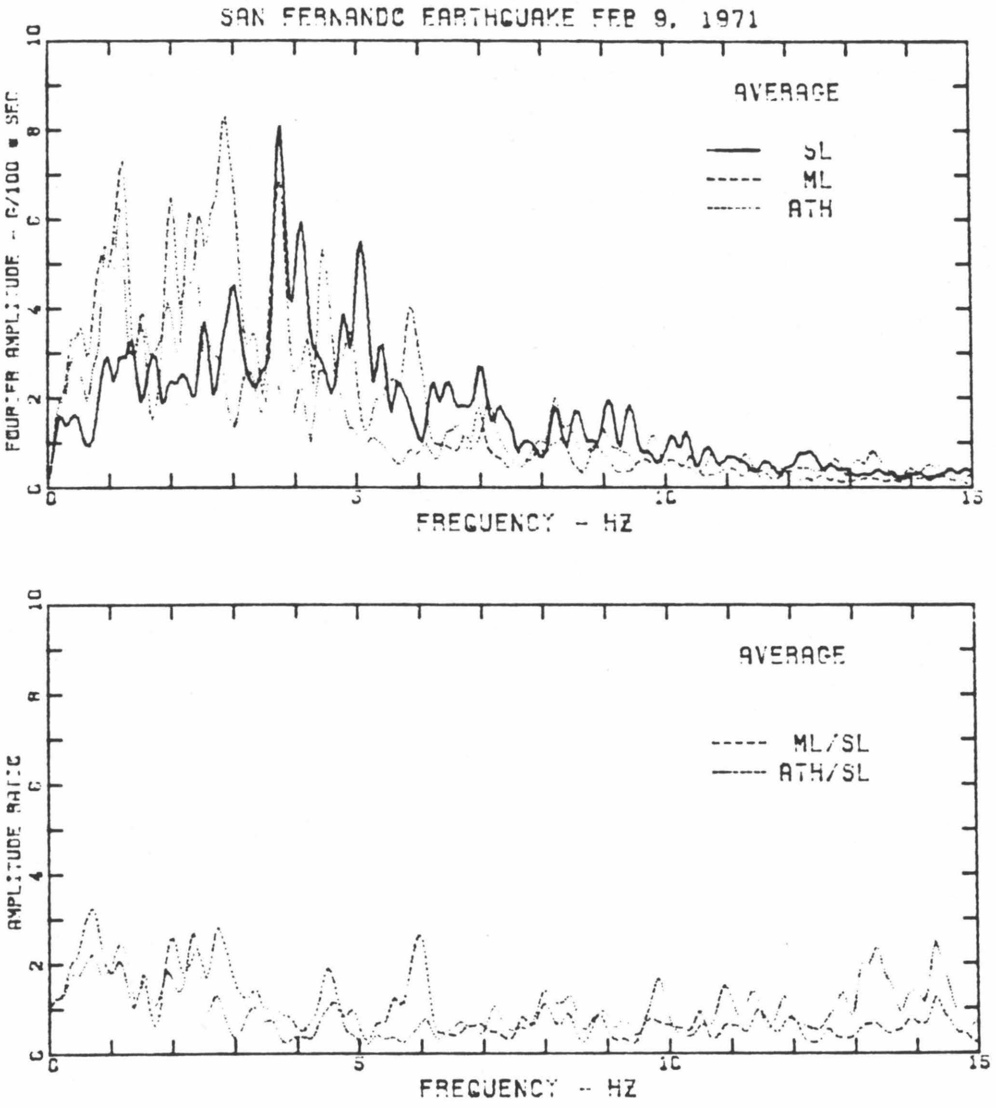

Fig. 4.5 Average Fourier amplitude spectra for ML, ATH and SL, and average observed amplitude ratios between ML, ATH and SL.

ML, ATH and SL have been observed in the trailing parts of the accelerograms. Some long-period waves are dominant in the ML and ATH trailing motions but not in the SL record. Although the trailing motions were smaller than the preceding strong motions, as a result of these motions the duration of the ground shakings at ML and ATH was longer than that at SL.

To investigate local geology effects on the trailing motions, the accelerogram was truncated by a 10.24-sec window at a selected trailing part. The truncated data were tapered and the corresponding Fourier transforms were computed. The observed amplitude ratios were then obtained by dividing the once-smoothed Fourier amplitudes at ML and ATH by those at SL. The accelerograms, once-smoothed Fourier amplitude spectra and once-smoothed amplitude ratios are shown in Figs. 4.6a, b and c for the north, east and vertical components, respectively. The dashed lines indicate the truncated data. It is clear from the Fourier amplitude spectra in these figures that most energy of the trailing motions at ML and ATH is concentrated at frequencies lower than 2.0 Hz. On the other hand, the SL amplitude spectra, showing the humps near 0.30 Hz and 5.0 Hz, are almost flat at frequencies lower than 2.0 Hz. Consequently, large amplitude ratios occur mainly at frequencies between 0.5 Hz and 2.0 Hz. As compared to the results in Figs. 4.2 and 4.3, the amplitude ratios for the trailing motions are larger than those for overall motions.

It should be noted that the amplitude ratios corresponding to small Fourier amplitudes near 0.0 Hz and at the high frequency end are ignored. The peaks in the Fourier amplitude spectra or the observed amplitude ratio spectra near 1.6 Hz in the north component and near 1.0 Hz in the east component are larger at ML than at ATH. The fundamental frequencies of the ML building vibrations during the earthquake in the NS and EW directions were about 1.6 Hz and 1.0 Hz (McVerry, 1979), respectively, thus inertia soil-structure interactions might have

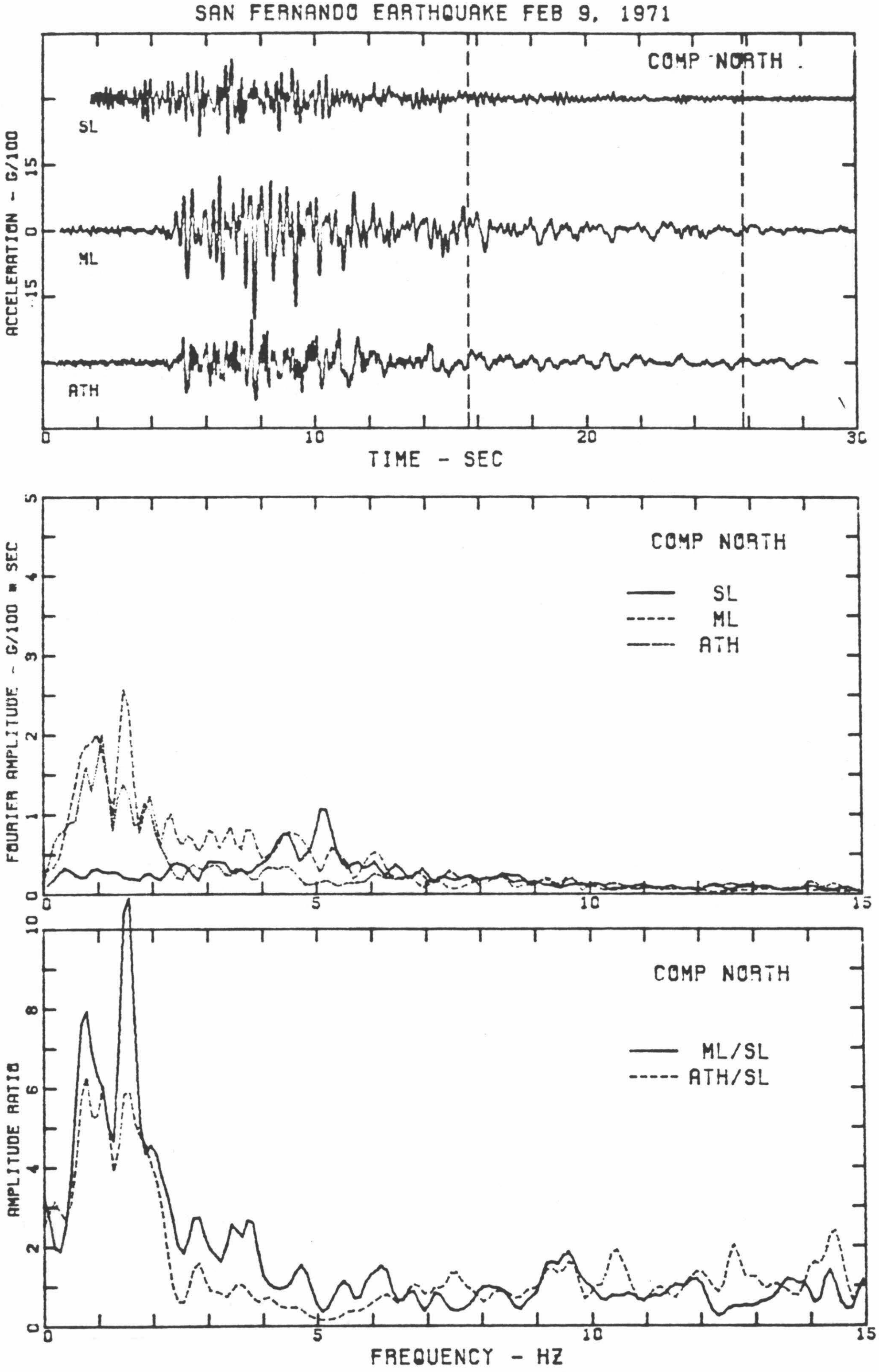

Fig. 4.6a Fourier amplitude spectra and Observed amplitude ratios for the trailing motions at ML, ATH and SL - north component. Dashed lines indicate the selected trailing accelerations from which the Fourier transforms are computed.

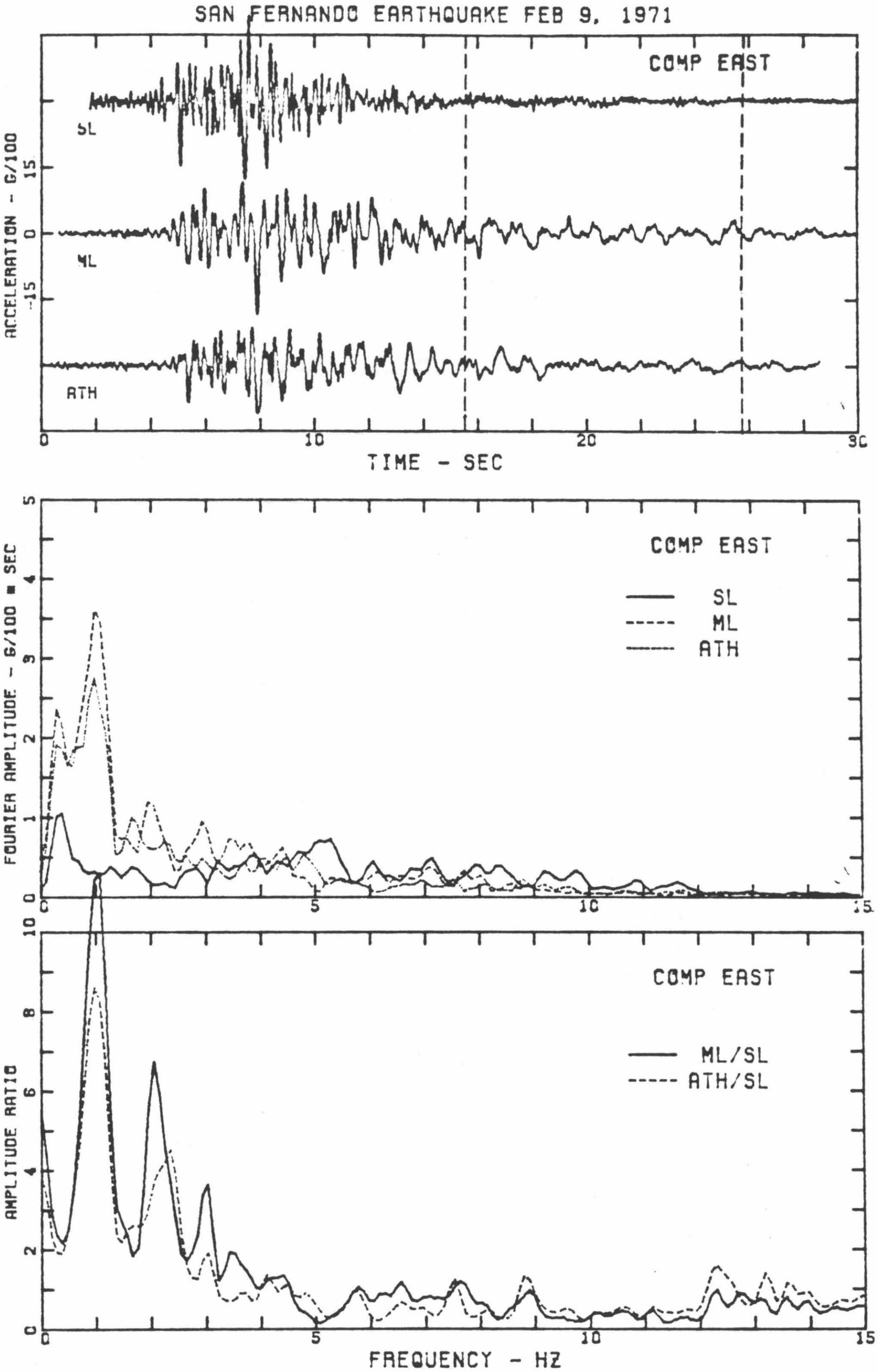

Fig. 4.6b Similar to Fig. 4.6a for the east component.

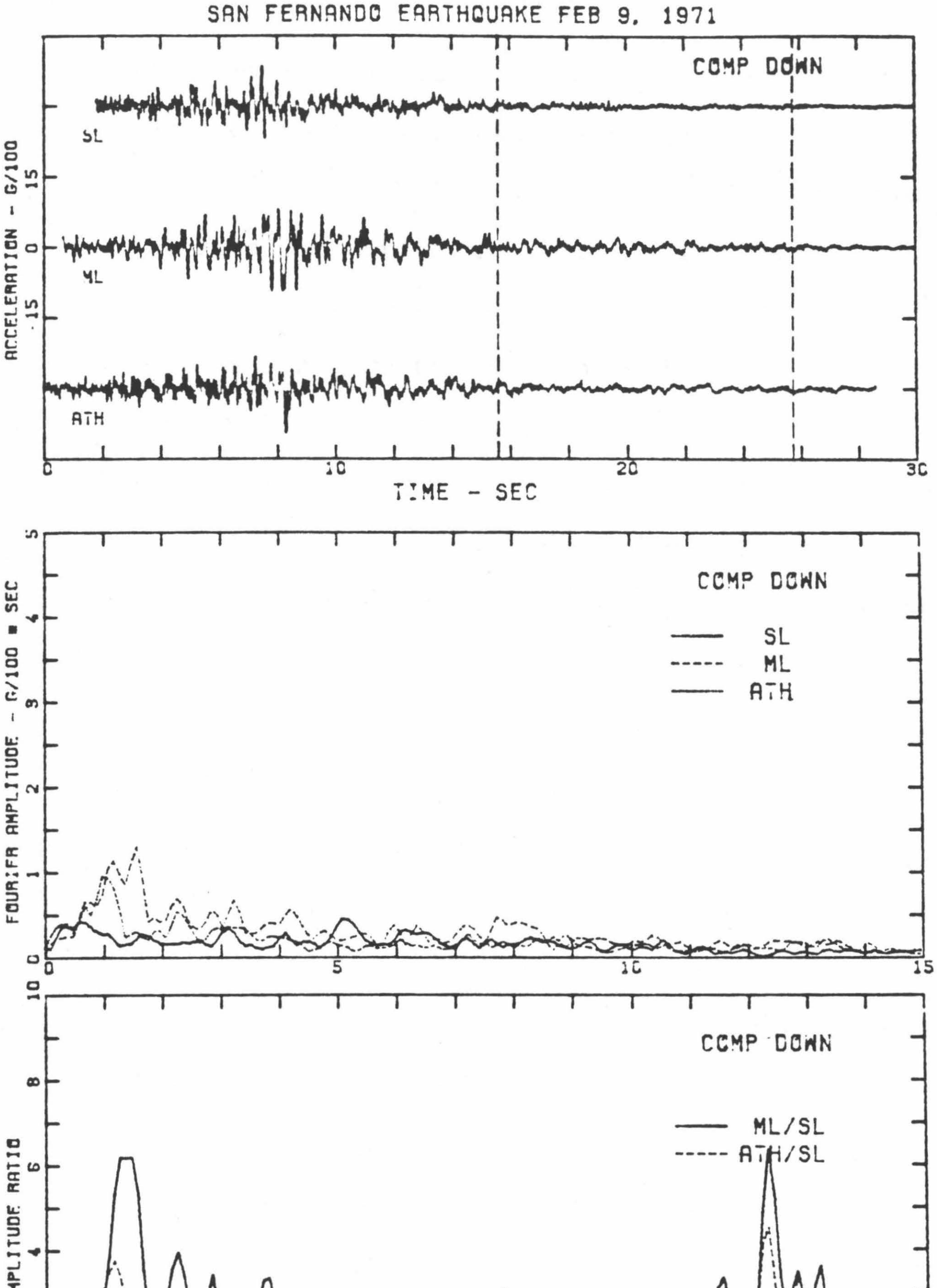

Fig. 4.6c Similar to Fig. 4.6a for the vertical component.

contributed to the trailing motions of ML basement.

Since the trailing motions at the ML and ATH consist of relatively long period waves, it is of practical interest to understand their origins and their influences on long-period structures. Fig. 4.7 shows the east component accelerograms obtained in the basement and the 10th floor of the Millikan Library during the 1971 San Fernando earthquake. The east-west fundamental period increased from 0.69-sec to 1.0-sec during the first ten seconds of the response, with the structure responding at this period during the remainder of the strong motion (McVerry, 1979). The dominant period of the trailing motions at the ML basement was 1.0-sec (Fig. 4.6b), which coincided with the the fundamental period of the building response. As a result, the building experienced essentially fundamental mode vibrations between 17 and 30 seconds.

Figs. 4.8a and b show the results for the transverse and radial components. The observed amplitude ratios are different in different directions. The amplifications of weak rock motions in the trailing part by the local geology do not appear to be associated with the late arriving body waves from the bedrock. If late arriving body waves had been strongly amplified at frequencies between 0.5 Hz and 2.0 Hz, the early arriving body waves would have also been strongly amplified. However, the amplifications of early arriving body waves were relatively small. Furthermore, the observed amplitude ratios of the trailing motions decay rapidly as frequency increases. As demonstrated by the numerical examples in Section 2.4, the amplifications of body waves in a multilayered system are not much higher at low frequencies than at high frequencies.

The difference in the trailing motions at ML, ATH and SL may be associated with local geology effects on the surface wave propagations. As surface waves propagate horizontally across the valley, complex wave scatterings along the

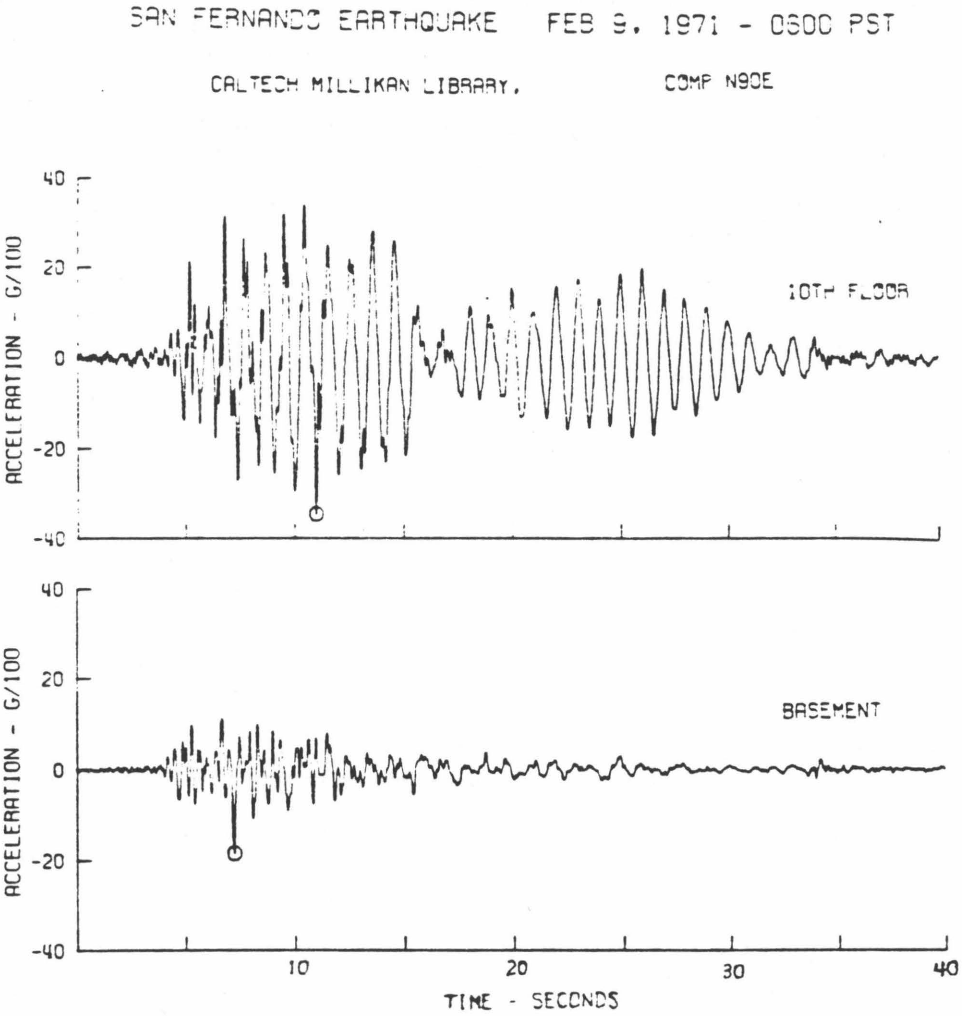

Fig. 4.7 Recorded accelerograms in the basement and the 10th floor of Millikan Library during the San Fernando earthquake - east component.

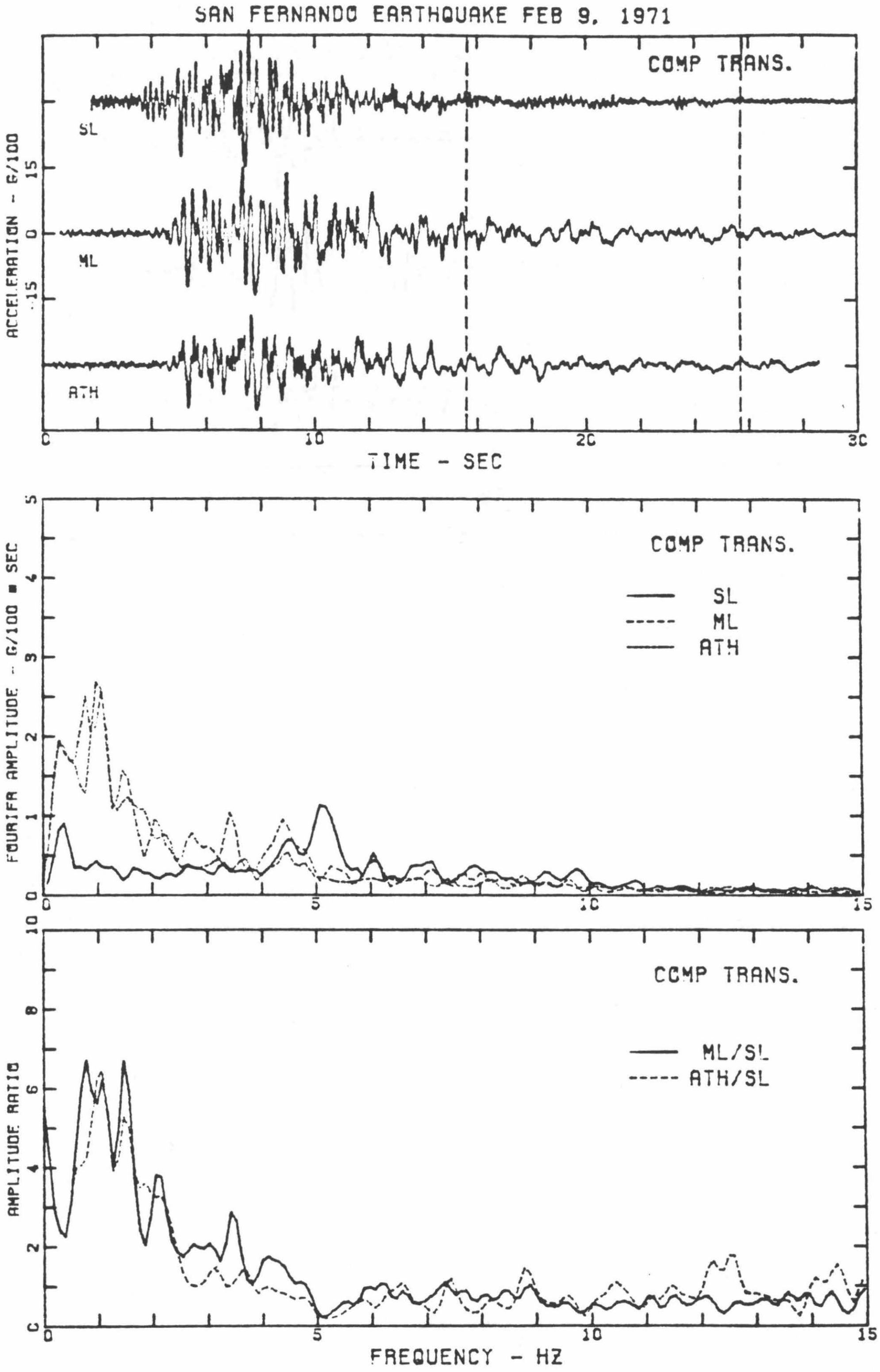

Fig. 4.8a Similar to Fig. 4.6a for the transverse component.

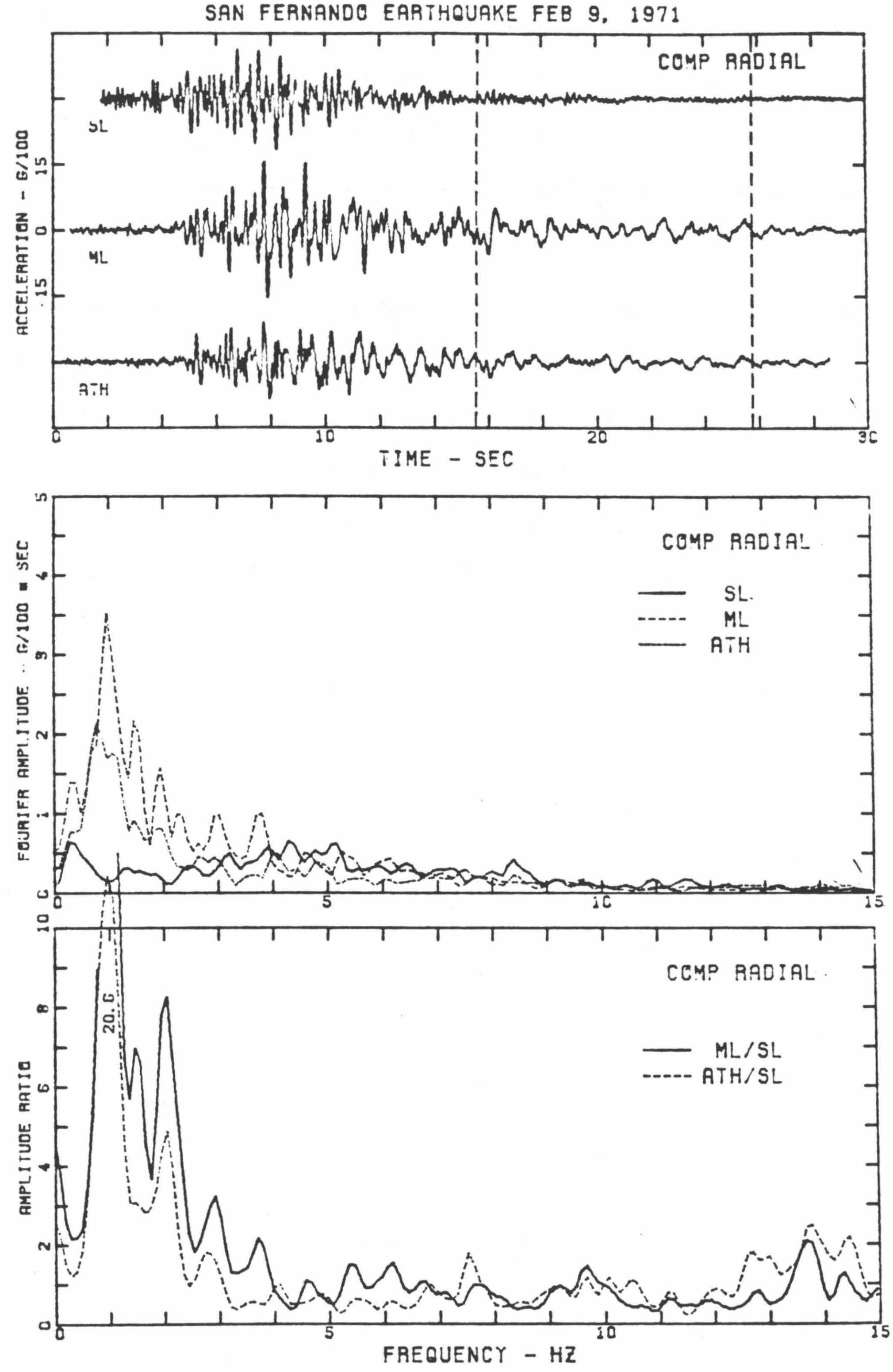

Fig. 4.8b Similar to Fig. 4.6a for the radial component.

nonhorizontal boundary between the bedrock and the alluvium will have occurred. Part of the energy of incident surface waves is scattered into body waves which are trapped inside the alluvial valley and propagate in surface-wave modes. Converted body waves resulting from the scattering of incident surface waves as well as transmitted surface waves might have contributed to the trailing motions at ML and ATH.

In Chapter 3, we presented the particle displacement trajectories for ML, ATH and SL on the plane consisting of the radial and vertical directions and noted that each trajectory was dominated by a large retrograde loop. The large retrograde loop, which was followed by the trailing motions considered here, was identified as the Rayleigh wave having 4- to 5-sec period. This long-period surface wave, having arrived at this area approximately 4.5 seconds after the first shear wave arrival, was not much affected by the local geology as it propagated from SL to ML and ATH. The wavelength of a 4-sec surface wave with 1.5 miles/sec velocity is about 6 miles. The propagation of such a long-period wave is not affected by the soil deposit whose vertical dimension at ML and ATH is about 900 ft being much smaller than the wavelength. The local geology effects are expected to increase with increase of frequency because the high frequency surface wave does not penetrate deeply and most of its energy is contained in the soil deposit near the surface. However, the observed amplitude ratios in Figs. 4.6 and 4.8 indicate that strong amplifications occurred at frequencies between 0.5 and 2.0 Hz but did not occur at frequencies higher than 2.0 Hz. This seems to be associated with the mode conversions of surface waves along the nonhorizontal interface between the soil and the bedrock, and the fact that a high frequency wave attenuates quickly within the soil. In fact the dipping structures can transmit part of the energy of incident fundamental Love and Rayleigh modes into higher Love and Rayleigh modes (Drake and Mal, 1972). The numerical results by Drake (1980) could be helpful in explaining why observed amplitude ratios were much higher at low frequencies than at high frequencies.

Drake (1980) studied surface wave propagations across an alluvial valley with a 45° dip at its side by the finite element model. In his numerical model, he found that there are large amplifications of surface wave motions within the alluvial valley at a frequency of 0.5 Hz. These large amplifications do not occur at frequencies higher than 0.5 Hz. He explained that at frequencies higher than 0.5 Hz, all of the energy in the incident fundamental Love or Rayleigh wave modes from the side of the alluvial valley is transferred within the alluvial valley to higher surface modes, which have smaller surface amplitudes than the corresponding fundamental mode in the soil deposit. Furthermore, soil damping within the alluvial valley is more effective on the surface amplitudes at frequencies higher than 0.5 Hz.

More numerical experiments by the finite element or the finite difference method are needed to throw light on the effects of local geology on the surface wave propagations.

4.4 Comparisions of Computed and Observed Site Transfer Functions

In this section observed amplitude ratios shown in Fig. 4.2c (vertical component) and Figs. 4.3a and b (transverse and radial components) are compared with the amplitudes of computed transfer functions to evaluate the applicability of the mathematical models described in Chapter 2. To compute site transfer functions, we have to specify the type of incident wave and the angle of incidence at the half-space.

As seen in Chapter 3, the portion of the accelerogram from which the Fourier transform was taken consists of body and surface waves. However, as imposed by the mathematical model, we can only consider body waves. The 1971 San Fernando earthquake had a focal depth of about 8 miles and the thrust-fault rupture extended to the ground surface. The stations in the Pasadena area were at epicentral distances less than 25 miles. Since the source dimension was comparable to the source-to-receiver distance, seismic waves from different parts of the fault must have approached the stations from different directions. This means that the observed ground motions rotated into transverse component are contributed not only by SH waves but by P and SV waves. Similarly, SH wave motions may also be seen in the radial component and we cannot really isolate SH waves from P and SV waves. However, it is difficult to determine the details and we shall consider SH waves in the transverse component, and P and SV waves in the radial and vertical components.

To specify the angle of incidence at the bedrock, it is noted that the first part of the accelerograms has indicated that seismic body waves have arrived from the bedrock at some angle other than 0°. Furthermore, seismic waves generated from different points of the fault might have been incident from the bedrock at different angles. However, for simplicity, we shall assume one incident angle.

The incident angle may be approximately estimated from the geometry of the earthquake source, the epicentral distance of the recording station, and the crustal structure in southern California. A 30° incident angle was chosen in this study.

Since the relative content of incident P and S waves from the bedrock is not known, we shall choose one type of incident wave to compute the transfer functions. Because the strong phase shakings are mainly contributed by incident shear waves, we shall consider only incident shear waves in the analysis, i.e., incident SH waves for the transverse component and incident SV waves for the radial and vertical components. With this choice we neglect the contributions of incident P waves from the bedrock. It should be noted that incident SV waves from the bedrock at 30° angle may produce a comparable amount of vertical motions to horizontal motions at the ground surface. This has been demonstrated by the numerical examples in Chapter 2 (e.g., Fig. 2.21).

The comparisons are presented in Section 4.4.1 for the transverse component and in Section 4.4.2 for the radial and vertical components. The amplitudes of the computed transfer function from the model are compared with the observed amplitude ratios between ML and SL as well as with those between ATH and SL. The initial estimates of model parameters shown in Fig. 4.1 are first utilized to compute site transfer functions. A systematic frequency domain identification method is then employed to determine the optimal model parameters which produce a least-squares match between the computed and observed amplitude ratios.

4.4.1 Transverse Component

The shear wave velocities of a 7-layered model shown in Fig. 4.1 and Table 4.1(a) are first utilized to calculate the site transfer function of 30° incident SH waves. The quality factors (Q's), which were not measured in situ, are estimated herein. The amplitudes of the computed transfer function are compared with the observed ML/SL and ATH/SL amplitude ratios in Fig. 4.9(a). Comparisons in this figure indicate that the computed and observed results do not compare so well in detail; the locations and the amplitudes of most of the peaks do not match. For example, the first peak of computed amplitude ratios is located near 0.90 Hz while the first observed peak is near 0.68 Hz. At frequencies higher than 3.0 Hz, the computed amplitude ratios are larger than the observed ratios. To reduce the computed amplitude ratios at high frequencies, the soil damping may be increased (i.e., decrease Q factor).

To investigate how well this simple 7-layered model predicts the observed amplitude ratios, a systematic frequency domain identification technique is performed by finding the values of the model parameters which produce a least-squares fit over a specified frequency band between the observed amplitude ratios and the computed amplitude ratios from the model. That is, we seek to minimize a measure-of-fit, J, which is defined by

$$J = \sum_{j=j_1}^{j=j_2} \left[(T_{ML/SL}(j\Delta f) - T(j\Delta f))^2 + (T_{ATH/SL}(j\Delta f) - T(j\Delta f))^2 \right] \tag{4.5}$$

where

$j\Delta f$ = frequency , j = integer, Δf = frequncy spacing in the spectra.

$T_{ML/SL}(j\Delta f)$ = observed amplitude ratios between ML and SL in the transverse component at frequency $j\Delta f$.

$T_{ATH/SL}(j\Delta f)$ = observed amplitude ratios between ATH and SL in the transverse component at frequency $j\Delta f$.

$j_1\Delta f \le f \le j_2\Delta f$ = the frequency band of identifications.

$T(j\Delta f)$ = computed amplitude ratios from the model of incident SH waves.

It is noted that the observed amplitude ratios in (4.5) were obtained from twice-smoothed Fourier amplitudes whereas the ratios shown in Figs. 4.2 and 4.3 have been further smoothed twice. The normalized error E defined as

$$E = \frac{J}{\sum_{j=j_1}^{j=j_2} \left[(T_{ML/SL}(j\Delta f))^2 + (T_{ATH/SL}(j\Delta f))^2 \right]} \tag{4.6}$$

may be used to indicate how good the match is. E will be reported when the results of the identifications are presented.

For simplicity, the model parameters allowed to vary during the course of the identification are the shear wave velocities, c_s's, the quality factors, Q's, and the incident angle at the bedrock, Θ_8. The thickness and the density of each layer, and the number of layers are unchanged. Hence the measure-of-fit J is a function of $c_{s1}, \cdots, c_{s8}, Q_{s1}, \cdots, Q_{s8}$ and Θ_8 (see Chapter 2 for notations). To obtain the least-squares fit, J is minimized with respect to c_{si}, Q_{si} $(i=1,2, \cdots ,8)$ and Θ_8 by the method of steepest descent. Appendix B gives a brief description on numerical minimization of a function of several variables with no constraint by the method of steepest descent.

The identification was first performed over the frequency band from 0.15 Hz to 2.54 Hz. The low frequency limit is chosen to avoid long-period data processing errors. The high frequency limit is set at 2.54 Hz because the locations of the peaks in the ML/SL and ATH/SL amplitude ratio spectra agree well at frequencies below 2.54 Hz. Initial values of model parameters for the analysis are those listed in Table 4.1(a). The initial match is shown in Fig. 4.9(a). The final estimates of model parameters are listed in Table 4.1(a) and the results are presented in Fig. 4.9(b). The match was pretty good at the peaks near 0.68 Hz and 2.34 Hz but several local peaks within the frequency band could not be produced by the 7-layered model. During the course of the identification, the normalized error was reduced from 0.279 for the initial estimates to a final value of

0.135. The final estimates of shear wave velocities for the 4th, 5th and 6th layers increased from their initial values while those for other layers decreased. Furthermore, the final shear wave velocity of the 7th layer is smaller than those of the 4th, 5th and 6th layers.

During the identification it was observed that the measure-of-fit J was insensitive to the changes in the quality factors and the incident angle. This is because of the low frequency band of identification we chose. The numerical examples in Chapter 2 (Fig. 2.15) have demonstrated that the transfer functions of incident SH waves at low frequencies are not sensitive to the changes in the quality factors and the incident angle. As a result, the final estimates of the quality factor and the incident angle were not much deviated from their initial values (Table 4.1(a)). Because of the high quality factors in the model, the computed amplitude ratios are larger than the observed ratios at frequencies beyond the frequency band of identifications.

Another match was performed by broadening the frequency band of identifications. The high frequency limit increases from 2.54 Hz to 7.91 Hz. It is noted that the amplitude ratios beyond 7.91 Hz corresponding to small amplitudes in the spectra (Fig. 4.3a) are ignored. The identification started with the final shear wave velocities obtained in the previous narrow-frequency-band identification. However, the initial values of the quality factors were reduced to bring down the computed amplitude ratios at high frequencies. The results of the identifications are listed in Table 4.1(b) and presented in Fig. 4.10. Fig. 4.10(a) shows the initial match between the observed amplitude ratios and the computed results from the initial model parameters in Table 4.1(b). The final match is shown in Fig. 4.10(b). The normalized error of final match is 0.22 which is too high for a good match. However, the final match does represent the best least-squares fit to the observations for a 7-layered model in the frequency

Table 4.1
Parameter Estimates of a 7-Layered Model for the Site at Caltech (Shear Wave Properties)

(a)
Frequency Band of Identifications = 0.15 - 2.54 Hz

Transverse Component (Inclined Incident SH Wave)						
	Initial Estimates		Final Estimates			
Layer No.	c_s (ft/sec)	Q_s	c_s (ft/sec)	Q_s	ρg (pcf)	H (ft)
1	620	8.00	568	8.00	100	6
2	1100	8.00	990	8.00	108	17
3	1600	10.00	1327	10.05	116	82
4	2000	15.00	3085	15.05	114	220
5	2500	20.00	2950	20.00	120	53
6	3100	25.00	3757	25.00	120	222
7	3600	30.00	2172	30.00	125	300
half-space	8000	100.00	7763	100.00	150	∞
Incident Angle	30.00		30.01			
	Normalized Error = 0.279		Normalized Error = 0.135			

(b)
Frequency Band of Identifications = 0.15 - 7.91 Hz

Transverse Component (Inclined Incident SH Wave)						
	Initial Estimates		Final Estimates			
Layer No.	c_s (ft/sec)	Q_s	c_s (ft/sec)	Q_s	ρg (pcf)	H (ft)
1	568	5.00	915	5.00	100	6
2	990	5.00	1617	4.99	108	17
3	1327	6.00	979	5.84	116	82
4	3085	8.00	3728	7.96	114	220
5	2950	8.00	3279	7.98	120	53
6	3757	10.00	3738	9.96	120	222
7	2172	12.00	2212	11.93	125	300
half-space	7763	100.00	7525	100.00	150	∞
Incident Angle	30.01		30.03			
	Normalized Error = 0.295		Normalized Error = 0.220			

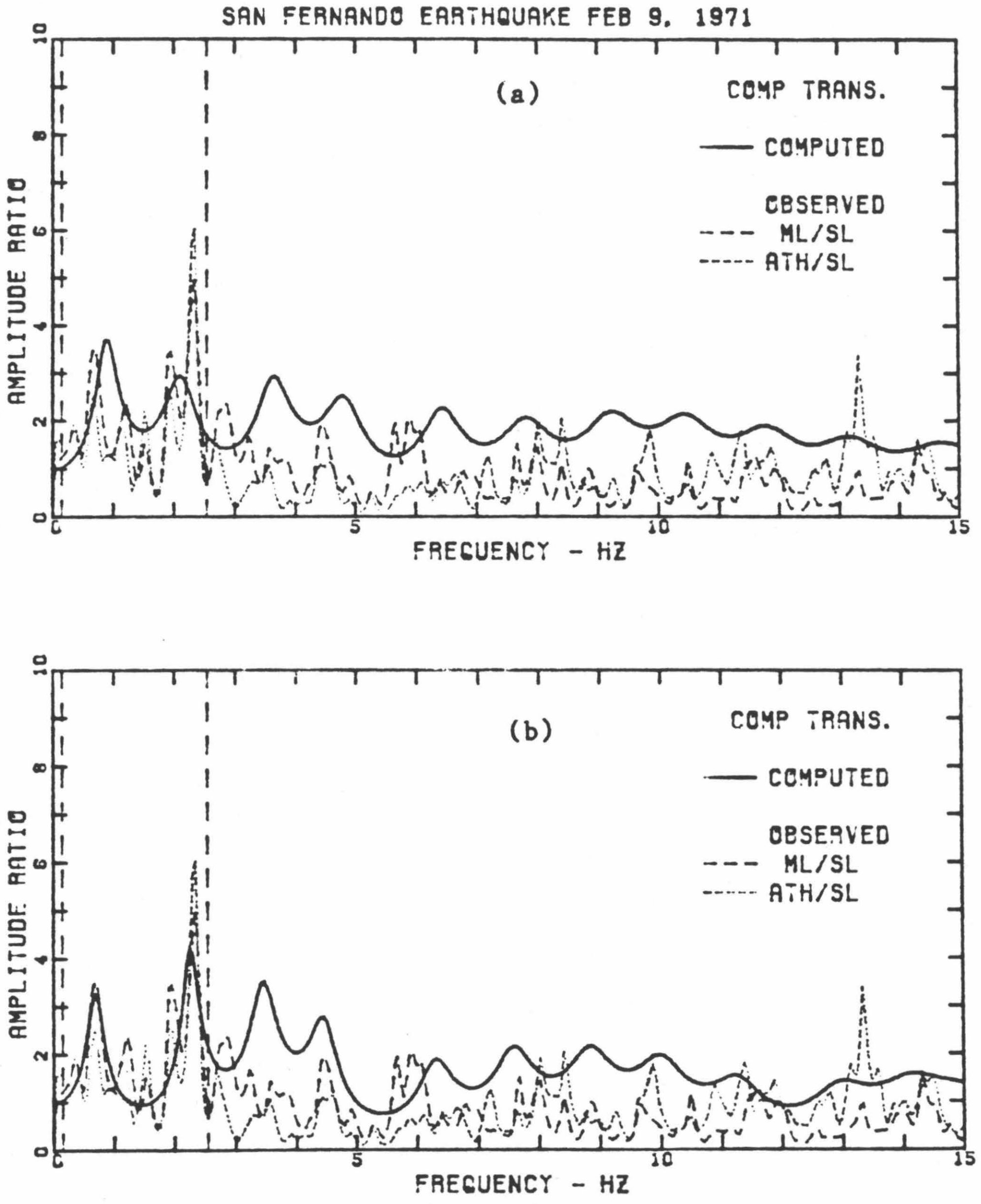

Fig. 4.9 Comparison of observed amplitude ratios and computed amplitude ratios from (a) initial estimates, (b) final estimates, of model parameters - transverse component. Dashed lines indicate the frequency band (0.15 - 2.54 Hz) of identifications.

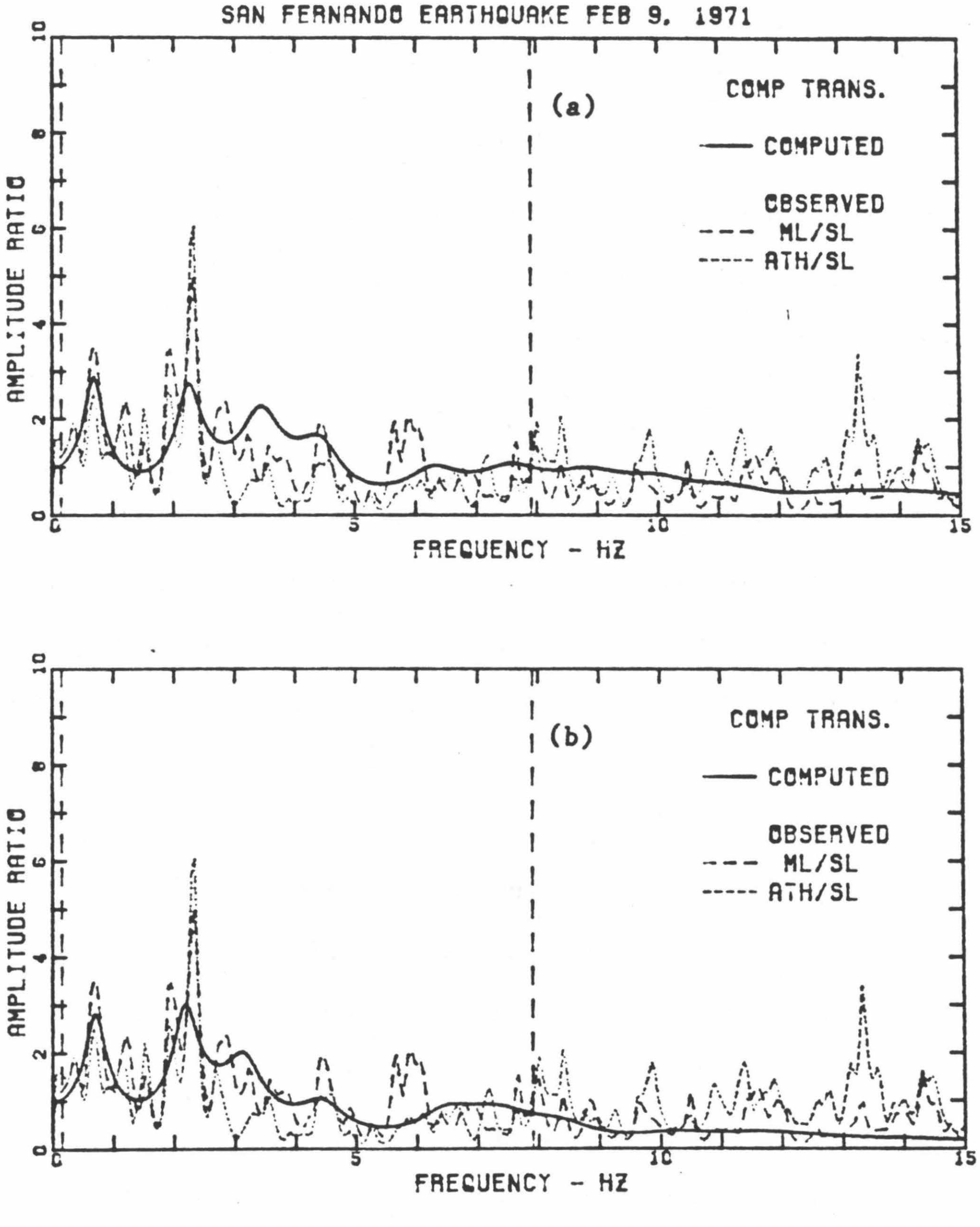

Fig. 4.10 Comparison of observed amplitude ratios and computed amplitude ratios from (a) initial estimates, (b) final estimates, of model parameters - transverse component. Dashed lines indicate the frequency band (0.15 - 7.91 Hz) of identifications.

band from 0.15 Hz to 7.91 Hz. The normalized error may be reduced by changing the number of layers in the model, but this is not easy to implement in the computer programs without sacrificing the computational efficiency. The thickness of each layer can be varied during the identification, but the total thickness of the subsoil profile should remain constant and an identification technique with this constraint must be employed.

It should be pointed out that the identification performed herein considers only the match of amplitudes. If an underlying bedrock record, having a common time base with the surface record, is available or the SL record is shifted exactly in the time axis to represent the corresponding input at the bedrock outcrop, the identification can be performed by matching both the amplitudes and phases. On the other hand, once the response at the free surface of a given subsoil profile subjected to the SL motions is computed, the time axes of ML and ATH records can then be approximately adjusted to compare with the computed surface motions. To do this, the final subsoil profile derived from the broad-frequency-band (0.15 - 7.91 Hz) identification is chosen. The transfer function of 30.03° incident SH waves has the amplitudes shown in Fig. 4.10(b) and the phases. The surface response is the inverse Fourier transform of the output transform which is the product of the Fourier transform of the SL motions and the transfer function. The computed surface motions are compared with the recorded transverse-component motions at ML and ATH in Fig. 4.11. It can be seen that the computed surface motions look more like the recorded motions at ML and ATH, especially the frequency content. However, the agreement is by no means perfect in detail. This is not surprising in view of many simplifications involved and from the fact that one computed output will never match simultaneously two different recorded outputs.

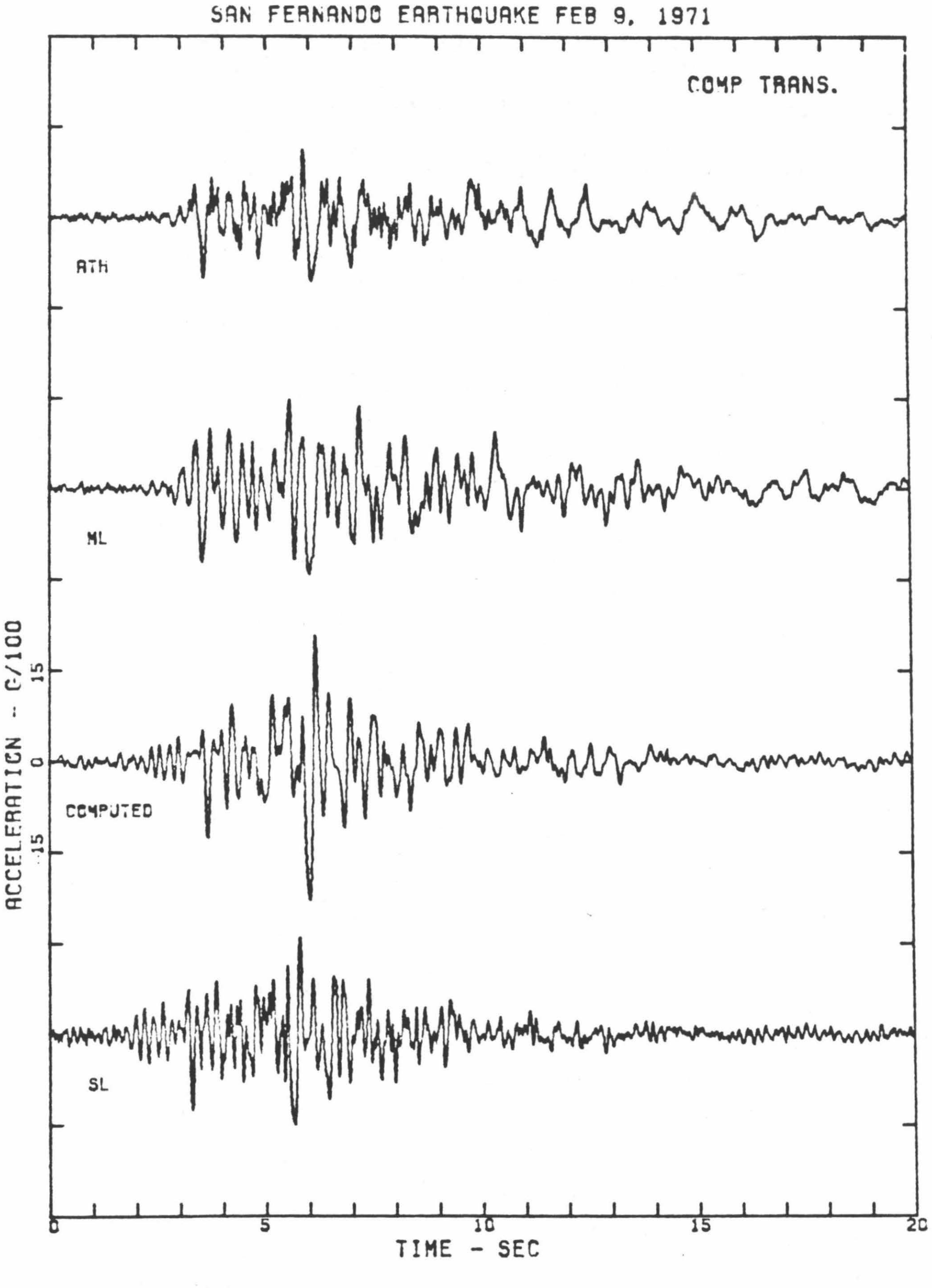

Fig. 4.11 Comparison of accelerograms recorded at ML, ATH and computed surface motions from the final model in Table 4.1(b) and the SL motions. Transverse component.

4.4.2 Radial and Vertical Components

The S-wave and P-wave velocities in Fig. 4.1 were used to compute the radial and vertical transfer functions of 30° incident SV waves. The quality factors were estimated. In each layer the P-wave quality factor is assumed to be the same as the S-wave quality factor, i.e., $Q_p = Q_s$. The amplitudes of computed transfer function are compared with the observed amplitude ratios in Fig. 4.12(a) for the radial component and in Fig. 4.13(a) for the vertical component. Obviously, the match is poor. To pursue a good match, the identification technique used for the transverse component was employed for the radial and vertical components. However, the measure-of-fit J herein is defined as

$$J = \sum_{j=j_1}^{j=j_2} \left[(R_{ML/SL}(j\Delta f) - R(j\Delta f))^2 + (R_{ATH/SL}(j\Delta f) - R(j\Delta f))^2 \right]$$

$$+ \sum_{j=j_1}^{j=j_2} \left[(V_{ML/SL}(j\Delta f) - V(j\Delta f))^2 + (V_{ATH/SL}(j\Delta f) - V(j\Delta f))^2 \right] \qquad (4.8)$$

where

$R_{ML/SL}(j\Delta f)$ = observed amplitude ratios between ML and SL in the radial component.

$R_{ATH/SL}(j\Delta f)$ = observed amplitude ratios between ATH and SL in the radial component.

$R(j\Delta f)$ = computed horizontal amplitude ratios from the model of inclined incident SV waves.

$V_{ML/SL}(j\Delta f)$ = observed amplitude ratios between ML and SL in the vertical component.

$V_{ATH/SL}(j\Delta f)$ = observed amplitude ratios between ATH and SL in the vertical component.

$V(j\Delta f)$ = computed vertical amplitude ratios from the model of inclined incident SV waves.

The normalized error E is defined as

$$E = \frac{J}{\sum_{j=j_1}^{j=j_2} \left[(R_{ML/SL}(j\Delta f))^2 + (R_{ATH/SL}(j\Delta f))^2 + (V_{ML/SL}(j\Delta f))^2 + (V_{ATH/SL}(j\Delta f))^2 \right]} \tag{4.9}$$

During the course of the identification, the wave velocities c_s, c_p of each layer and the incident angle were allowed to vary while the quality factor and the thickness of each layer are fixed. The identification was performed only over the frequency band from 0.15 Hz to 2.54 Hz. The results of identification are listed in Table 4.2(a) and presented in Figs. 4.12(b) and 4.13(b). The normalized error was reduced from 0.310 for the initial estimates to a final value of 0.197. It can be seen in these figures that the match is poorer for the vertical component than for the radial component. In the radial component, the first two peaks of observed amplitude ratios located near 0.54 Hz and 0.85 Hz could not be produced by the 7-layer model; instead the first computed peak is located between these two observed peaks at 0.73 Hz.

In computing the radial and vertical transfer functions we assumed the system was excited only by inclined incident SV waves. The radial and vertical responses at the bedrock outcrop and the free surface to inclined incident SV waves consist of converted P waves as well as SV waves. The poor match in the radial and vertical components might have indicated that the response of the system to inclined incident P waves cannot be neglected. To include the contributions from incident P waves, we have to know their amplitudes and arrival times relative to incident SV waves. As demonstrated in Figs. 2.23 and 2.24 in Chapter 2, the transfer function for the combination of incident P and SV waves is irregular and is sensitive to the changes in the relative amplitudes and arrival times which are usually different in different earthquakes. Moreover, one can probably never completely separate P-wave and S-wave motions generated by a

Table 4.2
Parameter Estimates of a 7-Layered Model for the Site at Caltech (S- and P-Wave Properties)

(a)
Frequency Band of Identifications = 0.15 - 2.54 Hz

Radial and Vertical Components (Inclined Incident SV Wave)							
	Initial Estimates		Final Estimates				
Layer No.	c_s (ft/sec)	c_p (ft/sec)	c_s (ft/sec)	c_p (ft/sec)	$Q_s=Q_p$	ρg (pcf)	H (ft)
1	620	1400	610	1394	5.00	100	6
2	1100	2200	1073	2183	5.00	108	17
3	1600	3100	1327	3019	6.00	116	82
4	2000	3800	1191	3888	8.00	114	220
5	2500	4500	2524	4561	8.00	120	53
6	3100	5600	3222	5836	10.00	120	222
7	3600	6400	3241	6713	12.00	125	300
half-space	8000	14000	8765	13673	100.00	150	∞
Incident Angle	30.00		29.94				
	Normalized Error = 0.310		Normalized Error = 0.197				

(b)
Frequency Band of Identifications = 0.15 - 2.54 Hz

Radial Component (Inclined Incident SV Wave)					
	Final Estimates				
Layer No.	c_s (ft/sec)	c_p (ft/sec)	$Q_s=Q_p$	ρg (pcf)	H (ft)
1	610	1394	5.00	100	6
2	1072	2183	5.00	108	17
3	1290	3019	6.00	116	82
4	1203	3880	8.00	114	220
5	2592	4559	8.00	120	53
6	3448	5833	10.00	120	222
7	3354	6713	12.00	125	300
half-space	8817	13638	100.00	150	∞
Incident Angle	29.94				
	Normalized Error = 0.182				

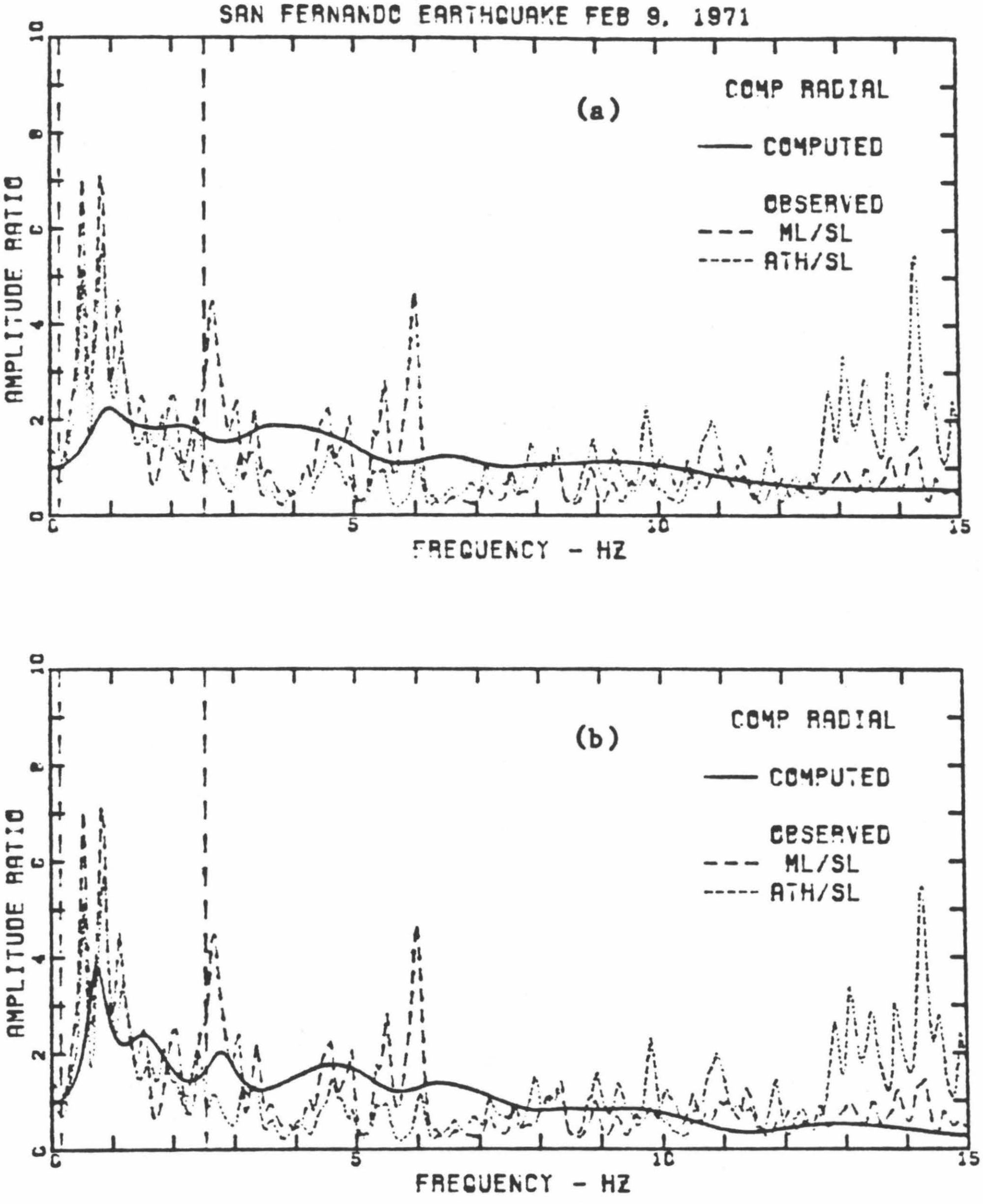

Fig. 4.12 Comparison of observed amplitude ratios and computed amplitude ratios from (a) initial estimates, (b) final estimates, of model parameters - radial component. Dashed lines indicate the frequency band (0.15 - 2.54 Hz) of identifications.

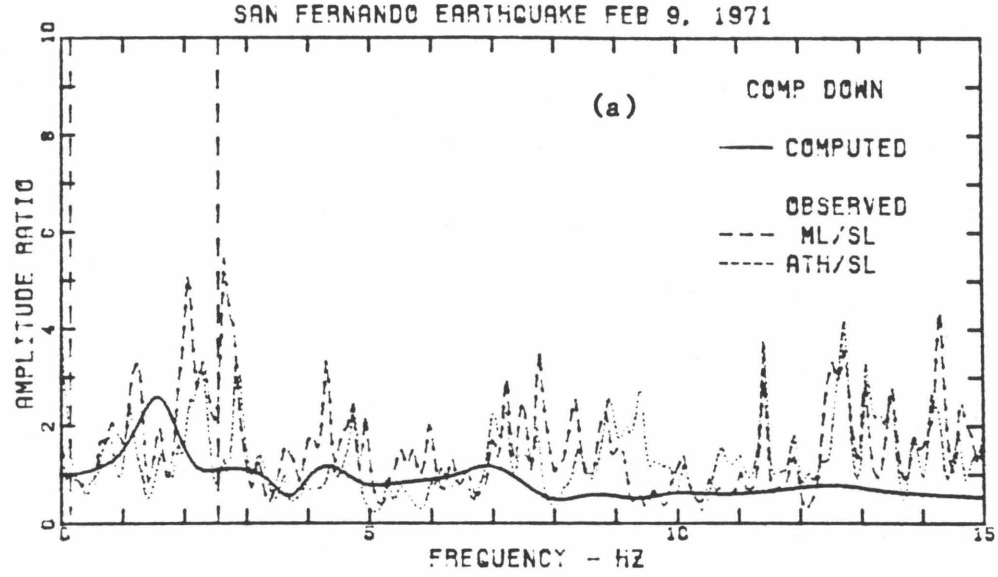

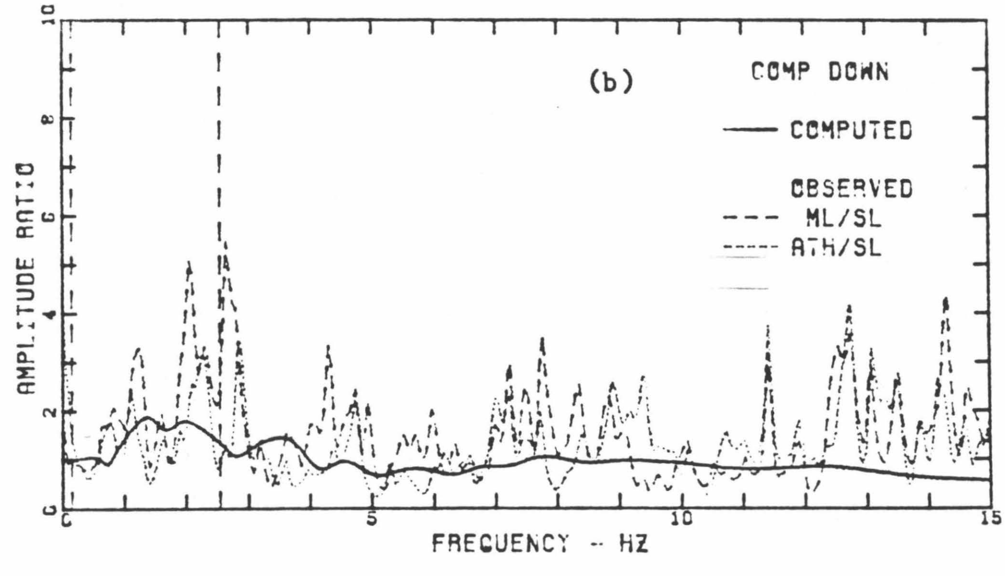

Fig. 4.13 Similar to Fig. 4.12 for the vertical component.

strong earthquake. Therefore, the model considering both incident P and SV waves was not used in this study.

It is interesting to note that when the measure-of-fit J in equation (4.8) was computed only for the radial component, the final estimates of wave velocities (Table 4.2(b)) were almost identical to those obtained by matching both the radial and vertical components. The final matches for the radial and vertical components shown in Fig.4.14 are not much different from those in Figs. 4.12(b) and 4.13(b).

The initial and final estimates of the wave velocities for the 7-layered subsoil profile are summarized in Fig. 4.15. In the initial profile indicated by the solid lines, the P-wave and S-wave velocities increase with increasing depth. As shown in Fig. 4.1, only the S-wave velocities down to 400 ft deep were measured, other velocities were initially estimated. The final estimates of the identifications are shown by the dashed lines in Fig. 4.15. The shear wave velocities are quite different in three final estimates and a unique subsoil profile was not achieved. It should be pointed out that Fig. 4.15 shows the optimal wave velocities for a 7-layered subsoil model to produce a least-squares match between the computed and observed amplitude ratios within a selected frequency band. Since the number of layers and the thickness of each layer were fixed during the identifications, no claim for the uniqueness of the subsoil profile can be made. The final Q factors range from 5.0 (10% critical damping) for the top layer to 12.0 (4.2% critical damping) for the bottom layer; the model with higher Q values led to computed amplitude ratios that were too high compared to observed amplitude ratios at high frequencies.

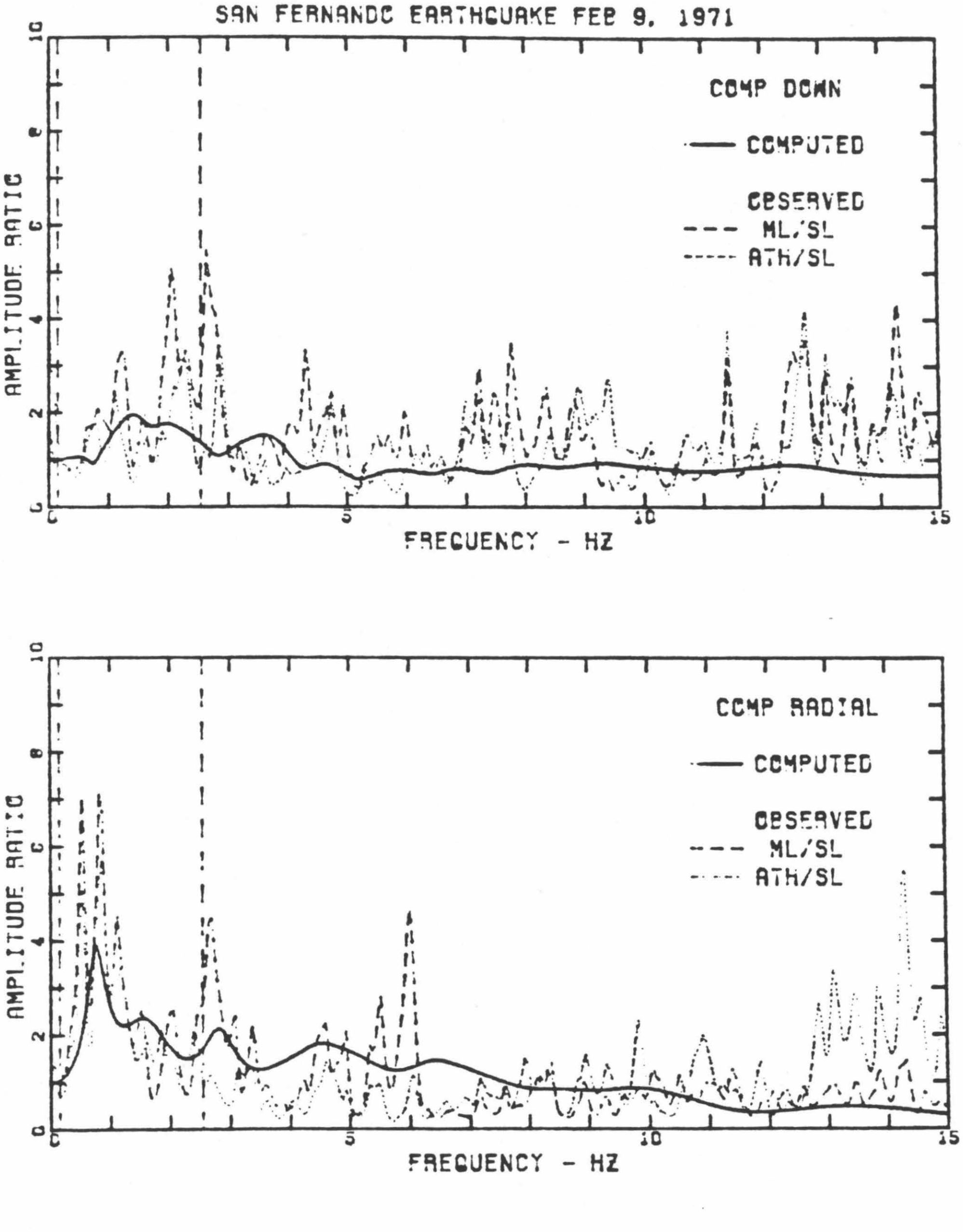

Fig. 4.14 Comparison of observed amplitude ratios and computed amplitude ratios from final estimates of model parameters which are obtained by matching the radial component only.

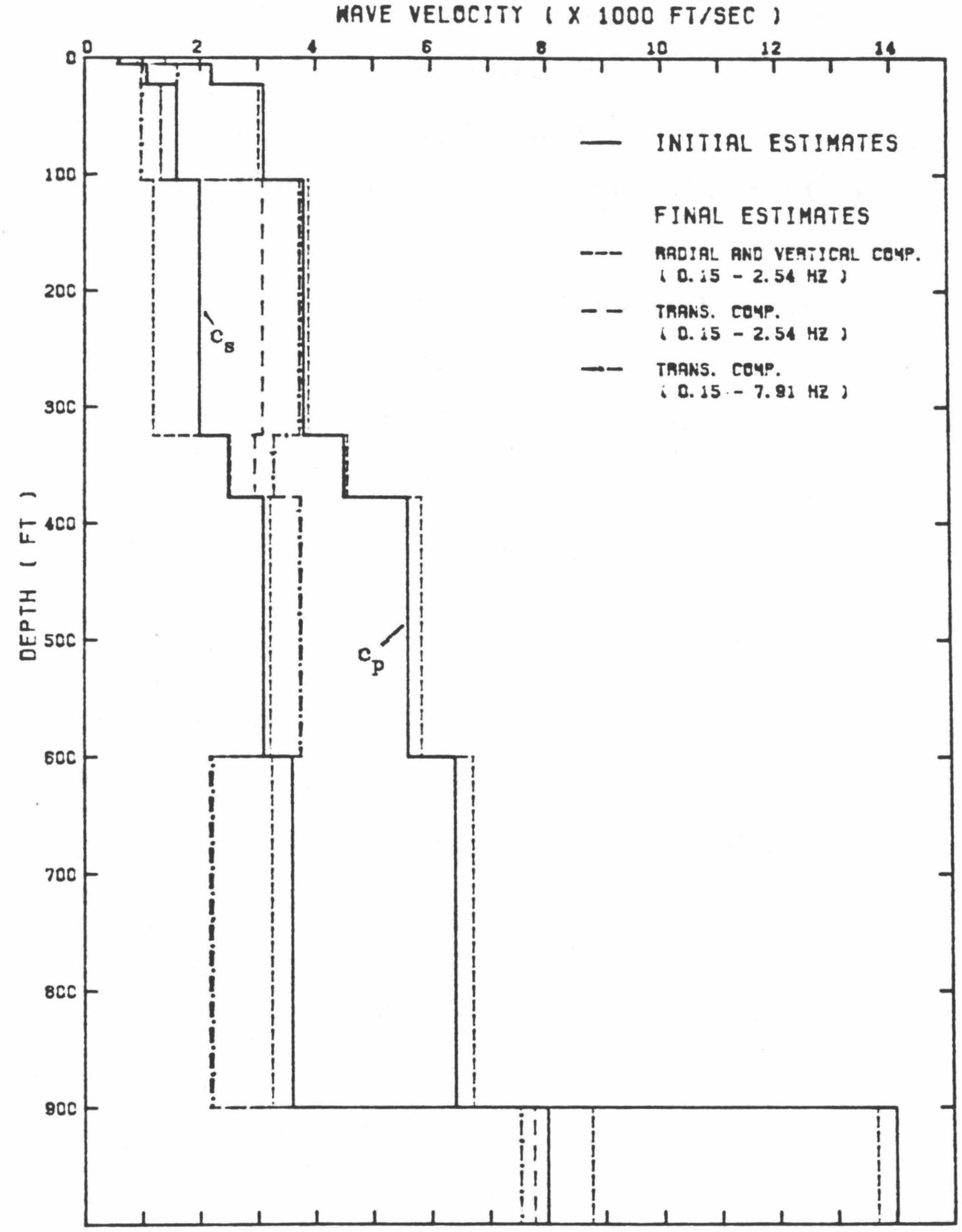

Fig. 4.15 The initial estimate and different final estimates of the subsoil profile underlying the Caltech campus.

4.4.3 Discussion

We have treated the soil column underlying the Caltech campus as a linear, time-invariant system. The recorded motions at ML and ATH during the 1971 San Fernando earthquake are the two outputs of the system. We assumed all the input excitations during the earthquake were represented by the body waves incoming from the underlying bedrock and neglected other body waves and surface waves from surrounding soils. This assumption is not completely valid for the San Fernando earthquake for which surface waves have significant contributions to the ground motions in the Pasadena area. Since the downhole records at the bedrock were not available, we further assumed that the recorded motions at SL were the input to the system.

To compute the transfer function between the input and the output of the system, we have to determine the type of body wave incident from the bedrock and the angle of incidence at the bedrock. The incident angle was chosen to be 30° in this study. The computed transfer function was not sensitive to the change in this angle, because the angle of propagation in each layer is small as the waves penetrate from the bedrock into the layers. We considered incident SH waves for the transverse component whereas for the radial and vertical components we considered only incident SV waves and neglected incident P waves. The transfer functions for the combination of incident P and SV waves can be obtained only if their relative amplitudes and arrival times are known. The applications of the model considering both incident P and SV waves are usually limited by the fact that relative contributions of P and S waves incident from the bedrock at different frequencies are not known and are usually different in different earthquakes. The analysis is usually performed in engineering by considering only incident SH waves. Furthermore, the theoretical transfer function for incident SH waves is not sensitive to the angle of incidence at the bedrock.

Therefore, most analytical models assume vertically propagating shear waves.

The fact that observed amplitude ratio is quite different for different directions might imply that the SL motions are not the appropriate input to the subsoil profile. However, because of the lack of downhole measured bedrock motions the recorded motions at SL were used as input to the subsoil profile. Regardless of the input, if the output (free surface response) can be predicted by the model the surface motions should not be different at two nearby points on the free surface. The fact that the ML and ATH motions are quite different implies that part of the motions is not site-dependent. The Fourier amplitude spectra shown in this chapter indicate that the agreement between the ML and ATH motions is only in the frequency band from 0.0 to 2.0 Hz or to 2.5 Hz. This frequency band is too narrow to give similar ground accelerations at two stations.

4.5 Summary

Local geology effects on strong earthquake ground motions have been investigated by studying the recorded accelerograms at ML, ATH (alluvium sites) and SL (rock site) in the Pasadena area during the 1971 San Fernando earthquake. Relative to SL, the ground accelerations at ML and ATH were dominated by lower frequency waves and were longer in duration. However, the ground shakings at ML and ATH were not significantly greater than those at SL.

The observed amplitude ratio has been obtained by dividing the Fourier amplitude of the motions at ML or ATH by that at SL. It is found that observed amplitude ratios differ markedly in different horizontal directions. The average observed amplitude ratio, which is based on the total energy and is independent of recording direction, is defined and can be adopted to represent the local geology effects. It could be useful to reduce the uncertainties in statistically evaluating the local geology effects from earthquake and nuclear explosion data.

The Fourier amplitude spectra of the trailing parts of the accelerograms indicate that most energy of the trailing motions at ML and ATH is concentrated at frequencies between 0.5 Hz and 2.0 Hz, while the SL amplitude spectra are almost flat at frequencies lower than 2.0 Hz. Observed amplitude ratios between ML(or ATH) and SL are much higher at low frequencies from 0.5 Hz to about 2.0 Hz than at high frequencies. The difference in the trailing motions at ML(or ATH) and SL may be associated with local geology effects on the surface wave propagations.

Observed amplitude ratios for overall motions were compared with the amplitudes of the computed transfer function from the analytical model given in Chapter 2. Some model parameters were adopted from geotechnical measurements. A 7-layered structure overlying a half-space was chosen to model the subsoils underlying the Caltech campus. The system is linear and time-invariant. To compute the transfer function for the system, a single incident wave at a specified angle of incidence from the half-space was assumed to be the only input to the system, i.e., incident SH wave for the transverse component and incident SV wave for the radial and vertical components.

The initial values of the model parameters produced poor matches between the observed and computed amplitude ratios. Therefore, a systematic frequency domain identification technique was employed to find the optimal model parameters, i.e., wave velocities and quality factors, which produce a least-squares match between the observed and computed amplitude ratios over a specified frequency band. The number of layers and the thickness of each layer were fixed during the course of the identification. It appears that the agreement between the computed and observed amplitude ratios is better for the transverse component than the radial and vertical components. The final shear wave velocities are quite different from the identifications of different components and a unique subsoil profile is not achieved.

Although the analytical model explains some of the differences between the SL records and the ML, ATH records, for example, the difference in the frequency content (Fig. 4.11), it is not capable of calculating the surface motions at ML and ATH very accurately from the SL records. The fact that observed amplitude ratios are quite different in different directions might imply that the SL motions are not the appropriate input to the subsoil system. Furthermore, the fact that the motions at ML and at ATH are quite different at frequencies higher than 2.5 Hz indicates that part of the motions is not site-dependent.

Possible limitations of the theory in evaluating the influence of local geology on earthquake ground motions were discussed. The analyses in this chapter indicate that the analytical method over-simplifies the actual seismic environment in the Pasadena area during the 1971 San Fernando earthquake. Using a simplified model and a nearby surface rock record to compute the surface motions at an alluvial site, regardless of the relative content of various wave types and the 3-dimensional local geological configuration, can involve large errors.

4.6 References

[1] Borcherdt, R. D. (1970), "Effects of Local Geology on Ground Motion near San Francisco Bay," *Bulletin of the Seismological Society of America*, Vol. **60**, No.1, February 1970, pp. 29-61.

[2] Drake, L. A. and Mal, K. K. (1972), "Love and Rayleigh Waves in the San Fernando Valley," *Bulletin of the Seismological Society of America*, Vol. **62**, No.6, December 1972, pp. 1673-1690.

[3] Drake, L. A. (1980), "Love and Rayleigh Waves in an Irregular Soil Layer," *Bulletin of the Seismological Society of America*, Vol. **70**, No.2, April 1980, pp. 571-582.

[4] Huang, M. J. (1982), "On the Characteristics of 3-Dimensional Earthquake Ground Motion," *Proceedings of the 3rd International Earthquake Microzonation Conference*, Seattle, June 28 - July 1, 1982, pp. 435-446.

[5] Johnson L. R. and Silva, W. (1981), "The Effects of Unconsolidated Sediments upon the Ground Motion during Local Earthquakes," *Bulletin of the Seismological Society of America*, Vol. **71**, February 1981, pp. 127-142.

[6] Joyner, W. B., Warrick, R. E. and Oliver, A. A. (1976), "Analysis of Seismograms from a Downhole Array in Sediments near San Francisco Bay," *Bulletin of the Seismological Society of America*, Vol. **66**, 1976, pp. 937-958.

[7] Joyner, W. B., Warrick, R. E. and Fumal, T. E. (1981), "The Effect of Quaternary Alluvium on Strong Ground Motion in the Coyote Lake, California, Earthquake of 1979," *Bulletin of the Seismological Society of America*, Vol. **71**, August 1981, pp. 1333-1349.

[8] McVerry, G. H. (1979), "Frequency Domain Identification of Structural Models from Earthquake Records," *EERL 79-02*, Earthquake Engineering Research Laboratory, California Institute of Technology, Pasadena, October 1979.

[9] Rogers, A. M. and Hays, W. W. (1978), "Preliminary Evaluation of Site Transfer Functions Developed from Earthquakes and Nuclear Explosions," *Proceedings of the Second International Conference on Microzonation*, San Francisco, 1978, Vol. **II**, pp. 753-763.

[10] Schnabel, P. B., Seed, H. B. and Lysmer, J. (1972), "Modification of Seismograph Records for Effects of Local Soil Conditions," *Bulletin of the Seismological Society of America*, Vol. **62**, NO.6, December 1972, pp. 1649-1664.

[11] Shannon & Wilson, Inc., and Agbabian Associates (SW-AA) (1978), "Geotechnical and Strong Motion Earthquake Data from U.S. Accelerograph Stations, Vol. 2, Pasadena, Santa Barbara, Taft, and Hollister, California," *NUREG-0029*, Vol. **2**, NRC-6A, Report to the U.S. Nuclear Regulatory Commission, June 1978.

[12] Shannon & Wilson, Inc., and Agbabian Associates (SW-AA) (1980), "Geotechnical Data from Accelerograph Stations Investigated during the Period 1975-1979, Summary Report," *NURE/CR-1643*, Report to the U.S. Nuclear Regulatory Commission, September 1980.

[13] Tsai, N. C. and Housner, G. W. (1970), "Calculation of Surface Motions of a Layered Half-Space," *Bulletin of the Seismological Society of America*, Vol. **60**, N0.5, October 1970, pp. 1625-1651.

CHAPTER 5

SUMMARY AND CONCLUSIONS

In what follows the studies presented in the previous chapters are briefly summarized and some general conclusions drawn are presented. Some suggestions for future research are also offered.

I. A two-dimensional model for inclined propagation of P and S plane waves in a horizontal-layered structure has been studied. This model is more realistic and closer to the actual seismic environment within a local geology than the one-dimensional model of vertically propagating waves. The transfer function between the free surface motions and the half-space outcrop motions to a single train of incident SH, P or SV wave from the half-space at a specified angle was derived by the matrix method. Two numerical examples were given to examine the effects of material damping and incident angle on the transfer function. The limitations of the two-dimensional model for evaluating local geology effects on earthquake ground motions were discussed. The general conclusions are

(1) The effects of material dampings on the transfer function are most significant at high frequencies. As damping increases, more high order reflections in the layered structure are attenuated, more high-frequency motions are dissipated, and the amplitudes of surface motions become smaller.

(2) The transfer function for an incident SH wave is not much affected by the incident angle, whereas the coupling effects on the transfer function for an incident SV or P wave become more prominent as the incident angle increases.

(3) If the amplitudes, arrival times and incident angles of all incident body waves from the bedrock are known, the surface response of a given layered

structure can be computed from the analyticl model by using the superposition principle and the Fourier transform method. However, the use of a two-dimensional model to compute the surface motions during a strong earthquake is not straightforward, because the relative content of incident P and S waves from the bedrock are not known.

(4) The transfer function between the surface response and the half-space outcrop response to multiple incident waves having different arrival times and different incident angles is more complicated than that for a single incident wave at an incident angle. Furthermore, the transfer function between the output and the input depends upon the detailed character of the input. For nearby shallow-focus earthquakes, seismic waves emitted from different parts of the fault will approach the bedrock from different directions and at different angles, hence, completely satisfactory results can not be expected when using the transfer function of a single incident wave to relate the motions at two different points of the subsoil profile during a nearby shallow-focus earthquake.

II. Analysis of the data recorded at four stations, i.e., SL (rock site), ML, ATH and JPL (alluvial sites), in the Pasadena area during the 1971 San Fernando earthquake gives the following conclusions:

(1) Compared to SL, the ML, ATH and JPL accelerations are richer in lower frequency waves (< 3.0 Hz), however, the intensities of shaking at ML, ATH and JPL are not significantly greater than those at SL.

(2) A high degree of coherence in the wave forms is observed in the ground velocities at all stations.

(3) Long-period (4- to 5-sec) surface waves are contained in all the accelerograms, which in fact dominate the ground displacements and are not

affected by the local geology in the area.

(4) The accelerograms at both rock and alluvial sites are dominated by a strong part having relatively high accelerations. This part is mainly due to the arrivals of shear waves from the source, and its duration(~ 8 seconds) is about the same as the duration of the slipping process of the fault.

(5) The motions having periods from 0.5- to 2.0-sec are prominent in the trailing portions of the accelerograms at ML, ATH and JPL, but not at SL. These trailing motions are associated with surface waves which propagated across the area, and body waves which were trapped within the surface layer.

III. Comparison of all the accelerograms recorded in the Pasadena area during four past earthquakes leads to the following conclusions:

(1) Local geology effects are less evident on the leading portions of the accelerograms than on the trailing portions.

(2) The accelerograms obtained from distant earthquakes exhibit surface waves with amplitudes comparable to the preceding body waves.

(3) No significant site periods have been identified at any of the sites. It is not appropriate to characterize such sites by a site period.

(4) The 3-dimensional configuration of local geology and the direction of arriving waves do have influence in modifying the incoming seismic waves. The analytical model, which assumes horizontal layers for the local geology, can not take into account the effect of nonhorizontal layered structure.

IV. The accelerograms recorded at SL, ML and ATH during the 1971 San Fernando earthquake have been used to evaluate the analytical model for the local geology in the Pasadena area. The observed amplitude ratio was obtained by dividing the Fourier amplitude of the motions at ML or ATH by that at SL.

Observed amplitude ratios were compared with the computed amplitude ratios from the analytical model. The two-dimensional model with 7 layers overlying a half-space was chosen to represent the subsoil profile underlying the Caltech campus. Values of some model parameters were adopted from geotechnical investigations. The transfer function was computed for a single incident SH or SV wave from the half-space at an incident angle. A systematic identification technique was also employed to find the optimal wave velocities and dampings of the 7-layered model which produce a least-squares fit between computed and observed amplitude ratios. The general conclusions are

(1) The assumption that the SL motions are the same as the motions at the bedrock outcrop underlying ML and ATH is not correct for the San Fernando earthquake, because observed amplitude ratios between the sites differ markedly in different horizontal directions.

(2) The proposed Average Observed Amplitude Ratio, which is based on the total energy and is independent of recording direction, is recommended for statistical evaluations of local geology effects upon earthquake and nuclear explosion motions.

(3) Observed amplitude ratios between the trailing motions at ML, ATH and those at SL are large at frequencies from 0.5 to about 2.0 Hz and decay rapidly at higher frequencies. The differences in the trailing motions at ML, ATH compared to SL are associated with the surface layer of alluvium at the ML and ATH sites. Numerical experiments, by the finite element or the finite difference method, are needed to throw light on the effects of such local geology on surface wave propagation.

(4) When using the SL motions as input to the subsoil profile with low soil damping, stronger surface motions are predicted than are actually observed at ML

and ATH.

(5) The San Fernando earthquake records indicate that the motions at ML and ATH differ markedly at frequencies between 2.0 and 6.0 Hz. There is no evidence of significant soil-building interaction. It is also unlikely that the local geology underlying these two stations can differ markedly to cause the difference. It is concluded that this difference must result from body waves refracting and reflecting within the alluvium layer.

(6) Although the analytical model explains the difference of the frequency content between the SL records and the ML, ATH records, it does not seem to be capable of accurately calculating the surface motions at ML and ATH from the motions at SL.

(7) The agreement between observed and computed amplitude ratios is improved, but not significantly, by using the optimal values of model parameters. Hence, the analytical model oversimplifies the local geological structure in the Pasadena area and the actual seismic environment in the area during the 1971 San Fernando earthquake.

V. The ground motions recorded at Mexico City during two distant earthquakes are often used to illustrate the success of the one-dimensional model, and Mexico City is often mentioned as a site where marked local geology effects can occur. However, it must be pointed out that the records obtained at Mexico City such as those shown in Fig. 1.2 contain essentially surface waves. The earthquake was located at approximately 260 kilometers from Mexico City and had a focal depth of about 20 kilometers. For such a shallow-focus earthquake at large distance, most seismic energy is expected to arrive in the form of surface waves. It is interesting to note that the Borrego Mountain earthquake was located at about 215 kilometers from Pasadena and had a focal depth of 9 kilometers (Tables 3.1 and 3.2). The records obtained in the Pasadena area during the Borrego Mountain earthquake (Fig. 3.18) have features similar to those recorded in Mexico City. Both records consist essentially of surface waves in their trailing parts. The dominant 2.5-sec motions in Mexico City are due to the effects of local geology on surface waves rather than on body waves.

VI. The strong motion data recorded in the Pasadena area have provided an opportunity for studying the nature of earthquake ground motions in the area and investigating local geology effects on ground motions. The general picture emerging from study of these data is more complicated than had been assumed for most analytical models. The results of this study indicate that a better understanding of the spatial variation of ground motions, of the role played by different types of waves and their relative contributions to an accelerogram, and of the propagation directions of the waves is needed for assessing local geology effects on ground motions. Further research should give a high priority to deploying a local array so that the data during future earthquakes will give a reasonably complete picture of the nature of ground motions in a local area. Since 1971, more accelerographs, in addition to the accelerographs already located in the basements of Millikan Library and Athenaeum, have been installed at several locations on the Caltech campus. Some are located in the basements of multistory buildings and some on the first floor of one-story buildings. These instruments are centered around Millikan Library where more instruments have been installed to measure structural response. The instruments added since 1971 will provide data for gaining a better insight into: (a) the local distribution of earthquake ground motions, (b) the soil-structure interaction phenomenon, (c) the free-field motion in the local area, (d) the effects of embedment of the building and the size of the building foundation on recorded ground motions. Furthermore, the records from different earthquakes will permit analysis of source effects and travel path effects.

The value of the data would be significantly increased by the following improvements: (a) All the accelerographs to have a common time base. (b) The orientations and the locations of the accelerographs should optimize the value of the data and should be determined accurately for future analysis purposes. (c) The accelerographs should be spaced closely enough so that the waves having frequencies lower than a certain frequency, e.g., 6.0 Hz, are not aliased; this requires spacing of about 100 feet.

It would be desirable to extend the array on the Caltech campus to include the SL and JPL stations. To provide data for the local geology effect and the variation of ground motions across the valley, the instruments can be installed at several locations between Seismological Laboratory, Jet Propulsion Laboratory and the campus. The more frequent occurrence of weak ground shaking makes it desirable to record these motions and to analyze them, especially, as the soil behaves linearly under small strains. Sensors with low trigger level and high gain recorders can be deployed to record small local earthquakes or large distant earthquakes, as well as large close earthquakes.

As funds are available, the array should be extended to include down-hole instruments. The data will permit analysis of the variation of ground motion with depth and assessment of the validity of the analytical models for the subsoil profile, and give a 3-dimensional picture of the nature of wave propagation through this local site. It is desirable to install the sensors at the depth of 50, 100, 300, 500, 700 and 900 (bedrock) feet.

APPENDIX A

List of Symbols in Chapter 2

Symbol	Meaning
a_j , b_j	upgoing and downgoing SH wave amplitudes within the jth layer (complex-valued), Eq. 2.2.1.
a_0	displacement amplitude of SH waves at the free surface (complex-valued), Eq. 2.2.9.
$[\mathbf{a}]_j$	4×4 matrix for the jth layer defined by Eq. 2.3.22.
a_{11} .. a_{44}	elements of matrix $[\mathbf{a}]_j$, Eq. 2.3.23.
$A_j(\omega)$, $B_j(\omega)$	coefficients defined by Eqs. 2.2.11 and 2.2.12.
A_{xj} , A_{zj}	x- and z-components of $\vec{A}_j$, Eq. 2.2.32.
A_1 , A_2	upgoing and downgoing P wave amplitudes within the jth layer (complex-valued), Eq. 2.3.1a.
$\vec{A}_j$	attenuation vector within the jth layer, Eq. 2.2.32.
$[\overline{A}]$	matrix defined by Eq. 2.3.27.
A_{1p}^{N+1}, B_{1s}^{N+1}	potential amplitudes of incident P and SV waves in the half-space, Eq. 2.3.33.
A_2^{N+1}, B_2^{N+1}	potential amplitudes of reflected P and SV waves in the half-space, Eq. 2.3.33.
A'_{2p} , B'_{2p}	potentials of reflected P and SV waves, respectively, in the half-space without top layers due to incident P waves, Eq. 2.3.38.
A'_{2s} , B'_{2s}	potentials of reflected P and SV waves, respectively, in the half-space without top layers due to incident SV waves, Eq. 2.3.46.
B_1 , B_2	upgoing and downgoing SV wave amplitudes within the jth layer (complex-valued), Eq. 2.3.1b.
$[\overline{B}]$	matrix defined by Eq. 2.3.32.
c, c_p, c_s	elastic wave velocities (real-valued), $c = c_p$ for P waves and $c = c_s$ for S waves, Eq. 2.2.20.
c_{hj}	constant for the jth layer defined by Eq. 2.2.33c.
c_{sj}	elastic shear wave velocity in the jth layer (real-valued), Eq. 2.2.18.
C_p , C_s	coefficients defined in Eq. 2.3.13a.
C_{up} , C_{wp}	coefficients defined in Eq. 2.3.40.
C_{us} , C_{ws}	coefficients defined in Eq. 2.3.48.
$CTR_p(\omega)$	crustal transfer function ratio for incident P waves, defined by Eq. 2.3.36.

$CTR_s(\omega)$	crustal transfer function ratio for incident SV waves, defined by Eq. 2.3.45.
D_p	coefficient defined by Eq. 2.3.35.
D_s	coefficient defined by Eq. 2.3.44.
H_j	thickness of jth layer.
$[H]_j$	matrix for the jth layer defined by Eqs. 2.2.8b and 2.2.29.
i	$i = \sqrt{-1}$
$[J(0)]_j$	propagation matrix at $z_j = 0$ in the jth layer, Eq. 2.3.16.
$[J(0)]_j^{-1}$	inverse of $[J(0)]_j$, Eq. 2.3.19.
$[J(H_j)]_j$	propagation matrix $z_j = H_j$ in the jth layer, Eq. 2.3.14.
$\vec{P}_j$	propagation vector within the jth layer, Eq. 2.2.32.
P_{xj} , P_{zj}	x- and z-components of $\vec{P}_j$, Eq. 2.2.32.
Q , Q_p , Q_s	quality factors, $Q = Q_p$ for P waves and $Q = Q_s$ for S waves, Eq. 2.2.20.
Q_j	quality factor of the jth layer, Eq. 2.2.17.
S_p, S_s	coefficients defined by Eq. 2.3.13b.
t	time.
$TF(j/k)$	transfer function between the motions at the top of layer j and the top of layer k due to incident SH waves, Eq. 2.2.13.
$TF(1/N+1)$	transfer function between the motions at free surface and the top of half-space due to incident SH waves, Eq. 2.2.15.
$TR(\omega)$	transfer function between the motions at free surface and the half-space outcrop due to incident SH waves, Eq. 2.2.16.
$TR_1(\omega)$	transfer function between the motions at free surface and the half-space outcrop in a single layered system due to incident SH waves, Eq. 2.4.1.
$TR_{1e}(\omega)$	transfer function between the motions at free surface and the half-space outcrop in a elastic single-layered system due to incident SH waves, Eq. 2.4.4.
$TR_{hp}(\omega)$, $TR_{vp}(\omega)$	horizontal and vertical transfer functions between the motions at free surface and the half-space outcrop due to incident P waves, Eqs. 2.3.41 and 2.3.42.
$TR_{hs}(\omega)$, $TR_{vs}(\omega)$	horizontal and vertical transfer functions between the motions at free surface and the half-space outcrop due to incident SV waves, Eqs. 2.3.49 and 2.3.50.
u, w	displacements of P and SV waves within the jth layer in the positive x- and positive z-directions, Eqs. 2.3.8 and 2.3.9.
u_0 , w_0	displacements at the free surface in the x- and z-directions due to incident P or SV waves from the half-space, Eq. 2.3.25.
u_{0p} , w_{0p}	displacements at the free surface in the x- and z-directions due to incident P waves from the half-space, Eq. 2.3.34.

u_{0s} , w_{0s}	displacements at the free surface in the x- and z-directions due to incident SV waves from the half-space, Eq. 2.3.43.
u_p' , w_p'	displacements at the half-space outcrop due to incident P waves, Eq. 2.3.39.
u_s' , w_s'	displacements at the half-space outcrop due to incident SV waves, Eq. 2.3.47.
$v_j(z_j,t)$	displacements of SH waves within the jth layer in the y-direction, Eq. 2.2.1.
V_{sj}	viscoelastic shear wave velocity of the jth layer defined by Eq. 2.2.18 (complex-valued).
V , V_p , V_s	viscoelastic wave velocities, $V = V_p$ for P waves and $V = V_s$ for S waves, Eq. 2.2.20 (complex-valued).
V_R ,V_I	real and imaginary parts of V, $V_R > 0$ and $V_I \geq 0$, Eq. 2.2.22.
x	x-coordinate for all layers, Eq. 2.3.1.
$\{X(0)\}_1$	displacement-stress vector at the free surface, Eq. 2.3.25.
$\{X(0)\}_j$	displacement-stress vector at $z_j = 0$ in the jth layer, Eq. 2.3.16.
$\{X(H_j)\}_j$	displacement-stress vector at $z_j = H_j$ in the jth layer, Eq. 2.3.14.
$\{Y\}_j$	potential vector in the jth layer, Eq. 2.3.14.
z_j	z-coordinate for the jth layer, Eq. 2.2.1.
α_j	complex impedance ratio between the jth and the j+1th layer, Eqs. 2.2.6 and 2.2.28.
$[\alpha]_j$	matrix for the jth layer defined by Eq. 2.2.8a.
γ_j	angle between the propagation and attenuation vectors in the jth layer, Eq. 2.2.32.
γ_{N+1}	angle between the propagation and attenuation vectors of incident waves at the half-space, Eq. 2.3.34b.
ζ , ξ	coefficients defined by Eq. 2.3.13c.
ζ_d	critical damping ratio, Eq. 2.2.19.
Θ	propagation angle of SV waves in the jth layer, Eq. 2.3.2a.
Θ_j	propagation angle of SH waves in the jth layer, Eq. 2.2.25.
Θ_{N+1}	incident angle of shear waves at the half-space, Eq. 2.2.30.
ϑ	propagation angle of P waves in the jth layer, Eq. 2.3.2a.
ϑ_{N+1}	incident angle of P waves at the half-space, Fig. 2.4.
κ	horizontal wavenumber defined by Eq. 2.3.4 for P, SV waves and by Eq. 2.2.30a for SH waves.
κ_c	complex wavenumber, P or S wave, defined by Eq. 2.2.21.
κ_R , κ_I	real and imaginary parts of κ_c, $\kappa_R > 0$ and $\kappa_I \leq 0$, Eq. 2.2.21.

κ_p , κ_s	P and SV wavenumbers in the jth layer, Eq. 2.3.3.
κ_{px} , κ_{pz}	horizontal and vertical P wavenumbers in the jth layer, Eq. 2.3.2a.
κ_{sx} , κ_{sz}	horizontal and vertical SV wavenumbers in th jth layer, Eq. 2.3.2b.
κ_{sj}	complex SH wavenumber in the jth layer defined by Eq. 2.2.2.
κ_{sxj} , κ_{szj}	horizontal and vertical SH wavenumbers in the jth layer defined by Eq. 2.2.25.
λ	Lame's constant, Eq. 2.3.10.
μ_j	shear modulus of the jth layer (real-valued), Eq. 2.2.17.
$\overline{\mu}_j$	complex shear modulus of the jth layer defined by Eq. 2.2.17.
ρ_j	mass density of the jth layer, Eq. 2.2.6.
σ_{zz}, σ_{zx}	shear stresses of P and SV waves within the jth layer in the z- and x-directions, respectively, Eqs. 2.3.10 and 2.3.11.
$\tau_j(z_j,t)$	shear stresses of SH waves within the jth layer in the y-direction, Eq. 2.2.3.
φ_j	angle between the propagation vector and the normal to the layer boundary in the jth layer, Eq. 2.2.32.
φ_{N+1}	angle formed by the propagation vector of incident waves from the half-space and the normal to the layer boundary, Eq. 2.3.34a.
Φ	P wave potential in the jth layer, Eq. 2.3.1a.
Ψ	SV wave potential in the jth layer, Eq. 2.3.1b.
ω	frequency, $\omega \geq 0$.

APPENDIX B

Numerical Minimization of a Function of Several Variables by the Method of Steepest Descent

Let F be a real, single-valued function of N real variables $x_1, x_2, \cdots, x_N$. The function F represents the measure-of-fit, J, and $x_1, x_2, \cdots, x_N$ the model parameters in Chapter 4. To minimize the function $F(x_1, x_2, \cdots, x_N)$ with respect to the variables $x_1, x_2, \cdots, x_N$ with no constraint, the method of steepest descent (or the first-order gradient method) is employed in Chapter 4. In what follows, we shall briefly describe this method.

To find the values of $x_1, x_2, \cdots, x_N$ which produce the minimum value of F, we may make initial estimates $x_1^0, x_2^0, \cdots, x_N^0$. A line search is then carried out along the negative gradient direction of F with respect to $x_1, x_2, \cdots, x_N$ at the point $x_1^0, x_2^0, \cdots, x_N^0$. In other words, the method of steepest descent is defined by the iterative alogrithm

$$\begin{Bmatrix} x_1^{k+1} \\ x_2^{k+1} \\ \vdots \\ x_N^{k+1} \end{Bmatrix} = \begin{Bmatrix} x_1^k \\ x_2^k \\ \vdots \\ x_N^k \end{Bmatrix} - s_k \begin{Bmatrix} \frac{\partial F}{\partial x_1}(x_1^k, \cdots, x_N^k) \\ \vdots \\ \frac{\partial F}{\partial x_N}(x_1^k, \cdots, x_N^k) \end{Bmatrix}$$

or in vector form

$$\mathbf{X}^{k+1} = \mathbf{X}^k - s_k\, \mathbf{G}^k$$

where s_k is the non-negative scalar s minimizing $F(\mathbf{X}^k - s\,\mathbf{G}^k)$. Thus, from the point $\mathbf{X}^k$ we search along the direction of the negative gradient $-\mathbf{G}^k$ (evaluated at $\mathbf{X}^k$) to find the point which minimizes F, this minimum point is taken to be

$\mathbf{X}^{k+1}$. The gradient of F is then evaluated at $\mathbf{X}^{k+1}$ and the process is repeated until a selected convergence criterion is satisfied. In problems in which the gradient is difficult to evaluate in closed form, the gradient can be approximately determined by numerical differentiation, i.e., evaluating F near $\mathbf{X}^k$ with one component of $\mathbf{X}^k$ perturbed slightly, the corresponding derivative being then approximated by the ratio of the change in F to the change in that component.

The line search for the minimum point s_k along the negative gradient direction is implemented by taking successive increments of s, that is, $s=0, \delta, 2\delta, \cdots$, and the step-size $\delta>0$. The value of $F(s)=F(\mathbf{X}^k-s\mathbf{G}^k)$ is evaluated at each s and the search terminates with three successive values such that $F(s_{i-1})>F(s_i)$ and $F(s_i)<F(s_{i+1})$ for $s_{i-1}<s_i<s_{i+1}$, so the minimum point lies between s_{i-1} and s_{i+1}. An upward concave parabola is then fit to three such points and the minimum of the parabola is determined at s_{min} which is given by

$$s_{min} = \frac{1}{2}\,\frac{(s_i^2-s_{i+1}^2)F(s_{i-1})+(s_{i+1}^2-s_{i-1}^2)F(s_i)+(s_{i-1}^2-s_i^2)F(s_{i+1})}{(s_i-s_{i+1})F(s_{i-1})+(s_{i+1}-s_{i-1})F(s_i)+(s_{i-1}-s_i)F(s_{i+1})}$$

s_{min} is taken to be the s_k which minimizes F along the line. The value of a new point $\mathbf{X}^{k+1}$ is found and $F(\mathbf{X}^{k+1})$ calculated. If $F(s=\delta)$ is bigger than $F(s=0)$, the value of step-size is too large and the search must be performed by using smaller step-size than δ, for example, $\frac{1}{2}\delta$. In the analysis of Chapter 4, if the fractional change of F between iteration k and k+1 is less than 0.002, convergence is assumed to have occurred and iteration is stopped, otherwise the iterative process is repeated.